

UNIVERSITÉ DU QUÉBEC

MASTER OF SCIENCE THESIS  
SUBMITTED IN PARTICULAR FULFILMENT OF THE REQUIREMENTS FOR  
THE DEGREE OF MASTER OF SCIENCE IN ENGINEERING  
IN THE DEPARTEMENT OF APPLIED SCIENCES AT THE UNIVERSITY OF QUÉBEC  
AT CHICOUTIMI

BY

THOMAS MEENKEN

**Analysis of the cooling capacity of water as a function of its  
quality during DC casting**

Chicoutimi

2002



### Mise en garde/Advice

Afin de rendre accessible au plus grand nombre le résultat des travaux de recherche menés par ses étudiants gradués et dans l'esprit des règles qui régissent le dépôt et la diffusion des mémoires et thèses produits dans cette Institution, **l'Université du Québec à Chicoutimi (UQAC)** est fière de rendre accessible une version complète et gratuite de cette œuvre.

Motivated by a desire to make the results of its graduate students' research accessible to all, and in accordance with the rules governing the acceptance and diffusion of dissertations and theses in this Institution, the **Université du Québec à Chicoutimi (UQAC)** is proud to make a complete version of this work available at no cost to the reader.

L'auteur conserve néanmoins la propriété du droit d'auteur qui protège ce mémoire ou cette thèse. Ni le mémoire ou la thèse ni des extraits substantiels de ceux-ci ne peuvent être imprimés ou autrement reproduits sans son autorisation.

The author retains ownership of the copyright of this dissertation or thesis. Neither the dissertation or thesis, nor substantial extracts from it, may be printed or otherwise reproduced without the author's permission.

## Summary

As in many thermal processing technologies, there is a delicate balance between productivity and quality during ingot cooling process. Higher cooling velocities increase productivity but also create higher temperature gradients inside the ingot. Such a fast cooling does not leave sufficient time to establish the equilibrium within the solid, thus in the most affected surface layer the composition and crystalline structure are different from those in the bulk metal. The heat flux plays a particular role for the production of alloys where different melting points and complex structure formation -depending on the temperature- are present. To prevent the two worst cases - cracking and remelting - during cooling a balance has to be found between good productivity and quality on the one side but also a high security on the other side. To avoid the negative effects of cracking and remelting, it is necessary to determine the heat flux as a function of the influencing parameters and to control the cooling in order to obtain a maximal productivity with the required quality. There is no widely accepted method for the quantitative characterization of the cooling capacity of the water. The cooling may be characterized by the heat transfer coefficients measured in different boiling regimes on the surface or directly by the heat flux. As the fluid flow and heat transfer phenomena are very complicate in the falling liquid-vapour film, using the heat transfer coefficients does not necessarily help the understanding of the underlying mechanisms. However, the correlation between the surface heat flux and temperature for a given surface roughness and water quality includes all the relevant information about the cooling process. Thus in the present project our main objective was to determine the surface

heat flux for a water cooled ingot as a function of the water quality in order to provide a tool for assuring a uniform quality in the cast-shop. A further objective was to improve the understanding of the flow of boiling liquid film along a solid surface. The first challenge in the project was the development of a surface temperature and heat flux measurement method which does not disturb the ingot surface. A heat flux sensor attached onto the surface would have negative effects on the film-nucleate boiling process and increase the surface roughness that affects the nucleation of bubbles. Furthermore it was important that the measurement method be fast responding and sensitive enough to detect very rapid and weak variations in the surface temperature. Thus an innovative surface temperature sensing method - using an open-tip thermocouple - was developed. This sensor was inserted into a null-point cavity from the backside of the aluminium ingot. The open-tip sensor combined with the null-point cavity forms a null-point calorimeter. Using the inverse solution of the general heat conduction equation, it is possible to determine the surface heat flux from the measured temperature history. For the analytical solution of the heat conduction equation in one dimension we used the so called Cook-Felderman equation. It was also investigated how well the assumptions of the Cook-Felderman equation are applicable to the actual conditions in our experimental setup. For this purpose a computer program was developed. The algorithm uses the finite volume approach; the program was written in C++ and calculates the transient 2D temperature distribution in the solid sample. The two-dimensional model uses the measured temperature histories as boundary conditions. The computer predictions were used to determine the horizontal and the vertical heat flux components during the cooling process. Furthermore it was analyzed how the heat flux

results obtained analytically by the Cook-Felderman equation compare to the more detailed numerical solutions. The cooling process is strongly influenced by the different water types and different ingot surfaces. Thus the investigations were focused on the difference between several water types such as tap water (conductivity:  $90\mu S$ ), plant water (conductivity:  $1900\mu S$ ) and water with higher conductivity (conductivity:  $3200\mu S$ ). These water types were tested on different ingot surfaces to eliminate the influence of the surface structure. In addition, the effects of some water additives and a water-oil mixture on the surface heat flux were investigated. The surface temperature measurements were accompanied by a visualization of the surface boiling effects. Furthermore the difference between different ingot surfaces was analyzed. The tests made on machined and a rough surface ingots provided information about the differences in the temperature cooling curves as well as information about the structure of the cooling water film. All collected measurement and visualization data were analyzed to explain the surface flow and boiling effects during the cooling process. The dynamic structure of the falling water film was investigated. Certain characteristics in the temperature cooling curves can be explained with the structure of the water film. We achieved a very good experimental repeatability. We found that the repeatability of the boiling phenomena itself depends on the measurement position (height along the ingot). It was observed that there are more fluctuations on a machined ingot than on a rough surface ingot. Even two different rough plates have different heat flux results. The tests using different water types have shown that there is almost no difference between tap and plant water, neither on a machined nor on a rough ingot. A difference could only be found between tap water and high conductivity water.

## Acknowledgements

I want to thank all those who helped me in my work. I especially thank Mr. Patrice Paquette for his help installing the thermocouples in the plate after each test and spending so much time producing those delicate open thermocouple tips. I would also like to thank Mr. Julien Tremblay, who drilled the precise holes in the plates and also for his help during the work of installation. Other thanks are also to Mr. Yves Lefebvre, who enthusiastically supported the project. His kindness made it a pleasure to work with. A lot of thanks also to Mr. Robert Leveque, Mr. Jean-Francois Landry and all the other people working in the plant of Alcoa Baie-Comeau for their contributions in the fabrication of the experimental setup, providing the samples etc. I want to thank also Romain Gagnon who made the films during the experiments. Last, but not least, I have to thank Prof. Kiss who made this Master thesis possible. I thank him for all his work with me even when I was still in Germany. He taught me everything I know about heat transfer, and much more. Every meeting was an exciting excursion in the world of physics, but he also cared for my personal affairs. In addition I have to thank him for all the ideas he gave for the experimental setup and his patience in correcting this whole work. I want to thank all of my group members who taught me French and cared for me the whole time I was here. I would like to thank my family for providing me with the ability to continue my education. Thanks all of you, thanks for all the ideas, inspiration and support you gave me.

# Contents

<b>Abstract</b>	<b>ii</b>
<b>List of Figures</b>	<b>x</b>
<b>List of Tables</b>	<b>xv</b>
<b>Symbols</b>	<b>xvi</b>
<b>1 Introduction</b>	<b>1</b>
1.1 Motivation . . . . .	1
1.2 Aluminium Production . . . . .	2
1.3 Influencing Parameters . . . . .	3
1.3.1 The Effect of the Material, Size and Shape of the Ingot . . . . .	3
1.3.2 Type of Cooling Water . . . . .	4
1.3.3 Flow Rate, Geometry and Velocity of the Cooling Water Jet . . . . .	4
1.3.4 Water Temperature . . . . .	5
<b>2 Basic Heat Transfer</b>	<b>7</b>
2.1 Boiling Heat Transfer . . . . .	7
2.1.1 Free Convection . . . . .	9
2.1.2 Nucleate Boiling . . . . .	9
2.1.3 Transition Boiling . . . . .	9
2.1.4 Film Boiling . . . . .	10
2.1.5 Influence of Surface Roughness on Bubble Formation . . . . .	10
2.2 Boiling . . . . .	11
2.3 Pool Boiling . . . . .	12
2.4 Flow Boiling in a Duct . . . . .	14
<b>3 Experimental Set-up</b>	<b>17</b>
3.1 Introduction . . . . .	17
3.2 Operating Procedure . . . . .	18
3.3 The Water Supply System . . . . .	22
3.3.1 Flowmeter . . . . .	26

3.3.2	The Pump . . . . .	27
3.4	Data Acquisition System . . . . .	27
3.4.1	The D.A.Q. HP 34970A . . . . .	29
3.5	Reference-block . . . . .	30
3.6	Furnace . . . . .	33
<b>4</b>	<b>Measurement Methods</b>	<b>38</b>
4.1	Introduction . . . . .	38
4.2	Inverse Method . . . . .	39
4.2.1	Simplification of the General Conduction Problem using the Duhamel's Theorem . . . . .	41
4.3	Calorimetry . . . . .	49
4.3.1	Null-Point Calorimeter . . . . .	50
4.3.2	Null-Point Validation . . . . .	54
4.4	Surface Temperature Measurement . . . . .	57
4.4.1	Open Tip Thermocouple . . . . .	58
4.4.2	Thermocouple Installation in the Cavity . . . . .	60
4.4.3	Temperature Conversion . . . . .	64
4.5	Visualization . . . . .	67
4.5.1	Synchronization . . . . .	69
4.5.2	Laser Sheet and other Laser Illumination Methods . . . . .	70
4.6	Test Series . . . . .	72
<b>5</b>	<b>Numerical Simulations</b>	<b>75</b>
5.1	Finite Difference Method . . . . .	75
5.1.1	Theory . . . . .	76
5.1.2	One-Dimensional Model . . . . .	80
5.1.3	Derivations for the One-Dimensional Model . . . . .	82
5.1.4	Curve fitting . . . . .	84
5.1.5	Interpolation . . . . .	86
5.1.6	Results . . . . .	90
5.1.7	Conclusion . . . . .	93
5.2	Finite Volume Method . . . . .	94
5.2.1	Transient Heat Transfer Problems in Solids . . . . .	94
5.2.2	The fully Implicit Scheme . . . . .	97
5.2.3	Set of Equations . . . . .	100
5.2.4	The C++ Source Code . . . . .	101
5.2.5	Comparison of Analytical and Numerical Solutions . . . . .	108
5.2.6	Numerical Solutions from the FVM Code . . . . .	118
<b>6</b>	<b>Experimental Results</b>	<b>155</b>
6.1	Different Plates . . . . .	155
6.2	Influence of Different Water Types . . . . .	160
6.3	Water with Additives . . . . .	169
6.3.1	Biodispersant . . . . .	170

6.3.2	Surfactant . . . . .	173
6.3.3	Water-Oil Mixture . . . . .	184
6.4	Mechanism of Cooling . . . . .	191
6.5	Structure of the Falling Water Film . . . . .	192
6.5.1	Three Dimensional Surface Water Flow . . . . .	194
6.5.2	Wetted Zone . . . . .	197
6.5.3	Unstable Film Boiling . . . . .	197
6.5.4	Stable Vapor Film . . . . .	198
6.5.5	Disintegrating Water Jet . . . . .	199
6.6	Characteristics of the Cooling Curves . . . . .	200
6.6.1	Temperature Drop before the Re-wetting Zone passed . . . . .	200
6.6.2	The Positioning of the Measurement Points Along a Rough Surface . . . . .	204
6.6.3	Re-wetting . . . . .	209
6.7	Repeatability of the Boiling Phenomena . . . . .	214
6.7.1	Repeatability depending on the Measurement Position . . . . .	217
6.7.2	Scale Deposition . . . . .	221
<b>7</b>	<b>Conclusions</b>	<b>222</b>
7.1	Experimental Results . . . . .	223
7.1.1	Repeatability . . . . .	225
7.1.2	Comparison of a Machined and a Rough Ingot . . . . .	225
7.1.3	Different Water Types and Additives . . . . .	225
7.1.4	Characteristics of the cooling curves . . . . .	226
7.1.5	Summary . . . . .	227
7.2	Numerical Results . . . . .	228
7.3	Short Conclusions from the Comparison of the Numerical and Analytical Results . . . . .	229
7.4	Short Experimental Conclusions . . . . .	229
	<b>Bibliography</b>	<b>231</b>
	<b>A Voltage to Temperature Conversion Mathcad Worksheet</b>	<b>234</b>
	<b>B Main Calculation Loop</b>	<b>236</b>
	<b>C Heat Flux Determination with Matlab Worksheet</b>	<b>239</b>
	<b>D Mathcad Worksheet</b>	<b>241</b>
D.1	Comparison Analytical and Numerical Solution . . . . .	241
D.2	Measurement Data Work Sheet . . . . .	242
	<b>E Finite Volume Program Code</b>	<b>243</b>
E.1	Finite Volume Source Code in C++ . . . . .	243

# List of Figures

1.1	Industrial ingot casting process . . . . .	2
2.1	Different boiling regimes of a heated horizontal wire [6] . . . . .	8
2.2	Formation of nucleate sites [6] . . . . .	10
2.3	Pool and flow boiling regimes . . . . .	12
2.4	Cavities on the surface serve as nucleation sites and help bubble formation [8] . . . . .	13
2.5	Boiling regimes in a duct [5] . . . . .	15
3.1	Photo of the mounted ingot . . . . .	18
3.2	Sketch of the ingot heating and cooling process . . . . .	19
3.3	Mould adjusted in front of the ingot . . . . .	20
3.4	Experimental setup scheme . . . . .	21
3.5	Main hardware of the experiment . . . . .	22
3.6	Working schedule for the experiment . . . . .	23
3.7	Water system . . . . .	25
3.8	Data acquisition used as measure and control unit . . . . .	28
3.9	Drawing of the reference-block . . . . .	32
3.10	Copper-thermocouple wire connection . . . . .	33
3.11	Reference block . . . . .	34
3.12	Furnace with its door and the mould . . . . .	34
3.13	Heater distribution inside the furnace . . . . .	35
3.14	Arrangement of the heating elements . . . . .	36
4.1	Unit step input at the surface and response function within the body . . . . .	43
4.2	Combination of unit step functions to imitate the real surface temperature history . . . . .	43
4.3	Gauge notation for thin and thick films . . . . .	50
4.4	Conceptual sketch of the null-point calorimeter . . . . .	51
4.5	Sensor installed in a calorimeter mass without a cavity . . . . .	53
4.6	Calorimetric mass with a huge cavity in the backside . . . . .	53
4.7	Null-point calorimeter analytical time response data [4] . . . . .	55
4.8	Null-point calorimeter analytical time response data (2) [4] . . . . .	56

4.9	Error Occuring when the sensor is not correctly placed. [4]	56
4.10	Thermocouple tip (closed, ungrounded)	57
4.11	Thermocouple prepared for installation with high temperature cement	58
4.12	Thermocouple in the null point cavity	59
4.13	Pendulum weight for the thermocouple	60
4.14	Measurement table	61
4.15	Ingot surface roughness	61
4.16	3-D map of a part of the ingot surface	62
4.17	Specialy developed cavity drill	63
4.18	Thermocouple position	65
4.19	Thermocouple temperature vs. voltage graph [17]	65
4.20	Seebeck coefficient vs. temperature [17]	66
4.21	Laser pointer synchronisation	70
4.22	Laser sheet to illuminate the re-wetting zone	71
4.23	List of experiments	73
5.1	Sketch of the slab with dimensions	81
5.2	Sketch of the boundary condition in one-dimension	81
5.3	Calculation loop for the one-dimensional model	83
5.4	Cook Felderman equation	85
5.5	Heat flux from numerical model and Cook F. equation	85
5.6	Curve fit algorithm	87
5.7	Surface heat flux comparison	88
5.8	Percent difference of the curve fit algorithm and finite difference results with the Cook Felderman equation	88
5.9	Interpolation loop	89
5.10	Result of analytically and numerically determined surface heat flux.	90
5.11	measured surface temperature in degree Celsius	91
5.12	Difference in percent between numerical and analytical solution	92
5.13	Difference of numerical and analytical solution with double slab thickness.	93
5.14	Two-dimensional Grid	96
5.15	Example for the curve interpolation	103
5.16	First step in the curve interoplation	103
5.17	Curve interpolation example using real cooling curves	105
5.18	Block diagram for the class correlation of the finite volume source code	107
5.19	Boundary conditions for the worked example	109
5.20	3D plot of analytical (dashed colormap) and numerical solution	112
5.21	Difference in percents between the numerical and analytical solution after 6 sec.	113
5.22	Difference in percents of the south est node	115
5.23	Analytical calculated temperature distribution at instant t=0	116
5.24	Difference between analytical and numerical solution at different points	117
5.25	Measured and interpolated temperature curves form point TC2	120
5.26	Influence of node numbers on the vertical component of the surface heat flux	121
5.27	Measured and interpolated temperature curves from 16.05.02 at point TC3	122

5.28 Measured and interpolated temperature curves from 20.02.02 at point TC2 123

5.29 Measured and interpolated temperature curves from 20.02.02 at point TC3 124

5.30 Comparison of the vertical heat flux from the test 16.05.02 and 20.02.02 . 125

5.31 Temperature curves from the 16.05.02 and the 20.02.02 . . . . . 126

5.32 Comparison of the vertical surface heat flux from the measurements 16.05.02 and 20.02.02 at point TC3 . . . . . 127

5.33 Function to fit the surface temperature points . . . . . 128

5.34 Interpolation of the temperature values at a given time step . . . . . 129

5.35 Regression of the surface temperature values . . . . . 129

5.36 Vertical surface heat flux calculated with three different methods . . . . . 130

5.37 Interpolation and its derivative . . . . . 131

5.38 Vertical heat flux distribution inside the plate for a random instant of time 133

5.39 Temperature distribution inside the plate . . . . . 134

5.40 Boundary conditions for the numerical model . . . . . 136

5.41 Different approximation methods to obtain the horizontal heat flux . . . . . 138

5.42 Difference between the approximation methods used . . . . . 139

5.43 Horizontal heat flux result from the measurement on the 16.05.2002 at TC2 140

5.44 Heat Flux at all measurement points . . . . . 141

5.45 Temperature histories from measurement 16.05.2002 . . . . . 141

5.46 Horizontal heat flux distribution inside the plate . . . . . 142

5.47 Temperature distribution for one of the last time steps . . . . . 143

5.48 Maximal heat flux during the cooling at the measurement position TC1 . 144

5.49 Horizontal heat flux at a random time step from measurement 16.05.2002 . 145

5.50 Heat flux : Cook Felderman Eq. and Regression . . . . . 147

5.51 Relative difference between the Cook Felderman solution and the numerical results . . . . . 147

5.52 Heat Flux at TC3 . . . . . 148

5.53 Relative difference in percents at TC3 . . . . . 149

5.54 Difference in percents from the measurement on 20.02.2002 . . . . . 150

5.55 Difference in percent from measurement data 16.05.2002 . . . . . 151

5.56 Difference in percents from measurement data 04.10.2002 . . . . . 152

5.57 Heat flux results from finite volume model and Cook Felderman equation . 153

6.1 Temperature measurement of experiment 08.10.2001 carried out using tap water on a machined ingot . . . . . 156

6.2 Rough surface experiment of 04.10.2001 carried out using tap water . . . . 157

6.3 Data of 08.05.2002 carried out using tap water on rough surface ingot . . . 157

6.4 Results from experiment 16.05.2002 carried out using a third rough surface plate . . . . . 158

6.5 Heat flux to temperature graph for measurement point TC2 . . . . . 159

6.6 Comparison of rough and machined ingots at measurement point TC3 . . 159

6.7 Temperature curves on a machined ingot at position TC2 (a) . . . . . 161

6.8 Temperature curves on machined ingot at position TC2 (b) . . . . . 162

6.9 Comparison of different water types on a machined ingot in a heat flux to temperature graph (TC2) . . . . . 163

6.10	Comparison of different water types on a rough ingot at position TC2 . . .	164
6.11	Measurement results on machined ingot at position TC3 . . . . .	165
6.12	Temperature curves on machined ingot at position TC4 . . . . .	166
6.13	Temperature history on a rough ingot at position TC3 . . . . .	167
6.14	Heat flux to temperature graph on machined ingot at position TC3 . . . .	168
6.15	Heat flux to temperature result on rough ingot at TC3 . . . . .	169
6.16	Surface temperature results from 22.04.2002 made with BIODISPERSANT	170
6.17	Surface temperature measurements from 25.04.2002 made with BIODIS- PERSANT on a rough ingot . . . . .	171
6.18	Experiment with tap water on the same rough ingot as for the biodispersant tests . . . . .	172
6.19	Comparison of heat flux measured using tap and biodispersant water at position TC3 . . . . .	172
6.20	Comparison of heat flux measured using tap and biodispersant water at position TC2 . . . . .	173
6.21	Comparison of heat flux measured using tap and biodispersant water at position TC3 . . . . .	174
6.22	Comparison of heat flux measured using tap and biodispersant water at position TC4 . . . . .	175
6.23	Cooling curves on the 26.04.2002 with 50 mg/l surfactant . . . . .	176
6.24	Cooling curves on the 10.05.2002 with 50 mg/l surfactant . . . . .	177
6.25	Heat flux comparison between tap and surfactant water at position TC1 .	178
6.26	Heat flux comparison between tap and surfactant water at position TC3 .	179
6.27	Heat flux comparison between tap and surfactant water at position TC4 .	180
6.28	Reference test with tap water on the rough surface ingot PL 3 . . . . .	181
6.29	Test on the 22.05.2002 made on plate PL 3 with 50 mg/l Solve CA . . . .	182
6.30	Test made on the 23.05.2002 with 250 mg/l surfactant on rough surface ingot PL 3 . . . . .	183
6.31	Reference measurement on a rough surface ingot (PL3) with tap water . .	185
6.32	Water-oil mixture on a rough surface ingot (PL3) on the 16.08.2002 . . . .	186
6.33	Water-oil mixture on a rough surface ingot (PL3) on the 19.08.2002 . . . .	187
6.34	Water-oil mixture on a rough surfacae ingot (PL3) on the 23.08.2002 . . . .	188
6.35	Heat flux vs time data using tap water on rough surface ingot (PL3) on the 16.05.2002 . . . . .	189
6.36	Heat flux vs time data using t water-oil mixture on a rough surface ingot (PL3) on the 16.08.2002 . . . . .	190
6.37	Temperature relapse during the water-oil mixture cooling . . . . .	190
6.38	Difference between tap water and water-oil mixture . . . . .	191
6.39	Vertical Leidenfrost effect . . . . .	193
6.40	Droplet separation from the surface . . . . .	193
6.41	Separated water film . . . . .	194
6.42	Four zones along the ingot . . . . .	195
6.43	Separating water jets . . . . .	196
6.44	Wavy water film at the surface . . . . .	196

6.45	Wavy surface water film (horizontal section) . . . . .	197
6.46	Estimated wetted zone borders . . . . .	198
6.47	Heat radiation causes evaporation of the covering water film . . . . .	199
6.48	Temperature measurement on a machined ingot . . . . .	200
6.49	Water film touches the surface due to its wavy setup . . . . .	202
6.50	Stable cooling film . . . . .	203
6.51	Less distinct behavior on a rough ingot . . . . .	204
6.52	Temperature relapse during the main cooling fall . . . . .	205
6.53	Surface structure around the measurement point TC1 on plate A . . . . .	206
6.54	Surface structure around measurement point TC1 on plate B . . . . .	206
6.55	Magnified temperature relapse . . . . .	207
6.56	Unstable vapor layer which collapses . . . . .	208
6.57	Temperature relapse at measurement position TC2 . . . . .	208
6.58	Straight re-wetting zone of test 20.02.2002 on a rough surface ingot . . . . .	209
6.59	Curved re-wetting zone of experiment 22.04.2002 . . . . .	210
6.60	Curved re-wetting zone of experiment 23.04.2002 . . . . .	211
6.61	Series of pictures during the cooling from experiment 22.04.2002 . . . . .	212
6.62	Photo of the plate deformation . . . . .	213
6.63	Deformation of the plate (bottom view) . . . . .	214
6.64	Measurement results made with a machined ingot and tap water . . . . .	215
6.65	Heat flux results on a rough surface ingot with tap water at TC3 . . . . .	216
6.66	Heat flux vs temperature data at the measurement point TC2 on machined ingot . . . . .	217
6.67	Heat flux vs temperature at the measurement point TC2 . . . . .	218
6.68	Results at measurement point TC4 . . . . .	219
6.69	Results at measurement point TC4 on a rough ingot . . . . .	220
7.1	Comparison of the tests and their results . . . . .	224

# List of Tables

4.1	Hole positions . . . . .	64
4.2	Polynomial coefficients . . . . .	67
4.3	Conversion coefficients . . . . .	68
5.1	Model parameter . . . . .	84
5.2	Start parameters . . . . .	90

# Symbols

$A$	area, $m^2$
$b$	effusivity or lumped thermal parameter = $\sqrt{k\rho c}$ , $\frac{J}{m^2 K s^{\frac{1}{2}}}$
$Bi$	Biot number
$Bi^*$	Biot number for finite-difference method
$C$	heat capacity rate, $\frac{W}{K}$
$C_t$	thermal capacitance, $\frac{J}{K}$
$c_p$	specific heat at constant pressure, $\frac{J}{kg K}$
$D$	diameter, m
$E$	thermal (sensible) internal energy, J
$\dot{E}_g$	rate of energy generation, W
$\dot{E}_{in}$	rate of energy transfer into a control volume, W
$\dot{E}_{out}$	rate of energy transfer out of a control volume, W
$\dot{E}_{st}$	rate of increase of energy stored within a control volume, W
$e_{AB}$	Seebeck voltage, V
$Fo$	Fourier number
$f$	friction factor
$g$	gravitational acceleration, $\frac{m}{s^2}$
$h$	convection heat transfer coefficient, $\frac{W}{m^2 K}$
$k$	thermal conductivity, $\frac{W}{m K}$
$L$	length, m
$m$	mass, kg
$M$	Module = $\frac{(\Delta x)^2}{\alpha \Delta t}$
$p$	pressure, Pa
$Q$	energy transfer, J
$q$	heat transfer rate, W
$\dot{q}$	rate of energy generation per unit volume, $\frac{W}{m^3}$
$q'$	heat transfer rate per unit length, $\frac{W}{m}$
$q''$	heat flux, $\frac{W}{m^2}$
Re	Reynolds number
$R_t$	thermal resistance, $\frac{K}{W}$
$T$	temperature, K or $^{\circ}C$
$t$	time, s
$V$	volume, $m^3$
$x, y, z$	rectangular cartesian coordinates, m
$\alpha_s$	Seebeck coefficient, $\frac{V}{^{\circ}C}$
$\alpha$	thermal diffusivity = $\frac{k}{\rho c}$ , $\frac{m^2}{s}$
$\rho$	density, $\frac{kg}{m^3}$
$\nabla$	nabla operator, $m^{-1}$
$\tau$	time, time variable for differentiation or integration, s

# Chapter 1

## Introduction

### 1.1 Motivation

As in many thermal processing technologies, there is a delicate balance between productivity and quality during ingot cooling process [13]. Higher cooling velocities increase productivity but also create higher temperature gradients inside the ingot. Such a fast cooling does not leave sufficient time to establish the equilibrium within the solid, thus in the most affected surface layer the composition and crystalline structure are different from those in the bulk metal. The heat flux plays a particular role for the production of alloys where different melting points and complex structure formations which are dependent on the temperature are present. To prevent the two worst cases -cracking and remelting- during cooling a balance has to be found between good productivity and quality on the one side but also a high security on the other side. The first main problem - cracks in the surface layer - occurs because the thermal stress depends on the temperature gradients; therefore fast non-uniform cooling can lead to thermal cracking of the ingot. The opposite happens if

the cooling is interrupted or insufficient. The hot liquid metal in the core of the ingot will then remelt the already established crust on the surface and the hot liquid metal flows out. To avoid this negative effect it is necessary to determine the heat flux as a function of the surrounding parameters and to control the cooling to obtain a maximal productivity with best quality. But also the question of safety involves the determination of heat flux and the cooling system for the reasons mentioned above.

## 1.2 Aluminium Production

In this section, the part of the industrial aluminium production that is related to the present project will be described. The casting process to produce an aluminium ingot, is illustrated in Figure 1.1. Liquid aluminium first solidifies on a downward moving starter

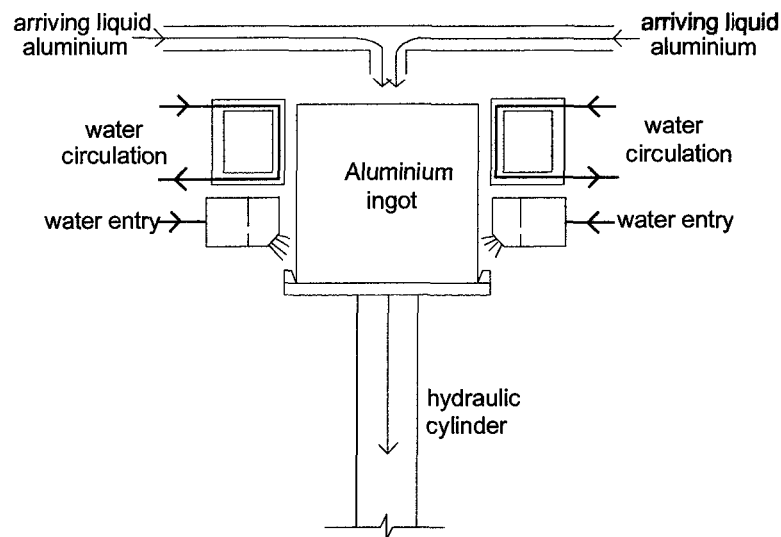


Figure 1.1: Industrial ingot casting process

plate and is cooled by a surrounding heat exchanger first. The plate carrying the ingot is

mounted to a hydraulic cylinder which moves slowly downwards. When the plate leaves the heat exchanger the outer surface of the aluminium is already in solid state. Under the heat exchanger a mould is mounted which sprays a water curtain on the ingot to cool it. This water film includes chemicals to avoid the oxidation of the ingot surface and cools the ingot by convection-boiling. This part of the process will be studied in order to determine the heat flux. The heat transfer between the surface of the ingot and the planar water jet has a rather complex character. The phenomena of jet -impingement, single phase film cooling, bubble and film- boiling- all are present. The used water is recycled and can be reutilized after treatment and recooling. Because of this procedure it is also of interest to determine the effects of water-quality corresponding to the different phases of the boiling process as a function of the surface temperature.

## **1.3 Influencing Parameters**

### **1.3.1 The Effect of the Material, Size and Shape of the Ingot**

The concept of the heat transfer coefficient was used in order to facilitate the analysis without solving the complicate heat transport problem in the solid-liquid system. Unfortunately in the ingot-water jet system the external cooling effect of the water is not independent of the heat conduction within the solid. Many important qualitative features of the flow, like for example the onset of boiling, the transition between bubble and film boiling depends on the local temperatures and their variation along the solid surface. These temperatures are influenced by the heat conduction within the ingot. This mechanism indicated above have a consequence on the selection of the appropriate measurement technique,

as the values of the heat transfer coefficient depend on the material and even on the size of the solid used in the experiments. The solid sample should have the same planar shape and the same surface roughness as the real ingot to assure that the bubble formation on the surface will be similar. Because the micro-geometry of the surface of the ingot, small solid particle depositions determine mostly the number of nucleation centers.

### **1.3.2 Type of Cooling Water**

The cooling water contains several foreign materials like casting lubricants, gases, dissolved or particulate solids which may effect the heat transfer between the ingot and water-film. For example the surface tension of a liquid depends on the amount of additives in it. The property of the water changes also if carbon dioxide gas is dissolved in the liquid because the gas reduces the equivalent conductivity of the water jet. Due to this reason, the cooling capacity of the water is affected by its composition not only because the additives or foreign materials change the thermal conductivity, but also because of their effect on the boiling characteristics. The presence of a continuous solid (aluminium-oxide) or liquid layers (for example lubricants) affects the re-attachment of the liquid at the transition from film boiling to nucleate boiling via the surface tension.

### **1.3.3 Flow Rate, Geometry and Velocity of the Cooling Water Jet**

The flow rate of the cooling water affects the heat transfer significantly via various mechanisms. First; the heating of the water along the contact surface depends on the mass flow rate. The average temperature along the interface of the falling film at different heights is formed by intermittent single or two phase flow as well as the different boiling regimes like

nucleate and film boiling. Furthermore, the velocity of the water affects the heat transfer in the single phase flow domain as well as the bubble behavior in the boiling zone. The shape of the jet is given as a continuous water-film. The geometrical properties like the angle of attack, flatness and contraction of the jet may be varied. A mould similar to that used in industry was chosen.

### 1.3.4 Water Temperature

The water temperature plays an important role in the heat removal because of the direct and indirect effect via heat transfer coefficient. These effects can be seen in the following equation.

$$Q = \int_A h_{local} \cdot (T_w - T_{fluid}) dA \quad (1.1a)$$

$$T_w = f(x), T_{fluid} = f(x), h_{local} = f(x) \quad (1.1b)$$

where  $Q$  is the total heat flow rate through the  $A$  cooled surface of the ingot,  $h_{local}$  is the local heat transfer coefficient,  $T_w$  and  $T_{fluid}$  are the surface and coolant temperatures, respectively. The temperatures and the heat transfer coefficient depend on the height  $x$  of the contact surface as it is remarked in Equation 1.1a. Furthermore the  $h_{local}$  depends also on the coolant temperature  $T_{fluid}$  that makes it very difficult to characterize the cooling potential of the water. Therefore it is necessary to apply an appropriate averaging procedure to characterize the existing local driving force of heat transfer. As it is easy to measure the water temperature in the mould, the heat transfer coefficient can be related to this value using the equation given below:

$$Q = h_{average} \cdot A \cdot (T_{w,average} - T_{fluid})$$

where  $h_{average}$  and  $T_{w,average}$  are the average values of the heat transfer coefficients and surface temperatures, respectively (Ref. [13]).

## Chapter 2

# Basic Heat Transfer

### 2.1 Boiling Heat Transfer

Boiling takes place when a heated surface is exposed to a liquid and the surface temperature is above the saturation temperature of the liquid. The heat flux will depend on the difference between the surface and the saturation temperatures. When a heated surface is submerged below a free surface of a large mass of liquid this process is called *pool boiling*. We will refer in all the following description to this process because it has been extensively studied and it helps to explain the conditions in our experiment. We differentiate between two boiling modes; the *saturated*, or *bulk boiling* and the *subcooled*, *local* or *surface boiling*. The saturated boiling correspond to a liquid maintained at its saturation temperature. Bubbles formed at the surface are then propelled through the liquid by buoyancy forces and escaping eventually from a free surface. In contrast to that is the subcooled boiling which occurs if the temperature of the liquid is below the saturation temperature and bubbles formed at the surface may condense in the liquid (Ref. [6]).

The different regimes of *saturated pool boiling* are indicated in Figure 2.1 where the heat flux data from an electrically heated platinum wire submerged in water are plotted against the temperature excess  $\Delta T_e = T_{wire} - T_{sat}$ . We differentiate between the following boiling regimes: free convection, nucleate boiling, transition boiling and film boiling. These different boiling regimes may be delineated according to the value of  $\Delta T_e$  shown in Figure 2.1.

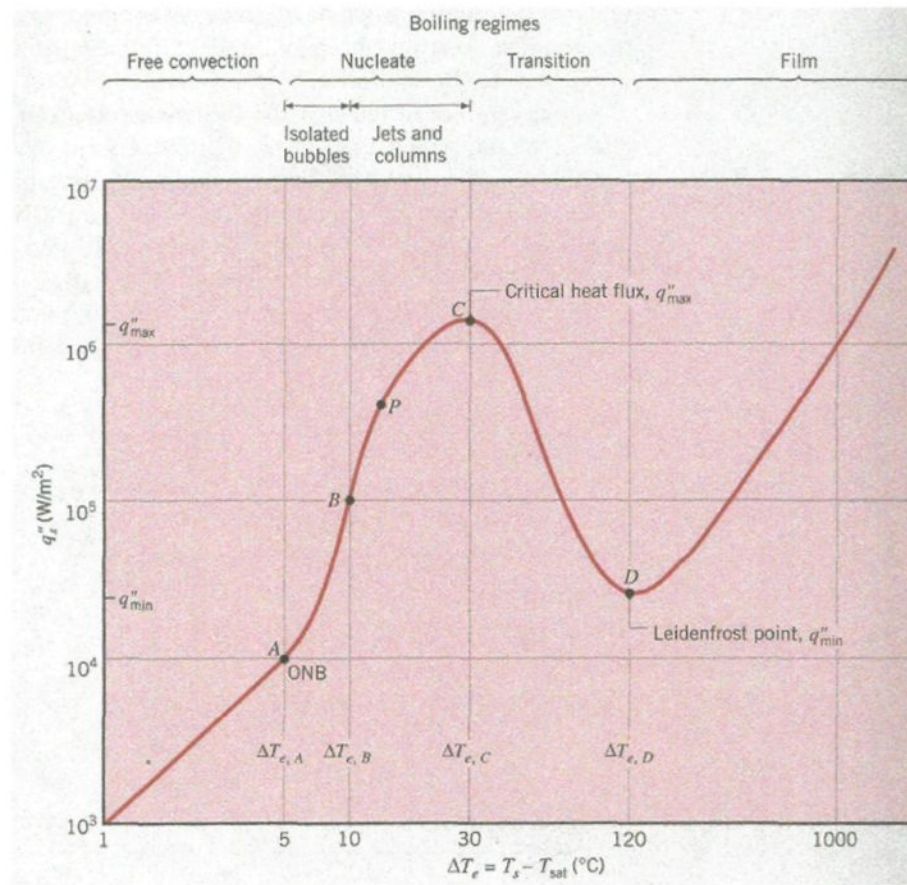


Figure 2.1: Different boiling regimes of a heated horizontal wire [6]

### 2.1.1 Free Convection

Free convection exists if  $\Delta T_e \lesssim 5^\circ C$ . In this region free-convection currents are responsible for the motion of the fluid near the heated surface and when the slightly superheated liquid rises to the surface it subsequently evaporates.

### 2.1.2 Nucleate Boiling

Nucleate boiling occurs in the range  $5^\circ C \lesssim \Delta T_e \lesssim 30^\circ C$ . In this range, two different flow regimes may be distinguished. In the region A-B bubbles begin to form on the surface of the wire and are dissipated in the liquid after breaking away from the surface. This separation induces considerable fluid mixing near the surface that increases  $q''_s$  as can be seen in Figure 2.1 and  $h$  the convection heat transfer coefficient. In this region most of the heat exchange is through direct transfer from the surface to liquid in motion at the surface, and not through the vapor bubbles rising from the surface. This change in the next region B-C in Figure 2.1 where more nucleation sites become active and increased bubble formation causes bubble interference and coalescence. This leads to escaping vapor as *jets* or *columns*, which subsequently merge into slugs of the vapor. At the point C of Figure 2.1 considerable vapor is being formed, making it difficult for the liquid to continuously wet the surface. The maximum heat flux, termed *critical heat flux*, is limited here because further increase in  $\Delta T_e$  is balanced by the reduction in the convection heat transfer coefficient  $h$ .

### 2.1.3 Transition Boiling

The region corresponding to  $30^\circ C \lesssim \Delta T_e \lesssim 120^\circ$  (see Figure 2.1) is termed *transition boiling*, *unstable film boiling*, or *partial film boiling*. The bubble formation is now so

rapid that a vapor film or blanket begins to form on the surface. There exists an oscillation between film and nucleate boiling but the part of the total surface covered by the film increases with increasing  $\Delta T_e$ . The thermal conductivity of the vapor is much less than that of the liquid, which means that the vapor isolates the hot surface from the liquid, therefore the heat flux  $q''$  decreases.

#### 2.1.4 Film Boiling

The film boiling regime exists for  $\Delta T_e \gtrsim 120^\circ C$ . At the point D in Figure 2.1 the heat flux has a minimum because the surface is completely covered by a vapor film. At this point, referred to as the *Leidenfrost point*, the heat transfer from the surface to the liquid occurs by the conditions through the vapor. As the surface temperature is increased, radiation through the vapor film becomes significant and the heat flux increases again with increasing  $\Delta T_e$ .

#### 2.1.5 Influence of Surface Roughness on Bubble Formation

The influence of surface roughness on the maximum heat flux is negligible. However, increased surface roughness can cause a large increase in heat flux for the nucleate boiling regime. This effect corresponds to numerous cavities in a rough surface that serve

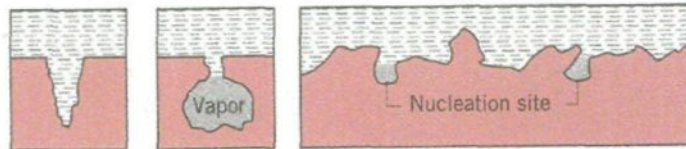


Figure 2.2: Formation of nucleate sites [6]

to trap vapor (Figure 2.2). These traps provide more and larger sites for bubble growth. It follows that the nucleation site density for a rough surface can be substantially larger than that for a smooth surface.

## 2.2 Boiling

Under this section we will discuss in detail the pool and flow boiling regimes that were already mentioned before. With the principles described below the occurring physical effects in the cooling water jet can be estimated and understood. At this moment there are not sufficient data available and not enough investigation done to be sure what exactly happens in the jet but it will be a main point of research in the future to determine all participating effects in the cooling jet. In Figure 2.3 the two main regimes namely pool and flow boiling are illustrated with their sub divisions. The pool boiling is well understood thus theoretical and experimental information can be found in almost each heat transfer book. The flow boiling in a tube is more complex but it was investigated thoroughly because of its importance in the reactor technology and heat exchangers. Many experimental methods as well as mathematical models exists to describe the flow and thermal effects. The special kind of flow boiling in a liquid film on the surface of a solid -in a water curtain- marked with a red frame in Figure 2.3, is not much investigated and there is no quantitative description of the internal mechanism available.

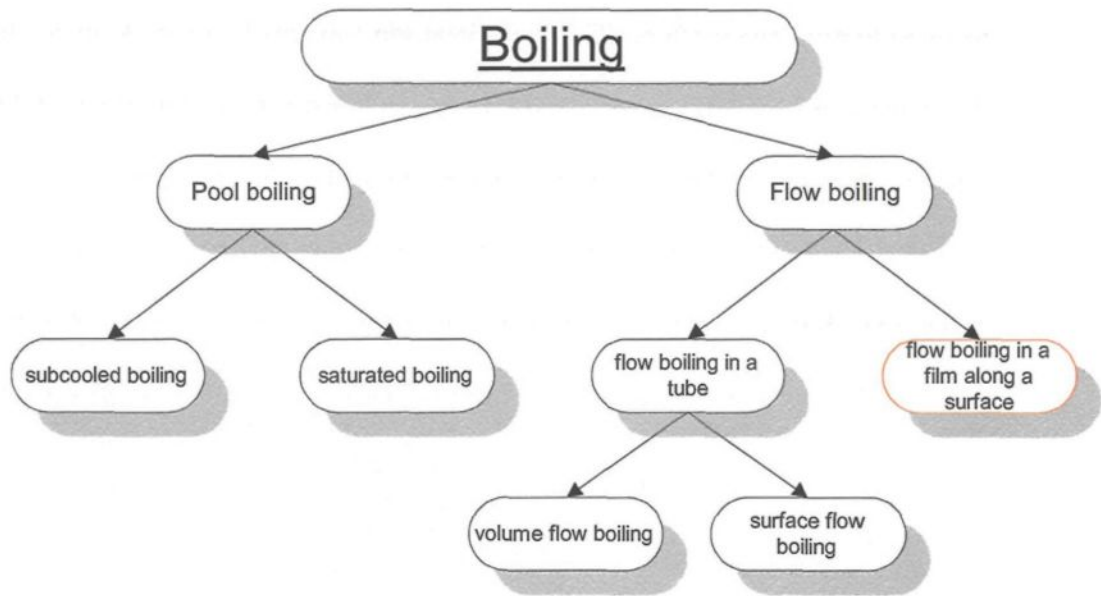


Figure 2.3: Pool and flow boiling regimes

## 2.3 Pool Boiling

The knowledge of the basic phenomena in pool boiling helps the understanding of other boiling regimes. For the interpretation of our experiments, the notion of subcooled boiling is especially important. As already mentioned in Chapter 2.1, the pool boiling starts when a heated surface submerged in a pool of water reaches the saturation temperature. Local boiling in the vicinity of the surface may take place even if the bulk temperature is below the boiling point. We call this process, where a liquid whose bulk temperature is below the saturation temperature but whose boundary layer is sufficiently superheated that bubbles form next to the heating surface, *subcooled pool boiling*. When the temperature reaches this point in certain places, known as nucleate sites, vapor bubbles are formed. Nucleation sites are very small inclusions in the surface which result from the process used

to manufacture the surface. The inclusions are too small to admit liquid because of the liquid surface tension and the resulting vapor pocket acts as a site for bubble growth, as illustrated in Figure 2.4. If the bubble is released, liquid flows over the inclusion trapping vapor, thus providing a start for the next bubble. The bubbles are at first small and collapse before reaching the surface, or if they are not released from the nucleation site, their volume may oscillate or collapse. An oscillation may occur when a bubble grows and pushes the

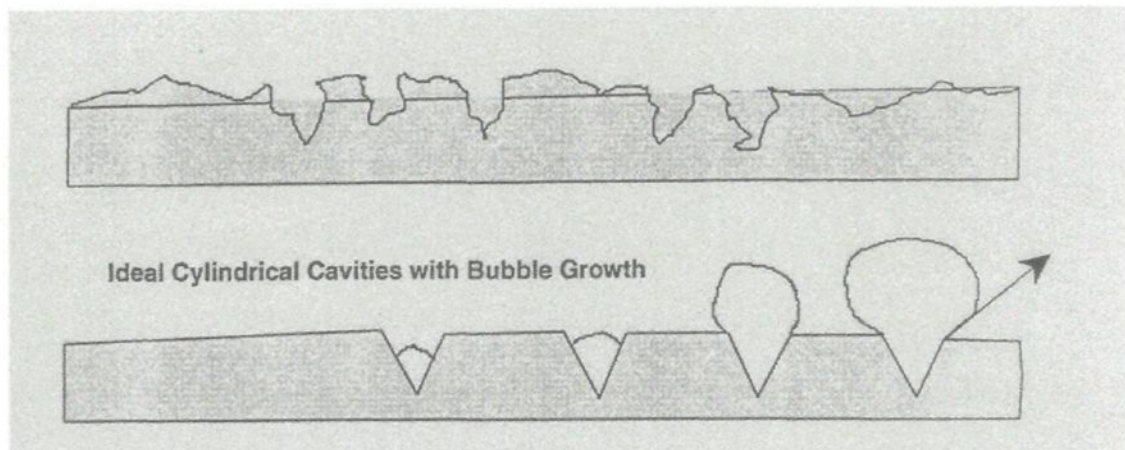


Figure 2.4: Cavities on the surface serve as nucleation sites and help bubble formation [8]

layer of superheated liquid above it away into the cooler liquid above. The top of the bubble surface extend into a cooler liquid where it loses more heat than it received by conduction from the heating surface. The inertia force have been dissipated and the bubble begins to shrink until its surface is again submerged under the superheated liquid layer that is at saturation temperature. Then the growth of the bubble restarts and the oscillation takes place. In the case when the bubble is not oscillating or collapsing on the surface, it may be carried away by buoyancy forces or convection forces. The bubbles increase in number while

their average lifetime decreases with decreasing bulk temperature at a given heat flux. As vapor bubbles form and grow on the heating surface, they push hot liquid from the vicinity of the surface into the colder bulk of the liquid. The intense micro-convection currents that set up when vapor bubbles are emitted and colder liquid from the bulk rushes toward the surface to fill the void is one effect why the heat flux increases and the temperature rises more strongly. The second effect is caused by the energy transfer from a condensating bubble to the surrounding liquid. Because of the phase change from vapor to liquid the bubble condensation rises the temperature of the surrounding liquid strongly.

When the bulk is heated to the saturation temperature by these effects the occurring regime is called *saturated boiling*. The bubble formation and growth on the surface is the same as already explained before. In the saturated boiling the bubble released from the surface rises forced by its buoyancy to the free liquid surface. The enclosed trapped vapor from the escaped bubble provides the conditions for a new bubble formation. See also Section 2.1.

## 2.4 Flow Boiling in a Duct

Also termed *boiling in forced convection*, flow boiling plays an important role in the design of boiling nuclear reactors, thermal control systems for spacecraft and space power plants, and other advanced power-production methods. However, the large number of experimental and analytical investigations which have been conducted in this area, it is not yet possible to predict all of the heat transfer, pressure drop and other characteristics of this process quantitatively. This is due to the complexity of two phase flow pattern and the

consequently large number of dependant variables due to the vapor-liquid mixture. Because of the sufficient observations a qualitative description of the process is possible. Below a few regimes will be denoted. We will consider a fluid at a temperature below its boiling point that enters a heated vertical duct which is heated so that progressive vaporization occurs. In Figure 2.5 part e a qualitative graph is shown on which the heat transfer coefficient at a specific location is plotted as a function of the local quality. Here the quality is defined

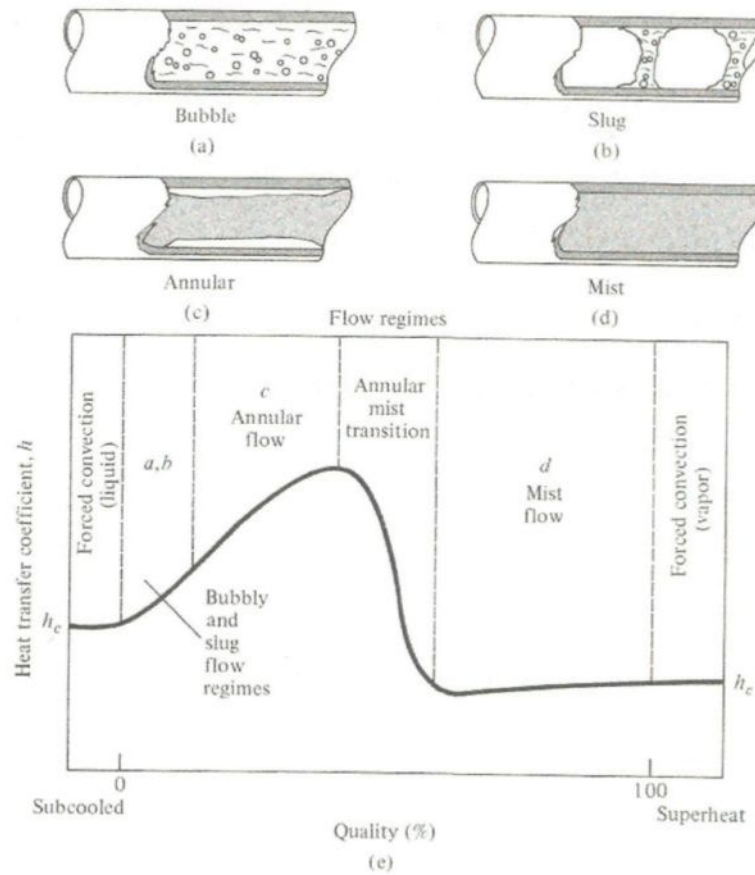


Figure 2.5: Boiling regimes in a duct [5]

as the ratio of a volume of vapor to a volume in the duct whereby the duct volume is filled

with water. As the fluid bulk temperature increases toward its saturation point, bubbles will begin to form at nucleation sites as known from the description of pool boiling. Then they will be carried away into the main stream as schematically illustrated in Figure 2.5 part a. This regime is known as the *bubbly-flow-regime*. Bubble flow occurs only at a very low quality and consists of individual bubbles of vapor entrained in the main flow.

As the vapor volume fraction increases, the individual bubbles begin to agglomerate and form plugs of vapor as shown in Figure 2.5 part b. Although in this regime, termed *slug-flow* regime, the mass fraction of vapor is generally much less than 1 percent, as much as 50 percent of the volume fraction may be vapor and the fluid velocity in the slug-flow regime may increase appreciably. The plugs of vapor are compressible which also produce flow oscillations within the duct even if the entering flow is steady. The heat transfer coefficient rises because of the increased liquid velocity as it can be seen in Figure 2.5 part e.

As the fluid flows farther along in the tube and the quality increases, a third flow regime, commonly known as the *annular flow* regime, appears. In this regime the wall of the tubes is covered by thin film of liquid and heat is transferred through this film. In the center of the tube vapor is flowing at a high velocity and, although there may be a number of active bubble nucleation site at the wall, vapor is generated primarily by vaporization from by the liquid-vapor interface inside the tube and not by the formation of bubbles inside the liquid annulus unless the heat flux is high. In addition to the liquid in the annulus at the wall, there may be a significant amount of liquid dispersed throughout the vapor core in the form of droplets.

## Chapter 3

# Experimental Set-up

### 3.1 Introduction

In the industrial casting-process -as explained in Section 1.2- a huge amount of aluminum near the fusion temperature descends slowly in front of the mould that attacks the hot surface of the aluminium with a water jet. To simulate this process in the laboratory a long preheated slab which passes at front of the cooling mould would be required. To enable the movement of the slab with an evidently high mass a huge device would be necessary. Such an installation represents unpredictable difficulties, unsuitable time as well as cost requirements. Due to these problems, a solution without a moving ingot was chosen and a transient measurement technique using a preheated slab of aluminium which is suddenly exposed to the cooling water film was proposed.

### 3.2 Operating Procedure

The realization of the idea mentioned above is quite simple. An aluminium plate vertically mounted in a furnace (see Figure 3.1) is heated near the melting temperature, then the door of the furnace can be opened and the mould is positioned in front of the ingot. In Figure 3.2 the process is illustrated. Point (a) in the Figure shows the furnace

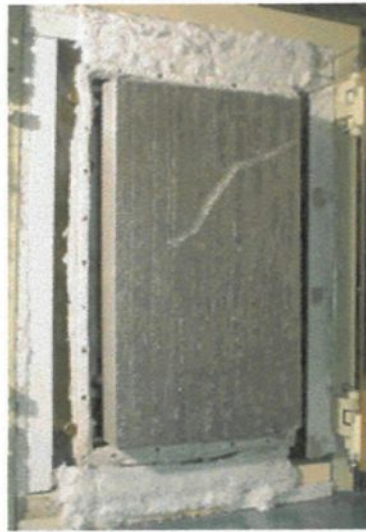


Figure 3.1: Photo of the mounted ingot

with the closed door doing the heating of the ingot up to a temperature of about  $550^{\circ}\text{C}$ . When this temperature is reached the door can be opened and the mould that is designed like a “second door” can be mounted in front of the ingot as displayed in the steps between (b) and (c) in Figure 3.2. As soon as the mould is placed in front of the slab as shown in Figure 3.3, the pump may be started to attack the plate with the water jet.

But this main idea needs a lot of supporting devices which enables the heating, cooling and measuring. All these devices together build up the experimental setup of

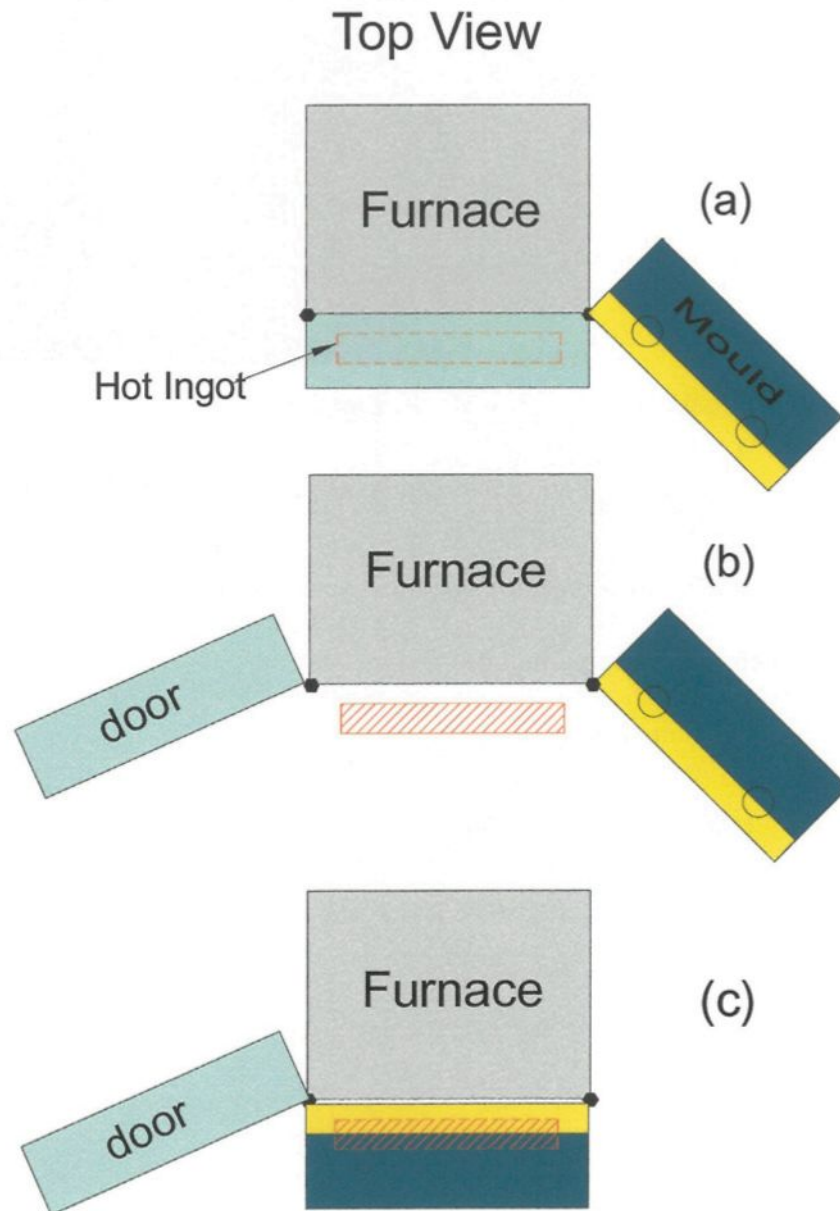


Figure 3.2: Sketch of the ingot heating and cooling process

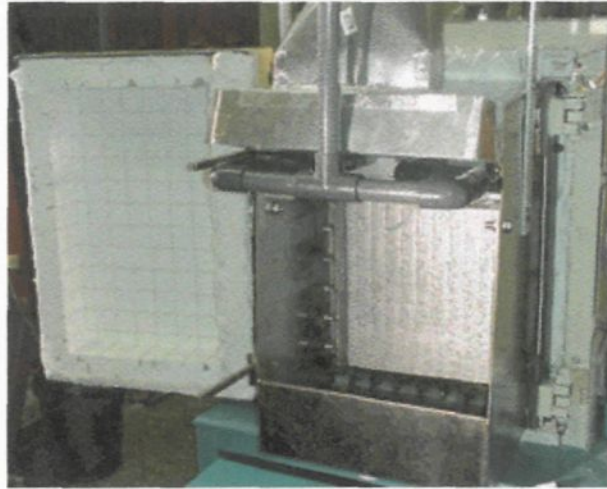


Figure 3.3: Mould adjusted in front of the ingot

the system. The experimental system is shown in Figure 3.4. In the following section, the components of the experimental system and their functions will be explained.

The main parts of the system are:

1. the ingot (aluminium slab)
2. the furnace
3. the mould
4. the thermocouples
5. the data acquisition system
6. the pump with all the tubes and valves
7. two reservoirs
8. the visualization

## 9. the rotameter

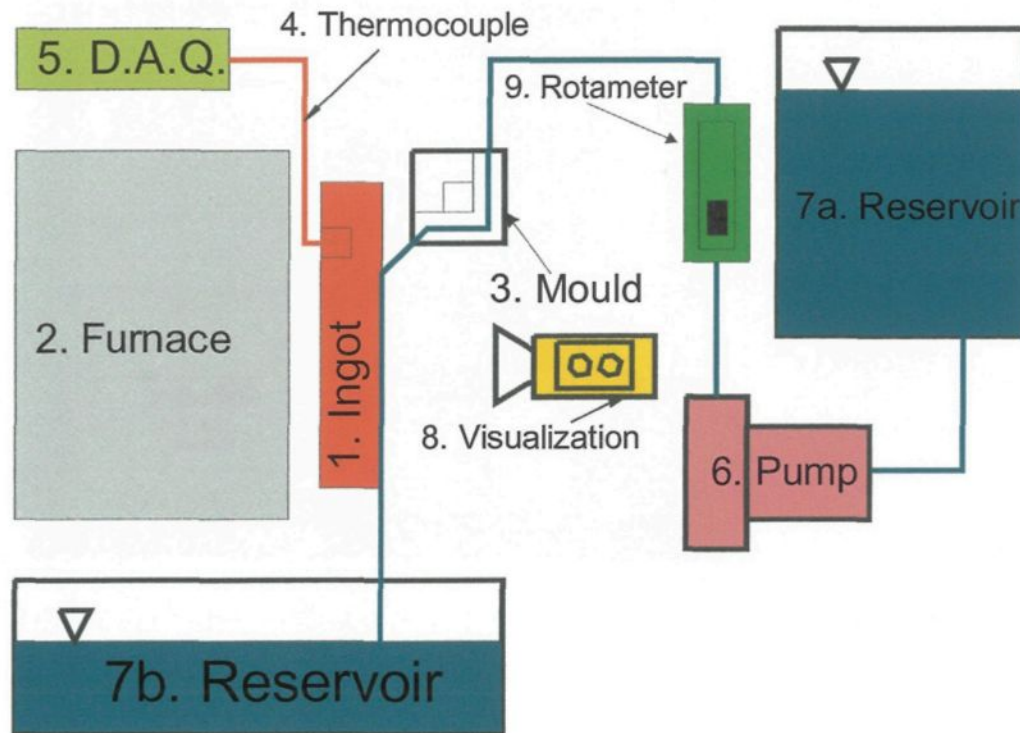


Figure 3.4: Experimental setup scheme

When the ingot (1) is heated up to about  $550^{\circ}\text{C}$  by the furnace (2) as already explained before, the pump (6) is started. Then the cooling water is pumped from the first reservoir (7a) through the rotameter (9) into the mould (3) from which it is sprayed onto the ingot. Before the jet attacks the surface, the data acquisition system (5) and the visualization (8) should be started. During the process of cooling the thermocouple (4) measures the surface temperature and the data acquisition system (5) amplifies and stores the data. The water not evaporated by the hot plate is collected by the second reservoir (7b). All these parts will be further explained in detail in Chapter 3. The main experiment

hardware is shown in Figure 3.5.

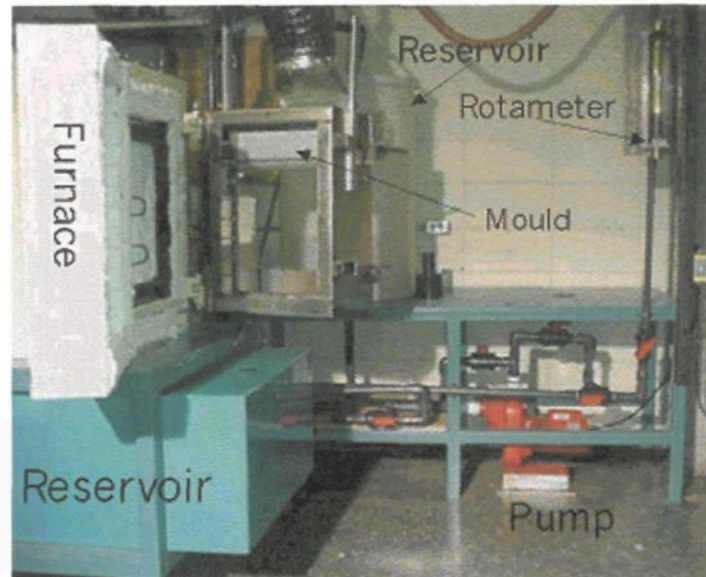


Figure 3.5: Main hardware of the experiment

The experiment is not automated therefore all steps like opening the door, starting the data acquisition system and the visualization, starting the pump and so on must be done by more than one person at the same time. A handling sequence assures that the ingot is not exposed longer than necessary to the surrounding air. A sequence schedule (see Figure 3.6) helps to organize the cycle and to distribute the tasks among all participants.

### 3.3 The Water Supply System

The water supply system includes the pump, the valves, the flowmeter, the tubes and the reservoirs and has to cover several tasks of the experiment. For example the properties of the attacking water jet should remain identical for various heating conditions

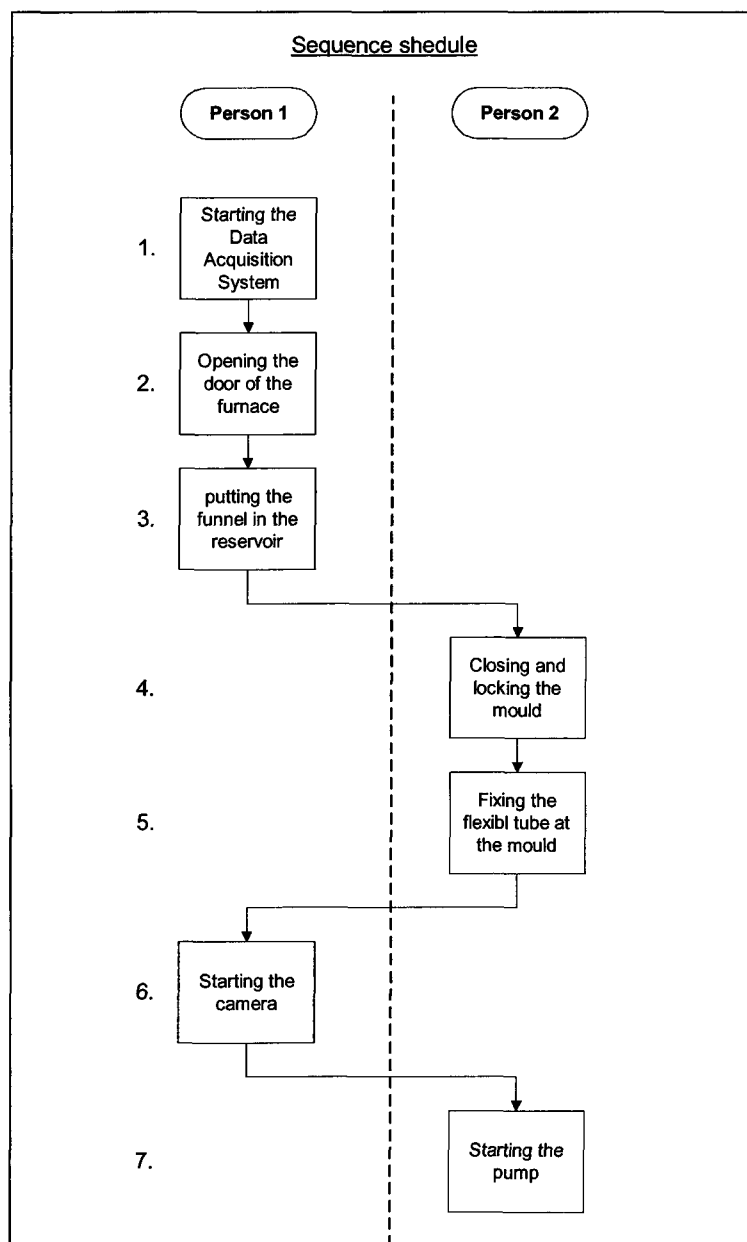


Figure 3.6: Working schedule for the experiment

using different velocities and the temperatures of the water. Also the used water should be recirculated to enable the usage of plant water or water with certain amount of additives. The water quality should not be changed by the system itself for example by dissolution of rust into the water. The water in the system can be changed and all the parameters influencing the water properties should be controlled. All these requirements are fulfilled by the system illustrated in Figure 3.7.

The cooling water is stored in the reservoir *R1* before the experiment starts. When the ingot is heated near the fusion temperature the pump *P1* carries the water from the reservoir *R1* to the mould *M1* passing through a flow meter *F1* to measure and adjust the velocity. The adjustment of the water velocity indicated by the flow meter is done using the bypass valve *V3* or/and the reduction valve *V6* before the real experiment. After the water passed the blue marked way in Figure 3.7 it reaches the mould and from it is sprayed on the ingot. The non-evaporated water is collected by the reservoir *R2* and can be recuperated by opening valve *V7* in the direction of connecting reservoir *R2* with valve *V2*. The direction of the valves *V2* and *V5*, respecting the default settings given below, must be changed also. If the pump is re-started the water will be retransferred into the reservoir *R1* indicated in the Figure 3.7 by the points  $\oplus P1$ . To explain the other functionality of the system we define the default settings as follows: valve *V1*, *V3* and *V7* are closed, valve *V2* and *V5* are directed as indicated by the blue line in Figure 3.7 and valve *V4* and *V6* are opened. With these default settings the liquid would take the blue marked way from the reservoir to the mould as explained before. If we want to pump the water directly from reservoir *R2* to the mould we must only turn the valve *V7* in the direction connecting reservoir *R2* with valve *V2*. To

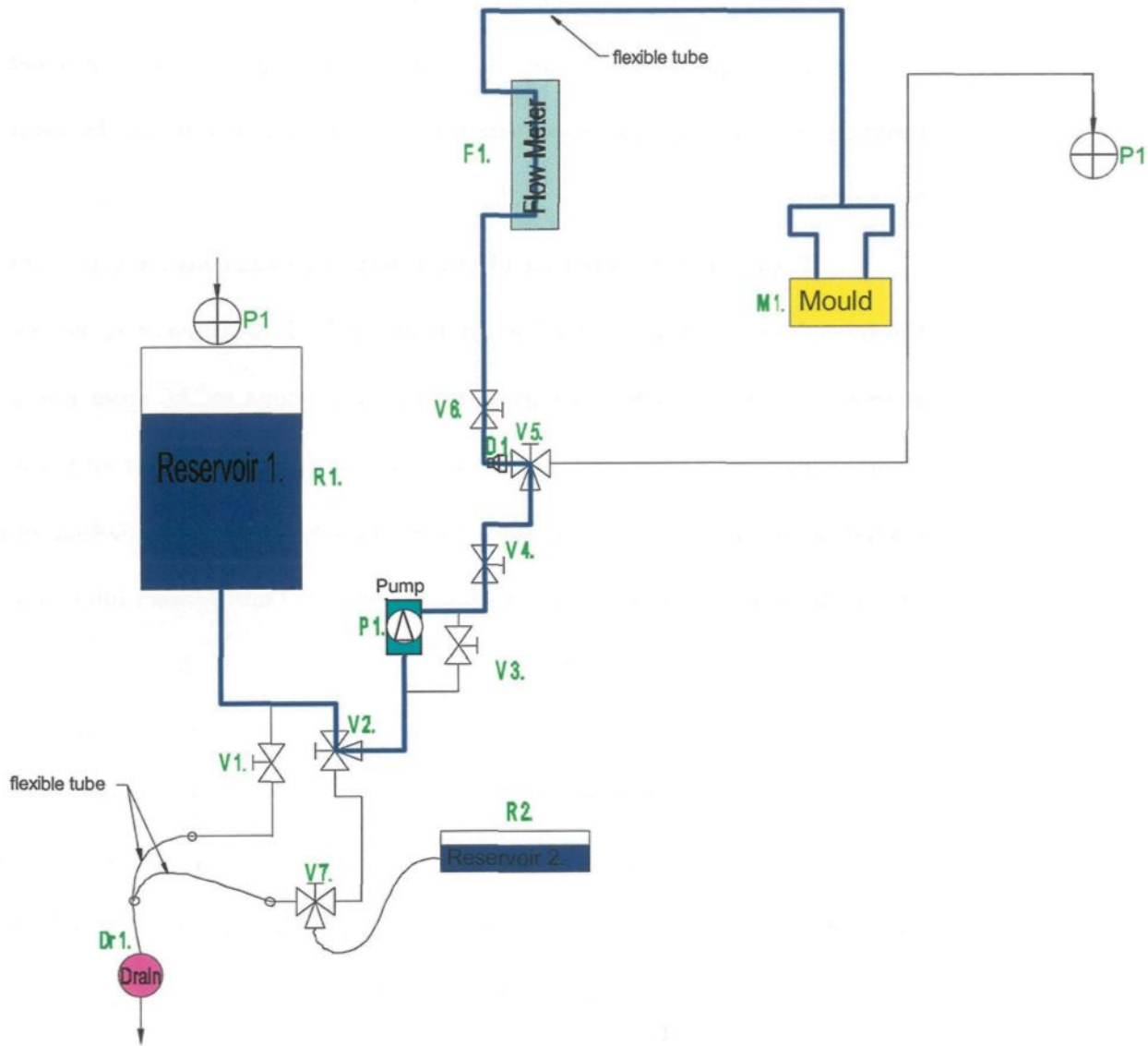


Figure 3.7: Water system

exhaust the reservoir *R1* the valve *V1* must be opened and then the water can flow into the drain. In almost the same manner reservoir *R2* can be evacuated by opening valve *V7* in the direction connecting reservoir *R2* with the drain *Dr1*.

The temperature of the water can be adjusted by installing a heater into the reservoir *R1*. The thermocouple installed in the mould also allows the control of the jet temperature.

To prevent the dissolution of rust into the water all chosen components used such as the tubes, the elbows and the valves are made of PVC. All connecting pieces of the system were ordered from IPEX ([www.ipexinc.com](http://www.ipexinc.com)) and belong to the order group connections schedule 40 in PVC. The pump was completely dismantled to cover all parts which are in contact with the water with an epoxy anti-corrosion color. After painting all pieces of the pump with this special paint they were heat-cured to improve the protection.

### **3.3.1 Flowmeter**

The flow meter used is an Industrial Rotameter FL 1661 manufactured by OMEGA for maximal flow rates up to 87.43 liter per minute. The accuracy of the 250mm long 10-100% scale is  $\pm 2\%$  of the full scale with a repeatability of  $\pm 0.5\%$  of full scale. During the industrial casting process the water jet cools the ingot with a flow rate of 60 liter per minute. Taking into account that the maximum flow rate of 87.43 liter per minute represents 100%

we can calculate the necessary rotameter reading as follows:

$$\begin{aligned}
 100\% &= 87.43 \frac{l}{\text{min}} \\
 \text{flow percentage} &= \frac{60 \frac{l}{\text{min}}}{87.43 \frac{l}{\text{min}}} = 0.6863 \\
 \text{rotameter reading} &= 68.6\%
 \end{aligned}$$

This value was set by using the bypass of the pump and the reduction valve installed before the rotameter.

### 3.3.2 The Pump

The cooling flow rate used in industry is  $Q = 60 \frac{l}{\text{min}}$ . The installed pump *Red Lion RLHE-75* manufactured by Winnipeg, Canada provides a pressure of about  $p = 2.7574 \cdot 10^5 \text{ Pa}$  ( $\approx 40 \text{ lbs/in}^2$ ) at a flow rate of  $Q = 60 \frac{l}{\text{min}}$ . The pressure drop calculations in the duct system were made in the thesis Ref [15]. It is shown that the pump is more than suitable for the duct system.

## 3.4 Data Acquisition System

Under this section not only the data acquisition system will be described but also all the components of the data acquisition system including all sensors and control applications as well as the components used for visual observation of the experiment. The main task of the data acquisition system (=DAQ) is to measure sensor readings which is in our case the voltage output of thermocouples. But in modern devices the possibility of setting a measurement dependent alarm, adding scaling factors and triggering the system by an external signal are taken for granted. These newly integrated instrument properties

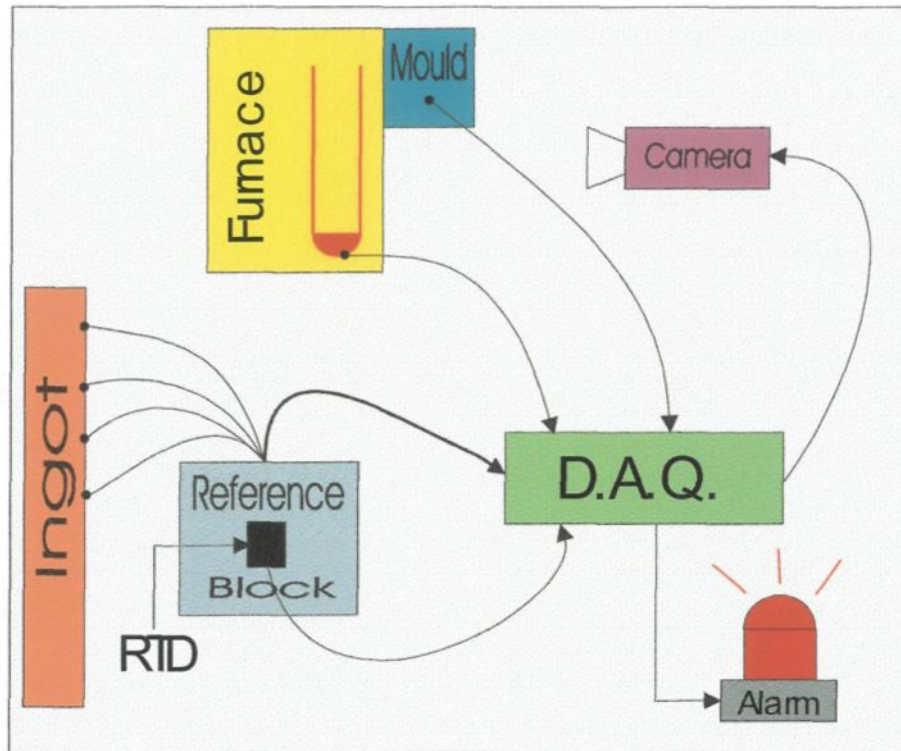


Figure 3.8: Data acquisition used as measure and control unit

offer the possibility of using the instrument not only for measuring and storing data but also for controlling the experiment. Especially in our case the required controlling elements are an alarm limit for the heating element temperature in the furnace, a scaling for a resistance temperature detector (RTD) placed in the reference block and the ability to detect a disconnection of a thermocouple. The connection scheme of the data acquisition system is illustrated in Figure 3.8. The first and most important task is to measure the voltage of the thermocouples installed in the ingot. They are not directly connected to the DAQ because the cold junction compensation is done by a hardware reference point as shown in Figure 3.8. The temperature of the reference block will be determined by a calibrated

RTD. The voltage reading of this sensor is directly transferred into a temperature output by scaling the value integrated in the device. The thermocouple installed in the mould to measure the water temperature may also be connected to the reference block to increase the accuracy when necessary. At the moment the voltage to temperature conversion is done by the instrument itself using the internal reference temperature at the thermocouple connectors. The tested accuracy of this internal compensation is about one degree Celsius which is better than the thermocouple tolerance guaranteed by the manufacturer. In any case, it is sufficient to observe the heating element temperature during the heat up to avoid its destruction, since 100% of the available power is applied to the heating element initially. If the temperature reaches the maximum allowed value the observing instrument recognizes this by comparing the reading with a former programmed alarm limit and initiates a visual or acoustic signal. The above mentioned settings are already installed and working well. In addition we used the alarm limits to synchronize the film made during cooling and data measurement. Four red light laser were installed in front of the ingot. Each of them pointed exactly on the measurement point. The alarm limit was programmed to turn on the laser if a certain temperature value was reached. Thus we could compare the film with the temperature curves, because we knew when the laser light turned on in the film (visual) the temperature reached a predetermined value (set alarm limit).

#### **3.4.1 The D.A.Q. HP 34970A**

The *Hewlett Packard* HP 34970 was chosen to accommodate the requirements mentioned above. There are three slots built into the rear of the instrument to accept switching modules which allows connection of up to 250 channels. For one single channel a data read-

ing rate of up to 600 readings per second is possible. In the actual experiment a reading rate of up to 100 readings per seconds per channel is sufficient in detecting the transient temperature history. The HP 34902A is the fastest multiplexer card available for these DAQ. We estimate maximal eight thermocouples placed directly under the ingot surface that will detect the transient temperature history. Taking into account the last three statements the Hewlett Packard data acquisition system with the chosen multiplexer card is suitable for the experimental requirements.

The device offers also the ability to set alarm limits for each channel. As explained in the former section it is necessary to observe the heating element's temperature during the heating up phase. If such a limit is reached, an acoustic signal can be resound or/and a output signal on the back side of the device can be taken to initiate a visual or/and acoustic signal, depending on the user settings.

By an interface cable (*RS 232 or HP-IB(IEEE-488)*) the instrument can be connected with a computer to handle all measured data. With the delivered system software all channels can be observed during the measurements as well as the set alarm limits. The software provides other capabilities that can be applied but they will not be explained here.

### **3.5 Reference-block**

If a thermocouple is directly connected to the data acquisition system an additional junction occurs. To give a short review: if the thermocouple wire, that is of a certain alloy, is connected to the panel terminals (copper) these connections create a new thermocouple at each connection. In the case that the front panel terminals have not the same

temperature, an additional voltage will disturb the thermocouple tension. We can avoid this error by putting all copper-thermocouple connections at the same temperature level. This requirement can be realized by a so called *reference block* which has to be a good electrical insulator but a good heat conductor. Normally this requirement is a disaccord because all metals are good heat conductors but also good electrical conductors. We solved the problem by combining a metal with a non-metal. We drilled a couple of holes in an aluminium block -that is a good heat conductor- as indicated in Figure 3.10. We filled the holes with transformer oil that is a good electrical insulator and is a better heat conductor than air. All thermocouple wires are soldered with a copper wire and the connection is submerged into the transformer oil. Because of the isothermal properties of the aluminium and the transformer oil, we assure that the connections have identical temperatures. The other end of the copper wires can be directly connected to the data acquisition system without inducing junction errors. This construction is illustrated in Figure 3.10. To determine the absolute temperature level, it is still necessary to measure the temperature of the reference block. At the beginning we did this with another thermocouple placed in the 1.6 mm hole of the isothermal block (see Figure 3.9) and the output was corrected by the internal cold junction compensation of the data acquisition system. This construction was chosen because we had no RTD at that time. To check the accuracy of the setup, a calibration test was carried out. The middle hole in the block allows the placement of a precise mercury thermometer which is used to verify the electronic temperature readings. With the determined block temperature a *software compensation* can be made. Figure 3.11 shows the reference block as it was used in the first experiment. The block was

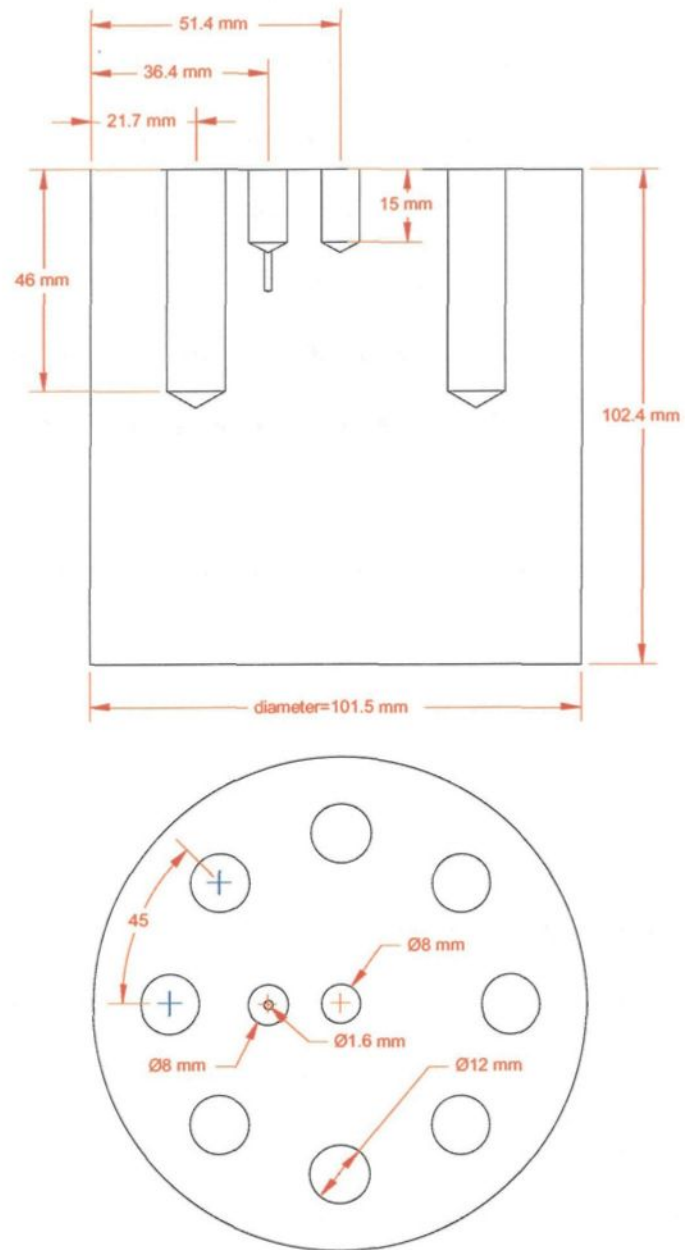


Figure 3.9: Drawing of the reference-block

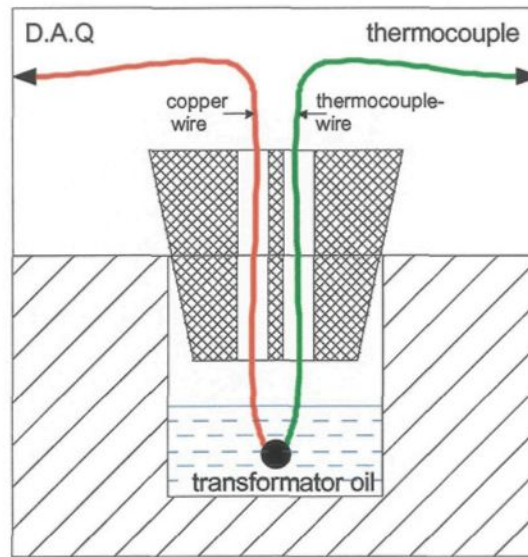


Figure 3.10: Copper-thermocouple wire connection

placed into a polystyrene block to assure a uniform temperature distribution.

### 3.6 Furnace

The role of the furnace is to heat the ingot to almost its melting temperature which is  $775\text{ K} \approx 502^\circ\text{C}$ . for an aluminum alloy 2024-T6 (4.5% Cu, 1.5% Mg, 0.6%Mn) In Figure 3.12 the furnace is shown with its door on the left and the mould on the right side. The furnace consists of a steel framework that holds the insulating walls. The insulation is a silicate based fibrous material held together by a binder, the insulator is named *B3 insulating board*. These B3 boards are 45.8 mm thick and resist a temperature up to about  $900^\circ\text{C}$ . According to the long heating time we added a layer of an insulating mat to improve the insulation. This mat is made of the same material like the B3 board but the binder is softer which makes the material more flexible. The slab is heated with still air as in a conventional

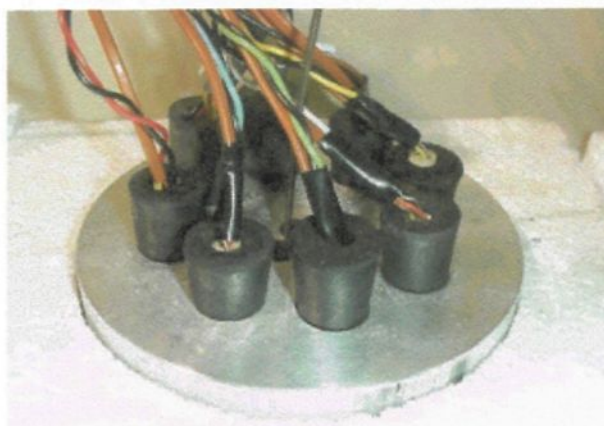


Figure 3.11: Reference block

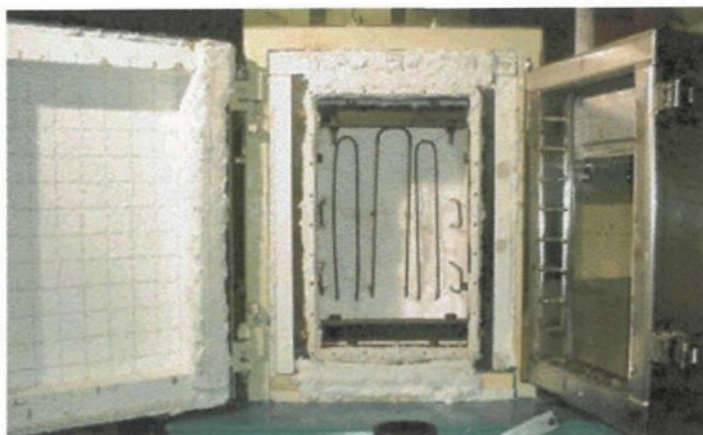


Figure 3.12: Furnace with its door and the mould

oven. The seven tubular heaters, installed in the oven, can reach a maximal temperature of 815 °C. These incoloy sheath heaters were produced and delivered by OMEGA. To assure that the ingot is heated uniformly the heaters in the oven are arranged in a certain manner as illustrated in Figure 3.13. The arrangement of the heaters are indicated by the different

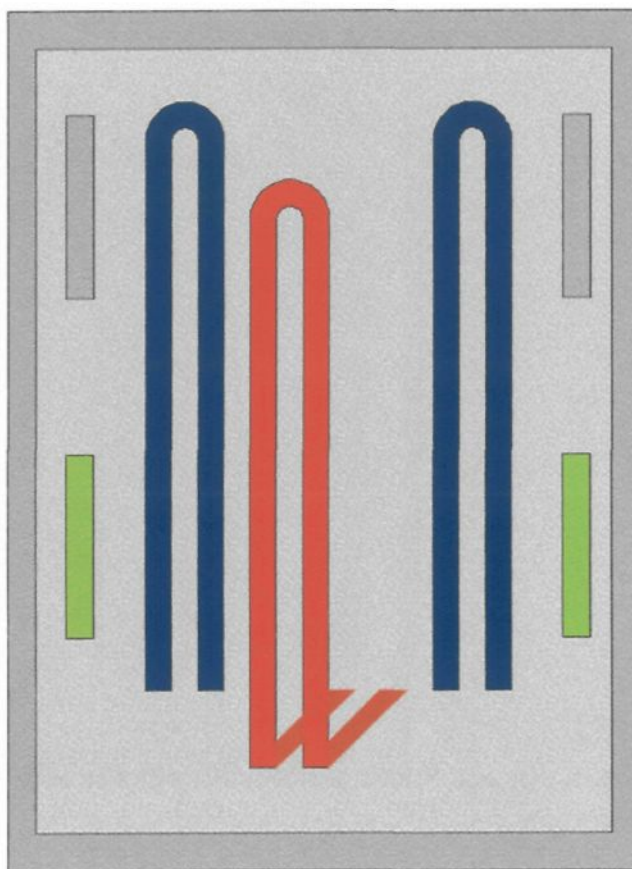


Figure 3.13: Heater distribution inside the furnace

colors in Figure 3.13. Each group can be independently controlled by the electrical control unit. The "red" heater is placed more advanced in the front as the others. In Figure 3.14 the placement can be seen more precisely. The heaters are controlled by a digital

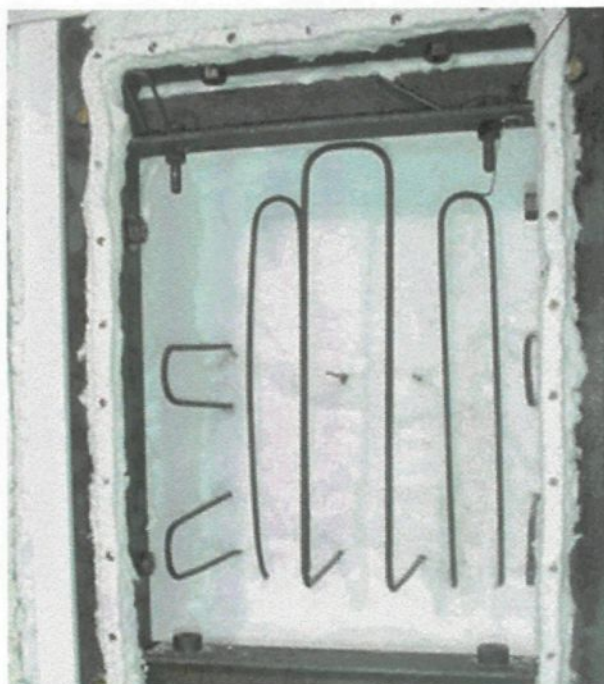


Figure 3.14: Arrangement of the heating elements

controller unit termed E5Ck produced by OMRON. This device revises the readings of two thermocouples installed inside the furnace. It controls the power of the heaters while the maximal supported power can be adjusted by the user taking this information into account. It was recommended to carry out the heating with 60% of the maximal allowable power of the elements to prevent a destruction of the heating elements, because the power density of the elements is limited to  $4.65 \cdot 10^{-2} \frac{\text{W}}{\text{mm}^2}$ . Due to the fact that the heating took about 5 hours, we decided to accelerate the process. Therefore the heating elements were supplied with 100% of the power but to prevent a destruction, the heater temperature was measured by a thermocouple installed later. This sensor touches directly the element while the control system thermocouples only measures the air temperature in the furnace. The new thermocouple is connected to our data acquisition system and not to the heater control system. The alarm limits, provided by the HP data acquisition system, follows the heating element temperature. When the limit is reached the power is decreased manually.

## Chapter 4

# Measurement Methods

### 4.1 Introduction

One of the basic purposes in our project is the determination of the surface heat flux during the cooling process. There are several methods to measure the surface heat flux. One method is to use a Heat Flux Meter. These heat flux meters are sensors that are attached or merged into the surface and indicate the temperature gradient which is directly proportional to the heat flux. The slug type heat flux meter and the Gardon heat flux meter are inserted in the object through which the heat flux should be determined. The heat flux meter proposed by Schmidt in the twenties is a sensor attached on the surface. All these principles of measurement have in common that they disturb the surface texture. Due to the fact that the boiling processes at the surface of the ingot depend strongly on the surface structure and texture, the presence of such a sensor would negatively influence heat flux measurement. In other words, the boiling phenomena occurring at the ingot surface would change with the presence of an attached or inserted sensor. Thus the measured heat flux

at the sensor point would not reflect the process of interest.

We measure the heat flux without disturbing the surface with a combination of two methods. The first one is based on the solution of an "inverse conduction problem". One special solution of the inverse problem is the Cook Felderman Equation. This solution allows the determination of a heat flux variation using only the surface temperature history. That means if we would be able to measure the surface temperature without disturbing the surface we would be able to calculate the surface heat flux. Such a possibility is given by the Null Point Calorimetry. Both the Cook-Felderman equation and the null point calorimetry are explained in detail below.

## 4.2 Inverse Method

In this Section; an inverse problem will be explained briefly. It has to be mentioned that inverse problems occur in every domain where differential equations are present. In the scope of this project, the inverse problem and its solution are restricted to thermal conduction problems. Nevertheless, some of the methods presented here can also be applied to other physical problems. For example, the sensitivity coefficient method is applicable to many problems in research that are dealing with the inverse solution of ill-posed problems.

We may pose the question,"What is an inverse problem". To answer this question we may consider any existing differential equation. Because in this project we are dealing with heat transfer problems, an example from this domain will be given as follows:

$$\frac{\partial^2 T}{\partial x^2} = \frac{1}{\alpha} \frac{\partial T}{\partial t} \quad (4.1)$$

where  $\alpha$  is the thermal diffusivity and  $T$  is the temperature depending on  $x$  (space) and

$t$  (time). The equation describes the one-dimensional transient temperature evolution in a solid where there is no internal heat generation and thermal conductivity is assumed constant. This equation is known as the heat diffusion equation and will be used as an example to demonstrate an inverse problem. Our equation describes an arbitrary, but real existing physical problem. The information that can be provided from this differential equation might be the temperature distribution. If we want to know the temperature distribution of an object, we can include the boundary and initial conditions of our problem, which are supposed to be known, and solve the differential equation. This is called a *direct problem*.

But it may happen that we already know the function of interest, namely the temperature is the present case, and we are looking for boundary or initial conditions. Then we call this an inverse problem. That is to say, it exists two kinds of inverse problems. The first one, the so called *external inverse problem*, refers to the already explained relation where we are looking for the boundaries and initial conditions, while we know the temperature function. The inverse problems are called *internal inverse problems* if we are looking for parameters of the differential equation, which may depend on the described function itself. For example, if the thermal diffusivity depends on the temperature  $\alpha(T)$  and we try to determine its value, then we talk about an internal inverse problem.

Inverse thermal problems have numerous applications in various branches of science and technology. Specially in the aerospace application the inverse method is used to determine outer surface conditions during the re-entry of space vehicles, or the surface conditions at the exhaust of a rocket or a jet engine, or the motion of a projectile over a gun

barrel surface etc. Inverse problems also arise in the design of casting processes because the fluxes and velocities at the solidification front determine the cast structure which is controlled by the external boundary fluxes.

#### 4.2.1 Simplification of the General Conduction Problem using the Duhamel's Theorem

In this Subsection it will be explained how to find a solution for a general conduction problem in a quite simple way, by using the Duhamel's theorem. The same result can also be obtained by taking the Laplace transformation method (see Subsection 4.2.1). If the surface conditions are prescribed functions of time and no internal heat generation is considered the solution that satisfies the general heat conduction equation without internal heat generation (4.2) can be obtained using the *Duhamel's<sup>1</sup> theorem* which is given below. It assumes constant surface conditions.

$$\nabla^2 T - \frac{1}{\alpha} \frac{\partial T}{\partial t} = 0 \quad (4.2)$$

**Duhamel's theorem** (ref. [7]) : *If  $T = F(x, y, z, \tau, t)$  represents the temperature at  $(x, y, z)$  at the time  $t$  in a solid in which the initial temperature is zero, while its surface temperature is  $\phi(x, y, z, \tau)$ , then the solution of the problem in which the initial temperature is zero, and the surface temperature is  $\phi(x, y, z, t)$ , is given by*

$$T = \int_0^t \frac{\partial}{\partial t} F(x, y, z, \tau, t - \tau) d\tau \quad (4.3)$$

---

<sup>1</sup>Mémoire sur la méthode général relative au mouvement de la chaleur dans les corps solides plongés dans les milieux dont la température varie avec le temps, cf. J. Éc. polyt. Paris, 14 (1833) Cah. 22, p. 20.

### Qualitative Explanation of the Duhamel's Theorem

The mathematical explanation of the Duhamel's theorem is given in (ref. [7] p. 30). To provide a clear understanding of the basic idea of the Duhamel's theorem we will take an example.

A semi-infinite planar solid might be considered, that is exposed to a surface temperature variation. To be in agreement with the previous definition we will define  $\phi(x, y, z, \tau)$  as the surface temperature. The reaction of the solid due to a change in the surface temperature would be a response temperature distribution within the body, if its initial temperature was zero. Unfortunately, the surface temperature and the "response" temperature distribution within the body are not independent. The signification of this independence may not appear obvious in the first moment. Therefore we will focus on this important point for a moment. Normally we do not know the surface temperature function previously. For example, in an experiment, the objective is to determine the surface heat flux. Therefore the surface temperature of an object is measured, that means that we do not know neither the surface temperature history nor the previous temperature distribution inside the body. Mathematically the dependence between the surface temperature function and the temperature distribution within the body pose the problem such that the we can not determine the temperature distribution, if the surface temperature history is not known.

The solution for this problem can be deduced from the combination of unit step functions replacing the surface temperature history. The basic idea in this concept is quite simple, we know the response function of a semi infinite planar object for a unit step input, which is the error function (see Figure 4.1). The next step is that one combines as many unit

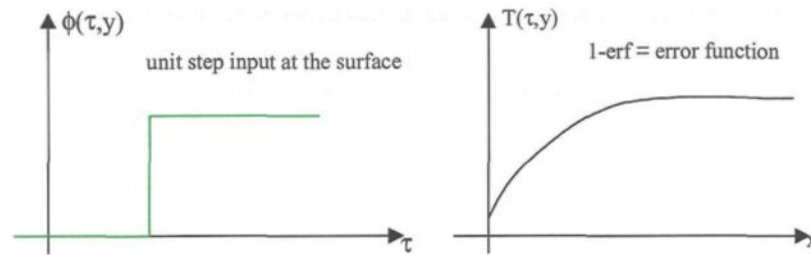


Figure 4.1: Unit step input at the surface and response function within the body

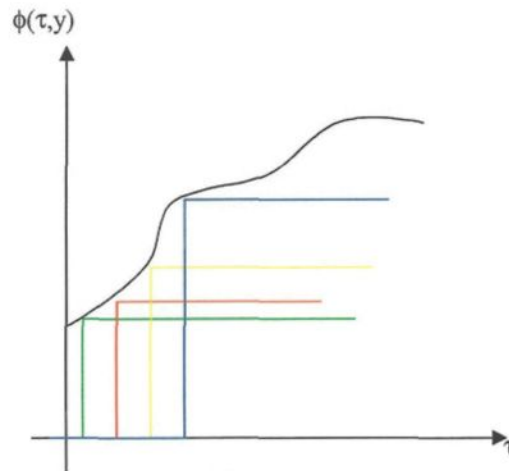


Figure 4.2: Combination of unit step functions to imitate the real surface temperature history

step functions as needed to imitate the real surface temperature variation as it can be seen in Figure 4.2. According to the combinations of the input, the unit step functions, as well as the response functions must be combined in a specified way. Exactly this combination of forming the response function of an arbitrary surface temperature variation is stated by the Duhamel's theorem. Now from this point of view we may interpret the theorem

$$T = \int_0^t \frac{\partial}{\partial t} F(x, y, z, \tau, t - \tau) d\tau$$

as follows. We sum up all elementary temperature distributions within the object which were caused by an arbitrary change in surface temperature.

### Solution of the Duhamel's Theorem for a Nonhomogeneous Input

In the previous section the relation between the surface temperature variation and the response temperature distribution within the body described by the Duhamel's theorem, was explained. To obtain a useful solution, one has to apply a suitable input function to the theorem. For this function the response that will form within the body should be known. In accordance with to the example from Section 4.2.1 we will use the unit step function for this purpose. As already mentioned before the error function is a solution for a unit step surface temperature rise, derived from the differential heat conduction equation. The mathematical formulation of the idea explained in the prior section will now be presented without proof. The solution of the Duhamel's theorem for a unit step input at the surface temperature is stated in (ref. [16] p. 143). While the Duhamel's theorem in its general form covers a multidimensional case, its solution for a unit step function is only one-dimensional.

*If  $R(x, t)$  is the response of a linear system (whose initial condition is 0) to a single nonhomogeneous input given by  $G(x)l(t)$ , the response  $T(x, t)$  of the same system to an input  $G(x)\phi(t)$  is given by:*

$$T(x, t) = \int_{\tau=0}^t R(x, t - \tau) \frac{\partial}{\partial \tau} \phi(\tau) d\tau + \sum_{i=0}^I R(x, t - \tau_i) \Delta\phi_i \quad (4.4)$$

*The unit-step function  $l(t)$  is defined 0 for  $t < 0$  and 1 for  $t > 0$ . From time  $\tau = 0$  until time  $\tau = t$ ,  $R(\tau)$  has a total of  $I$  steps. Step  $i$  occurs at time  $\tau_i$  and  $\Delta\phi_i = \phi(\tau_i^+) - \phi(\tau_i^-)$  where  $\phi(\tau_i^+)$  is the value of  $\phi(\tau)$  right after step  $i$  and  $\phi(\tau_i^-)$  is the value of  $\phi(\tau)$  just prior*

to step  $i$ . In between successive steps  $\phi(\tau)$  is continuous. The integral is the sum of the integrals over the continuous portions of  $R(\tau)$ . The summation term accounts for the steps  $\Delta\phi_i$  in  $\phi(\tau)$  that occur at time  $\tau_i$ .

### Development of the Cook-Felderman Equation

With the information of the temperature distribution within an object, provided by the Duhamel's theorem, we are able to develop a relation between the surface heat flux and the surface temperature. This relation yields to a very powerful tool to calculate a heat flux acting on a surface if only the surface temperature is known. This equation is named as the Cook-Felderman equation and its derivation will be shown below.

First we will introduce a new term in our solution of the Duhamel's theorem expressed in Equation (4.4). We remember that we assumed the initial temperature of our body as zero in Duhamel's theorem. However, one may modify this assumption, because it is not necessary that the absolute temperature of the body is zero. Considering a uniform temperature distribution within the object yields to an additional term in equation (4.4). This term  $T_0$  stands for an offset of the former assumed zero temperature and will be added in our temperature distribution equation as follows:

$$T(x, t) = T_0 + \int_{\tau=0}^t R(x, t - \tau) \frac{\partial}{\partial \tau} \phi(\tau) d\tau + \sum_{i=0}^I R(x, t - \tau_i) \Delta\phi_i \quad (4.5)$$

where  $T_0$  is the uniform initial temperature (for  $t \leq t_0$ ) in the body.

Because we are interested in the heat flux, we only have to consider the Fourier's law at the surface

$$q(t) = -k \frac{\partial T(x, t)}{\partial x} \Big|_{x=0} \quad (4.6)$$

where we can substitute the temperature distribution from Equation (4.5).

$$q(t) = -k \frac{\partial T(x, t)}{\partial x} \Big|_{x=0} = -k \int_{t_0}^t \frac{\partial R(x, t - \tau)}{\partial x} \Big|_{x=0} \frac{\partial}{\partial \tau} \phi(\tau) d\tau \quad (4.7)$$

In order to apply Equation (4.7), the derivative of the unit step function must be known.

The response to a unit step function for a semi-infinite planar solid and its space derivative is:

$$T(x, t) = 1 - \operatorname{erf} \left( \frac{x}{2\sqrt{\alpha t}} \right) \quad (4.8)$$

$$\frac{\partial T}{\partial x} \Big|_{x=0} = \frac{-1}{\sqrt{\pi \alpha t}} \quad (4.9)$$

So that we obtain the following solution for a semi-infinite planar solid

$$q(t) = \sqrt{\frac{k \rho c}{\pi}} \int_{t_0}^t \frac{\phi'(\tau)}{\sqrt{t - \tau}} d\tau \quad (4.10)$$

Since Equation (4.10) is not suited for numerical evaluation because of the involved derivative of the temperature integral, it can be transformed to:

$$q(t) = \sqrt{\frac{k \rho c}{\pi}} \left\{ \frac{1}{\sqrt{t}} [\phi(t) - \phi(t_0)] + \frac{1}{2} \int_{t_0}^t \frac{\phi(t) - \phi(\tau)}{(t - \tau)^{\frac{3}{2}}} d\tau \right\} \quad (4.11)$$

Equation (4.11) comes from integration by parts of Equation (4.10). It should be mentioned that both of these forms have singularities at  $\tau = t$ . If a purely numerical procedure is used, these singularities can cause some difficulty.

Normally the data received from a sensor, for example from a thermometer, are values measured at discrete times. Therefore it would be interesting to transform Equation (4.10) into a discrete form. Assuming that the surface temperature between the successive time steps  $t_j$  varies linearly with time, we may integrate Equation (4.10) analytically. The

result is:

$$q(t) = 2\sqrt{\frac{k\rho c}{\pi}} \sum_{i=1}^M \frac{\phi_i - \phi_{i-1}}{\sqrt{t_M - t_i} + \sqrt{t_M - t_{i-1}}} \quad (4.12)$$

In Equation (4.12) we have to make the restriction that  $q(t)$  is an estimated value. This equation is known as Cook-Felderman Equation. (Ref. [9])

### Laplace Transform

The result obtained by using the Duhamel's theorem (Equation 4.10) can also be derived in another way. In the following a short introduction will show that a result similar to that found in the previous Section can be obtained using the Laplace transformation.

As for the Duhamel's theorem, we assume an one-dimensional heat flux. Using this assumption we can write the heat conduction equation, where  $\alpha$  is the thermal diffusivity, as follows:

$$\frac{\partial T}{\partial \tau} = \alpha \frac{\partial^2 T}{\partial x^2} \quad (4.13)$$

If we take  $q(0, \tau) = -k \frac{\partial T(0, \tau)}{\partial x}$  and  $T(x, 0) = 0$  as boundary conditions, then we obtain for a semi-infinite slab with constant properties the solution of the heat conduction equation as:

$$T(x, \tau) = \frac{1}{\sqrt{\pi \rho_s C_{p_s} k_s}} \int_0^\tau \frac{q(0, t)}{\sqrt{\tau - t}} e^{-\frac{x^2}{4k_s(\tau-t) \rho_s C_{p_s}}} dt \quad (4.14)$$

This solution was derived using a convolution integral of the Laplace transformation (Ref. [19]). At the surface of the object the relation between the slab temperature and the heat flux can be expressed as follows, because  $x$  becomes 0:

$$T(0, \tau) = \frac{1}{\sqrt{\pi \rho_s C_{p_s} k_s}} \int_0^\tau \frac{q(0, t)}{\sqrt{\tau - t}} dt \quad (4.15)$$

So we can write for the surface heat flux  $q$  as a function of the surface temperature:

$$q(0, \tau) = \sqrt{\frac{\rho_s c_{p_s} k_s}{\pi}} \int_0^\tau \frac{dT(0, t)}{dt} \frac{1}{\sqrt{\tau - t}} dt \quad (4.16)$$

Equation (4.16) and Equation (4.10) that we developed in Subsection 4.2.1 using the Duhamel's theorem are identical.

Equation 4.16 is not suited for numerical evaluation due to the fact that the first derivative of the temperature is involved in the integral. To avoid this disadvantage, Equation 4.16 can also be expressed like this:

$$q(0, \tau) = \sqrt{\frac{\rho_s c_{p_s} k_s}{\pi}} \left[ \frac{T(\tau)}{\sqrt{\tau}} + \frac{1}{2} \int_0^\tau \frac{dT(\tau) - T(t)}{(\tau - t)^{\frac{3}{2}}} dt \right] \quad (4.17)$$

It was proved that two different technics yield to the same result. These results then can be used to calculate the surface heat flux, as it was shown in Subsection 4.2.1. The equations developed here provide the possibility to determine the heat flux on a surface by measuring only the surface temperature. The advantage of using this method is that the object itself can be used to measure a heat flux. It is not necessary to attach an additional heat flux sensor onto the surface. Of course this method is limited to transient problems, a steady state heat flux can not be determined. However a lot of applications exist in heat transfer research where it is necessary to determine the surface heat flux without attaching an additional sensor onto the surface, and where it is inconvenient to install two thermocouples inside the body, as it is normally required for a heat flux meter.

### Assumptions

As we have seen before, the Cook-Felderman equation was obtained by making the following assumptions. First, the body has to be semi-infinite in the direction in which the

heat flux is calculated. Second, the Cook-Felderman equation is valid for an one dimensional heat flux only and the heat transfer coefficient is not a function of the temperature. Of course we can not validate these assumptions for the experimental conditions used without a verification. Therefore, we will investigate the validity of these assumptions using a numerical model later.

### 4.3 Calorimetry

This Section presents some applications of the previous section which discusses the solution methods of inverse thermal problems. As it was shown when a thermal mass is considered, its surface heat flux can be determined by measuring only the surface temperature. Based on this idea, there are two possibilities to create a heat flux sensor.

The first one is to use the body - that may be the outer hull of a re-entry vehicle or a air-craft wing- itself as the calorimetric mass. Then, a temperature distribution caused by the surface heat transfer will develop within the object and the heat flux can be obtained by measuring the surface temperature. There are two different realizations ways of measuring the surface temperature, the null-point calorimeter and the thin-film gauge methods. The difference between the two methods is that in the null-point calorimeter the sensor (a thermocouple) is embedded in the object so that its surface is not influenced by the sensor itself. In contrary, the thin-film gauge is a sensor attached onto the surface of the object. Thus the null-point calorimeter is a better choice for our purposes and will be described in the next section.

The second possibility to create a heat flux sensor using the inverse method is to

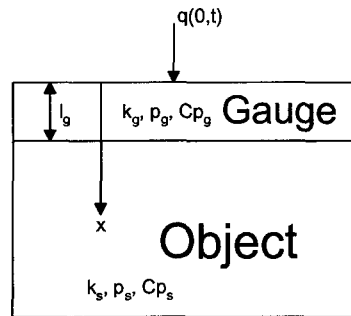


Figure 4.3: Gauge notation for thin and thick films

attach an additional body, which acts as a calorimetric mass, onto the object (see Figure 4.3). The thick-film gauge is an example for this application.

#### 4.3.1 Null-Point Calorimeter

To measure the surface temperature of our aluminium ingot, normally it is necessary to place the thermocouple on the surface. But this installation would have negative effects on the film-nucleate boiling process and increase the surface roughness which effects the bubble formation. To avoid this negative effect and to assure that the ingot surface has the same physical properties as the ingot produced in the plant we have to look for another surface temperature measurement method. The Null-Point Concept was developed in aerospace research to measure the heat flux on the hull of a re-entry vehicle. Due to the very high heat transfer rates the sensor (thermocouple) had to be protected in a certain way because even the most rugged sensors exposed a few milliseconds to a temperature that rises up to  $4150\text{ }^{\circ}\text{C}$  could not survive [4]. In the null-point concept the sensor is embedded in a mass which acts like a calorimeter. The protection stops the destruction of the sensor

working in a high energetic environment. The idea using a null-point calorimeter is quite simple. We take a mass and expose it to a heat flux. The temperature distribution formed within the body can be determined by a solution of the general heat conduction equation for a semi-infinite planar body. If we are interested in the heat flux, we only have to measure the surface temperature history of the mass and then use a solution of the one-dimensional inverse heat conduction equation for a semi-infinite solid e.g. the Cook-Felderman Equation, as explained in Subsection 4.2.1. But to measure the surface temperature, normally a temperature sensor must be attached on the surface, and it can thus be easily destroyed while exposed to the prior discussed high heat transfer rates.

This negative effect can be prevented if the sensor is installed directly under the surface of the mass. Consider a thermal mass of the length  $L$  with a flat bottom cylindrical hole with a radius " $a$ " drilled from the backside of the mass to within a distance  $b$  from the front surface as shown in Figure 4.4. The location  $0, b$  on the centerline of the cylindrical

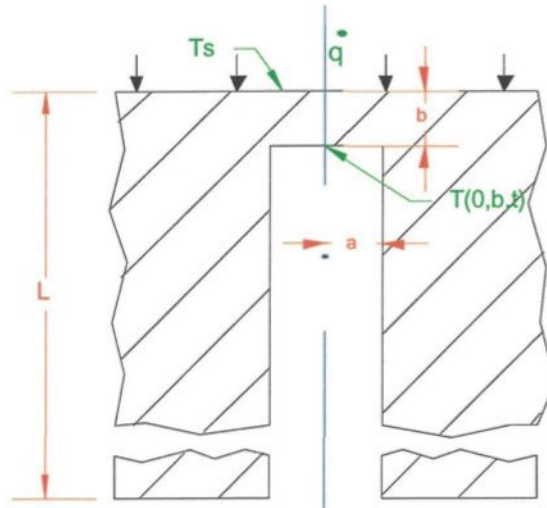


Figure 4.4: Conceptual sketch of the null-point calorimeter

cavity is defined as the null point. To determine the surface temperature the assumption has to be made that the transient backside temperature  $T_b(0, b, t)$  measured at the null point is identical to the surface temperature history  $T_s(r, 0, t)$  on the outside surface of the same thermal mass in the absence of the cavity. This assumption will become acceptable if we respect two points. First, if the distance  $b$  between the outer surface and the cavity bottom becomes very small, the measured and the sought temperatures will be almost the same. It should be mentioned that the resolution of the sensor, that might be a thermocouple, is not high enough to detect the difference, if  $b$  is small enough. The second point that gives credibility to the null-point concept is the compensation of measurement errors described below.

First, we shall consider a temperature sensor that is installed under the surface inside our calorimetric mass without a cavity, as shown in Figure 4.5. We impose a heat flux in the normal direction to the surface, for example by a cooling water film on the surface ( $T_i > T_{environment}$ ). The heat flux is indicated by the thick arrows in Figure 4.5. Because of the conduction of heat from the backside to the surface it is obvious that the temperature at the measurement point  $T_m$  is higher than the surface temperature  $T_s = \phi$ .

The next example will show the contrary to the previous case. We consider again a calorimetric mass but this time with a huge cavity in the backside (see Figure 4.6). Similar to the first case, we force a high heat flux in the normal direction to the surface indicated by the thick arrows. For establishing the temperature  $T_m$  on the bottom of the null-point cavity, two tendencies compete: being deeper in the solid, the temperature of this point is higher than that of the surface; on the other hand the supply route of the heat is longer

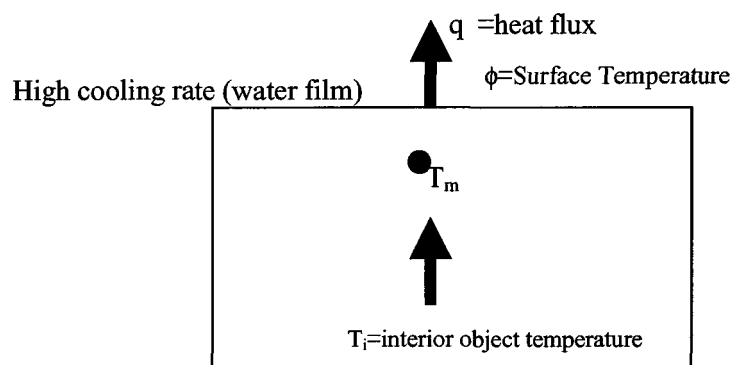


Figure 4.5: Sensor installed in a calorimeter mass without a cavity

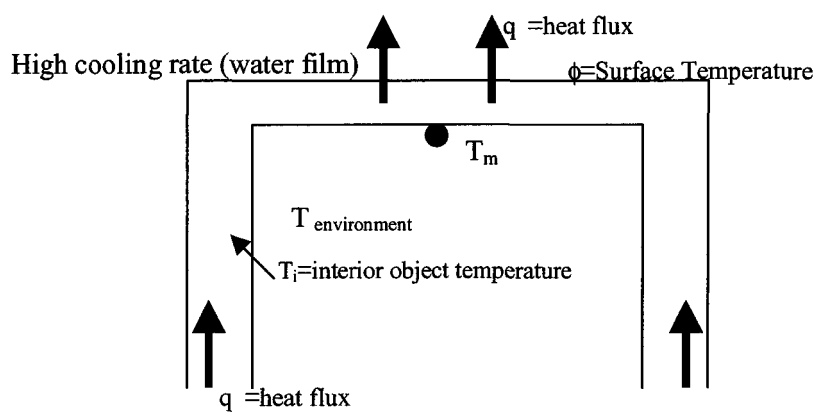


Figure 4.6: Calorimetric mass with a huge cavity in the backside

due to the presence of the hole that makes possible to cool that point more strongly than the others at the same depth.

Repeating the two presented cases, if we are measuring the temperature under the surface of a mass in which a high heat flux is in the normal direction to the surface we may consider two possibilities. First, if there is no cavity in the object, the measured temperature is higher than the surface temperature ( $T_m > T_s$ ). Second, if there is a huge cavity in the backside of the object, the measured temperature is lower than the surface temperature ( $T_m < T_s$ ).

One may now find a way to combine the two extremes to compensate these two errors. In other words, we will create a cavity in the backside of our calorimetric mass with a certain ratio of the distance between surface and cavity bottom to the cavity diameter, in order to compensate the previously explained measurement errors. The optimal ratio of  $\frac{a}{b}$  (where  $a$  and  $b$  refers to Figure 4.4) can be determined with a numerical method, as it was done in [4]. The numerical investigation presented in [4] gave the value for the optimal ratio of  $\frac{a}{b}$  as follows:

$$\frac{a}{b} = 1.375$$

### 4.3.2 Null-Point Validation

The validation of the null-point method was carried out with a finite-element heat conduction solver in [4]. The *effects of changes in dimensional parameters* reflecting the time response velocity of a step heat-flux input depend on the ratio  $\frac{a}{b}$ . An optimum value for this ratio is defined as a value which yields the fastest time response to a step heat-flux input and maintains a constant value of indicated  $\dot{q}$  / input  $\dot{q}$  (see Figure 4.7). The result

determined by the finite-element method is shown in Figures 4.7 and 4.8 . At the optimum

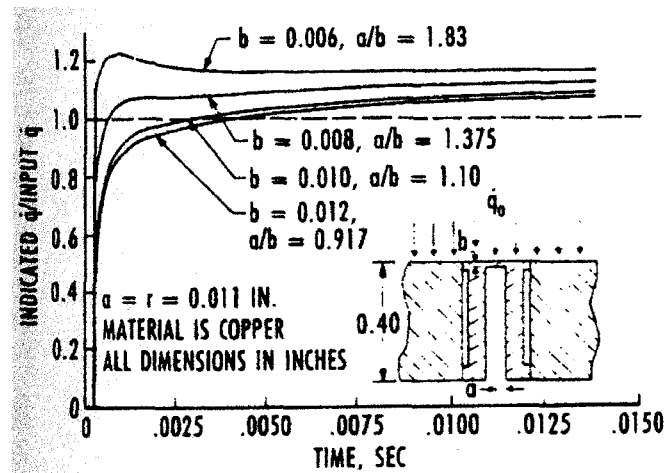


Figure 4.7: Null-point calorimeter analytical time response data [4]

response, 95 percent of full scale is reached in less than 1 millisecond and the asymptote for  $\dot{q}/\dot{q}_0$  approaches to 1.1 which is illustrated in both Figures. The data in Figure 4.7 were calculated by keeping the radius  $b$  constant and varying the thickness  $a$ . In Figure 4.8 the opposite procedure was applied to determine the results keeping the thickness constant and varying the radius. We recognize that in both calculations the optimum could be determined at the ratio  $\frac{a}{b} = 1.375$ .

The effects of locating the temperature sensor off the axial centerline were analyzed also to estimate the error caused by slight displacement of the thermocouple, because it can not be assured during the installation that the temperature sensor will be located exactly on the axial centerline of the cylindrical cavity as assumed in the finite-element calculation. Figure 4.9 shows that the placement of the temperature sensor at a location of up to  $r_0/a = 0.5$  will cause an error of less than 3 percent. This error is usually acceptable and

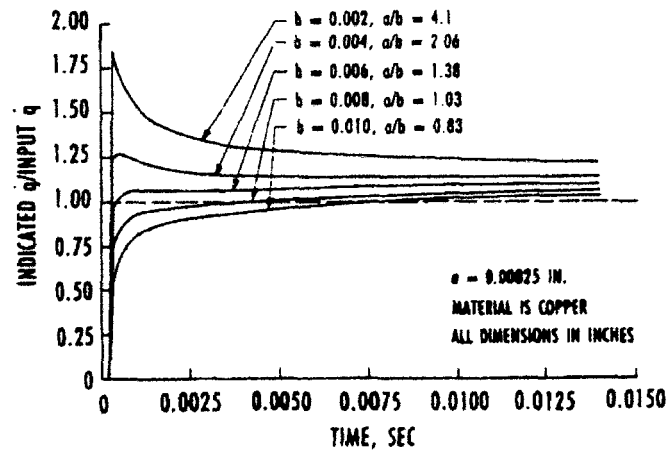


Figure 4.8: Null-point calorimeter analytical time response data (2) [4]

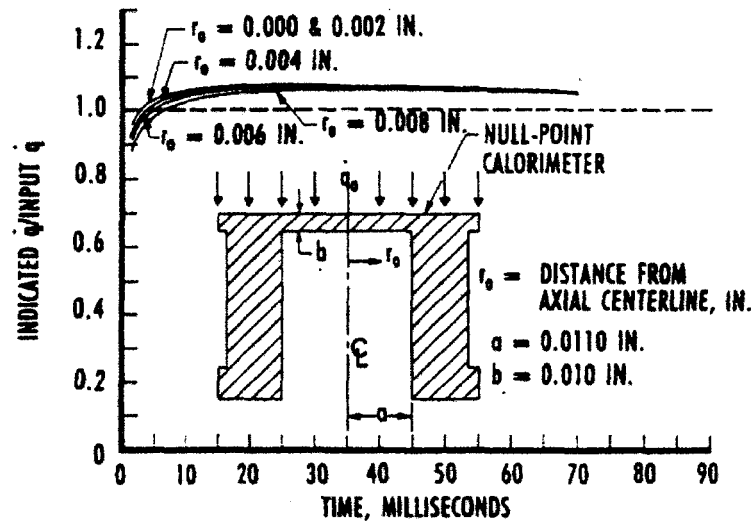


Figure 4.9: Error Occuring when the sensor is not correctly placed. [4]

adds credibility to the null-point concept showing that a strict centerline location of the thermoelements is not essential to obtain high-quality data.

#### 4.4 Surface Temperature Measurement

As we have seen in the section describing the Null Point Calorimeter, it is absolutely necessary to install a fast responding temperature sensor at the bottom of the null point cavity. In the beginning of the project we pressed closed tip thermocouples in the cavities. But the problem with this measurement method is the fact that the closed tip thermocouple consists of two soldered thermocouple wires embedded in a ceramic which is covered by a metal shield(see Figure 4.10). Thus the temperature obtained from this kind

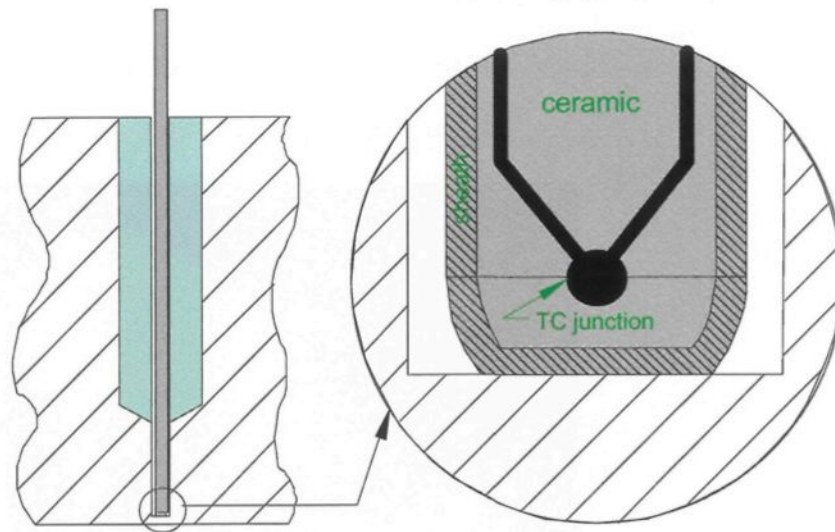


Figure 4.10: Thermocouple tip (closed, ungrounded)

of sensor is influenced by the contact resistance between thermocouple and the bottom of the cavity and the conduction through the embedded alloy. The measured temperature

with a closed tip thermocouple is not sufficiently close to the real temperature in the cavity bottom. The assumption of the null point calorimetry that the cavity bottom temperature is identical to the surface temperature is no longer acceptable. Therefore a new idea was developed where the cavity bottom is the junction of the two thermocouple wires.

#### 4.4.1 Open Tip Thermocouple

To realize the idea of the thermocouple junction in the cavity bottom the two thermocouple wires have to be connected to the cavity material. Thus the first step is to take an exposed junction thermocouple and to cut of the soldered junction. Then we get the two free standing thermocouple wires. Around these thin wires we must apply a reinforcing layer of high temperature cement. In Figure 4.11 a thermocouple with two separated wires and the cement is shown. We used a thermocouple with a sheath diameter of 0.75 mm. The cement head has a length of 5 mm. The cement will strengthen the tips of the cut wires so

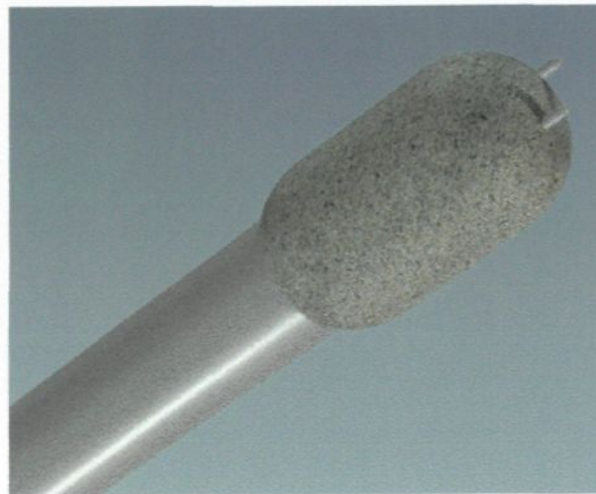


Figure 4.11: Thermocouple prepared for installation with high temperature cement

that we are able to point them into the aluminium of the cavity bottom. After some tests with different enamels, we took the high temperature cement from OMEGA to embed the thermocouple wires which gave better results. The open tip thermocouples prepared this way were installed in the cavity (see Figure 4.12). The two thermocouple wires stick in

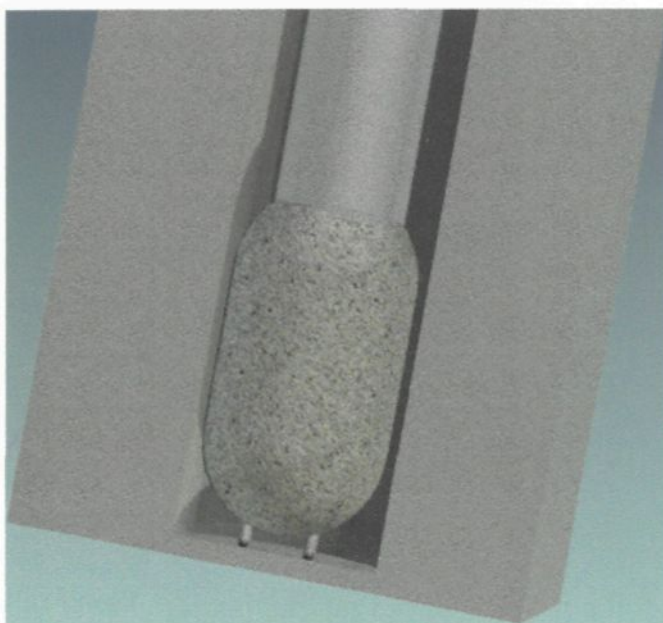


Figure 4.12: Thermocouple in the null point cavity

the bottom and establish an electrical contact. This contact is the temperature sensitive junction and is situated directly in the cavity bottom. The installed thermocouple has its measurement zone directly in bottom of the cavity. According to the null point calorimetry principle, we measure the real surface temperature this way. During the heating and cooling, the thermocouple is exposed to a thermal expansion. To assure that the two thermocouple wire tips still rest in contact with the cavity bottom, we applied a permanent force on the thermocouple. The easiest way to realize this was by a pendulum weight which exerts a

constant force on the thermocouple shaft. In Figure 4.13 the weight and the thermocouple shaft (indicated red) are shown.

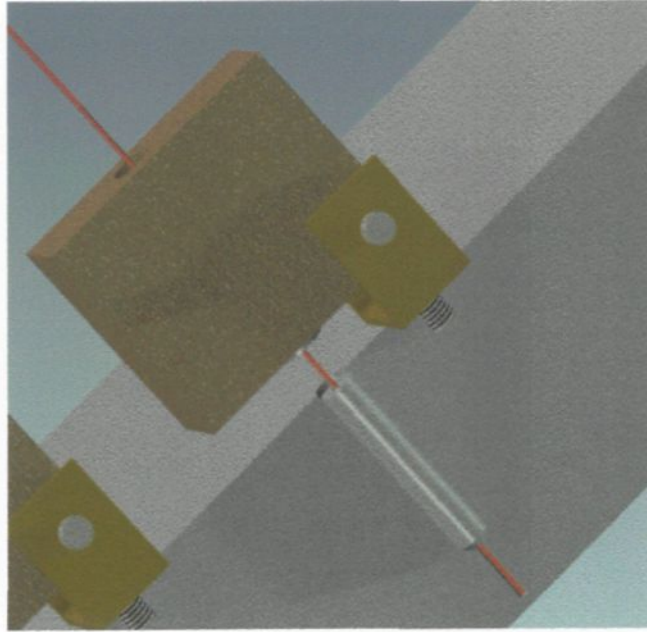


Figure 4.13: Pendulum weight for the thermocouple

#### 4.4.2 Thermocouple Installation in the Cavity

As it was explained in Section 4.3.1 the ratio of the distance between the surface and cavity bottom to the radius of the cavity is important to obtain a good response time and an accurate measurement. Due to the fact that drilling holes of arbitrarily small diameters precisely is limited by the tools used such as drills, the necessary distance-to-radius ratio has to be determined by the thickness between the cavity bottom and the cooled surface of the slab. It is desired to use the ingot surface as produced in the plant during the experiments, the problem of drilling a hole with a highly accurate distance to the

surface in an ingot with a maximal surface roughness of  $\pm 0.7$  mm becomes a problem. The surface roughness was investigated with a coordinate measuring machine with a resolution of  $1/100$  mm and an accuracy of  $\pm 0.05$  mm for each axis. The measurement table is shown in Figure 4.14. The surface roughness has the same order of magnitude as the distance between



Figure 4.14: Measurement table

cavity bottom and surface so that the roughness data must be taken into account in the placement of the thermocouples. The photo presented in Figure 4.15 gives an impression of the ingots surface roughness. Thus a three-dimensional map was made for each part

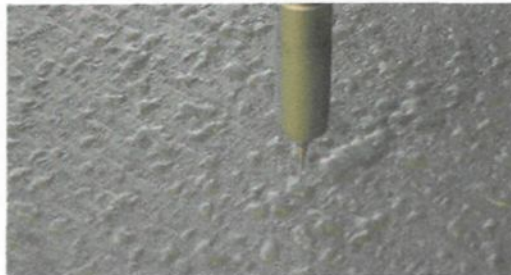


Figure 4.15: Ingot surface roughness

of the ingot where a thermocouple should be placed, like it is illustrated in Figure 4.16.

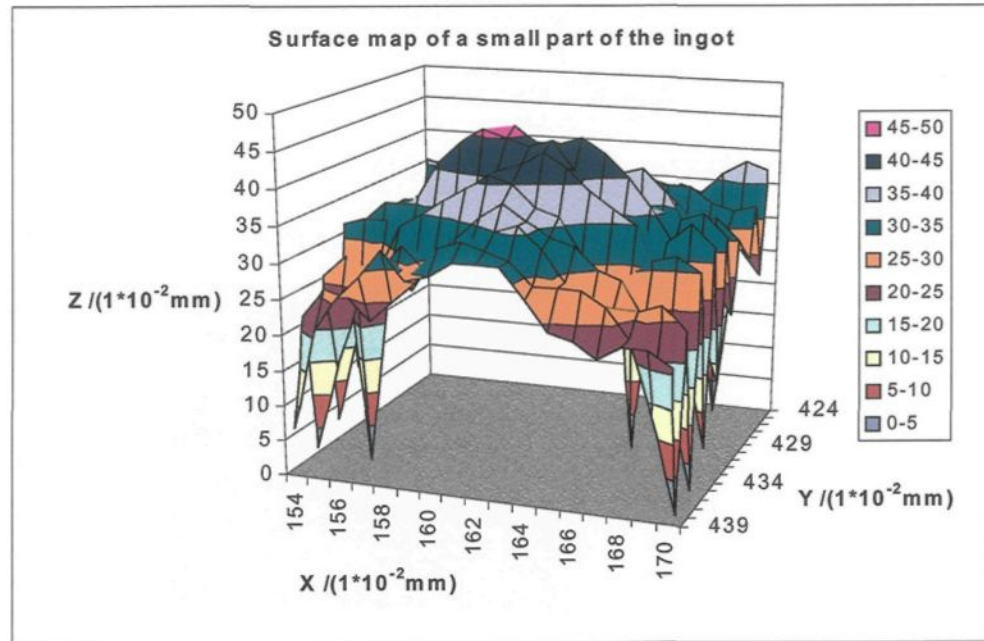


Figure 4.16: 3-D map of a part of the ingot surface

Then it was determined whether the area around the selected position is plane enough. The difference in height around the thermocouple position had to be less than 0.05 mm in order to meet the conditions required by the correct functioning of the null-point calorimeter. The coordinates of the center were used to drill the plug hole. The accuracy of the plug hole depth will influence the spacing between the rough surface and the cavity because the cavity hole will be made with the especially developed drill shown in Figure 4.17. That device uses the bottom of the plug hole to define the spacing of the cavity in the slab. This method has the advantage that only the plug hole has to be checked during the drilling to adjust the accurate depth, then the cavity hole follows automatically without problems ensuring the correct spacing. The plug hole was made by using a high precision coordinate table that is coupled with a drilling machine. The length and width coordinates of the position

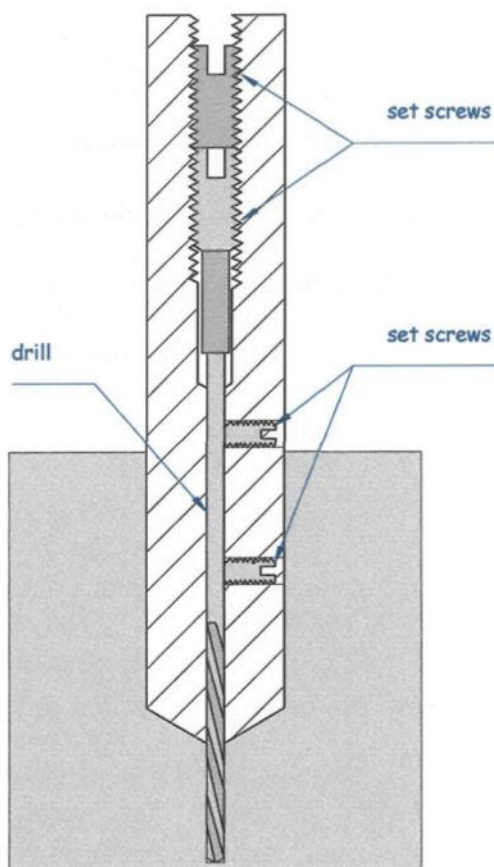


Figure 4.17: Specialty developed cavity drill

	length in mm	height in mm	width in mm
Hole TC1	134.74	145.49	63.59
Hole TC2	224.96	135.68	63.26
Hole TC3	317.52	144.90	63.78
Hole TC4	407.16	158.03	63.84

Table 4.1: Hole positions

of the hole were taken by the reference point set at the corner of the slab to position the drill exactly at the determined place. For each plate the hole position is different depending on the surface roughness. An example for the hole positions can be seen in Table 4.1. As it can be seen there, the distance between the measurement positions are about 90 mm. The cavity diameter was exactly 2 mm. In the sketch shown in Figure 4.18 the position is indicated for the thermocouples. From now on all following descriptions refer to this setup.

#### 4.4.3 Temperature Conversion

Unfortunately, the temperature versus voltage relationship of a thermocouple is non-linear. This can be easily seen in Figure 4.19 where the output voltage as a function of the temperature is plotted. Another evidence which indicates a non-linear behavior of the thermocouple voltage as a function of temperature is the Seebeck coefficient  $\alpha_s$ . When we plot the Seebeck coefficient vs. temperature, a horizontal line would indicate a constant  $\alpha_s$  however, as it is shown in Figure 4.20 it is not the case. Only the K-type thermocouple approaches a constant over a temperature range from  $0^\circ C$  to  $1000^\circ C$ . But even for this type, to have a better accuracy we have to fit the slope of the voltage using the following

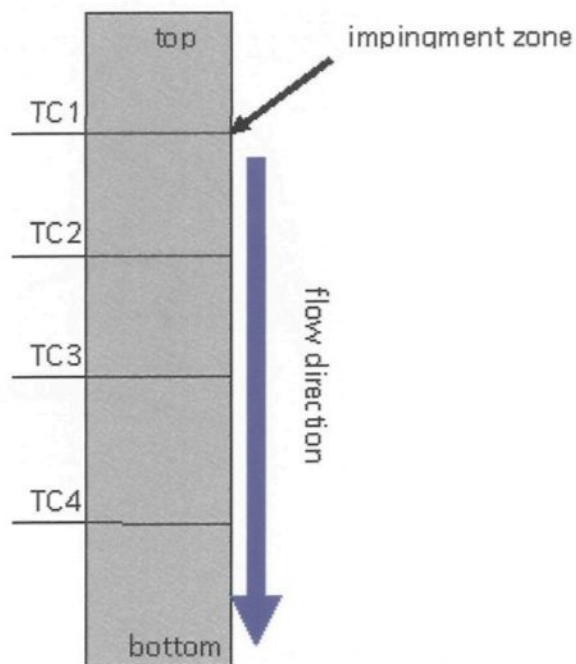


Figure 4.18: Thermocouple position

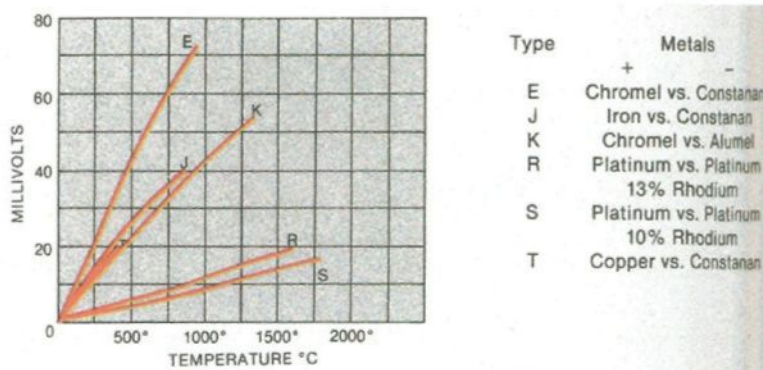


Figure 4.19: Thermocouple temperature vs. voltage graph [17]

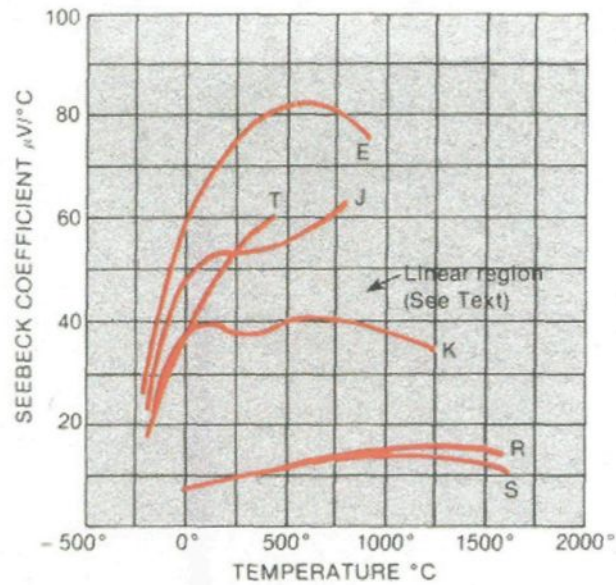


Figure 4.20: Seebeck coefficient vs. temperature [17]

polynomial equation.

$$T = a_0 + a_1x + a_2x^2 + \dots + a_nx^n$$

where

T = temperature,  $^\circ\text{C}$

x = thermocouple voltage, V

a = polynomial coefficient unique to thermocouple

n = maximum order of the polynomial

As n increases to the number of n = 9, the accuracy improves to  $\pm 1^\circ\text{C}$ . To

save execution time the computer can be programmed with a *nested* polynomial form. The

different coefficient for the different thermocouple types are shown in the table in Table 4.2<sup>2</sup>.

This coefficients should not be used outside the denoted temperature range. We changed

the K-type thermocouple after some experiments to N-type thermocouples because they are

more resistant against oxidation and aging. The N-type thermocouple needs to be replaced

<sup>2</sup>On the web site [www.OMEGA.com](http://www.OMEGA.com) the actual coefficients can be found.

	TYPE E	TYPE J	TYPE K	TYPE R	TYPE S	TYPE T
	Nickel-10% Chromium(+) Versus Constantan(-)	Iron(+) Versus Constantan(-)	Nickel-10% Chromium(+) Versus Nickel-5%(-) (Aluminum Silicon)	Platinum-13% Rhodium(+) Versus Platinum(-)	Platinum-10% Rhodium(+) Versus Platinum(-)	Copper(+) Versus Constantan(-)
	-100°C to 1000°C* ± 0.5°C 9th order	0°C to 760°C* ± 0.1°C 5th order	0°C to 1370° C* ± 0.7°C 8th order	0°C to 1000°C* ± 0.5°C 8th order	0°C to 1750°C* ± 1°C 9th order	-160°C to 400°C* ± 0.5°C 7th order
a <sub>0</sub>	0.104967248	-0.048868252	0.226584602	0.263632917	0.927763167	0.100860910
a <sub>1</sub>	17189.45282	19873.14503	24152.10900	179075.491	169526.5150	25727.94369
a <sub>2</sub>	-282639.0850	-218614.5353	67233.4248	-48840341.37	-31568363.94	-767345.8295
a <sub>3</sub>	12695339.5	11569199.78	2210340.682	1.90002E + 10	899073066.3	78025595.81
a <sub>4</sub>	-448703084.6	-264917531.4	-860963914.9	-4.82704E + 12	-1.63565E + 12	-9247486589
a <sub>5</sub>	1.10866E + 10	2018441314	4.83506E + 10	7.62091E + 14	1.88027E + 14	6.97688E + 11
a <sub>6</sub>	-1.76807E + 11		-1.18452E + 12	-7.20026E + 16	-1.37241E + 16	-2.66192E + 13
a <sub>7</sub>	1.71842E + 12		1.38690E + 13	3.71496E + 18	6.17501E + 17	3.94078E + 14
a <sub>8</sub>	-9.19278E + 12		-6.33708E + 13	-8.03104E + 19	-1.56105E + 19	
a <sub>9</sub>	2.06132E + 13				1.69535E + 20	

TEMPERATURE CONVERSION EQUATION:  $T = a_0 + a_1 x + a_2 x^2 + \dots + a_n x^n$

NESTED POLYNOMIAL FORM:  $T = a_0 + x(a_1 + x(a_2 + x(a_3 + x(a_4 + a_5 x))))$  (5th order)

Table 4.2: Polynomial coefficients

Ref. [17]

less frequently. The coefficients for the N-type thermocouple could be found on the internet site: Ref. [1]. To calculate the temperature I used the eight coefficients ( $n = 7$ ) illustrated in Table 4.3. The transformation from the thermocouple voltage to temperature was made in a MATHCAD worksheet. In Appendix A the functions used to determine the temperatures from the measured voltages are shown. The conversion includes the correction for the used reference junction.

## 4.5 Visualization

The visualization is the key to investigate the occurring surface boiling effects. To carry out a fundamental analysis of the boiling mechanism and its influence on the local heat transfer coefficients, the surface temperature measurement data must be synchronized with the visualization system. Then, the effects on the heat flux can be related to the

coefficient	value for a K-Type TC
$a_0$	0
$a_1$	3.86896E+1
$a_2$	-1.08267
$a_3$	4.70205E-2
$a_4$	-2.12169E-6
$a_5$	-1.17272E-4
$a_6$	5.39280E-6
$a_7$	-7.98156E-8

Table 4.3: Conversion coefficients

Ref. [1]

boiling mechanism which leads to a better understanding of the influencing parameters.

There are different suitable methods to investigate the water and vapor flow at the ingot surface during the cooling. The most used one presently is a normal video film with different illumination methods. In some experiments two video cameras were used. One camera was used to film the entire cooling process to gather information about the development of the re-wetting zone and the water film during the whole experiment. The other camera was used to shoot a close up view of the re-wetting zone to investigate bubbles or the unstable vapor film formation. Unfortunately we were not able to visualize any vapor fluctuations or bubbles. Even when we used a zoom up to 20 we could not see any bubbles. We also used other illumination methods like a laser sheet to visualize the surface flow characteristics. An illumination only by laser light was also considered.

One problem was the contrast; there is not a really big difference in contrast between the water and vapor layer. Of course this problem could be improved by changing the illumination. Since each experiment needs a long preparation time we could not make as many experiments as we want. So we did not have the possibility to adjust the illumination

as it would be necessary. In addition, the whole cooling process is not longer than two and a half minutes. Thus it does not permit the adjustment of all the illumination parameters during the cooling. As a summary numerous experiments and expertise are required to develop a suitable illumination and recording method to visualize the surface flow. Due to the limited number of experiments carried out and the short cooling duration these expertise can only be gained slowly.

#### 4.5.1 Synchronization

As mentioned before the most important benefit of the visualization can be obtained if it is synchronized with the appertaining measurement data. The best would be the case where the measurement time could be directly displayed in the film. Unfortunately our data acquisition system did not provide any output of the measurement time. There might be a possibility to get this information displayed by using the connected host computer. But this would need a software which has to be programmed. Then the problem how to transfer it into the film display still exists.

One way to achieve a synchronization is by using optical indicators which are turned on at prescribed values of the measured temperatures. In our case we used four laser pointers which projected light spots onto the measurement position along the ingot. Then an alarm limit was programmed in the data acquisition software which switched on the laser pointers once the programmed value was achieved. For example we used the alarm limit of 200 °C. When the re-wetting zone passed the measurement point the temperature fell below the value of 200 °C. Then an entry was saved in the log file of the DAQ system and the laser pointer was switched on (see Figure 4.21). This way we can compare the

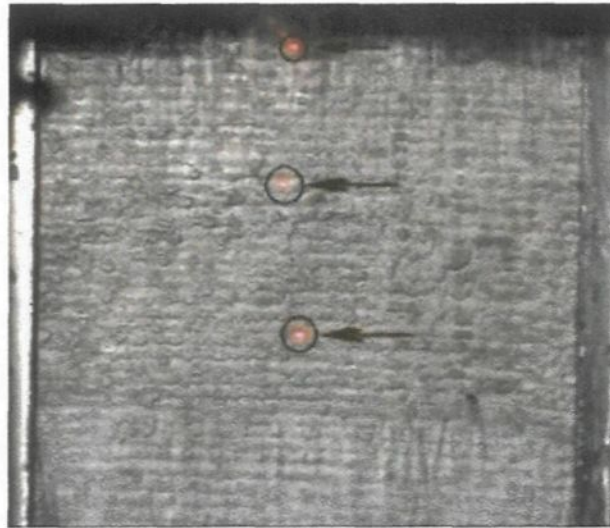


Figure 4.21: Laser pointer synchronisation

time of the video camera and the time of the DAQ system. The method is not perfectly accurate due to the fact that we have to determine the time it takes to switch the laser on. Nevertheless this method provides a possibility to easily compare the movie with the measurement data.

#### 4.5.2 Laser Sheet and other Laser Illumination Methods

The laser sheet method was used to obtain surface flow information. Two tests were made using this visualization method. Unfortunately the films of these experiments can not be used because the laser light was not intense enough to provide sufficient light for the video camera. A further problem was related to the adjustment of the focus. The focus was set to the centerline of the plate where the laser sheet was projected. But the water between the camera and the laser sheet disturbed the image in a way that no sharp pictures could be taken. The installation of a more powerful laser source was completed too late to

use during the experiments.

Another idea uses a laser sheet in a different manner to illuminate the liquid-vapor mixed flow. We considered an illumination which is pointed directly to the re-wetting zone. Thus the light might emphasize the unstable vapor film fluctuations we assume existing in the vicinity of the re-wetting zone. In Figure 4.22 a scheme of the setup is shown. The light

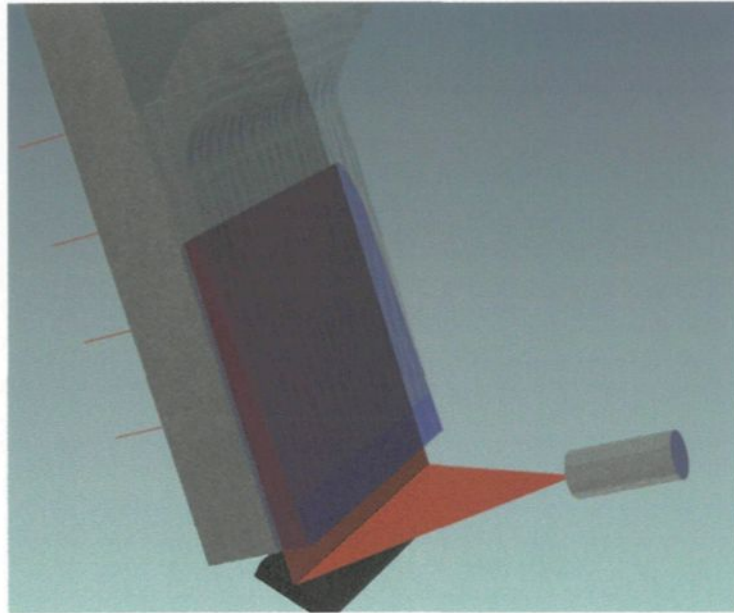


Figure 4.22: Laser sheet to illuminate the re-wetting zone

emitted from the laser sheet is reflected by a mirror installed directly under the ingot. The laser light is reflected and forms a curtain of light in the vapor layer until it reaches the re-wetting zone. The first trial with this method did not work because of the insufficient laser power. The water falling on the mirror diffuses a big portion of the light so that the rest was not strong enough to illuminate the re-wetting zone.

The images obtained by the visualization method will be discussed in the Chapter

6.4.

## 4.6 Test Series

In the following we will give an insight of all experiments carried out using the new open tip thermocouple measurement method. The conditions of all the experiments are listed in Figure 4.23. It has to be mentioned that the investigations could not cover the whole range of parameters and all possible combinations of them. As one successful test requires at least one week of preparation and as one specimen (plate) can be used only in a limited number of tests, the 36 experiments that were completed required a very long period. We identified those parameters which show measurable variations on the cast-shop (conductivity and oil content of the water, effects of additives, surface roughness) and we compared the cooling capacity of water with perturbed parameters to that of "standard" or tap water. It can be seen that several test were conducted with different water types on different plates. First we investigated the influence of the surface roughness on the heat flux using different plates and tap water (see Group A and B in Figure 4.23). After conduction about four test with the same setup we have reached a conclusion about the repeatability of the surface boiling effects. Then we used the machined ingot to test the difference between tap, plant and high conductivity (HC) water ( see Group B, C and D). After the eleventh experiment the deformation of the machined ingot did not permit further tests. Because of the accumulating scale layer (see Subsection 6.7.2) on the surface of the machined ingot it was necessary to repeat the experiment with tap and high conductivity water (HC) on the new rough surface ingot PL2 (see E and F). Then we started a new

Line	Measurement Dates	Ingot Surface	Water Type	Visualization	Failures		
1	25.09.2001	Rough (PL A)	Tap Water		TC 4	A	
2	01.10.2001	Rough (PL A)	Tap Water		TC 4		
3	03.10.2001	Rough (PL A)	Tap Water		TC 4		
4	04.10.2001	Rough (PL A)	Tap Water				
5	05.10.2001	Rough (PL A)	Tap Water				
6	07.10.2001	Machined Ingot	Tap Water			B	
7	08.10.2001	Machined Ingot	Tap Water				
8	09.10.2001	Machined Ingot	Tap Water				
9	10.10.2001	Machined Ingot	Tap Water		TC 1	C	
10	17.10.2001	Machined Ingot	Plant Water		TC 1		
11	18.10.2001	Machined Ingot	Plant Water		TC 1 & TC2		
12	25.10.2001	Machined Ingot	Plant Water				
13	26.10.2001	Machined Ingot	Plant Water			D	
14	08.11.2001	Machined Ingot	Plant Water		TC 4		
15	12.11.2001	Machined Ingot	HC Water		TC 4		
16	13.11.2001	Machined Ingot	HC Water			D	
17	14.11.2001	Machined Ingot	HC Water		TC 1 & TC 4		
18	20.02.2002	Rough (PL 2)	Plant Water	Front View & Close up		E	
19	28.02.2002	Rough (PL 2)	HC Water	Laser Sheet		F	
20	16.04.2002	Rough (PL 2)	100mg/l BI			G	
21	18.04.2002	Rough (PL 2)	100mg/l BI	Laser Sheet			
22	22.04.2002	Rough (PL 2)	100mg/l BI	Front View & Close up			
23	23.04.2002	Rough (PL 2)	100mg/l BI	Front View	TC 4		
24	25.04.2002	Rough (PL 2)	100mg/l BI				
25	26.04.2002	Rough (PL 2)	50mg/l SU	Side View & Close up	TC 2	H	
26	08.05.2002	Rough (PL 2)	Tap Water			I	
27	10.05.2002	Rough (PL 2)	50mg/l SU			J	
28	16.05.2002	Rough (PL 3)	Tap Water			K	
29	22.05.2002	Rough (PL 3)	50mg/l SU			L	
30	23.05.2002	Rough (PL 3)	250mg/l SU		TC 4	M	
31	03.06.2002	Rough (PL 3)	100mg/l CI		TC 4	N	
32	23.07.2002	Rough (PL 3)	100mg/l CI	Laser Sheet (green light)			
33	16.08.2002	Rough (PL 3)	Water-Oil Mixture	Front View		O	
34	19.08.2002	Rough (PL 3)	Water-Oil Mixture	Front View			
35	23.08.2002	Rough (PL 3)	Water-Oil Mixture	Front View			
		Legend:	BIODISPERSANT = BI				
			SURFACTANT = SU				
			CORROSION INHIBITOR = CI				

Figure 4.23: List of experiments

series with the biodispersant water agent (see Section 6.3), as shown in group G. After this serie we tested a surfactant water agent (see Group H, J, M). The surfactant water agent is a liquid cleaner additive. In between it was necessary to perform a reference measurement as shown in group I. With this measurement we could study the effect of ageing of the ingot. The rough ingot PL2 was exchanged after its ninth test because of its deformation. With the newly installed rough surface (as-cast surface) ingot PL3 we performed two tests with the agent surfactant water agent before we changed to test with a corrosion inhibitor agent. This water agent is a water-based corrosion inhibitor and deposit control agent. The corrosion inhibitor agent was tested only at one concentration ( $50 \frac{\text{mg}}{\text{l}}$ ), thus the analysis is not included here. Nevertheless, the results indicate that there is no difference between the corrosion inhibitor containing cooling water with a concentration of  $50 \frac{\text{mg}}{\text{l}}$  and tap water. In group O experiments were conducted using water-oil mixture (84 ppm oil content). Similarly as shown above, in this case we tested only one oil concentration and we compared those results to the results of cooling with tap water. The results do not show a significant difference.

## Chapter 5

# Numerical Simulations

### 5.1 Finite Difference Method

The purpose of this work, was to create a numerical model to simulate the process of ingot cooling. In the scope of this section; the developed model will be presented and its prediction will be compared with the analytical solution obtained with the Cook Felderman equation. The simulation was carried out using the experimental conditions, to provide an easy comparability of measured and calculated results. The model was developed for one and two dimensional cases. For the one-dimensional model a finite difference method was used. The two dimensional case was achieved using a finite difference method. The two different methods will be presented in the following sections.

In this section the implementation of the finite difference method will be described. The algorithms were developed in the **MATCAD** environment. The advantage of using this program is the easy handling of the results obtained, that are normally matrices. The data can be plotted directly in the program and mathematical expressions like matrix

functions are implemented. Thus, for the development, where a lot of verifications and mathematical operations are necessary, working with such an environment is useful. The disadvantage is the computation time. For a large number of nodal points and time steps, the computation time might take up to one hour. Therefore the precision of some of the results could be improved by using a higher mesh density. Because of the long computation times, the number of nodal points were not increased to stay in reasonable time frame. Due to this reason the results for the two dimensional problem could not approach desired precision. The simulations carried out using the finite volume method and a C++ source code could achieve more accurate results (see Chapter 5.2). Thus the solutions for a two dimensional case will be not presented here. However, the simulation in one-dimension already provided some important conclusions. The geometry of the slab used in the experiment is shown in Figure 5.1. Of course, for the one-dimensional simulation only the thickness is of interest.

### 5.1.1 Theory

Analytic solutions to transient problems are normally restricted to simple geometries and boundary conditions. For more complicated geometries and boundary conditions we can use numerical methods such as *finite-difference* methods. Actually in our case, the geometry is quite simple and an analytic solution exist for the cuboid shape. But the need of a numerical model is based on the fact that our boundary conditions can not be described in such a way that the system equations can be solved analytically. Because the wetting and re-wetting process as well as the bubble formation on the surface are so complex that an analytical description is not possible. Therefore we want to develop a numerical model

to which we can enter the measured boundary conditions. This Section will give a short description of the basic principles of the finite difference method.

The finite difference technique enables the determination of the temperature only at *discrete* points. To define these points we subdivide the domain of interest into a number of smaller regions and we assign to each of them a reference point that is at its center.

With this step we introduced the *nodal network* with its reference points, termed *nodal point*. The nodal points are designated by a numbering scheme. For a two-dimensional system, they are denoted by the  $m$  indices for the  $x$  direction and by the  $n$  indices for the  $y$  direction. Each node represents a certain region, and its temperature is a measure of the *average* temperature of the region. With a large number of nodal points an extremely accurate solution can be obtained because the numerical accuracy of the calculation depends strongly on the number of designated nodal points. Now we have to consider for any interior node the energy conservation requirements, for our two-dimensional system. Considering a steady-state problem with no energy generation and a uniform thermal conductivity within the node-region the energy conservation is given by the heat Equation 5.1.

$$\frac{\partial^2 T}{\partial x^2} + \frac{\partial^2 T}{\partial y^2} = 0 \quad (5.1)$$

This differential equation can be transformed into a finite-difference equation by taking the *forward* and *backward differences* of the point  $m, n$ . The following two differences will be composed to the approximate value of the derivative at the  $m, n$  nodal point.

$$\begin{aligned} \frac{\partial T}{\partial x} \Big|_{m-\frac{1}{2},n} &\approx \frac{T_{m,n} - T_{m-1,n}}{\Delta x} && \text{:backward difference} \\ \frac{\partial T}{\partial x} \Big|_{m+\frac{1}{2},n} &\approx \frac{T_{m+1,n} - T_{m,n}}{\Delta x} && \text{:forward difference} \end{aligned}$$

Substituting in

$$\frac{\partial^2 T}{\partial x^2}$$

we obtain

$$\frac{\partial^2 T}{\partial x^2} \Big|_{m,n} \approx \frac{\frac{\partial T}{\partial x} \Big|_{m+\frac{1}{2},n} - \frac{\partial T}{\partial x} \Big|_{m-\frac{1}{2},n}}{\Delta x} \quad (5.2a)$$

$$\frac{\partial^2 T}{\partial x^2} \Big|_{m,n} \approx \frac{T_{m+1,n} + T_{m-1,n} - 2T_{m,n}}{(\Delta x)^2} \quad (5.2b)$$

The same procedure can be applied in the  $y$  direction and using a network where  $\Delta x = \Delta y$ .

Substituting the second derivatives of temperatures in Equation 5.1 we obtain the following *algebraic equation*.

$$T_{m,n+1} + T_{m,n-1} + T_{m+1,n} + T_{m-1,n} - 4T_{m,n} = 0$$

This approximation, the *finite difference form of the heat equation* for steady conduction without internal heat generation, is applicable to any interior node that is equidistant from its four neighboring nodes.

We can simply extend this method to a transient conduction problem by adding the rate of change of the internal energy to the steady-state heat Equation 5.1.

$$\frac{\partial^2 T}{\partial x^2} + \frac{\partial^2 T}{\partial y^2} = \frac{1}{\alpha} \frac{\partial T}{\partial t} \quad (5.3)$$

This equation is valid under transient conditions with constant properties and without internal heat generation. To transform the time dependent part of our differential equation into a finite-difference form we use the same procedure as for the spatial term. It is only necessary to introduce an integer variable  $p$  to denote the time dependence of the temperature  $T$ . We introduce for this purpose

$$t = p \Delta t$$

and express the finite difference approximation of the time derivative in Equation 5.3 as follows:

$$\frac{\partial T}{\partial t} |_{m,n} \approx \frac{T_{m,n,p+1} - T_{m,n,p}}{\Delta t} \quad (5.4)$$

where  $p+1$  indicates the new and  $p$  the previous time. If we consider that the finite-difference approximation of the spatial derivative is evaluated for the *previous* time we may substitute the approximation of the spatial steady-state equation 5.2a and the approximation of the time dependence term given in equation 5.4 into equation 5.3. We obtain:

$$\frac{1}{\alpha} \frac{T_{m,n,p+1} - T_{m,n,p}}{\Delta t} = \frac{T_{m+1,n,p} + T_{m-1,n,p} - 2T_{m,n,p}}{(\Delta x)^2} + \frac{T_{m+1,n,p} + T_{m-1,n,p} - 2T_{m,n,p}}{(\Delta y)^2}$$

Solving for a nodal temperature at the new ( $p+1$ ) time and assuming that  $\Delta x = \Delta y$  :

$$T_{m,n,p+1} = \frac{1}{Mo} (T_{m+1,n,p} + T_{m-1,n,p} + T_{m,n+1,p} + T_{m,n-1,p}) + \left(1 - \frac{4}{Mo}\right) T_{m,n,p} \quad (5.5)$$

where  $Mo$  is a modulus in the finite difference method

$$Mo = \frac{(\Delta x)^2}{\alpha \Delta t}$$

For a one-dimensional system with an interior node  $m$  the equation simplifies as:

$$T_{m,p+1} = \frac{1}{Mo} (T_{m+1,p} + T_{m-1,p}) + \left(1 - \frac{2}{Mo}\right) T_{m,p} \quad (5.6)$$

The Equations 5.5 and 5.6 are *explicit* because the *unknown* nodal temperatures for the new time are determined exclusively by *known* nodal temperatures at a previous time. The accuracy of the finite-difference solution may be improved by decreasing the values of  $\Delta x$  and  $\Delta t$ .

An undesirable feature of the *explicit method* is that it is not unconditionally *stable*.

In a transient problem, the solution for the nodal temperatures of the explicit method should

continuously approach final (steady-states) values with increasing time. But the numerical calculation induce an oscillation into the solution which may become *unstable*. This is physically impossible and causes a divergence between the solution and the actual steady-state condition. To avoid these instabilities we introduce a stability criterion, such that the coefficient associated with the node of interest at the previous time should be greater than or equal to zero. In our case the stability criterion for a one-dimensional interior node is  $(1 - \frac{2}{Mo}) \geq 0$ , or

$$Mo \leq 2$$

and for two-dimensional node, it is  $(1 - \frac{4}{Mo}) \geq 0$ , or

$$Mo \leq 4$$

If these requirements are respected during the calculation of the temperature distribution within a given region the numerical solution will not diverge.

### 5.1.2 One-Dimensional Model

The first attempt to the numerical analysis was done using an one-dimensional model. The main purpose of this step was to compare the numerical solution with an analytical solution of heat conduction in a semi-infinite solid in one dimension, the solution of Cook Felderman equation. The Boundary conditions for this model are quite simple. At the surface of the front we used a prescribed temperature, the boundary condition of the first kind. At the backside we assumed a perfect insulated surface (see Figure 5.2).

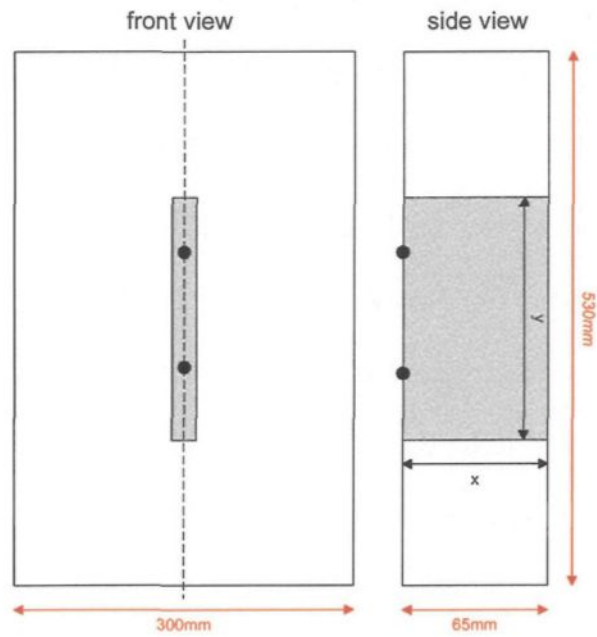


Figure 5.1: Sketch of the slab with dimensions

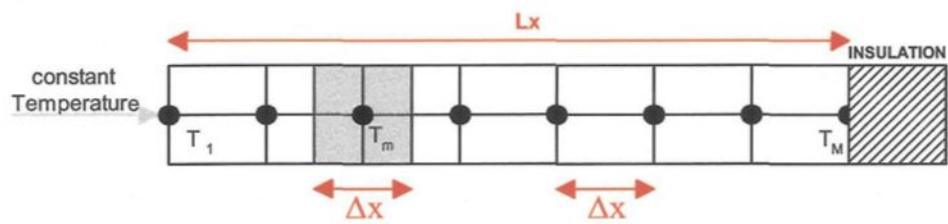


Figure 5.2: Sketch of the boundary condition in one-dimension

### 5.1.3 Derivations for the One-Dimensional Model

The derivation for the internal temperature at the nodes in one-dimension are already done in Section 5.1.1. In equation 5.6 the final form of the equation is presented. Now we have to consider the boundary conditions at the front and back of the slab. As stated before, we use the boundary conditions of the first kind for the front side of the slab. Due to the fact that we already measured the surface temperature during an ingot cooling these data are used as boundary condition in the numerical model. This boundary condition can be incorporated to the model by writing the known temperature value in the temperature matrix.

Due to the fact that during an experiment the temperature at the back of the slab was not determined yet, we assumed the backside to be insulated. To improve the solution it is recommended to replace this boundary condition with the measured backside temperature in the future. We will apply the energy balance method to a boundary nodal point. This means that we apply the energy conservation to the control volume (see grey area in Figure 5.2) of the nodal region.

If we have to take into account that there is no heat flux coming from the insulation the heat transfer rate  $Q_{insulation-T_M}$  is zero. The energy balance for the nodal point at the boundary  $M$  can be written as follows:

$$k (\Delta x \cdot 1) \frac{(T_{M-1,p} - T_{M,p})}{\Delta x} = \rho c_p \left( \frac{\Delta x}{2} \Delta x \right) \frac{(T_{M,p+1} - T_{M,p})}{\Delta t}$$

Rearranging this equation and solving for the temperature at the next time step we obtain:

$$T_{M,p+1} = \frac{2k\Delta t}{\Delta x^2 \rho c_p} [T_{M-1,p} - T_{M,p}] + T_{M,p}$$

```

T :=
  for m ∈ 1..M
    T1,m ← Data1,1
  for p ∈ 1..P
    Tp,1 ← SurfaceTempp
  for p ∈ 1..P-1
    for m ∈ 2..M-1
      Tp+1,m ←  $\frac{1}{Mo} (T_{p,m+1} + T_{p,m-1}) + \left(1 - \frac{2}{Mo}\right) \cdot T_{p,m}$ 
      Tp+1,M ←  $\frac{2}{Mo} (T_{p,M-1}) + \left(1 - \frac{2}{Mo}\right) \cdot T_{p,M}$ 
    T

```

Figure 5.3: Calculation loop for the one-dimensional model

Which can be simplified using the finite difference modulus  $Mo$

$$Mo = \frac{(\Delta x)^2}{\alpha \Delta t}$$

where  $\alpha$  is the thermal diffusivity with  $\alpha = \frac{k}{c_p \rho}$

$$T_{M,p+1} = \frac{2}{Mo} [T_{M-1,p}] + \left(1 - \frac{2}{Mo}\right) T_{M,p} \quad (5.7)$$

Now we can develop the calculation loop for the temperature matrix which is shown in Figure 5.3. Each column of the matrix stands for the temperature distribution within the solid for an instant of time and each row represents a further time step. The variable  $M$  denotes the maximal number of nodes in the model and the variable  $P$  stands for the total number of time steps.  $Mo$  is the finite difference modulus. The first for loop of the model presented in Figure 5.3 writes the initial temperature, that is stored in  $Data_{1,1}$ , in the matrix. In the second loop the measured surface temperature is written in each first cell of the matrix. The next two loops calculate the internal temperature nodes using equation

$c_p = 903 \frac{\text{J}}{\text{kg}} \text{ K}$ : specific heat	$k = 237 \frac{\text{W}}{\text{m}} \text{ K}$ : thermal conductivity
$L = 0.065 \text{ m}$ : thickness of the slab	$\rho = 2702 \frac{\text{kg}}{\text{m}^3}$ : density
$Mo = \frac{\Delta x^2}{\alpha \Delta t}$ : finite difference modul	$\alpha = \frac{k}{\rho c_p} \frac{\text{m}^2}{\text{s}}$ : thermal diffusivity

Table 5.1: Model parameter

5.6 and the insulated backside temperature nodes from equation 5.7. The parameters used are shown in Table 5.1.

The length (L) will be changed to investigate its effect on solution later. The maximal numbers of nodes are calculated according to the stability criteria:

$$\left(1 - \frac{2}{Mo}\right) \geq 0$$

If the stability is granted then we can determine the number of nodes using the following equation:

$$M = \frac{L}{\sqrt{\alpha \Delta t Mo}} \text{ with } Mo \geq 2$$

To verify the model, the results of the numerical model and the Cook Felderman solution should be compared using experimental data. Thus we took a surface temperature measurement of a former experiment and used this data for the prescribed surface temperature in the model. In addition, the surface heat flux was determined with the same temperature data using the Cook Felderman equation (see Figure 5.4).

#### 5.1.4 Curve fitting

A problem surfaced when the first results were obtained. The heat flux calculated by the numerical model was determined by the following equation:

$$\dot{q} = -k \frac{T_{p,1} - T_{p,2}}{\Delta x} \quad (5.8)$$

$$\begin{array}{l}
 \text{qf} := \\
 \left. \begin{array}{l}
 \text{for } p \in 2..P \\
 \text{qf}_p \leftarrow -2 \sqrt{\frac{k \cdot \rho \cdot c p}{\pi}} \cdot \sum_{i=2}^P \frac{(\text{SurfaceTemp}_i - \text{SurfaceTemp}_{i-1})}{[\sqrt{\Delta t \cdot p - i \cdot \Delta t} + \sqrt{p \cdot \Delta t - (i-1) \cdot \Delta t}]} \\
 \text{qf}
 \end{array} \right\}
 \end{array}$$

Figure 5.4: Cook Felderman equation

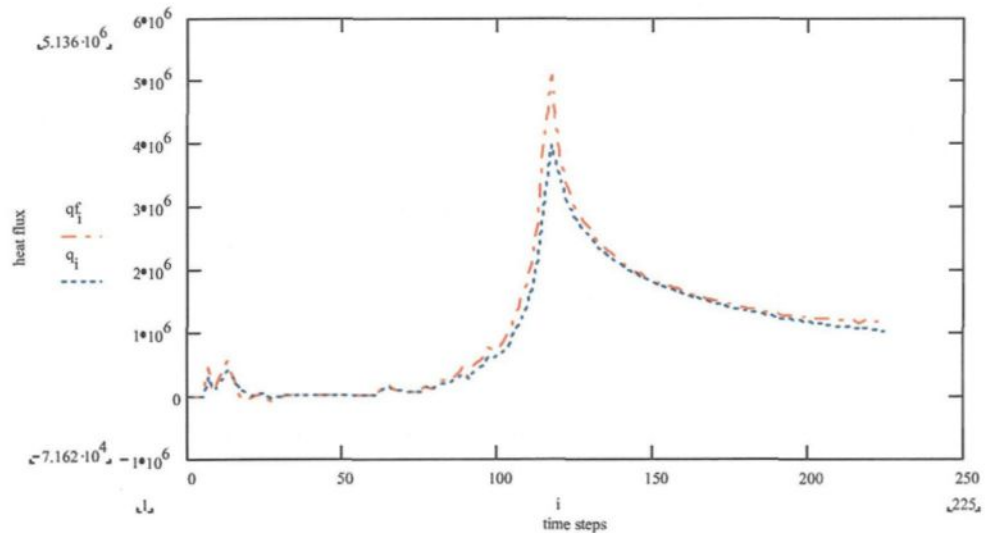


Figure 5.5: Heat flux from numerical model and Cook F. equation

where  $T_{p,1}$  is the temperature of the surface node and  $T_{p,2}$  the first temperature node within the slab at the instant  $p$ . But using this equation the maximal heat flux at the surface every time was found smaller than the one determined by the Cook Felderman (see Figure 5.5). One reason might be the number of nodal points was not sufficiently large enough. But due to the fact that the stability criteria had to be satisfied, the number of nodes could not be increased more than a certain number of points. It was necessary to calculate the temperatures accurately near the surface. Such a precision was not necessary at the interior

nodes. To avoid the need of an unsymmetrical grid, we took the surface node and the two adjacent nodes and we fit a third order polynomial passing through these points. The heat flux is given as:

$$\dot{q} = -k \frac{dT}{dx} \quad (5.9)$$

where  $T$  is the temperature function going through the three temperature points. The curve fit algorithm is shown in Figure 5.6, the parameter  $n$  is the number of points used which is three in this case. The surface heat flux determined using this approach is closer to the solution of the Cook Felderman equation than the one obtained initially (equation 5.8) especially near the peak. Figure 5.7 shows this effect, where  $q_f$  is the heat flux determined by the Cook Felderman equation,  $q$  the heat flux calculated using equation 5.8 and  $q_{fit}$  the heat flux at the surface using the curve fit algorithm. To underline the improvement, the percent differences in percent between the Cook Felderman and the curve fit result and also the Cook Felderman and the finite difference result are plotted in Figure 5.8. There  $dif\_curve$  stands for the difference between the Cook Felderman solution and the curve fit solution while  $dif\_q$  was calculated taking the difference between the Cook Felderman result and the surface heat flux obtained by equation 5.8. It can be seen that the error is 4 times smaller when the curve fit is used.

### 5.1.5 Interpolation

One possibility to improve our model is to increase the number of nodal points. Due to the fact that we used experimental data, which are measured at given time intervals, time step  $\Delta t$  was fixed. Thus we could not infinitely decrease the spacial difference  $\Delta x$

```

q_fit := for p ∈ 1..P
  for h ∈ 1..n
    y_h ← Temp_{p,h}
    x_h ← Δx(h-1)
    M ← [
      [ n, ∑_{i=1}^n x_i, ∑_{i=1}^n (x_i)^2 ],
      [ ∑_{i=1}^n x_i, ∑_{i=1}^n (x_i)^2, ∑_{i=1}^n (x_i)^3 ],
      [ ∑_{i=1}^n (x_i)^2, ∑_{i=1}^n (x_i)^3, ∑_{i=1}^n (x_i)^4 ]
    ]
    v ← [
      [ ∑_{i=1}^n y_i ],
      [ ∑_{i=1}^n y_i · x_i ],
      [ ∑_{i=1}^n y_i · (x_i)^2 ]
    ]
    C ← lsolve(M, v)
    Y(r) ← ∑_{i=1}^n C_i · r^{i-1}
    q(r) ← k · (d/dr Y(r))
    q_fit_p ← q(0)
  q_fit

```

Figure 5.6: Curve fit algorithm

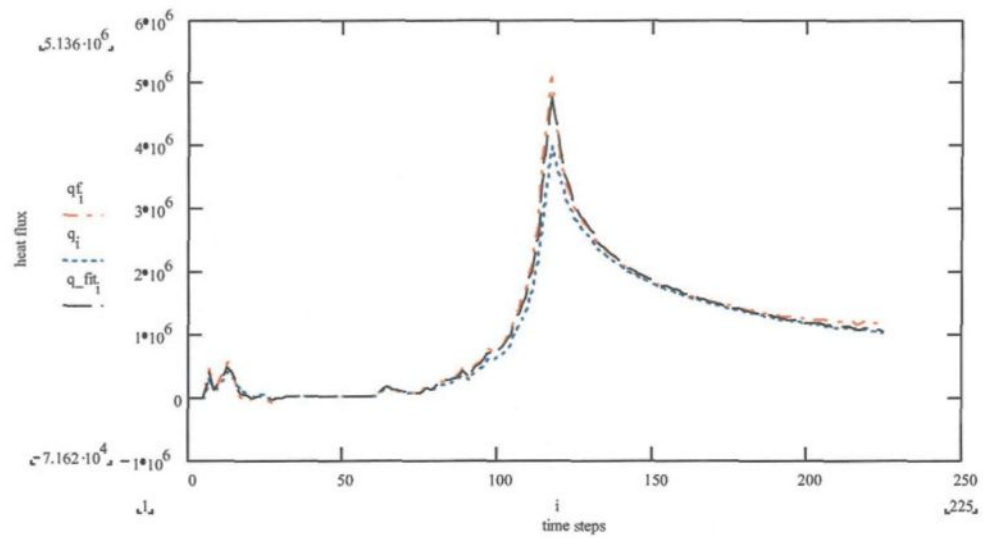


Figure 5.7: Surface heat flux comparison

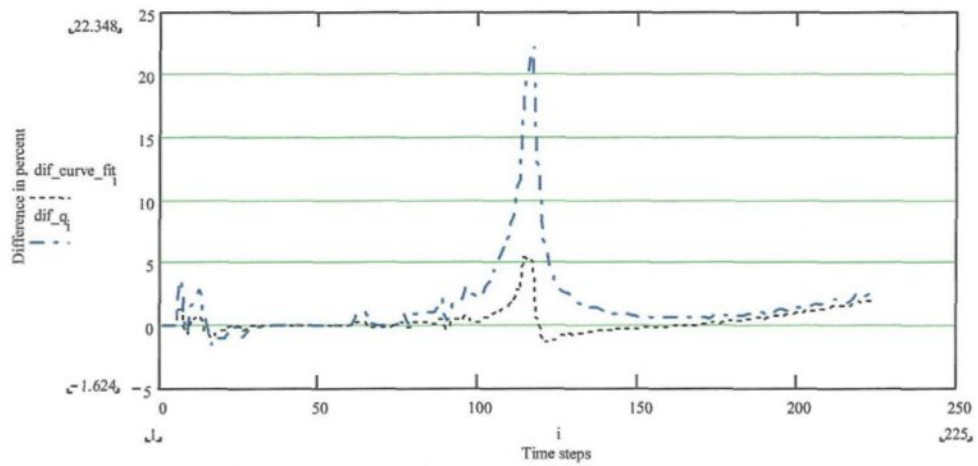


Figure 5.8: Percent difference of the curve fit algorithm and finite difference results with the Cook Felderman equation

```

SurfaceTemp := help ← SurfaceTemp
               for p ∈ 1.. P - 1
                 for f ∈ 1.. (Faktor - 1)
                   helpp·Faktor+1 - Faktor+f ←  $\left( \frac{\text{SurfaceTemp}_{p+1} - \text{SurfaceTemp}_{p \cdot f}}{\text{Faktor}} \right) + \text{SurfaceTemp}_p$ 
                   helpp·Faktor+1 ← SurfaceTempp+1
                 SurfaceTemp ← help
               SurfaceTemp

```

Figure 5.9: Interpolation loop

without violating the stability criteria.

$$Mo = \frac{\Delta x^2}{\alpha \Delta t} \geq 2$$

But using the former stated parameters the maximal possible number of nodal points where  $M = 8$ , which was not sufficient for an accurate result.

Therefore a linear interpolation was carried out between the experimental measurement points. According to the number of interpolations between two real measurement points it was possible to decrease the time difference  $\Delta t$ . The new  $\Delta t$  was determined using a variable *Faktor*:

$$\Delta t_{new} = \frac{\Delta t_{old}}{Faktor}$$

This variable denotes how many times shorter the new time step is. With the new, smaller time step  $\Delta t_{new}$  also the spacial step  $\Delta x$  could be decreased, what allowed the use of more nodal points. The new surface temperature array was calculated with the loop in Figure 5.9. Where  $P$  is the number of total time steps. After the interpolation this number had to be re-calculated because now there are more time steps than before, due to the shorter  $\Delta t$ .

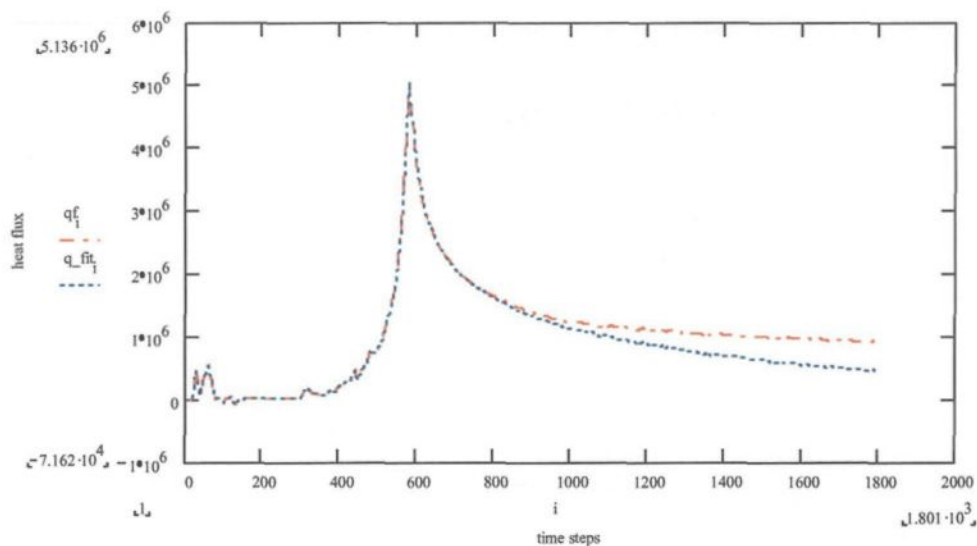


Figure 5.10: Result of analytically and numerically determined surface heat flux.

$M = 25$	$Mo = 2.423$	$\Delta t_{new} = 0.028 \text{ s} (Faktor = 10)$
$P = 1801$	$\Delta x = 2.56 \cdot 10^{-3}$	$L = 0.065 \text{ m}$

Table 5.2: Start parameters

The following relation was used to update the total number of time steps:

$$P_{new} = P_{old} (Faktor - 1) + 1$$

### 5.1.6 Results

Using the techniques described above we were able to calculate the following results. The surface heat flux determined by the Cook Felderman equation ( $qf$ ) and the numerically determined surface heat flux ( $q\_fit$ ) are plotted in Figure 5.10. The start parameters used for the numerical model are shown in table 5.2.

The measured surface temperature history, which was used to calculate the sur-

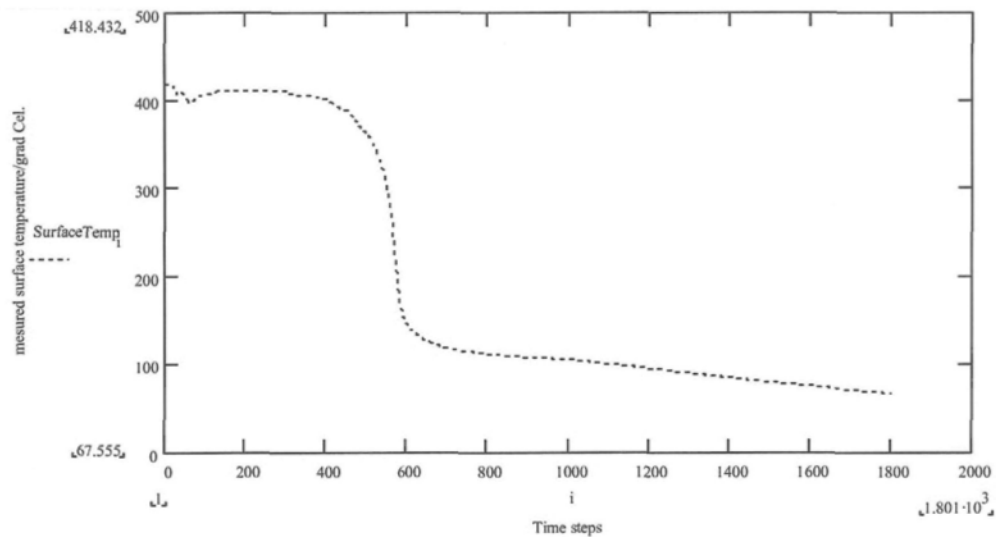


Figure 5.11: measured surface temperature in degree Celsius

face heat flux with the Cook Felderman equation is shown in Figure 5.11. In Figure 5.10 it is obvious that after the maximal heat flux the curve of the numerical solution has a different slope than the analytical one. This is better seen in the percent difference of both curves, plotted in Figure 5.12. Here it can be seen that the difference between the two solutions increases significantly after the time step of about 1000.

The explanation for this effect is that the solution of Cook Felderman uses the assumption of an semi-infinite solid. But in our case the plate is only 65 mm thick and it can not be considered as semi-infinite. The results of the Cook Felderman equation are valid as long, as the temperature decrease does not occur the backside of our slab. But once the temperature fall occurs on the back side the assumptions of the analytical solution is not valid any more.

This statement can be proved by increasing the slab thickness. The thickness is

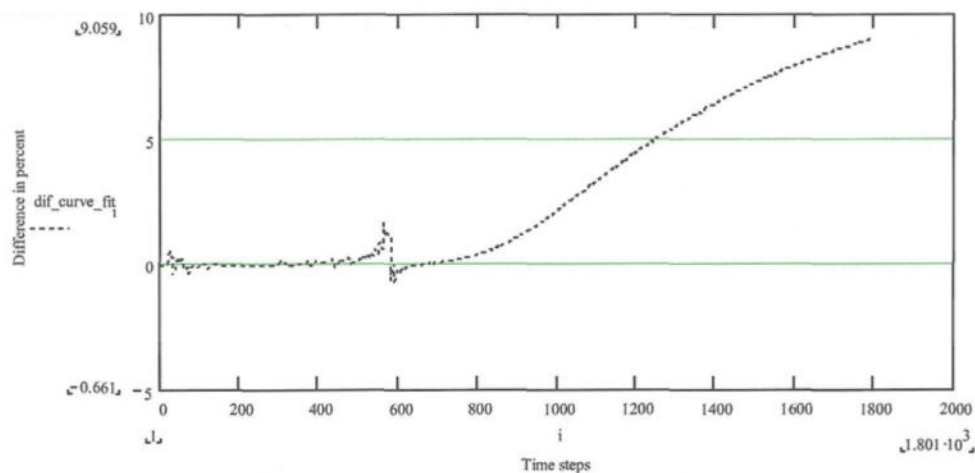


Figure 5.12: Difference in percent between numerical and analytical solution

increased as  $L = 0.125$  which is almost the double of the original plate thickness. Then also the total number of nodal points are increased to  $M = 50$ . All other parameters stay the same as in the case before. The result represented by the two surface heat flux curves is so close that only their difference in percent will be presented in Figure 5.13. This figure shows that the difference between the two solutions decreased to less than 0.5 percent. A comparison of Figure 5.13 with Figure 5.12 makes clear, that the difference in the slope after the maximal peak almost disappeared.

Nevertheless, there is still a maximal average error between the two methods of about 2 percent. Especially in the heat flux fluctuations there is a big difference. The biggest error occurs in the peak (in Figure 5.13 around time step 600), the maximal heat flux. It may be possible to decrease this error by increasing the nodal points. But then the interpolation would negatively influence the sensibility to fluctuations on the surface. It is recommended to carry out a new surface temperature measurement experiment, using

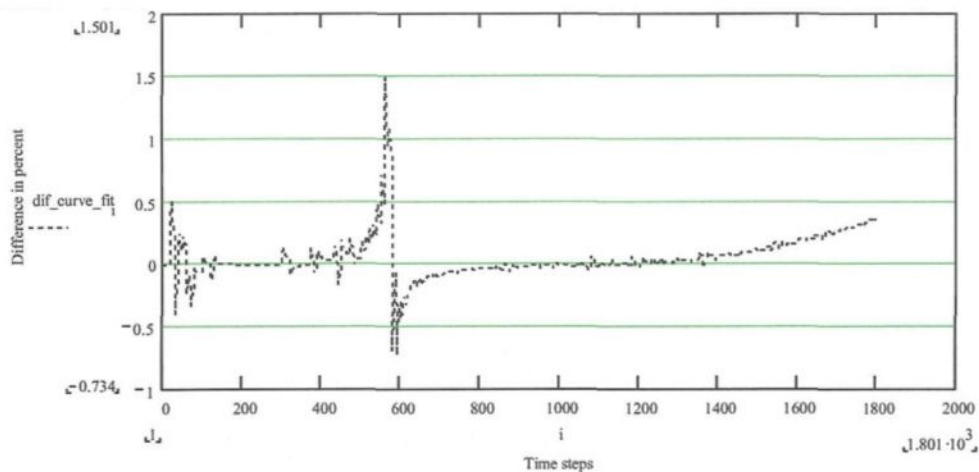


Figure 5.13: Difference of numerical and analytical solution with double slab thickness

shorter time intervals. Then, this measurement can be used as boundary condition.

### 5.1.7 Conclusion

We have seen that the one dimensional numerical result is close to the result obtained using the Cook Felderman equation. There is still an error of about 2 percent at the maximal heat flux. This might be improved by increasing the nodal number. The most important conclusion we can derive from the one dimensional simulations is that the assumption of a semi infinite solid can not be applied to our experimental setup. Thus the heat flux curve calculated using the Cook Felderman equation is not correct once the temperature decrease occurs at the backside of the slab.

## 5.2 Finite Volume Method

### 5.2.1 Transient Heat Transfer Problems in Solids

To develop the finite volume equations for an unsteady heat transfer problem we will consider the general conservation law for the transport of a scalar. The general conservation law in its differential form is expressed as

$$\frac{\partial}{\partial t}(\rho\phi) + \text{div}(\rho\vec{u}\phi) = \text{div}(\Gamma \text{grad}\phi) + S_\phi \quad (5.10)$$

where  $\rho, \phi, \vec{u}, \Gamma, S_\phi$  are the density, value of property per mass unit, velocity vector, diffusion coefficient and sources (or sink), respectively. This equation is used as the starting point for the computational procedures in the finite volume method. By setting  $\phi$  equal to  $T$  for temperature and  $\Gamma$  to  $k$  for thermal conductivity we obtain the specific form of the equation for heat conduction. Working only with molecular transport the convection term  $\text{div}(\rho\vec{u}\phi)$  disappears. This leads to the following equation

$$\rho c \frac{\partial T}{\partial t} = \frac{\partial}{\partial x} \left( k \frac{\partial T}{\partial x} \right) + \frac{\partial}{\partial y} \left( k \frac{\partial T}{\partial y} \right) + S \quad (5.11)$$

which describes the unsteady two-dimensional heat conduction. In addition to the already explained variables we have  $c$ , the specific heat of the material in  $\frac{J}{kg K}$ . Then we must integrate this equation over a finite control volume (CV) and repeat the integration over a finite time step  $\Delta t$ . We obtain the following equation:

$$\int_t^{t+\Delta t} \int_{CV} \rho c \frac{\partial T}{\partial t} dV dt = \int_t^{t+\Delta t} \int_{CV} \left[ \frac{\partial}{\partial x} \left( k \frac{\partial T}{\partial x} \right) + \frac{\partial}{\partial y} \left( k \frac{\partial T}{\partial y} \right) \right] dV dt + \int_t^{t+\Delta t} \int_{CV} S dV dt \quad (5.12)$$

In order to derive an useful form of the discretised finite volume equation also for miscellaneous domains we will take the general form of the conservation law (Equation 5.10).

Neglecting again the convection term will give:

$$\int_t^{t+\Delta t} \int_{CV} \rho \frac{\partial \phi}{\partial t} dV dt = \int_t^{t+\Delta t} \int_{CV} \left[ \frac{\partial}{\partial x} \left( \Gamma \frac{\partial \phi}{\partial x} \right) + \frac{\partial}{\partial y} \left( \Gamma \frac{\partial \phi}{\partial y} \right) \right] dV dt + \int_t^{t+\Delta t} \int_{CV} S dV dt \quad (5.13)$$

Now we will look at each term of Equation 5.13 for the first discretization step.

$$\int_{CV} \frac{\partial}{\partial x} \left( \Gamma \frac{\partial \phi}{\partial x} \right) dV \quad (5.14)$$

This term covers the conduction through a certain control volume in one dimension for a steady state problem. The discretization will be carried out using a general nodal point  $P$  and its neighbors in a two-dimensional space. The nodes to the west and east are identified by  $W$  and  $E$  respectively. The north node will be defined as  $N$  and the south node as  $S$ . The side faces of the control volume for each direction are referred by its uncapitalized letter. For example, the west side face of the control volume is denoted by  $w$ . The distances between the central node  $P$  and its neighbor nodes are identified by  $\delta x_{WP}, \delta x_{PE}$  for the nodes in east west direction and  $\delta y_{NP}, \delta y_{PS}$  for the north south direction. Figure 5.14 shows a mesh with  $dx = \Delta x = \delta x_{WP} = \delta x_{PE}$  and  $dy = \Delta y = \delta y_{NP} = \delta y_{PS}$ . The discretised form of Equation 5.14 at the nodal point  $P$  can be written as:

$$\int_{CV} \frac{\partial}{\partial x} \left( \Gamma \frac{\partial \phi}{\partial x} \right) dV = \left( \Gamma A_x \frac{\partial \phi}{\partial x} \right)_e - \left( \Gamma A_x \frac{\partial \phi}{\partial x} \right)_w \quad (5.15)$$

Here  $A_x$  is the cross-sectional area of the face of the control volume. In order to derive useful forms of the discretised equations, the diffusion coefficient  $\Gamma$  and the gradient  $\frac{d\phi}{dx}$  at the east ('e') and west ('w') are required. The values of the property  $\phi$  and the diffusion coefficient are defined and evaluated at nodal points. Thus we will use linear approximation to calculate the values and gradients at the interface. In a uniform grid the linearly interpolated values

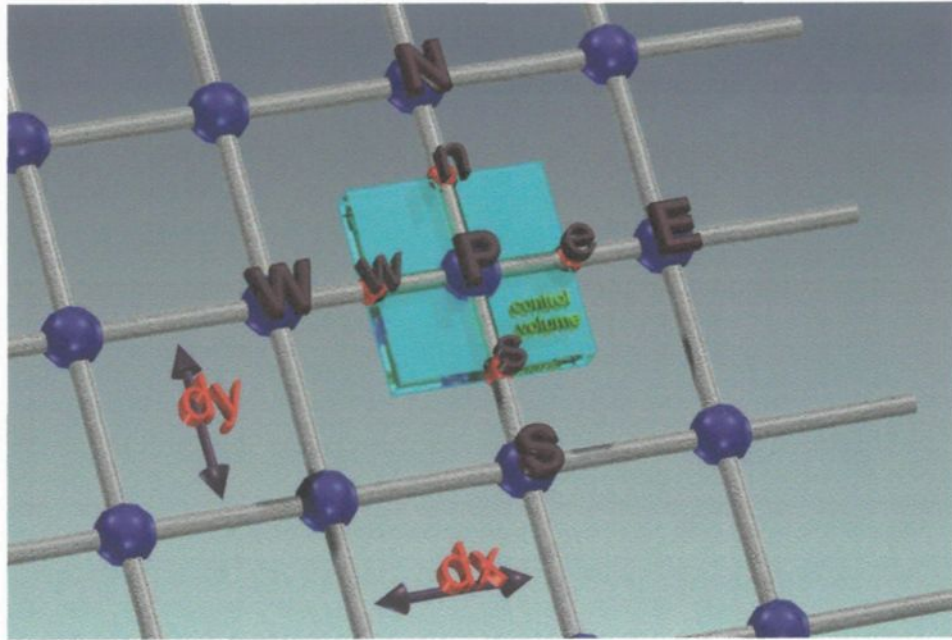


Figure 5.14: Two-dimensional Grid

for  $\Gamma_e$  and  $\Gamma_w$  are given by

$$\Gamma_w = \frac{\Gamma_W + \Gamma_P}{2} \quad (5.16)$$

$$\Gamma_E = \frac{\Gamma_E + \Gamma_P}{2} \quad (5.17)$$

the diffusive flux terms are evaluated as

$$\left( \Gamma A_x \frac{d\phi}{dx} \right)_w = \Gamma_w A_w \left( \frac{\phi_P - \phi_W}{\delta x_{WP}} \right) \quad (5.18)$$

$$\left( \Gamma A_x \frac{d\phi}{dx} \right)_e = \Gamma_e A_e \left( \frac{\phi_E - \phi_P}{\delta x_{PE}} \right) \quad (5.19)$$

By using the fragment Equation 5.14 we arrived to the discretization of Equation 5.13 in one direction and only in space. Now we will use the same development for the north south

direction. Inserting all results in Equation 5.13 will give

$$\int_t^{t+\Delta t} \int_{CV} \rho \frac{\partial \phi}{\partial t} dV dt = \int_t^{t+\Delta t} [\{De - Dw\} + \{Dn - Ds\}] dt + \int_t^{t+\Delta t} \bar{S} \Delta V dt \quad (5.20)$$

with

$$De = \Gamma_e A_e \left( \frac{\phi_E - \phi_P}{\delta x_{PE}} \right) \quad (5.21)$$

$$Dw = \Gamma_w A_w \left( \frac{\phi_P - \phi_W}{\delta x_{WP}} \right) \quad (5.22)$$

$$Ds = \Gamma_s A_s \left( \frac{\phi_P - \phi_S}{\delta y_{PS}} \right) \quad (5.23)$$

$$Dn = \Gamma_n A_n \left( \frac{\phi_N - \phi_P}{\delta y_{NP}} \right) \quad (5.24)$$

Where  $A_e, A_w, A_n, A_s$  are the face areas of the control volume for each direction,  $\Delta V$  is its volume.  $\bar{S}$  is the average source term.

If the temperature at a node is assumed to prevail over the whole control volume, the left hand side of Equation 5.20 can be written as

$$\int_t^{t+\Delta t} \int_{CV} \rho \frac{\partial \phi}{\partial t} dV dt = \rho (\phi_p - \phi_p^0) \Delta V \quad (5.25)$$

In Equation 5.25 the superscript '0' refers to properties at time  $t$  while properties at time  $t + \Delta t$  are not superscripted. To evaluate the right hand side of Equation 5.20 we need to make an assumption about the variation of  $\phi_P, \phi_E, \phi_W, \phi_N$  and  $\phi_S$  with time. We could use properties at time  $t$  or at time  $t + \Delta t$  to calculate the time integral or alternatively a combination of both.

## 5.2.2 The fully Implicit Scheme

In the scope of this work the fully implicit scheme was used, because of its superior stability. For further information please refer to literature Ref. [14]. The time differentiation

approach can be expressed as

$$I_\phi = \int_t^{t+\Delta t} \phi_P dt = \phi_P \Delta t \quad (5.26)$$

Using formula 5.26 and 5.25 in Equation 5.20, and dividing by  $\Delta t$ , we have

$$a_P \phi_P = a_W \phi_W + a_E \phi_E + a_S \phi_S + a_N \phi_N + a_P^0 \phi_P^0 + S_u \quad (5.27)$$

where

$$a_P = a_w + a_E + a_S + a_N + a_P^0 - S_P \quad (5.28)$$

with the coefficients

$$a_W = \frac{\Gamma_w A_w}{\delta x_{WP}}, \quad a_E = \frac{\Gamma_e A_e}{\delta x_{PE}} \quad (5.29)$$

$$a_S = \frac{\Gamma_s A_s}{\delta y_{SP}}, \quad a_N = \frac{\Gamma_n A_n}{\delta y_{PN}} \quad (5.30)$$

and

$$a_P^0 = \rho c \frac{\Delta V}{\Delta t} = \rho c \frac{\Delta x \Delta y}{\Delta t} \quad (5.31)$$

In our two-dimensional case the cell face areas are

$$A_w = A_e = \Delta y \quad (5.32)$$

$$A_n = A_s = \Delta x \quad (5.33)$$

To apply the above equations to the transient heat conduction we will replace the property  $\phi$  by the temperature  $T$ , and the diffusion coefficient  $\Gamma$  by the thermal conductivity  $k$ . Referring the distance between the central node  $P$  and its neighbors  $W, E, S$  and  $N$  as the grid spacing  $\Delta x$  and  $\Delta y$  which are constant over the considered domain, we obtain the

following relations:

$$a_W = \frac{k \Delta y}{\Delta x}, \quad a_E = \frac{k \Delta y}{\Delta x} \quad (5.34)$$

$$a_S = \frac{k \Delta x}{\Delta y}, \quad a_N = \frac{k \Delta x}{\Delta y} \quad (5.35)$$

Hereby we made the assumption that the thermal conductivity is constant in time and space. The source terms depend on the boundary condition. If we consider a case with no internal heat generation, the source terms for all interior nodes will be zero. For an exterior node which is exposed to a fixed temperature, a so called boundary condition of the first kind, we obtain the equation:

$$S_u = \frac{2kA_w}{\Delta x} T_B, \quad S_P = -\frac{2kA_w}{\Delta x} \quad (5.36)$$

for the horizontal x-direction and,

$$S_u = \frac{2kA_n}{\Delta y} T_B, \quad S_P = -\frac{2kA_n}{\Delta y} \quad (5.37)$$

for the vertical y-direction, where  $T_B$  is the temperature at the surface. The second possibility as a boundary condition is for a prescribed heat flux. The boundary condition of the second kind yields to the following source terms for the x-direction (east west direction)

$$S_u = A_w q_B, \quad S_P = 0 \quad (5.38)$$

and y-direction (north south direction)

$$S_u = A_n q_B, \quad S_P = 0 \quad (5.39)$$

The heat flux at the surface is indicated by  $q_B$ .

### 5.2.3 Set of Equations

Now we can collect all the derived equations and summarize them to obtain our final system of equations. Taking equation 5.27 and replacing the property  $\phi$  with the temperature  $T$  yields to:

$$a_P T_P = a_W T_W + a_E T_E + a_S T_S + a_N T_N + a_P^0 T_P^0 + S_u \quad (5.40)$$

Equations 5.28 and 5.31 are already in the right form and can be used as denoted before.

$$a_P = a_w + a_E + a_S + a_N + a_P^0 - S_P \quad (5.41)$$

where  $a_P^0$  is

$$a_P^0 = \rho c \frac{\Delta x \Delta y}{\Delta t} \quad (5.42)$$

We will obtain the coefficients for equation 5.40 by using equation 5.34 and 5.35:

$$a_W = \frac{k \Delta y}{\Delta x}, \quad a_E = \frac{k \Delta y}{\Delta x} \quad (5.43)$$

$$a_N = \frac{k \Delta x}{\Delta y}, \quad a_S = \frac{k \Delta x}{\Delta y} \quad (5.44)$$

This definition for the coefficients is valid for all interior nodes. We call a node an interior node, if there are four neighbor nodes around. In the case that there is at least one neighbor node missing,  $P$  would be an exterior (or boundary) node. For example in Figure 5.14 point  $E$  would be an exterior node, because its east neighbor node does not exist. For the non existing neighbor nodes the coefficients are zero. The source terms  $S_u$  and  $S_P$  are zero for the interior nodes.

Taking a closer look at equation 5.40 shows that both sides contain the temperature at the new time step. Thus a system of algebraic equations must be solved at each time

level. The time marching procedure starts with a given initial field of temperatures  $T^0$ . The system of equations (5.40) is solved after selecting time step  $\Delta t$ . Next the solution  $T$  is assigned to  $T^0$  and the procedure is repeated to progress the solution by a further time step.

It can be seen that all coefficients are positive, which makes the implicit scheme unconditionally stable for any size of time step. Since the accuracy of the scheme is only first-order in time, small time steps are needed to ensure the accuracy of results.

#### 5.2.4 The C++ Source Code

After we have seen the theoretical basis of the finite volume method we can use this method to develop a numerical algorithm. The purpose of this algorithm is to determine the internal temperature distribution of an object for every instant in time using appropriate boundary conditions. The model developed here is specialized to the needs of our project. For example, we have only boundary conditions of the first (fixed temperature) and second kind (fixed surface heat flux) during the cooling process. Thus the program uses only this two types of boundary conditions. Furthermore we have a cubic block that is cooled by the water jet. As discussed already, we assume the surface cooling to be symmetric in the horizontal direction. In addition, we are able to measure the surface temperature along a vertical line at the surface. Therefore, we will use a two-dimensional model. To summarize, the finite volume source code developed here determines the internal temperature distribution for a rectangular block in two dimensions using boundary conditions of the first and second kind.

## Surface Boundary Conditions

As already stated before we have two different kinds of boundary conditions. There are parts of our ingot like e.g. the top and bottom where we do not have cooling. These parts are assumed to be insulated. In our model a heat flux is taken equal to zero at the top and bottom of the block. For the part that is cooled by the water film we measured the surface temperature. These data can be directly used as boundary condition. Instead of a constant boundary as we have for the insulated sections we will have a temperature which changes within time. The problem is that we do not have a measured temperature for every node of our model. Due to the time required for each measurement and limited space on the ingot backside we could install only 4 measurement points. The solution to this problem is the creation of virtual cooling curves by interpolating between the physical measurement points.

**Determination of the Cooling Curves by Interpolation** In the following Subsection we will explain how the interpolation between the two measurement points was implemented. We created two curves (see Figure 5.15) which show the characteristic temperature decrease of an experimental cooling curve. As it can be seen in Figure 5.15 there is a certain delay between the cooling curves P1 and P2. This can be explained by the movement of the re-wetting zone that passes along the surface during the cooling process. The first step for the interpolation is to shift the two curves together in a way that the least square deviation becomes minimal. In Figure 5.16 this first step is shown. The curve P2 was shifted 5 time

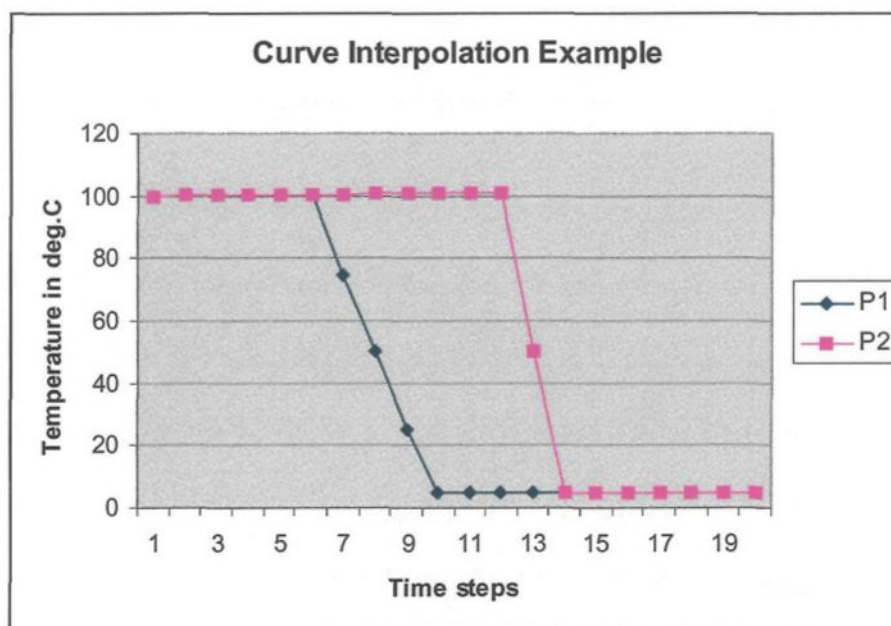


Figure 5.15: Example for the curve interpolation

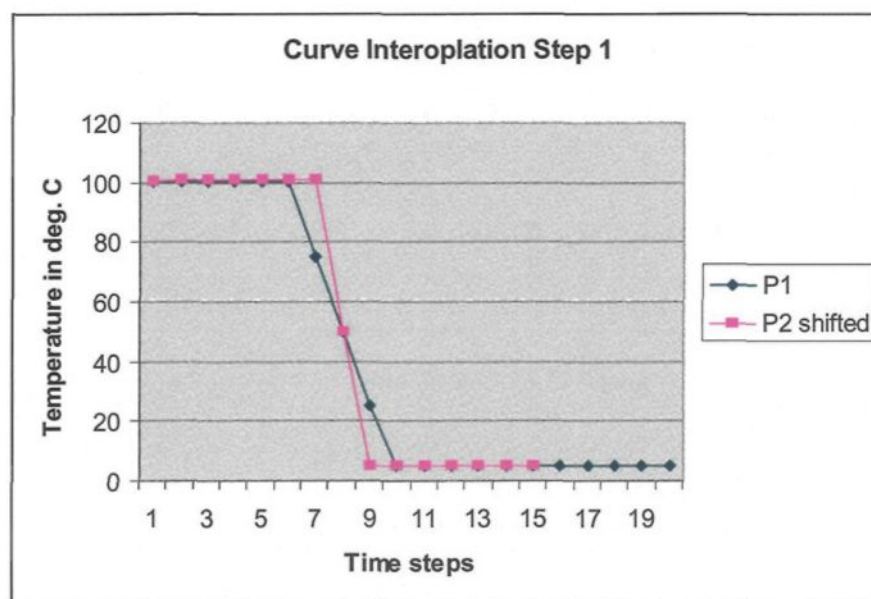


Figure 5.16: First step in the curve interpolation

steps back to fit the condition

$$\sum_{t=1}^N (P1(t) - P2(t))^2 = \text{minimal} \quad (5.45)$$

The next step will be the creation of new cooling curves between the two original curves P1 and P2. Therefore we find the average temperature value from P1 and P2 for each instant. Then we add a weight factor which depends on the position of the newly created curve. For example if this virtual curve is closer to the curve P1 it will own more characteristics from curve P1 than from P2. Let us define D as difference in time steps between curve P1 and P2. Using t as position index on the time steps scale the equation for a new curve P3 can be expressed as follows

$$P3(t) = \frac{D-t}{D}P1(t) + \frac{t}{D}P2^*(t) \quad (5.46)$$

where  $P2^*(t)$  is the best fit shifted curve (see Figure 5.16). An example of interpolation using experimental cooling curves calculated with equation 5.46 is presented in Figure 5.17. The newly created curve is called  $P_{new}$  and is identified by the dashed line.

**Creation of Boundary Conditions** The developed finite volume source code needs a boundary condition for each surface node at each instant of time. The boundary condition file for the nodes situated at the insulated parts of the plate are easy to create. Since the conditions do not change in time these files can be created using a heat flux which is equal to zero for each instant in time. For the part of the contour that is cooled by the water film, the boundary conditions for the nodes at the measurement points can be taken directly from the measurement. The nodes in between these determined points are created using the method explained in the previous subsection. Thus for each exterior node a boundary

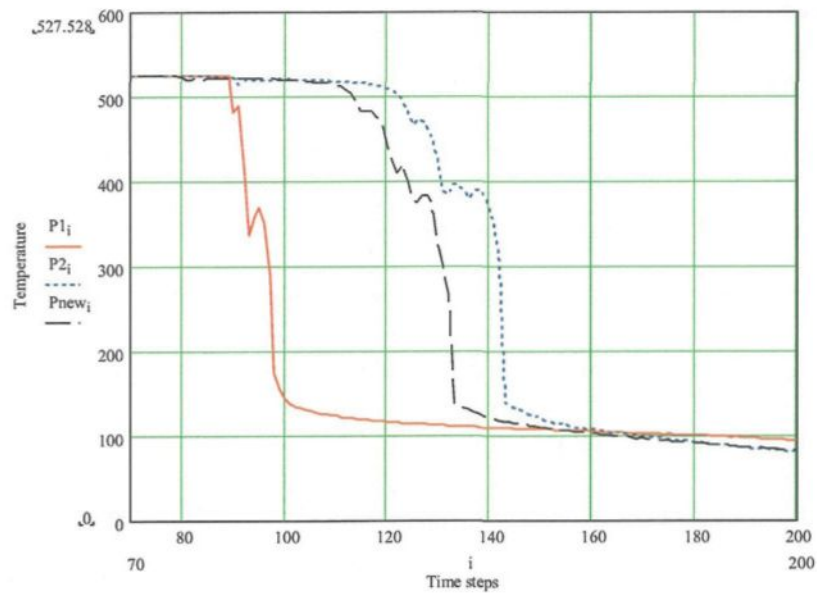


Figure 5.17: Curve interpolation example using real cooling curves

condition file was created by a self written CURVE CREATION program.

### Finite Volume Source Code

The source code to determine the internal temperature distribution in our ingot uses the finite volume equations from subsection 5.2.3. The implicit scheme requires an iterative method to solve the set of linear algebraic equations. We choose the tri-diagonal matrix algorithm (TDMA) or also called Thomas algorithm to solve the linear algebraic equations. The TDMA is actually a direct method for one-dimensional situations, but it can be applied iteratively, in a line-by-line fashion, to solve two-dimensional problems (see Ref. [14]). The program contains several object classes. The task and their connection to each other will be explained below.

**Class Structure of the Finite Volume Program** The main class is the Solver class. This class contains the TDMA solver algorithm and calculates the temperature matrices. From the Solver class the nodes are created too. Each node is represented by an object which is integrated in the Node class. The elements of the Node class are the coefficients  $a_W$ ,  $a_E$ ,  $a_S$ ,  $a_N$  and the source terms according to subsection 5.2.3. These coefficients are re-calculated for each instant in time. To do so the values of the boundary conditions are needed. The information about the boundary conditions are saved for each node in a file. The class `b_element` reads and converts these data and pass them to the Node class. Thus the Solver class uses the node elements to calculate the temperature distribution. In addition to these main classes there are some server classes. In the Properties class for example all information about the plate are saved. Another serving class is the Calculation\_Properties class. This class contains information about the iteration steps, the time step  $dt$  and other important data for the calculation. The File class passes the file names in which the results will be saved and the file names of the source data to different classes. This correlation between all classes is also shown in the block diagram in Figure 5.18. Beside the described classes there are some others. Although they are important for the functionality of the code they will not explained here because they perform tasks that are not discussed here.

### Main Solver Loop

The most important part of the finite volume program is the Solve function from the solver class (see Appendix E). In this function the temperature matrix for each instant of time is calculated according to the node coefficients. In Appendix B the main calculation

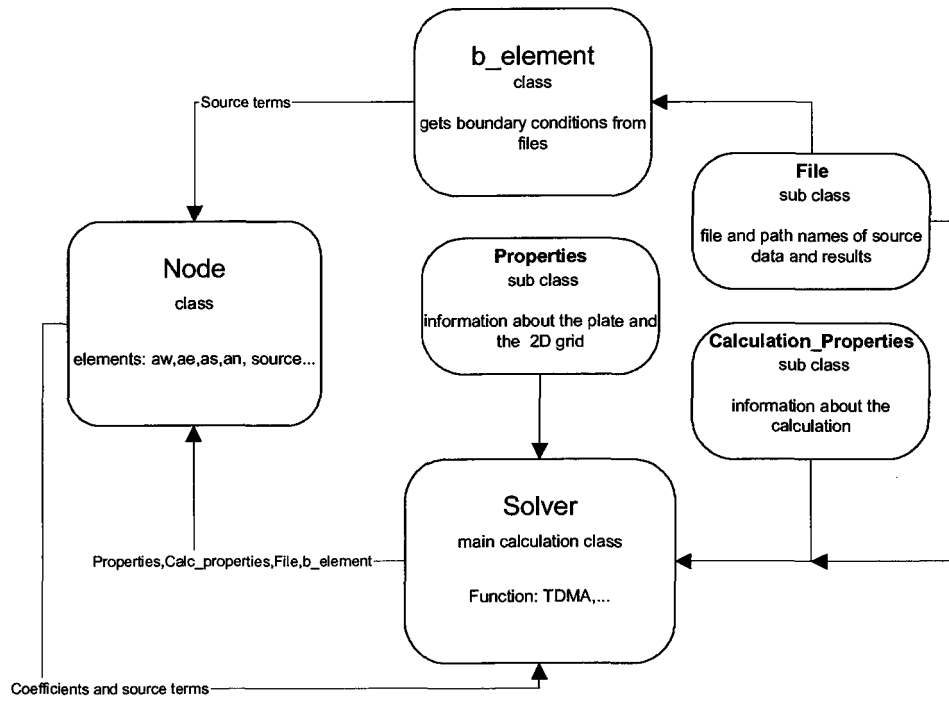


Figure 5.18: Block diagram for the class correlation of the finite volume source code

loop of the solve function is printed. For easier reference, the important lines are markers with the index `//#` plus the line number. In the first line we can see that the time loop is also the main loop. In other words for each time step all inner loops will be executed. The next line shows a function call where the coefficients of the node like  $a_w, a_e...$  etc. are calculated depending on the time step  $t$ . The coefficients are needed in the next loop, in the iteration loop (see line 3). The temperature matrix determined in the next loop will be iterated to achieve a convergence. This temperature matrix is formed in the next loop. In line 4 and 5 according to Appendix B the node coefficients are assigned to the TDMA arrays. For a two-dimensional problem the TDMA must be applied for each column (line 5) of the matrix (see Ref [14] p159). After all coefficients are assigned to the TDMA arrays (line 5 and 6) the function TDMA calculates the temperature values for the actual column in line 7. After this, the two-dimensional temperature matrix is calculated. The temperature matrix obtained so is iterated by the loop in line 3. Once the iteration is done the resulting temperature distribution is used to calculate the heat flux using the functions in line 8. Then the result for that instant of time is saved in a file in line 9. Before the calculations can be carried out for the next time step the result has to be transferred to a matrix, where the former time step is memorized (line 10). This matrix will be used in the next time step as starting conditions.

### 5.2.5 Comparison of Analytical and Numerical Solutions

In the following Subsection we will compare the numerical results of a two-dimensional unsteady conduction problem with an analytical solution to assess the accuracy of the method and to assure that the developed algorithms work properly.

### Boundary conditions and analytical solution

In our example we have a thin rectangular plate with two insulated faces and the other two faces with a fixed temperature (see Figure 5.19). The length in x direction  $Lx$

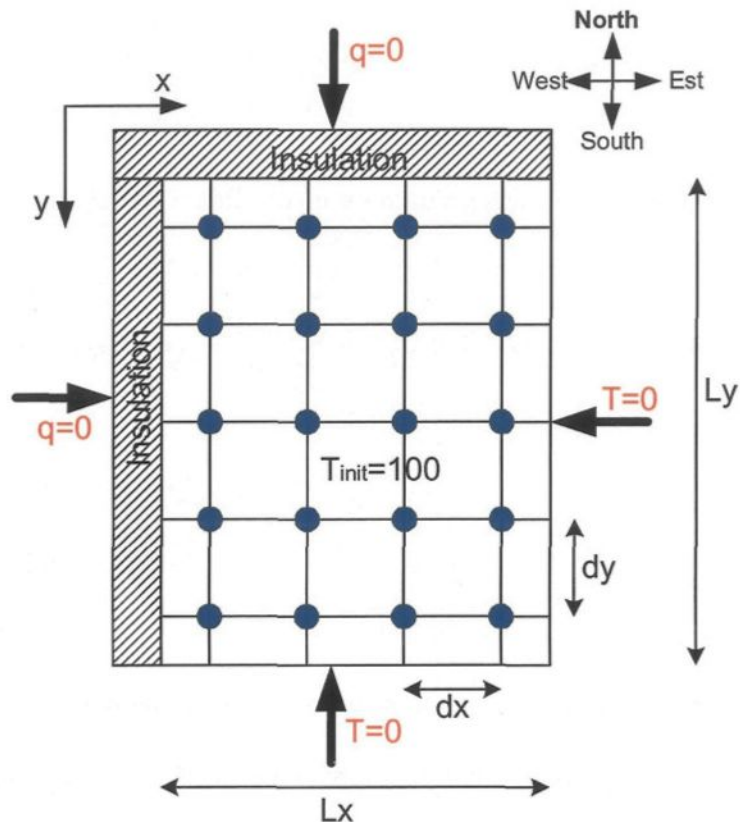


Figure 5.19: Boundary conditions for the worked example

was chosen to be 0.1 m, the length in  $y$  direction  $Ly = 0.25$  m. The material properties like the density, the specific heat and the thermal conductivity are  $\rho = 2702 \frac{\text{kg}}{\text{m}^3}$ ,  $c = 903 \frac{\text{J}}{\text{kgK}}$  and  $k = 237 \frac{\text{W}}{\text{m}^2\text{K}}$ , respectively. The initial temperature  $T_{init}$  is  $100^\circ\text{C}$  at  $t = 0$ . As shown

in Figure 5.19 we have the following boundary conditions

$$\begin{aligned}\frac{\partial T}{\partial x} &= 0 \quad \text{at} \quad x = 0, t > 0 \\ \frac{\partial T}{\partial y} &= 0 \quad \text{at} \quad y = 0, t > 0 \\ T &= 0 \quad \text{at} \quad x = Lx, t > 0 \\ T &= 0 \quad \text{at} \quad y = Ly, t > 0\end{aligned}\tag{5.47}$$

The analytical solution is given in literature Ref. [14] for a one-dimensional heat conduction problem as

$$T(x, t) = T_{init} \left( \frac{4}{\pi} \sum_{n=1}^{\infty} \frac{(-1)^{n+1}}{2n-1} \exp(-\alpha \lambda_n^2 t) \cos(\lambda_n x) \right)\tag{5.48}$$

where

$$\lambda_n = \frac{(2n-1)}{2Lx}\tag{5.49}$$

$$\alpha = \frac{k}{\rho c}\tag{5.50}$$

To create the analytical solution in two-dimensions within a cuboid we use the theorem stated in Ref. [2] p.291 that it is possible to express an unsteady two-dimensional problem as the product of two unsteady one-dimensional problems. Thus we can take the one-dimensional solution for a plate as given in Equation 5.48 for the north-south and for the east-west directions. Then the product of the two one-dimensional solutions will give the solution of the two-dimensional case. Once the two-dimensional solution is determined a matrix must be calculated. The values of the elements of the matrix correspond to the temperature nodes of the numerical model. The calculation as well as the comparison with the numerical results were carried out using MATHCAD. A Mathcad worksheet can be seen in Appendix D.

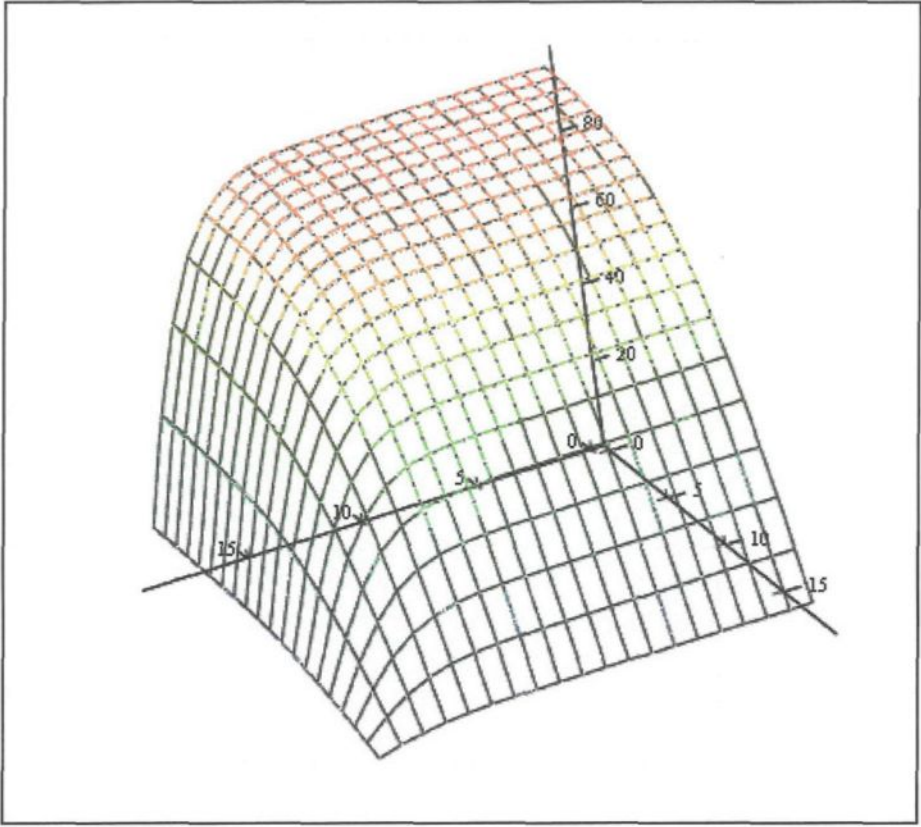
## Numerical Solution

The numerical solution was calculated with the C++ code which can be found in Appendix E. The boundary conditions were created by the program using to the boundary conditions, given in Figure 5.19. The value for the time step  $dt$  was fixed as  $dt = 0.1$  s. The number of iteration for the implicit method was 100 iteration cycles per time step.

Using the boundary conditions as described before may cause a problem. Because of the multiplication with zero all boundary terms disappear. Thus an error in these equations could not be detected using the selected example. For that reason the boundary conditions for the numerical calculations were changed. The fixed temperatures at the east and south side was set to  $T_{est,south} = 0.1$  °C. The heat flux at the insulated sides was changed from  $q = 0 \frac{\text{W}}{\text{m}^2}$  to  $q = 0.1 \frac{\text{W}}{\text{m}^2}$ . Due to the imposed error the numerical result can not be as close to the analytical solution than for a case with exactly the same boundary conditions. Therefore we will compare first the numerical results with the analytical solution with the changed boundary conditions. Once the result is validated, we will repeat the numerical method with exactly the same boundary conditions as we have for the analytical solution.

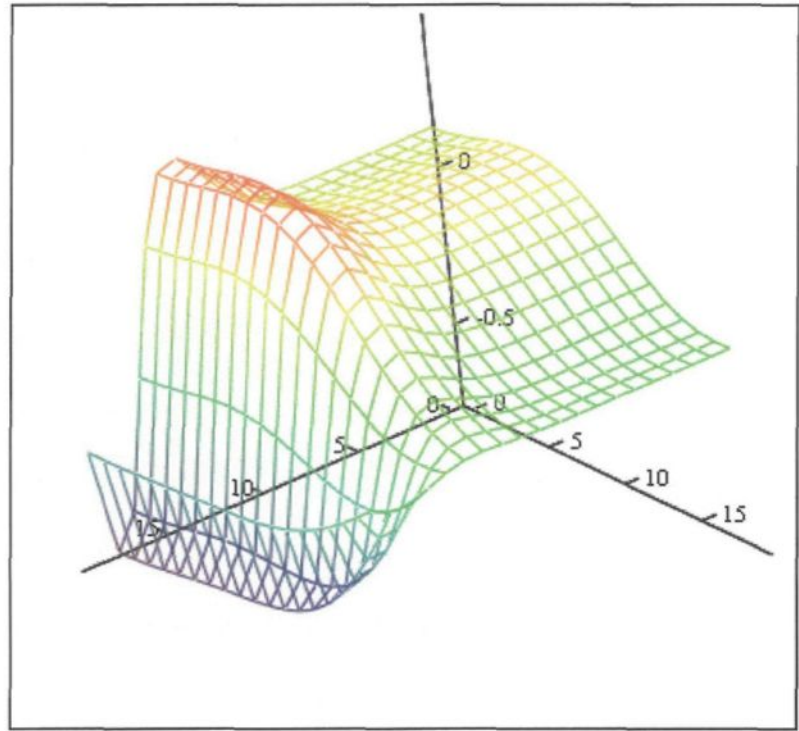
## Comparison with Respect to Space

In Figure 5.20 the analytical result after 6 seconds is plotted with a dashed colormap, while the numerical solution is denoted by a black grid. Using this kind of plot seems not proper because no obvious difference appears. Therefore we will plot the difference between the two solutions in percent (see Figure 5.21). As it can be seen the difference vary in an interval of  $+0.46\%$  and  $-0.73\%$ . This values are acceptable keeping in mind



Tmatrix\_function(p), T

Figure 5.20: 3D plot of analytical (dashed colormap) and numerical solution



$$\frac{T_{\text{matrix\_function}(p)} - T_{\text{init}}}{T_{\text{init}}} \cdot 100$$

Figure 5.21: Difference in percents between the numerical and analytical solution after 6 sec.

that we took even not exactly the same boundary conditions. Now we will investigate the behavior of our numerical model using the boundary conditions as stated for the analytical solution. The difference determined with the original boundary condition is almost equal to the previous result. After 6 seconds the maximal difference is  $+0.46\%$  and the minimal difference is  $-0.67\%$ . We still have to investigate whether the error changes in time or rests constant.

### Comparison with Respect to Time

The first step is to compare how the difference between the numerical and analytical solution changes with time. Therefore we will extract one node for each time step at several positions from the analytical and numerical solution matrix. We will start with the node at the south east corner. In Figure 5.22 we see the difference between the numerical and analytical solutions in percents plotted for the calculation time of 60 seconds. As it can be clearly seen the maximal error occurs in the first second. This difference of 9.36 percent is unique in the error analysis. In the following second we still have an error that is higher than all other values. However after the two seconds the error seems to stabilize to an acceptable level of less than 0.12 percent. We now will take a closer look to the whole temperature matrix of the analytical solution in the first seconds of the process. In Figure 5.23 we see the analytically determined temperature distribution for the time zero. Due to the fact that we are very close to the zero point of the function we obtained an oscillation. This oscillation reflects not the physical temperature distribution but is an error in the analytical solution. Thus the big error in the first time step of our investigation may come from the inaccuracy of the analytical solution. For a time bigger than 1 second all errors

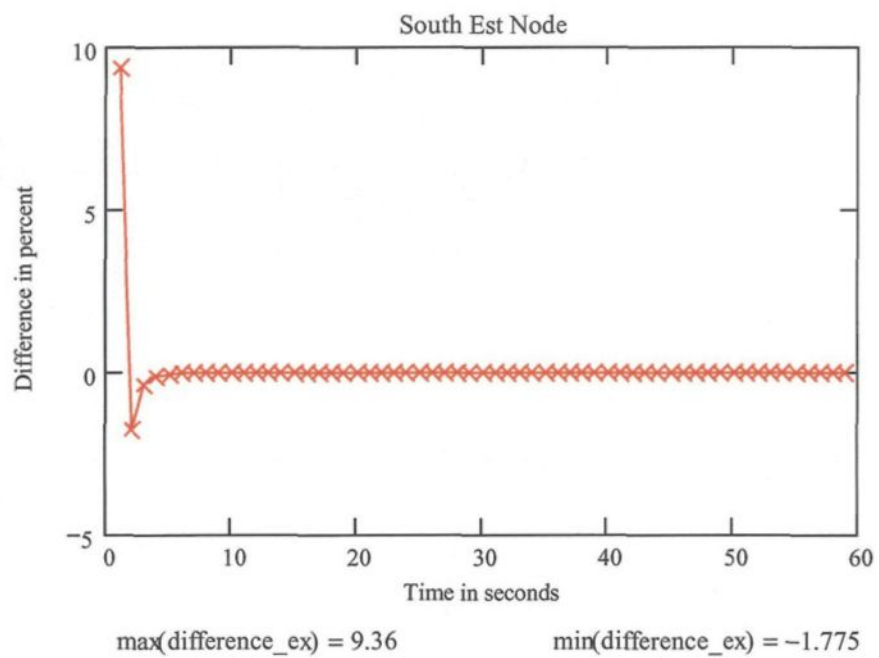
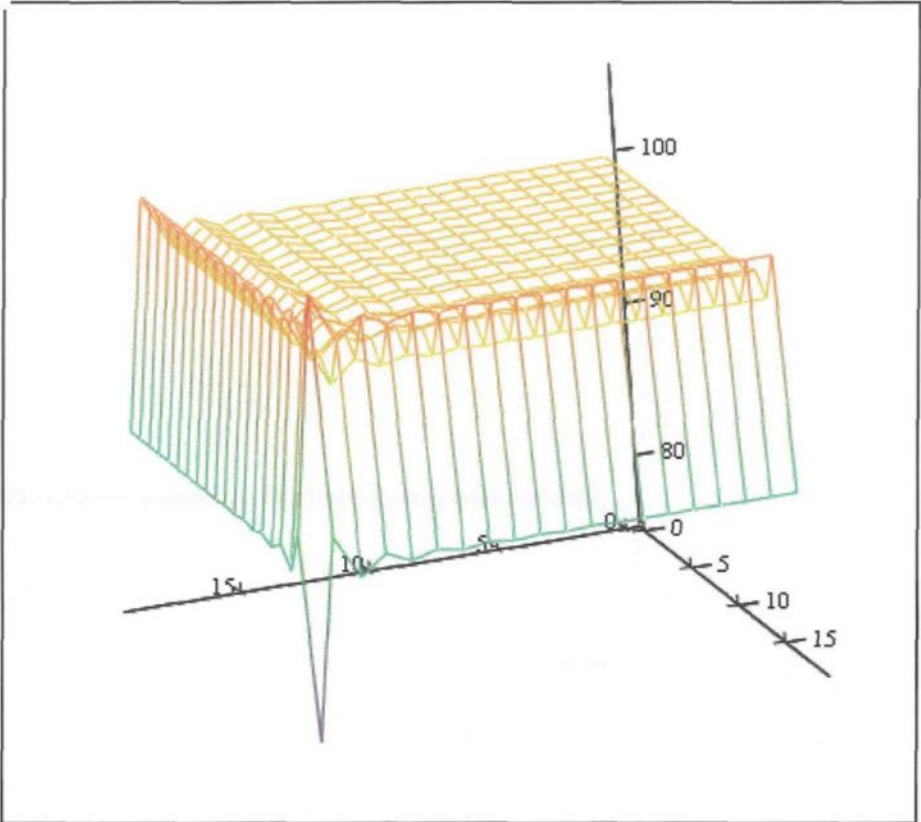


Figure 5.22: Difference in percents of the south est node



Tmatrix\_function(p)

Figure 5.23: Analytical calculated temperature distribution at instant t=0

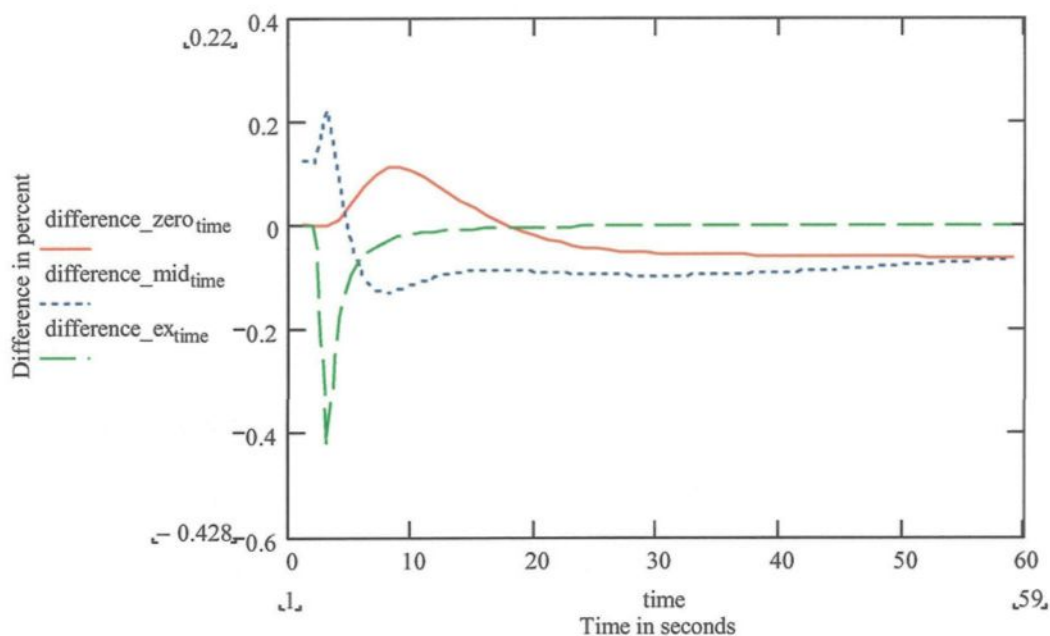


Figure 5.24: Difference between analytical and numerical solution at different points

are in an acceptable range. To prove this statement we also examined the behavior of a node situated in the middle of the matrix (Point 10,10) and a node at the north west corner (Point 0,0). In Figure 5.24 the middle point is denoted by the dotted line (blue), the point at the north west corner by a solid line (red) and the node at the south east corner by a dashed line (green). For a better visibility the two first values of the south east node were set to zero.

## Conclusion

As a conclusion, the error between the numerical and analytical results is in an acceptable range. Nevertheless, the inaccuracy of the analytic solution at the first instant after the start of the process leaves an uncertainty. We can not determine whether the error

in the first second comes from the numerical model or from the instability of the analytical solution.

### **5.2.6 Numerical Solutions from the FVM Code**

There are several benefits of developing a numerical model for the surface cooling process. One of the main objectives of model development was to investigate the influence of a vertical heat flux on the cooling process. We used the Cook-Felderman Equation to determine the heat flux at the surface. Thus we had to make the assumption that there is only a heat flux in one dimension. Having a closer look on the re-wetting zone makes clear that there has to be a high temperature gradient between the part where the water is already in contact with the ingot and the part that is still insulated by the vapor film. Therefore, there should also be an effect by the vertical component of the heat flux. The task for the numerical model was to find out how much this vertical component influences the surface heat flux distribution.

A second point of interest was the comparison of the heat flux obtained by the Cook-Felderman Equation with those calculated by the model. There might be some doubts whether the assumptions of the Cook-Felderman equation are applicable to our cooling experiment. Thus we have to verify if the results obtained by the Cook-Felderman equation are in agreement with the numerical solutions.

#### **Vertical Heat Flux Component**

To determine the heat flux in the vertical direction we would need the values of the temperature at each surface node. Therefore we could use the temperature distribution

calculated by the finite volume program. But this would not be the heat flux directly at the surface. Due to the fact that the "surface" nodes are situated at a half-node distance under the surface we would not get the heat flux at the surface. In our model we applied a fixed temperature boundary condition to each node for the water cooled faces at each instant. These temperature values must be used to determine the vertical surface heat flux component. In subsection 5.2.4 the method to interpolate between the measurement points was explained. In fact it is this interpolation between the measurement points that creates the temperatures not the finite volume program. For the overall heat flux distribution in the plate along both the vertical and the horizontal directions we need of course the results of the finite volume program. However, we can determine the vertical heat flux component at the surface by using only the boundary conditions.

**Influence of the Node Number on the Vertical Heat Flux** The vertical surface heat flux is described by the vertical component of the temperature gradient for a given node. Thus we need the neighboring temperatures of the node to calculate the gradient. In the scope of this work all solutions were found using the node of interest plus two temperatures of two nodes at its left and right side. The first question is that how the number of nodes affect the vertical component of the surface heat flux. To answer this question we used the measurement results from the cooling experiment on the 16.05.2002 and carried out a curve interpolation using different node numbers. We took the measurement results at point TC2 and TC3 (see Figure 5.40) and two interpolated curves on the right and left side. In Figure 5.25 the solid line represents the measured result and the dashed lines are interpolated for 60 nodes. This interpolation was made for 15, 40, 60 and 100 nodes. Then the heat flux was

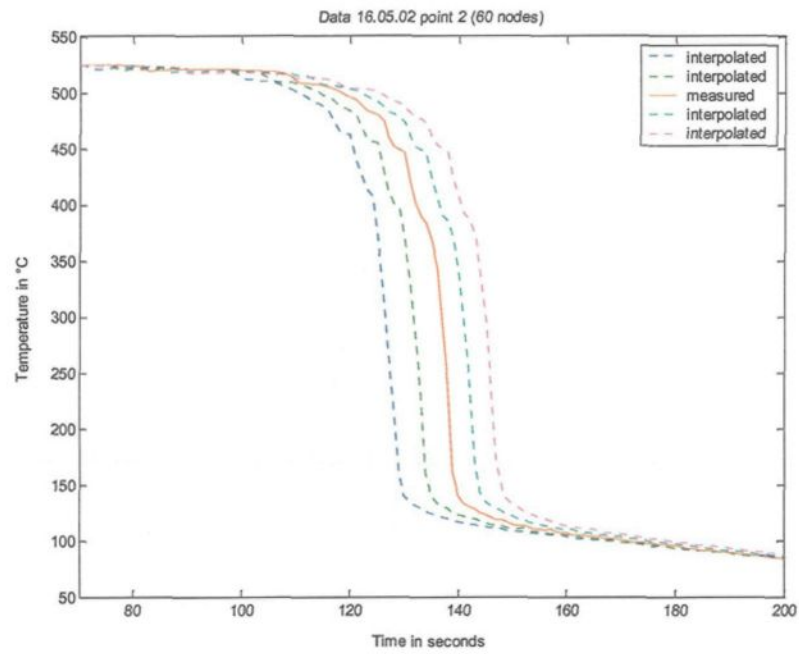
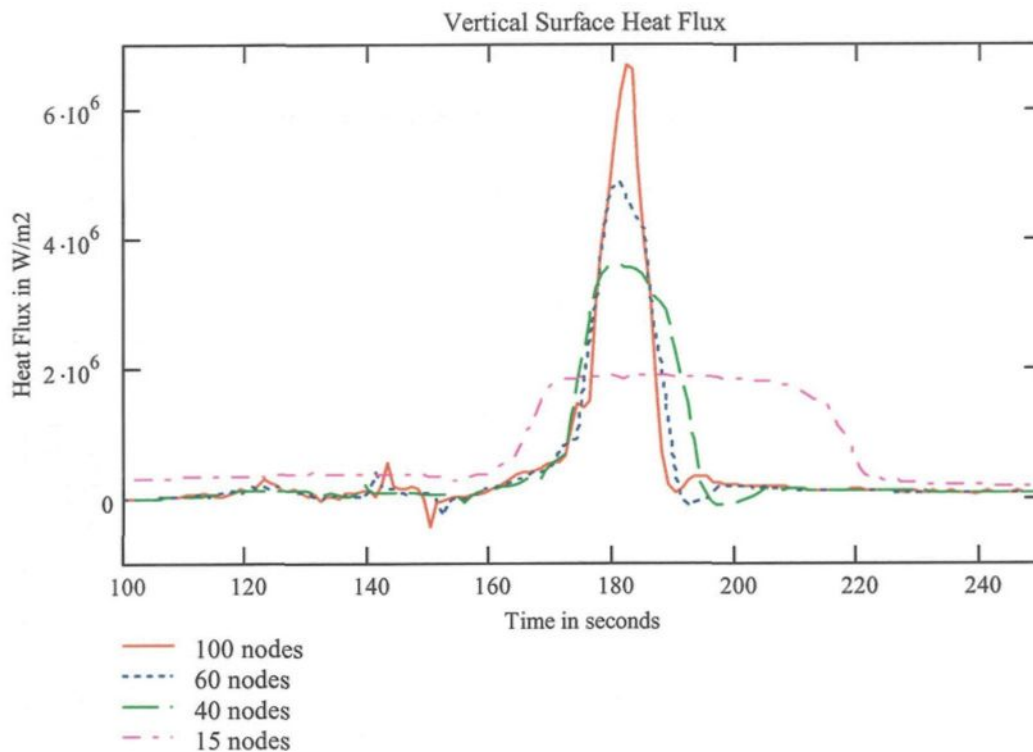


Figure 5.25: Measured and interpolated temperature curves form point TC2

calculated making the derivation of a third order polynomial regression of the temperature points. The MATLAB worksheet that determines the heat flux is shown in Appendix C.

The surface heat flux in the vertical direction for different node numbers are shown in Figure 5.26. It can be seen that the shape of the three curves using 40, 60 and 100 nodes



$$\max(qy_{100}) = 6.664 \times 10^6 \quad \max(qy_{60}) = 4.868 \times 10^6 \quad \max(qy_{40}) = 3.582 \times 10^6$$

Figure 5.26: Influence of node numbers on the vertical component of the surface heat flux

resemble. The curve found using 15 nodes is not at all representative. Thus we can conclude that we must take at least 40 nodes to have a certain precision in the vertical heat flux results. The difference between the result obtained with 100, 60 and 40 nodes is reasonable. We can observe that the curves are getting closer ( $\Delta y$  becomes smaller) when we have an

interpolation with 100 nodes instead of 60 and the gradient becomes stronger. To be able to make a statement of the magnitude of the vertical heat flux we will first investigate the heat flux at another measurement point. In addition we will compare a second measurement with the one we used.

**Comparison of Two Different Measurement Data** In the following we will compare two vertical heat flux results obtained from two different measurements. In Figure 5.25 we have already seen the measurement data from the test 16.05.2002 at the measurement point TC2. Now we will also investigate the measurement point TC3 (see Figure 5.40). The measured and for 60 nodes interpolated data can be seen in Figure 5.27. We will compare

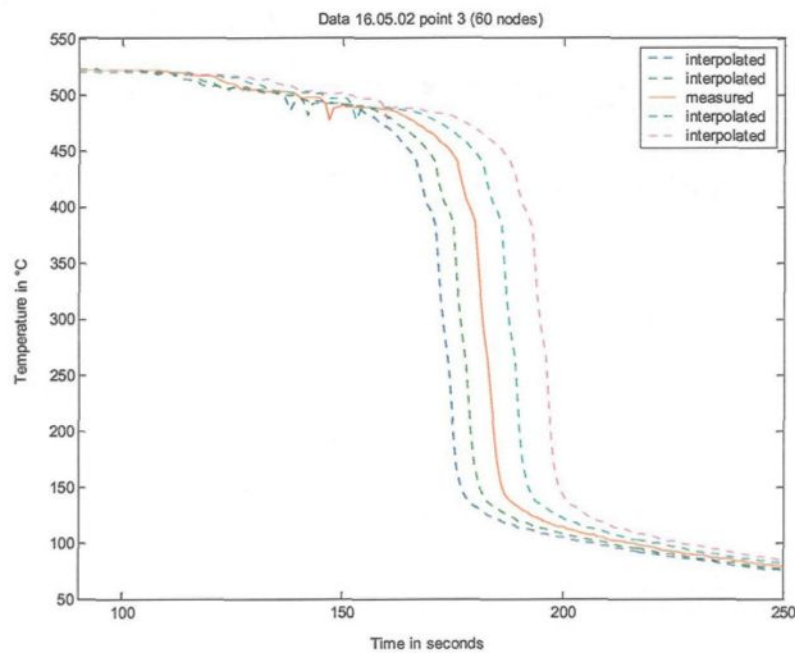


Figure 5.27: Measured and interpolated temperature curves from 16.05.02 at point TC3

these data with the measurement results from the test 20.02.2002. As shown in Figure 5.28

and Figure 5.29, the temperature curves have more fluctuations than that of the 16.05.2002.

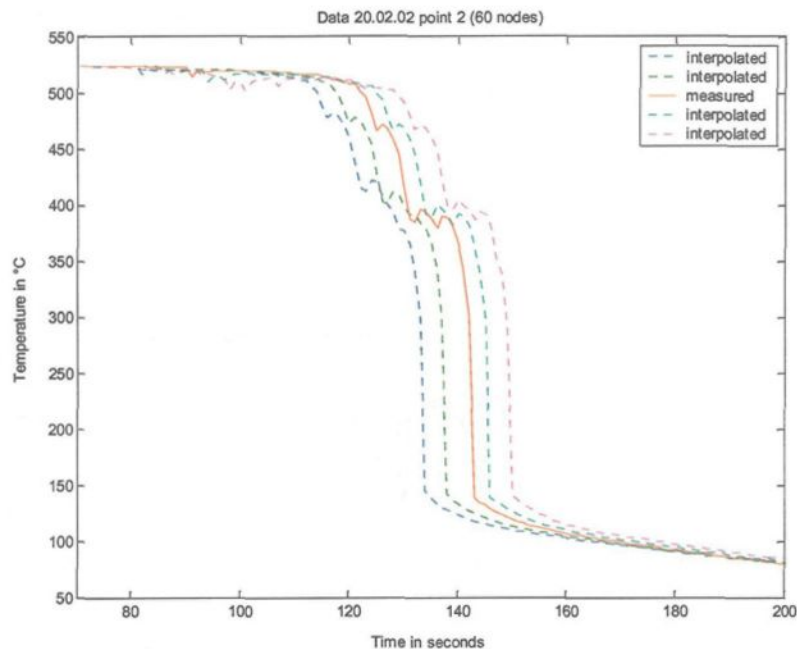


Figure 5.28: Measured and interpolated temperature curves from 20.02.02 at point TC2

All the following heat flux curves were calculated using the MATLAB worksheet presented before. First we will compare the vertical surface heat flux at the point TC2. The result in Figure 5.30 shows that the shape of both curves are almost identical. Obviously there is a shift between the two curves. This can be explained by the fact that the sharpest decrease of the temperature curve does not occur at the same time (see Figure 5.31). However, the maximal heat flux value in both curves is about  $4.5 * 10^6 \frac{W}{m^2}$ . The cause of different fluctuations in the heat flux are the fluctuations in the temperature curves. In Figure 5.32 we can see the two heat flux curves from the measurements 16.05.02 and 20.02.02 at the point TC3. Except the fluctuations at the beginning we have almost the similar curves.

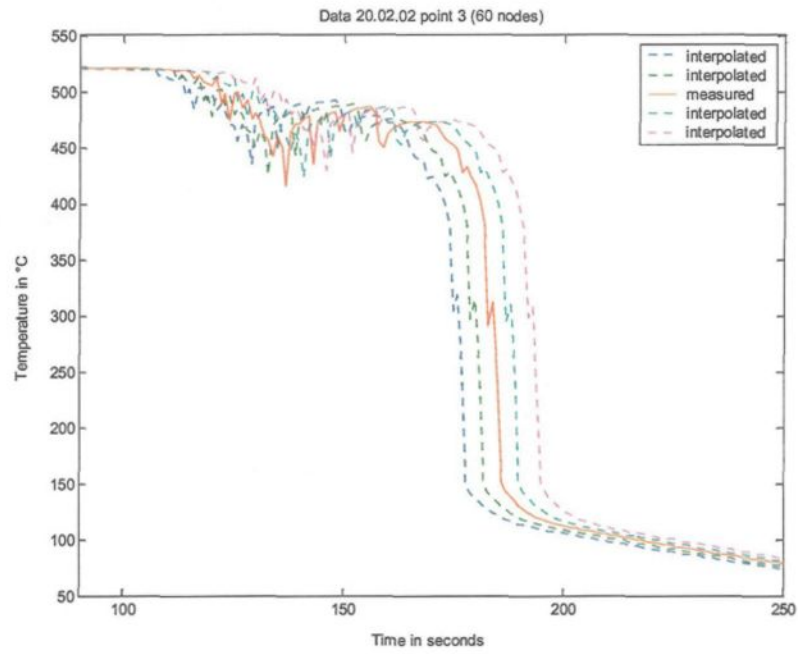


Figure 5.29: Measured and interpolated temperature curves from 20.02.02 at point TC3

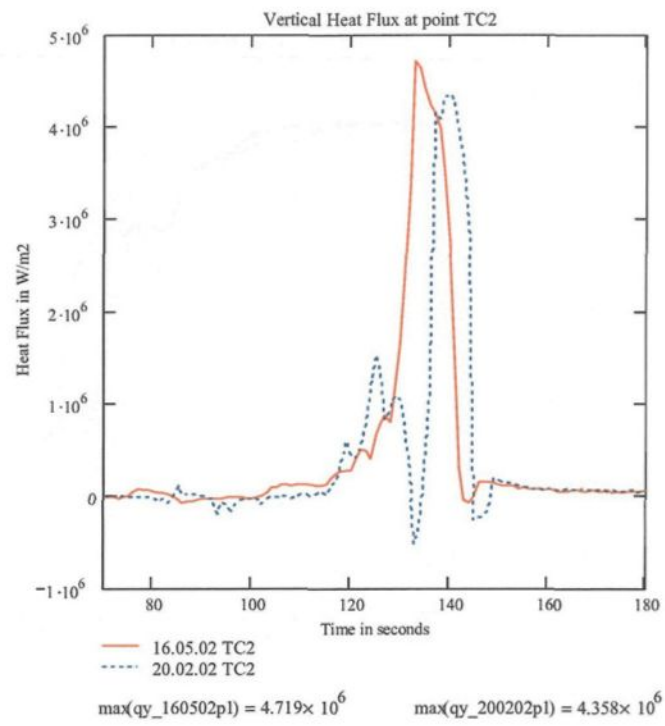


Figure 5.30: Comparison of the vertical heat flux from the test 16.05.02 and 20.02.02

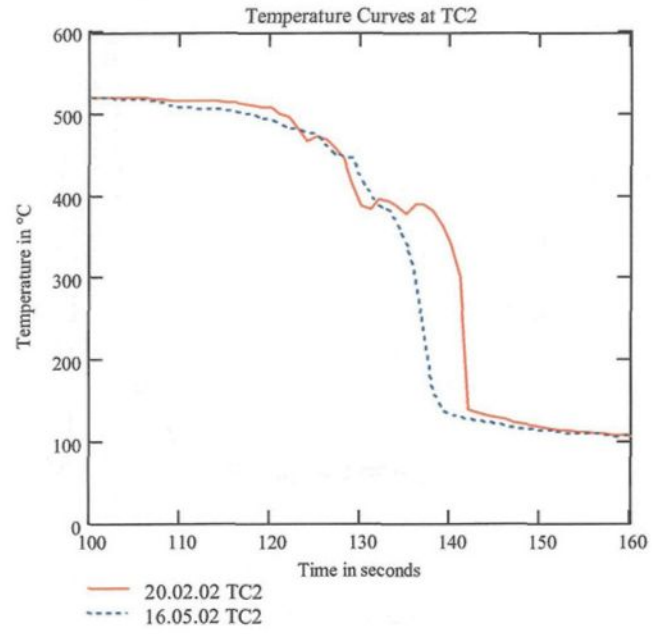


Figure 5.31: Temperature curves from the 16.05.02 and the 20.02.02

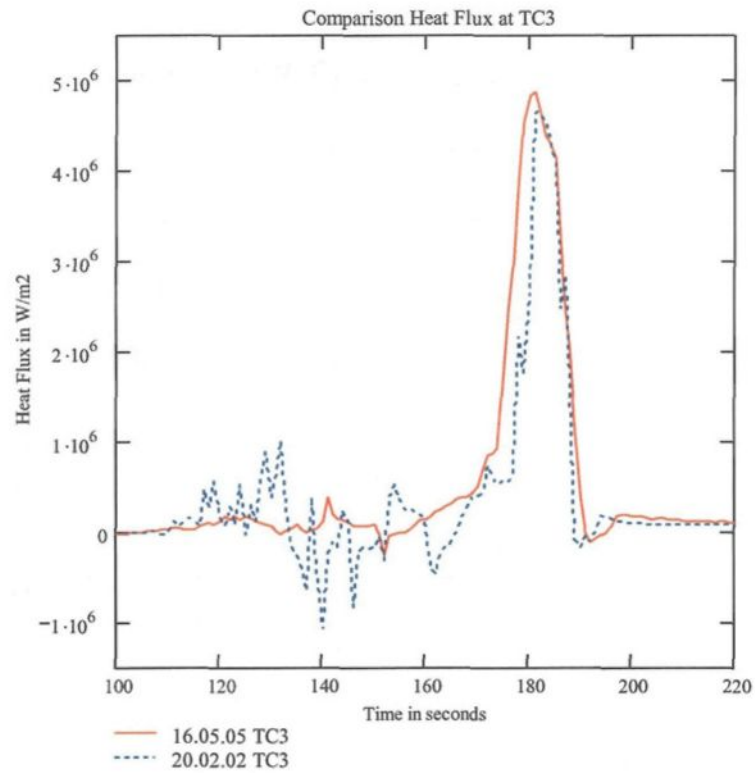


Figure 5.32: Comparison of the vertical surface heat flux from the measurements 16.05.02 and 20.02.02 at point TC3

Even the maximal heat flux is equal, about  $4.7 * 10^6 \frac{W}{m^2}$ . Comparing this result with the former one we can state that the maximal heat flux is about the same value for all cases compared. Nevertheless, we used the same regression method for all calculations. The next step will be to determine how strongly the heat flux depends on the regression method.

**Different Approximation Methods** Up to now we used the polynomial curve fitting function which is provided by MATLAB. We took a third order polynomial and determined the heat flux from its derivative (see MATLAB worksheet). In this subsection we will verify in detail how accurate this result is. We will compare a regression, an interpolation and a simple difference method. The interpolation of the temperature values was found using spline function, with linear endpoints (see Figure 5.33) The derivative of this function at

$$\begin{array}{l}
 j := \left\{ \begin{array}{l} \text{for } i \in 1.. \text{points} \\ x_1 \leftarrow \Delta y \cdot i \\ x \end{array} \right. \quad \text{fit\_i(x)} := \left\{ \begin{array}{l} \text{for } i \in 1.. \text{timesteps} \\ \left\{ \begin{array}{l} \text{for } n \in 1.. \text{points} \\ T_n \leftarrow \text{Matrix}_{1,n} \\ z \leftarrow \text{lspline}(j, T) \\ q_i \leftarrow \left( \frac{d}{dx} \text{interp}(z, j, T, x) \right) \cdot 237 \end{array} \right. \\ q \end{array} \right. \\
 T_n := \text{Matrix}_{\text{FRAME}, n} \\
 a := \text{lspline}(j, T) \\
 \text{temp\_i(x)} := \text{interp}(a, j, T, x)
 \end{array}$$

Figure 5.33: Function to fit the surface temperature points

the point  $3\Delta y$  multiplied with the thermal conductivity gives the vertical heat flux on the surface. In Figure 5.34 an interpolation for a certain time step is denoted. The regression was made in the same manner. Instead of using the built-in function *lspline()*, another built-in function, *regress()* was used. The resulting curve for the same time step as in

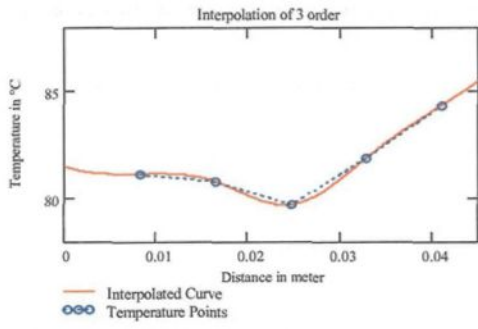


Figure 5.34: Interpolation of the temperature values at a given time step

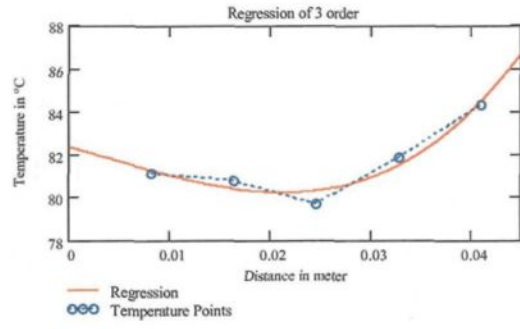


Figure 5.35: Regression of the surface temperature values

Figure 5.34 is plotted in Figure 5.35. The last method used for calculating the heat flux is carried out by taking the difference between two temperature values and dividing them by  $\Delta y$ .

$$q = \frac{T_3 - T_4}{\Delta y}$$

The three different heat flux curves calculated with these three different methods are shown in Figure 5.36. As we can see in this figure the result obtained using the regression (solid red line) and that using the interpolation are almost identical. Their difference is one order

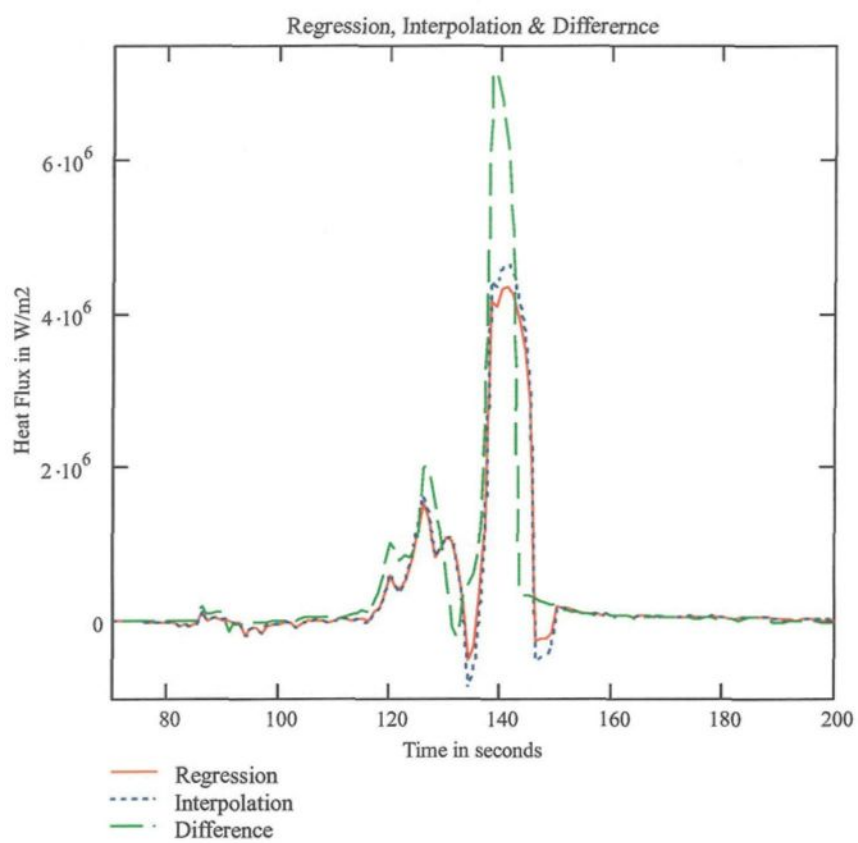


Figure 5.36: Vertical surface heat flux calculated with three different methods

of magnitude smaller than the maximal heat flux. However, the maximal values of these two curves are much smaller than the heat flux calculated with the difference method. If we take a closer look on the temperature distribution for the time around 140 seconds where the maximal heat flux occurs we will find the answer. In Figure 5.37 we can see

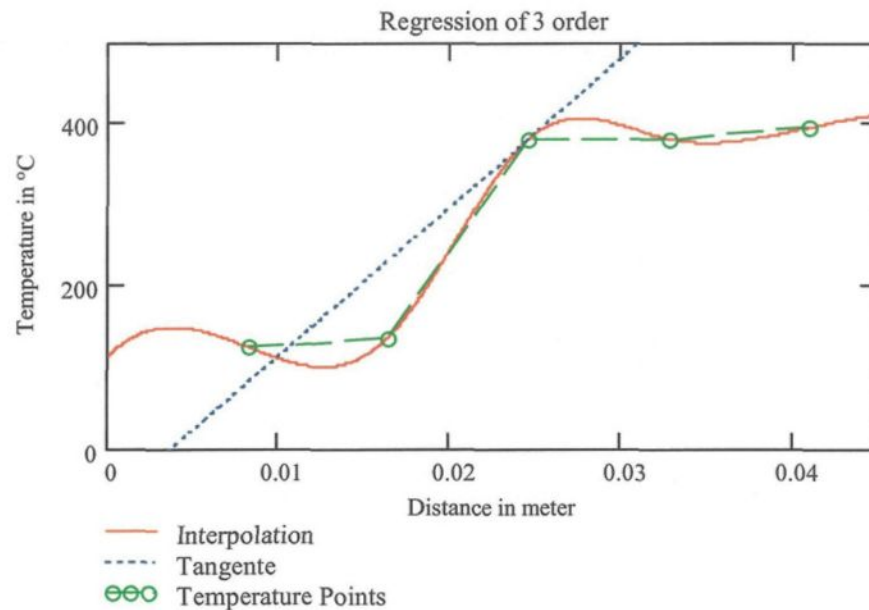
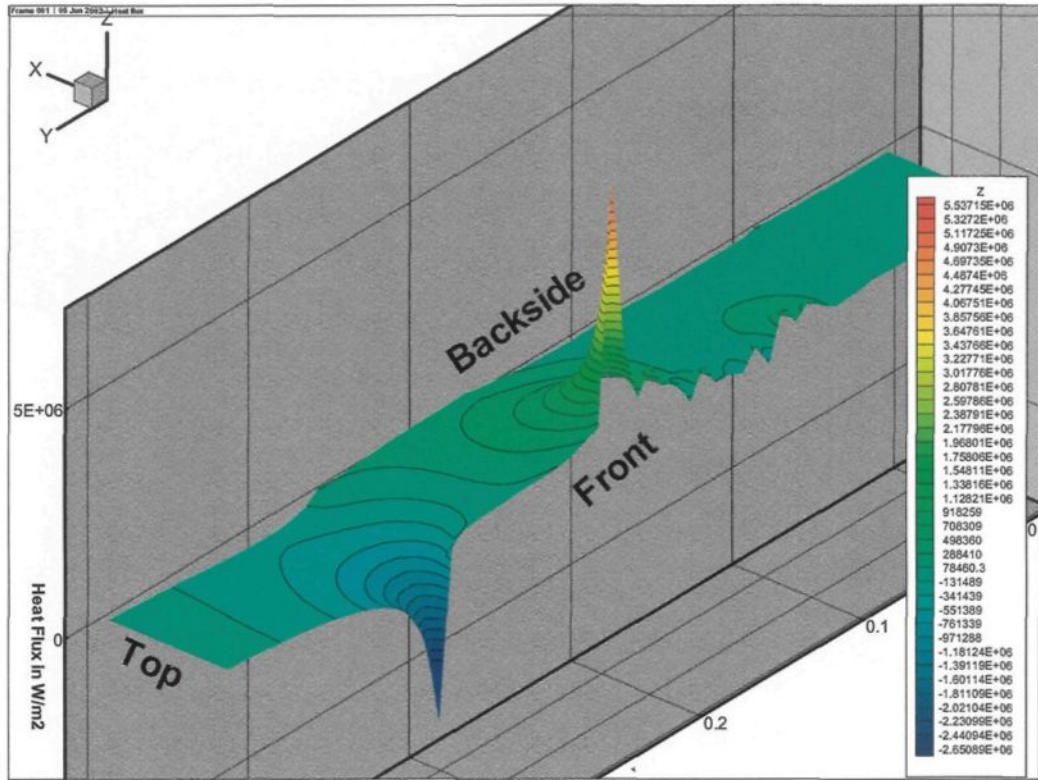


Figure 5.37: Interpolation and its derivative

how the interpolation follows the temperature points (green dashed line). The blue dotted line is the derivative at the point where we calculate the heat flux. If we compare the slope of the tangent and the slope of the line between temperature points at 0.016 m and 0.024 m we see that the gradient of the tangent is smaller. Thus the heat flux calculated using the difference of the two temperature points is bigger than the one determined using the derivative at point 0.024 m. We might say that the interpolation smooths out the temperature distribution. Therefore, it might be better to calculate the maximal heat flux

value using the difference method.

**Two Dimensional Vertical Heat Flux inside the Plate** In the subsection before, we calculated the vertical heat flux only at the surface of our ingot. Now we will take a closer look at the vertical component of the heat flux vector inside the plate. To do this we need the numerical solutions given by the finite volume algorithm. In the example discussed here we used the measurement data from the experiment made on the 20.02.02. The resolution of our grid is 60 nodes for the length and 60 nodes for the thickness of our plate. The timestep for the calculation was predetermined by the measurement data with  $\Delta t = 0.476$  s. The heat flux was calculated using the difference method as explained before. We obtained for each time step a heat flux distribution. Unfortunately it is not possible to demonstrate all these results with a videoclip here. Nevertheless, in Figure 5.38 we can see the heat flux distribution inside the plate in an arbitrary time step. The numerical solution does not take the measured boundary conditions into account. In other words, the heat flux distribution shown in Figure 5.38 was calculated with the temperature values determined by the finite volume program. But these results do not make use of the measured temperature histories we applied to the model. The maximal temperature variation occurs between the surface temperature and the first node. Therefore, the maximal heat flux is not as high as we determined in the subsection before. The negative heat flux next to the top of plate is present as shown in Figure 5.38 since the cooling started. It can be explained by the fact that the part above the impingement zone is hot during the cooling. This part is cooled by conduction through the plate and more weakly by convection from the surrounding air. Thus there is a temperature gradient between this hot region and the already cooled part.



In Figure 5.39 we have shown the temperature distribution for the same instant of time for which the heat flux was calculated. Here we can see the two sharp temperature drops which

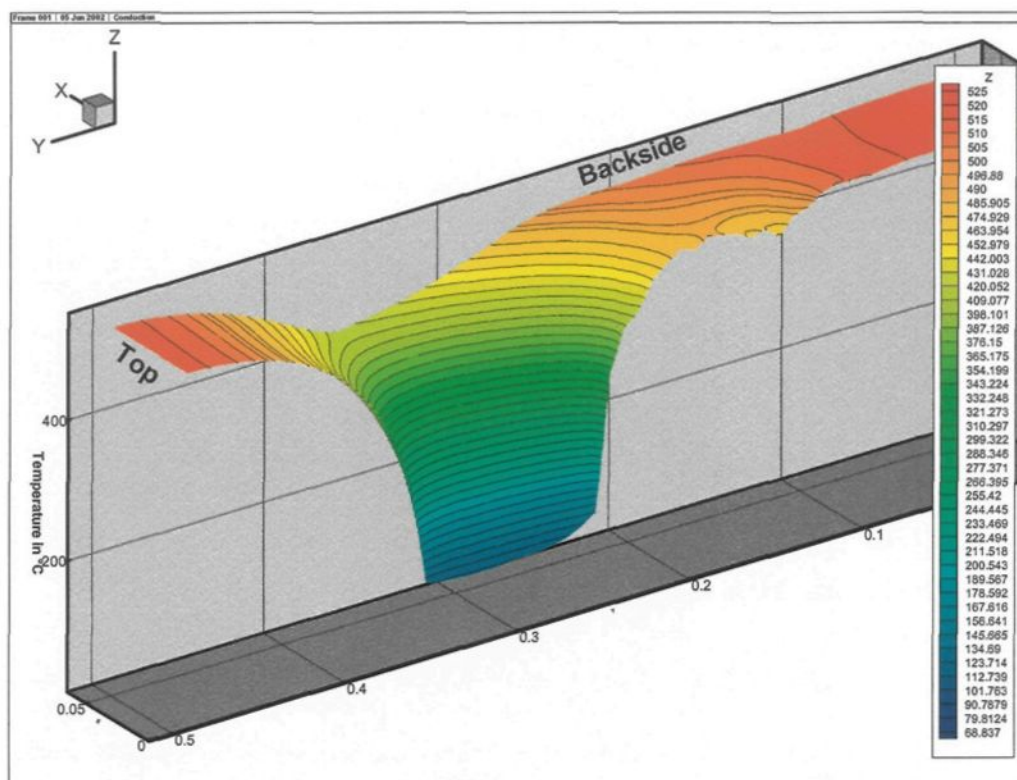


Figure 5.39: Temperature distribution inside the plate

cause the peaks in the heat flux graph (see Figure 5.38).

## Conclusion

The results can be summarized as follows: First, the calculated surface heat flux in the vertical direction depend strongly on the number of nodes used. We have found a minimum node number of 40 where the results can be considered as representative. We have also seen that the vertical heat flux is not affected much when two different measurement

data are used. Of course, the random fluctuations on the temperature history are reflected in the heat flux curve. The maximal value of the vertical heat flux depends more on the number of nodes used than on the temperature curve. At last we could remark that a regression or an interpolation smoothes the temperature variations. On the other hand it may also be possible that the discrete results from the numerical interpolation change too abruptly. So the correct value is probably between these two solutions. To give an approximate value for the maximal vertical heat flux we should keep in mind that we determined our solutions with a given number of nodes. Nevertheless, we estimate that a typical value is about  $6 * 10^6 \frac{\text{W}}{\text{m}^2}$ .

### **Horizontal Heat Flux**

The horizontal heat flux refers to the component of the heat flux vector that points from the hot interior to the surface where the cooling occurs (in the horizontal plane). For the analysis of the horizontal heat flux we use the results obtained from the finite volume algorithm. The specifications for the model will be given in the following subsection.

**Part Definition** The finite volume program needs a boundary value at each surface node for every instant of calculation time. A boundary value could be either a temperature or a heat flux. In our model we use the heat flux boundary conditions only to specify an insulated surface. Because we can not measure the temperature history for each surface node around the plate we insulated certain parts. Between two measurement points we could interpolate the temperature history as we explained in subsection 5.2.4. In Figure 5.40 the definitions for the boundary conditions are given. There we can see that the

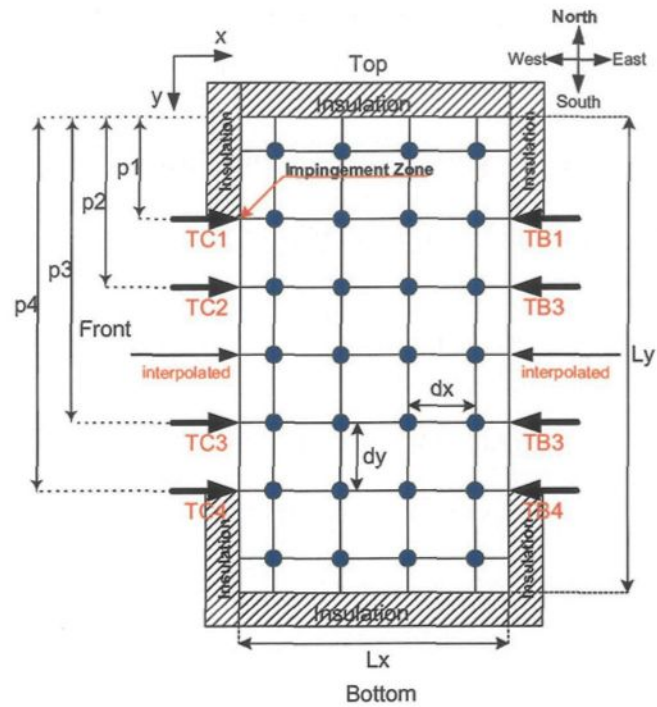


Figure 5.40: Boundary conditions for the numerical model

top and bottom of the plate are insulated. The part above the impingement zone is also considered to be insulated. Starting with the first measurement point, denoted by **TC1** in Figure 5.40, we assigned the measured temperature values to the surface nodes. On the backside or eastside of the plate we assigned the temperature measured at the backside. Between two measurement points we took the interpolated temperature histories between TC2 and TC3 as shown in Figure 5.40. The section below TC4 at the front should not be taken as insulated. Due to the lack of a measurement point at the south west surface node we can not interpolate between this point and TC4. Thus we had no other choice than insulating this part. This approximation does not correspond the conditions in the experiment. An additional thermocouple was later installed at this point to obtain a fifth measurement point. Unfortunately this installation did not work properly at the beginning so most of the simulations used the boundary conditions as described above. Later we will present also some results with an additional measurement point at the south west corner.

The coordinates for the measurement points TC1 to TC4 for the 0.49 m high and 0.063 m thick plate are:

$$TC1 = 0.135 \text{ m}$$

$$TC2 = 0.230 \text{ m}$$

$$TC3 = 0.320 \text{ m}$$

$$TC4 = 0.407 \text{ m}$$

These values were converted by the curve creation program to nodal positions in function of the maximal node number selected.

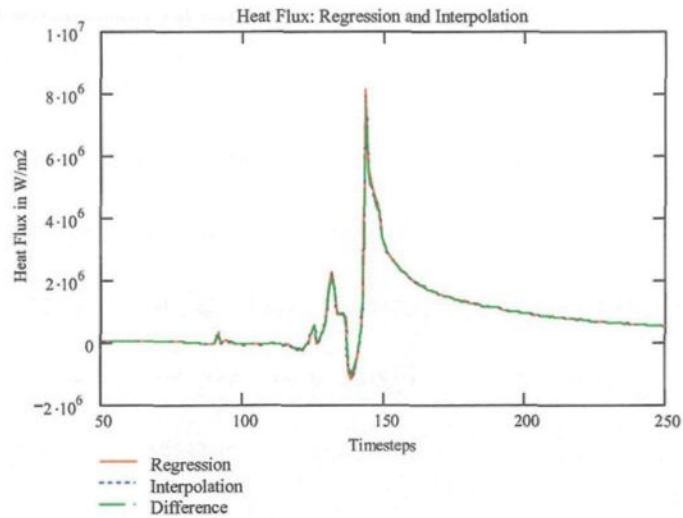


Figure 5.41: Different approximation methods to obtain the horizontal heat flux

**Different Approximation Methods** For the determination of the horizontal heat flux we will use the same interpolation and regression methods as already described in subsection 5.2.6 for the vertical component. To obtain the real surface heat flux we have to use the measured or interpolated boundary temperature plus the results of the numerical calculations. For example, to determine the heat flux at the measurement point TC2 we take the measurement data plus the 5 adjacent temperatures of the temperature distribution in the horizontal direction at the same height as TC2. Then we fit a curve through these points and obtain the heat flux using the space derivative of the curves at the surface. The heat flux result shown in Figure 5.41 was calculated using the measurement data of the measurement on 20.02.2002 at the measurement point TC2. The backside was insulated in this simulation with 40 nodes in each direction. There is no obvious difference between the heat flux obtained by regression, interpolation and differentiation in the figure as shown.

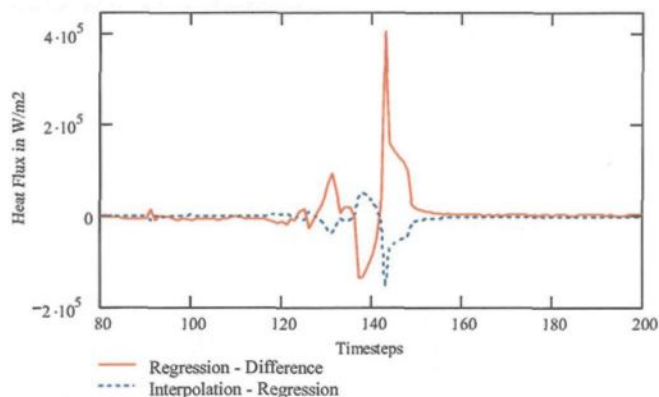


Figure 5.42: Difference between the approximation methods used

More information about the different types of approximating the heat flux are provided by the difference between them. The difference between the regression and interpolation as well as the difference between the regression and difference method is plotted in Figure 5.42. We can see that the differences between the curves are an order of magnitude smaller than the maximal heat flux. For a better understanding we will present another result using the measurements on the 16.05.2002. In this simulation we assigned the measured backside temperatures to the model. The heat flux is also shown for the measurement point TC2. The simulation used 60 nodes in each direction to determine the temperature distribution inside the plate. As we can see in Figure 5.43, the shape of the curve and the maximal heat flux are similar to those of the measurement on the 20.02.2002. Of course there are differences in the random fluctuations right before the maximal heat flux occurs, but these are based on the fact that measurement data is different. However, there are no major changes due to the variation of the number of nodes or due to using measured the temperature histories on the backside as boundary condition instead of an insulated surface.

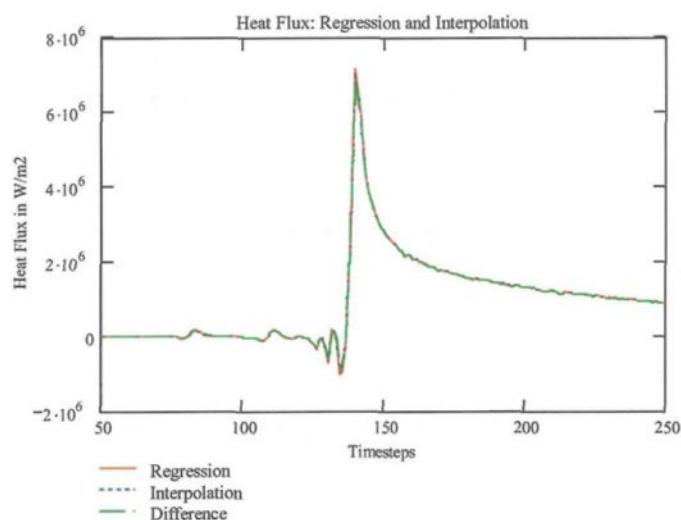


Figure 5.43: Horizontal heat flux result from the measurement on the 16.05.2002 at TC2

**Analysis of the Overall Heat Flux Distribution** Now we will take a closer look at the heat flux at all measurement points. In Figure 5.44 the heat fluxes for points TC1 to TC4 were calculated using the difference approximation. The results were obtained using the data of the test 16.05.2002 with a 60 node resolution. The first thing one may recognize is the value of the maximal heat flux at TC1. It is about twice as high as the heat flux from the other measurement points. To examine this behavior we will have a look at the temperature history in Figure 5.45. There we can see that the temperature fall at TC1 is very steep. Thus the higher heat flux for this thermocouple seems to be correct. The most likely reason for that is that TC1 is situated at the impingement zone. Another particularity in Figure 5.44 is the behavior of heat flux values at the end of the cooling. The values of TC2 and TC3 are almost falling back to zero, while the heat flux values of TC1 and TC4 approach the same level of about  $2 \cdot 10^6 \frac{\text{W}}{\text{m}^2}$ . This behavior might be caused by the way

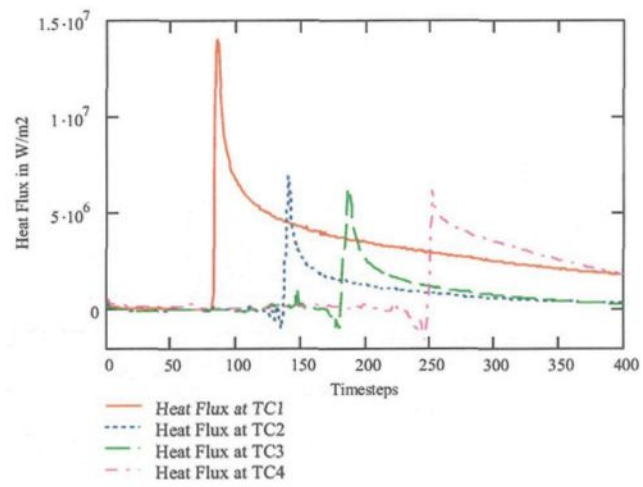


Figure 5.44: Heat Flux at all measurement points

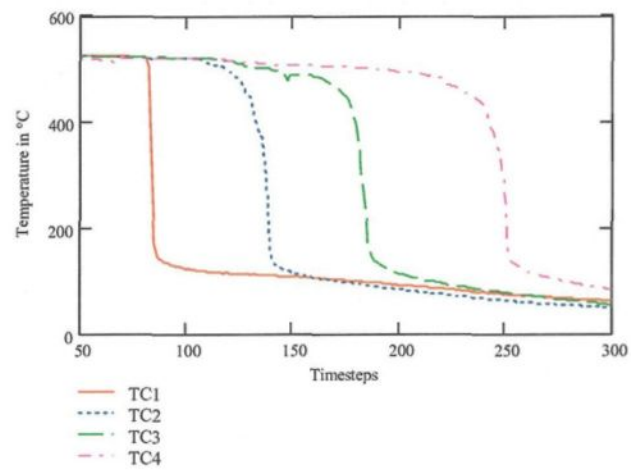


Figure 5.45: Temperature histories from measurement 16.05.2002

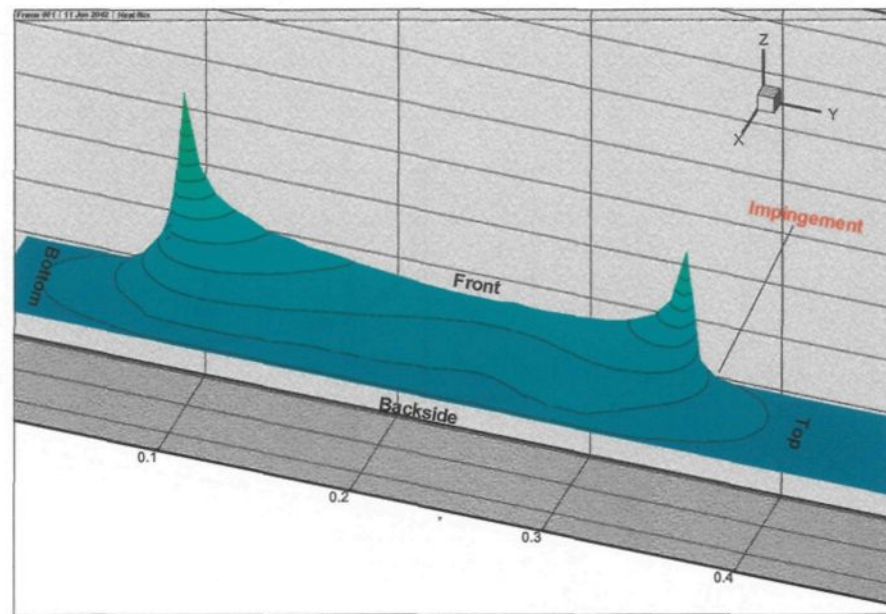


Figure 5.46: Horizontal heat flux distribution inside the plate

the boundary conditions are imposed. The measurement points TC1 and TC4 are situated at the border of an insulated part of the plate (see Figure 5.40). That means that heat is conducted from this non-cooled part into the well cooled zone. Thus we have a temperature gradient that does not disappear during the cooling. To prove this statement we will plot the computed heat flux and temperature distributions inside the plate for one of the last timesteps (see Figure 5.46). The two peaks in the Figure are at the measurement points TC1 and TC4. The peak at the impingement zone never disappeared since the cooling began. Once the front of the maximal heat flux reached the point TC4 this peak also stayed for the rest of the cooling process. The temperature distribution in Figure 5.47 was plotted for the same timestep. Here we can see the two temperature gradients appearing because of the two insulated sections at the front side. It has to be admitted that the insulated

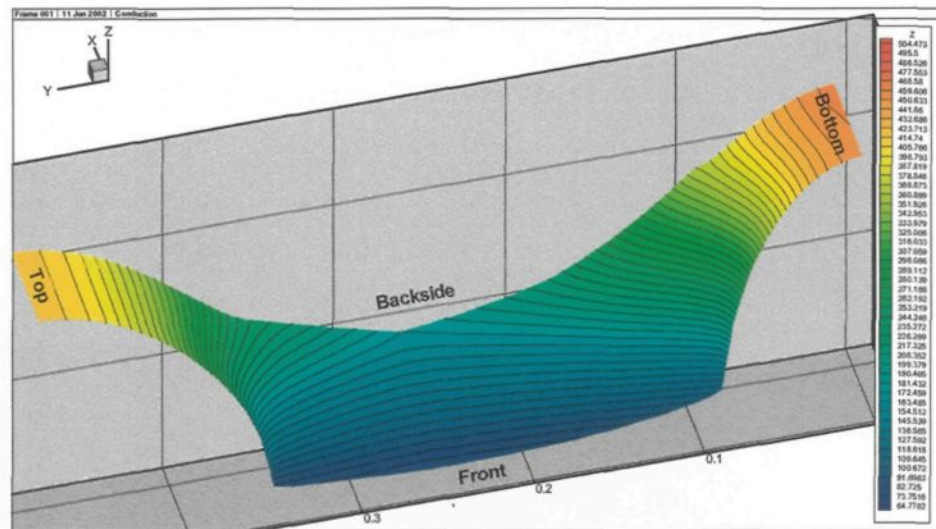


Figure 5.47: Temperature distribution for one of the last time steps

part at the bottom is disturbing the result at TC4 and below and does not reflect at all the experimental conditions. Therefore the following studies will be carried out only at the measurement points TC2 and TC3.

**Horizontal Heat Flux Distribution Inside the Plate** The former investigations were focused on the surface heat flux. Of course, the surface heat flux plays a major role in the scope of this project. Nevertheless we want to present some results showing the horizontal heat flux distribution inside the plate. The two dimensional heat flux was calculated for each time step during the cooling. The only way to show all these data together would be with a film. Unfortunately we can not insert a film here. Therefore we will show instantaneous results in the following figures. In Figure 5.48 we see the instant where the first temperature fall occurs at measurement point TC1. This peak will shrink but never disappear, due to the heat conduction from the insulated part above. The horizontal heat flux distribution

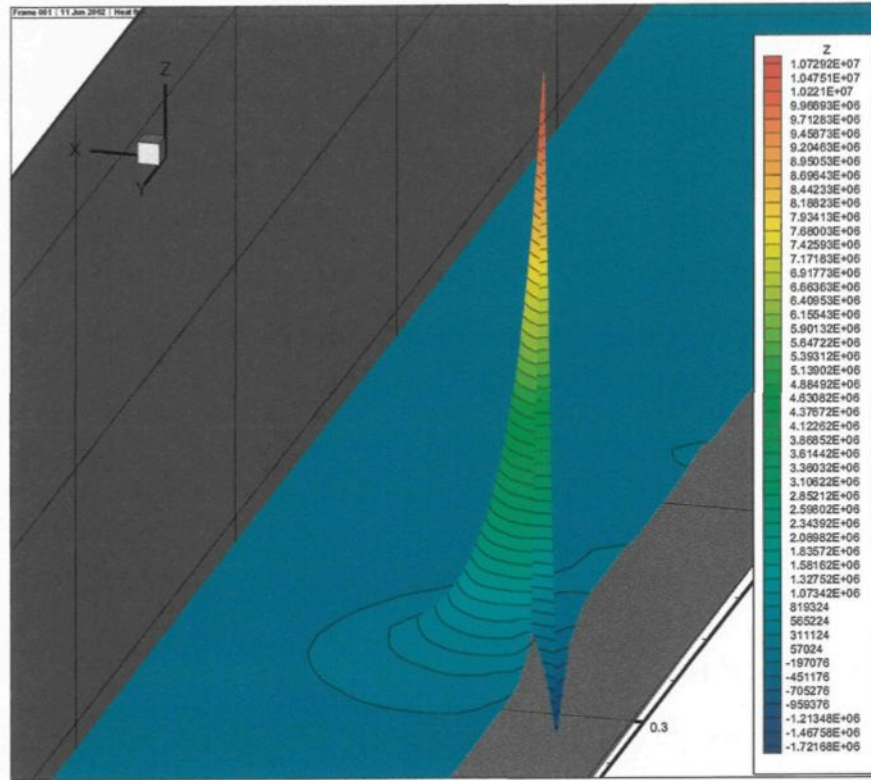


Figure 5.48: Maximal heat flux during the cooling at the measurement position TC1

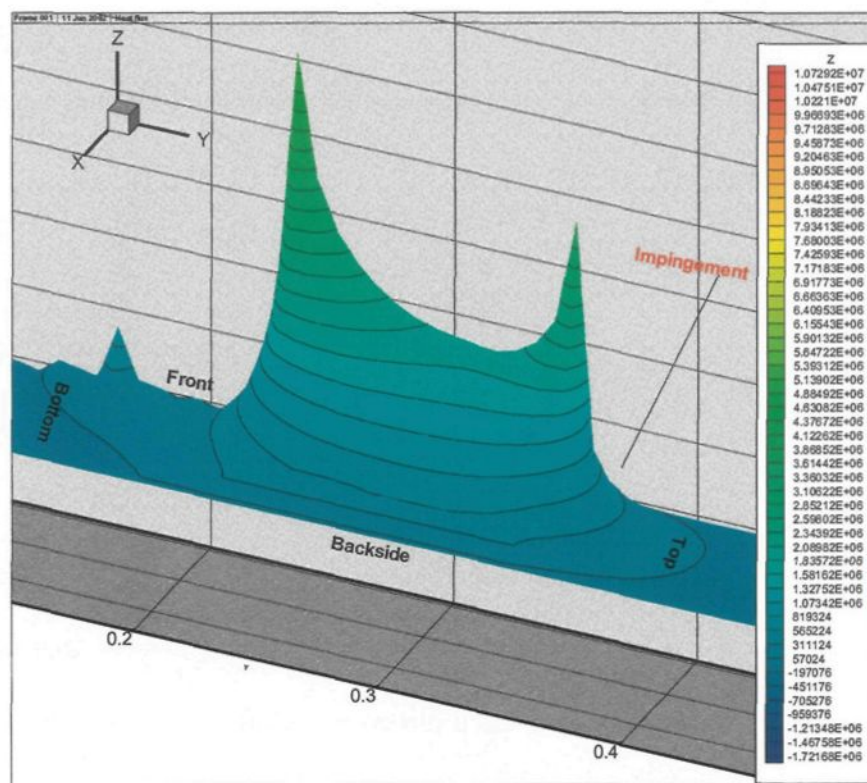


Figure 5.49: Horizontal heat flux at a random time step from measurement 16.05.2002

plotted in Figure 5.49 was calculated for a randomly chosen timestep. The first peak close to the top is the same as the one shown in Figure 5.48. The second one is the advancing re-wetting zone at the surface.

### Comparison of the Numerical Heat Flux Results with the Solution of the Cook-Felderman Equation

In the following subsection we will focus on the investigation of the difference between the heat flux results obtained by the numerical simulation and the one calculated using the inverse solution by Cook and Felderman. The numerically determined heat flux

was calculated using the regression method as described in subsection 5.2.6. For the heat flux evaluated with the Cook Felderman Equation the following function written in MathCad was used.

$$\begin{array}{l}
 k := 237 \quad \rho := 2702 \quad cp := 903 \\
 \text{flux}(\text{Temp}, \text{Time}) := \left\{ \begin{array}{l}
 \text{for } p \in 2..P-2 \\
 qf_p \leftarrow -2 \sqrt{\frac{k \cdot \rho \cdot cp}{\pi}} \cdot \sum_{i=2}^p \frac{(\text{Temp}_i - \text{Temp}_{i-1})}{(\sqrt{\text{Time}_p - \text{Time}_i} + \sqrt{\text{Time}_p - \text{Time}_{i-1}})} \\
 qf_p \leftarrow 0 \\
 qf
 \end{array} \right.
 \end{array}$$

First we will compare the Cook Felderman results with the numerical results of the measurement on the 20.02.2002. We use two different models. One numerical solution was calculated with 40 nodes in each direction and an insulated backside while the other was obtained with a model using 60 nodes in each direction and the measured backside temperatures. All three curves were evaluated for the measurement point TC2 and can be seen in Figure 5.50. We can already see in this figure that the result by the Cook Felderman equation does not follow closely the fluctuations. However, at least the tendency of the fluctuations is followed by the Cook Felderman solution. It is obvious that the peaks are more distinct in the simulation with 60 nodes. That may be caused by the smaller node distance. Figure 5.51 provides a better insight of the differences between the presented curves. In this figure, the percent difference between the numerical results and the Cook Felderman calculation is shown. We see that the deviation between the regression made with 40 nodes is less than the one obtained with 60 nodes. Saying that the model using less nodes provides more accurate results is not appropriate. For the moment there exist no way to verify which one of the results is reflecting better the reality. A better explanation for

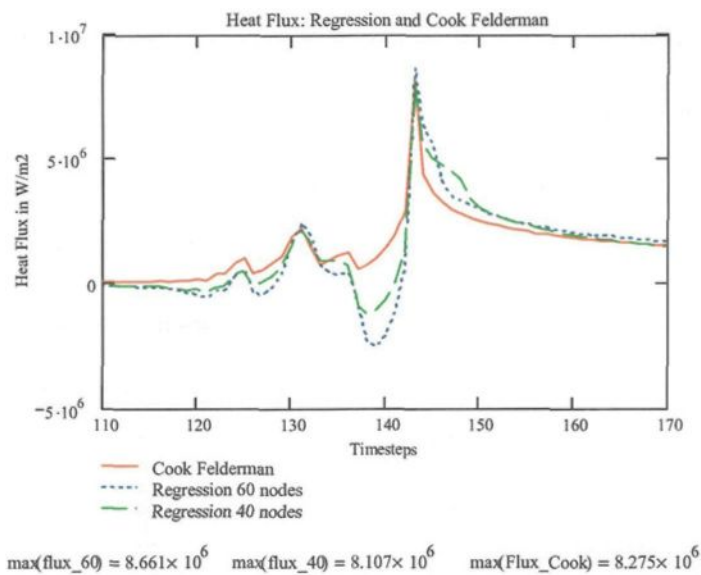


Figure 5.50: Heat flux : Cook Felderman Eq. and Regression

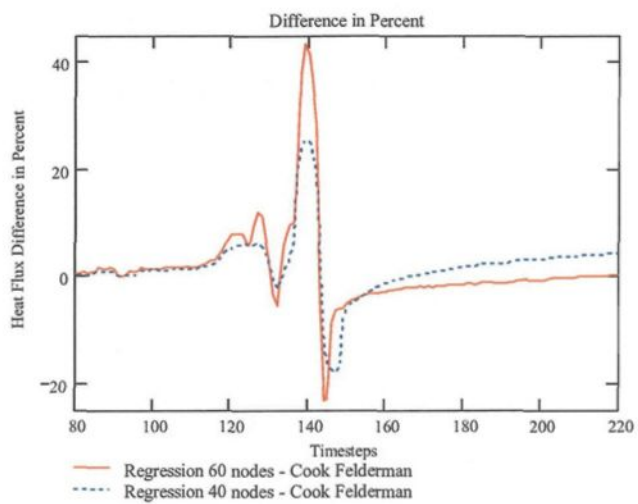


Figure 5.51: Relative difference between the Cook Felderman solution and the numerical results

the bigger variation between the 60 nodes model and the Cook Felderman equation could be that both the 40 nodes and the Cook Felderman solution do not follow the temperature variations fast enough. This could be an indication of smoothing properties of the Cook Felderman equation. To emphasize the observations the results for the measurement point TC3 are plotted in Figure 5.52 and Figure 5.53. The difference in percents is almost the same. We also can see that the Cook Felderman solution does not follow so fast the fluc-

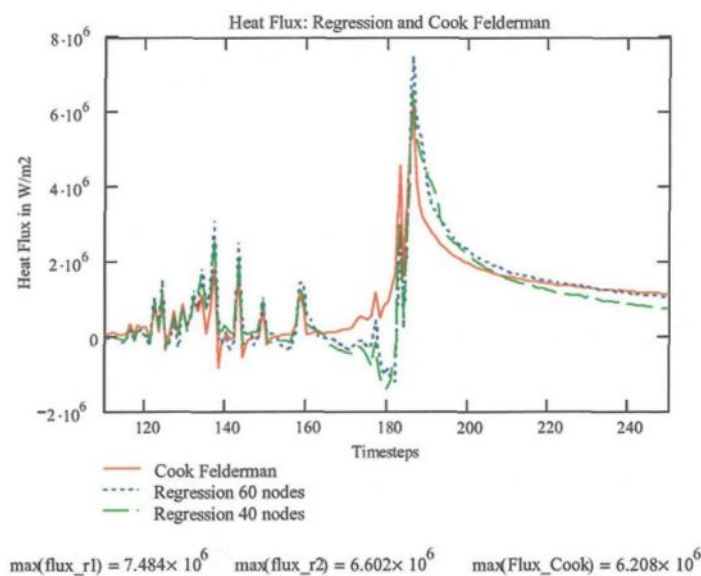


Figure 5.52: Heat Flux at TC3

tuations as we have already seen for the point TC2. A benefit of the verification done here could be an estimation of the approximate error between the Cook Felderman equation and the numerical solution. As we have already seen in Figure 5.51 and Figure 5.53 the error is about +45% and -35%. Here the positive peak denotes the variation according to the fluctuations before the maximal heat flux. The negative value refers to the difference between the maximal heat flux itself of both solutions. But this was only for the measurement

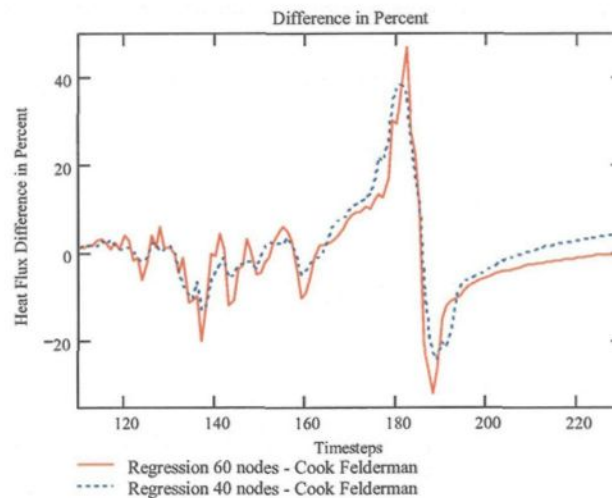


Figure 5.53: Relative difference in percents at TC3

points TC2 and TC3. In Figure 5.54 the difference in percents from the measurement at the 20.02.2002 is plotted for all measurement points. We can observe a maximal error of about 104 percent for the TC1. More information are provided by another measurement result. The graphs shown in Figure 5.55 denote the difference in percents between the Cook Felderman solution and the numerical results based on the measurement data of the 16.05.2002. The shape as well as the maximal and minimal differences are similar to the one from the measurement of 20.02.2002. To complete the verification we will consider a third simulation result. This result was calculated with a timestep of  $\Delta t = 0.1955$  s. This corresponds to more than the half of the time which was used for the other simulations. The comparison of this result with the Cook-Felderman equation can be seen in Figure 5.56. Here the maximal deviation in the positive direction amounts to 62.6%. Thus we can conclude for the measurement points TC2 to TC4 that an approximate difference between

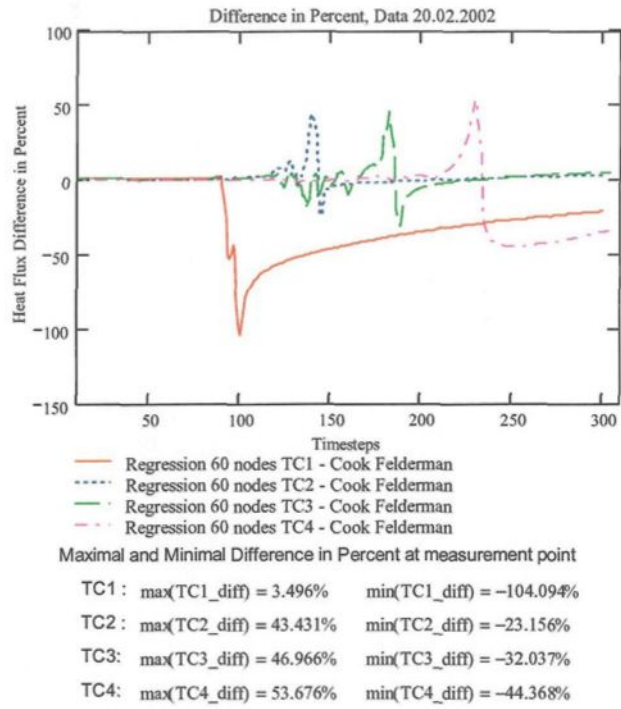


Figure 5.54: Difference in percents from the measurement on 20.02.2002

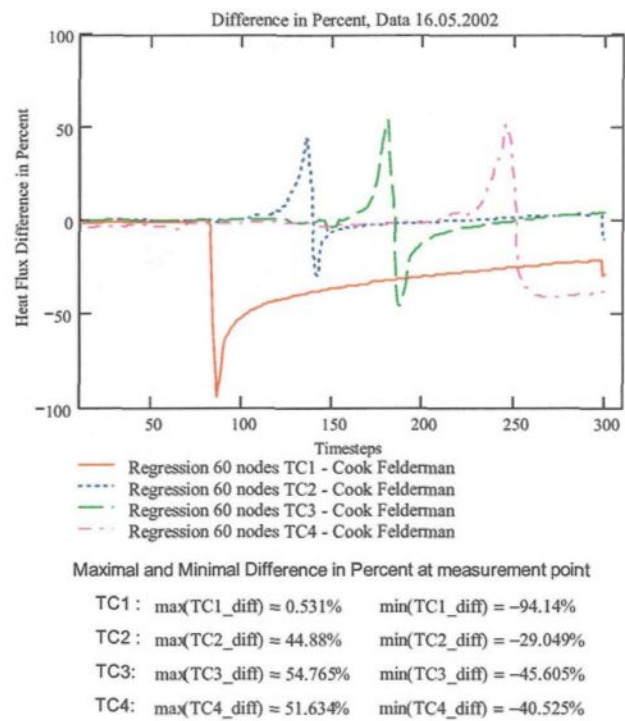


Figure 5.55: Difference in percent from measurement data 16.05.2002

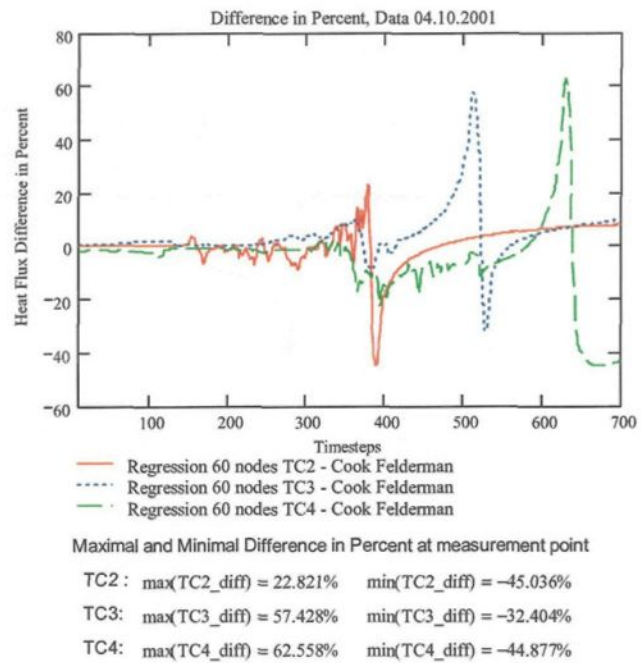


Figure 5.56: Difference in percents from measurement data 04.10.2002

the simulation and the Cook-Felderman results of +65% and -45%, where the positive value indicates the error according to the fluctuations before the maximal heat flux occurs, while the negative value indicates the error according to the maximal heat flux. For the impingement zone at TC1 we have a difference higher than +100% for the maximal heat flux.

Not only the maximal and minimal difference can be found using previously presented graphs. If we take a closer look to the curves of TC1 and TC4 in Figure 5.54 and Figure 5.55 we will see that the difference does not fall back to zero after the negative maximum such as for TC2 and TC3. This behavior can be better seen in Figure 5.57 where the heat flux -which was calculated with the finite volume model and the Cook Felderman equation- is plotted for the measurement points TC1 and TC4 . It is obvious that the two

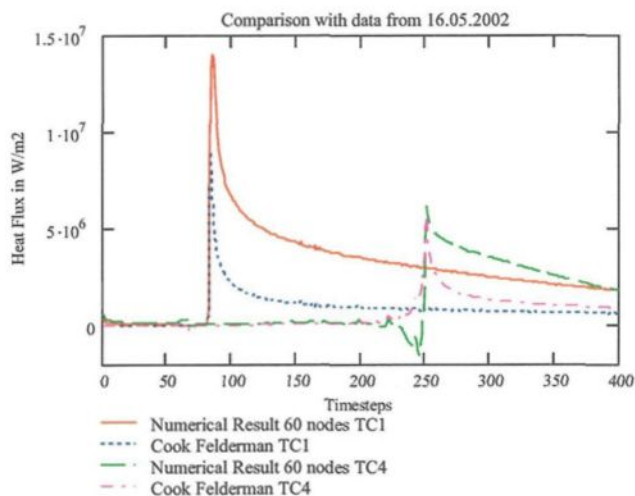


Figure 5.57: Heat flux results from finite volume model and Cook Felderman equation

numerical results converge to a certain non-zero value while the heat flux from the Cook

Felderman equation approaches zero for timesteps higher than 350. We have already seen that the heat flux at the measurement points TC2 and TC3 converge to zero. The difference between the end measurement points TC1 and TC2 and the middle points TC3 and TC4 is the fact that the end points have an insulated neighborhood. Thus the conduction from this non cooled parts establish a temperature gradient once the re-wetting zone passed. For the point TC4 this boundary condition is not desired because it's not reflecting the experimental cooling process. This is contrary for point TC1 where the part above the impingement zone can be assumed to be insulated for the experiment. Here the Cook Felderman solution does not include the boundary condition of an insulated part below because it is only considered for an one-dimensional problem. Therefore the results obtained by the Cook Felderman equations at the measurement points beside an insulated part are not correct.

## Chapter 6

# Experimental Results

### 6.1 Different Plates

In this section it will be shown that there is a difference in the heat flux measurements between the machined and the rough ingot. We will now take a closer look on these differences. The experiments discussed in the following section were carried out using tap water. The most obvious difference can be seen by comparing two typical experimental results carried out a machined and a rough surface ingot. The thermocouple position can be found in Figure 4.18. In Figure 6.1 we see the temperature measurements of the experiment carried out on the 08.10.2001 with a machined ingot. The time interval between the readings was about  $\Delta t \simeq 0.2$ s. From this figure, it can be seen that the first and second temperature fall (TC1 and TC2) influences the temperatures read by the thermocouples below (TC3 and TC4). Therefore there are strong fluctuations in the cooling curve of each thermocouple after the first water contact to the surface was established. An explanation of the physical processes that are responsible for this behavior will be given later. The

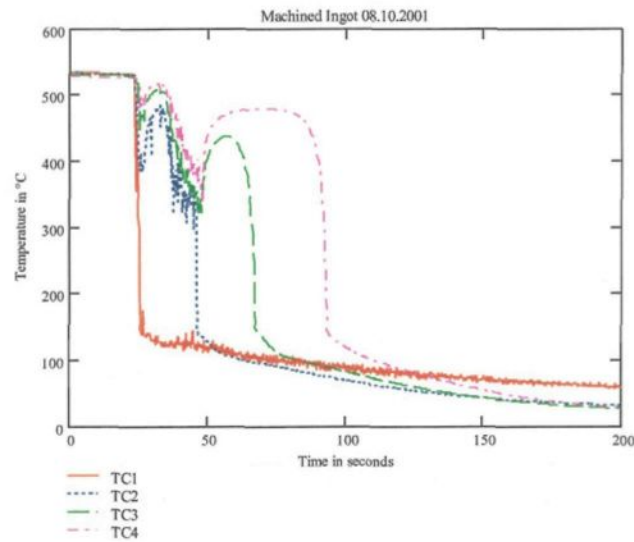


Figure 6.1: Temperature measurement of experiment 08.10.2001 carried out using tap water on a machined ingot

oscillations of thermocouple TC1 around  $100\text{ }^{\circ}\text{C}$  are caused by an electrical contact error. Now we will compare these cooling curves with the one obtained on a rough surface ingot. The results of the experiment carried out on 04.10.2001 were obtained with tap water. We can see here that there are less fluctuations. Even the temperature curves from two different rough surface plates prepared seven months apart are quite similar. The cooling curves presented in Figure 6.3 belong to a test carried out using another rough surface plate and tap water (08.05.2002). This comparison of two almost equal cooling processes on two different rough ingots shows the effect of surface roughness is significant as can be seen if the rough surface ingot measurements are compared to those of the machined ingot. Also the repeatability for different plates with the same surface properties is not always that good as we have seen in the two previous examples. The graphs shown in Figure 6.4 shows the result of the experiment carried out on the 16.05.2002 using tap water and a third ingot

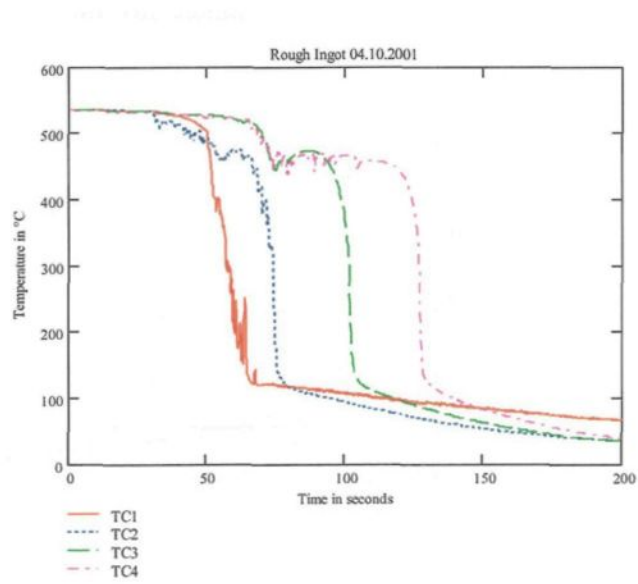


Figure 6.2: Rough surface experiment of 04.10.2001 carried out using tap water

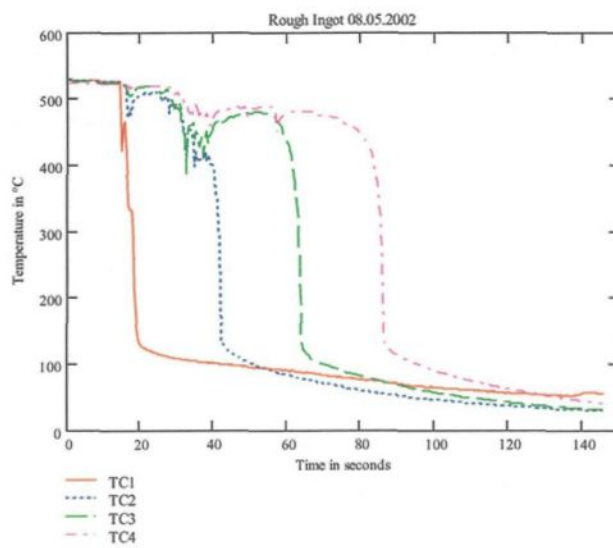


Figure 6.3: Data of 08.05.2002 carried out using tap water on rough surface ingot

with a rough surface. Here there are almost no fluctuations during the cooling. There

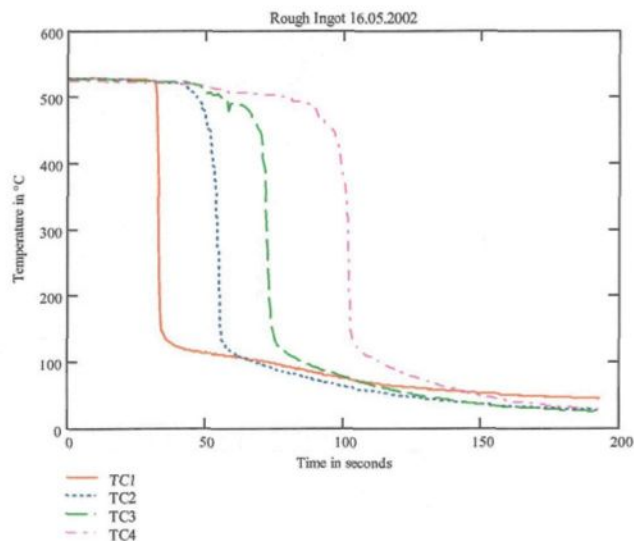


Figure 6.4: Results from experiment 16.05.2002 carried out using a third rough surface plate

might be several reasons for this observation. An important factor might be the different surface structures. Another factor could be identified as structure of the water film flow itself but this mechanism will be analyzed in detail later. During the temperature measurements for the rough plates (04.10.2001 and 08.05.2002) we have seen that the temperature curves show similar tendencies. How far these similarities can be retrieved in the heat flux to temperature graph is shown in Figure 6.5. In this figure the heat flux to temperature curves are shown for the measurement point TC2. It is obvious that the machined ingot has stronger fluctuations in the zone above 300 °C. The results for the rough surface ingot are different. One must remember that the repeatability of the cooling curves measured on the same plate at the point TC2 was not good. Furthermore the results at the measurement point TC3 -presented in Figure 6.6- show the same effect. It seems that the two different

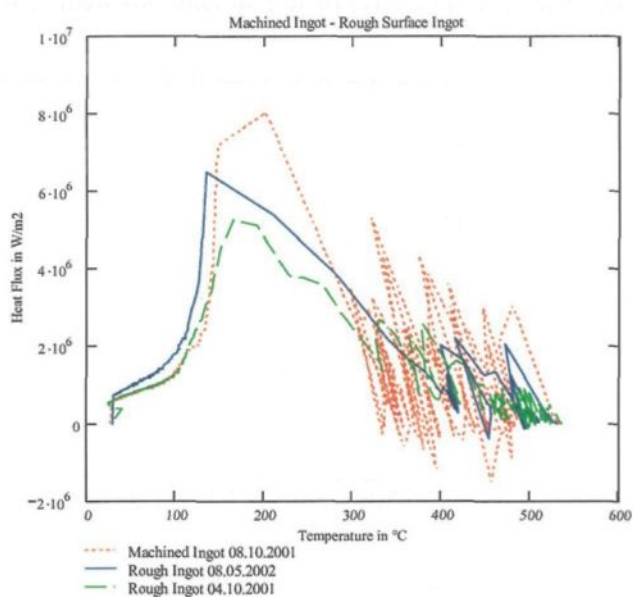


Figure 6.5: Heat flux to temperature graph for measurement point TC2

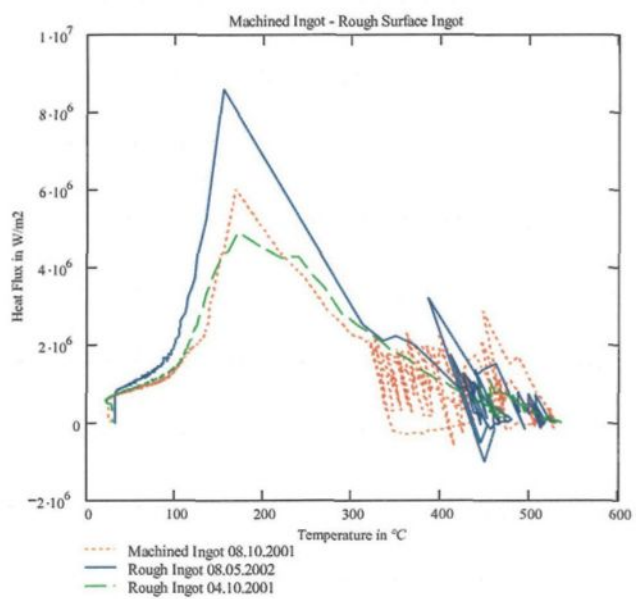


Figure 6.6: Comparison of rough and machined ingots at measurement point TC3

rough plates have also quite different heat flux vs temperature curves, especially in the region under  $400\text{ }^{\circ}\text{C}$  where the maximal heat flux occurs. Even the fluctuations above  $400\text{ }^{\circ}\text{C}$  are not comparable. Different factors influence the surface boiling for rough and machined plates. The difference in surface microstructure influences the number of nucleation sites. The changing orientation of the surface elements results in different retention forces for the liquid film, which ultimately influences the stability of the vapor bubbles on the surface.

## 6.2 Influence of Different Water Types

We will now discuss the effect of using different water types on the heat flux. One of the objectives of this investigation was to answer the question of how using normal tap water or recycled water in the cast shop affect the cooling. Thus tests with plant and tap water were performed using a rough surface ingot as well as a machined ingot. Later another type of water with a high electrical conductivity was tested. The properties of the tap water can be described by an average conductivity of about  $90\mu\text{S}$  and an average pH of 6.8. The average conductivity for the plant water was approximately  $1900\mu\text{S}$  while its average pH varies around 8.1. The high conductivity water had the following properties: average conductivity about  $3200\mu\text{S}$ , average pH about 8.1. At first we will compare the results of the experiment conducted using the machined ingot. We carried out three tests with each water type. In Figure 6.7 and Figure 6.8, the temperature vs time curves on a machined ingot with the three different water types (plant, tap and high conductivity water) are shown at position TC2. The two figures show clearly the effect of the three water types on temperature. The slope of temperature vs time curve for high conductivity water is really

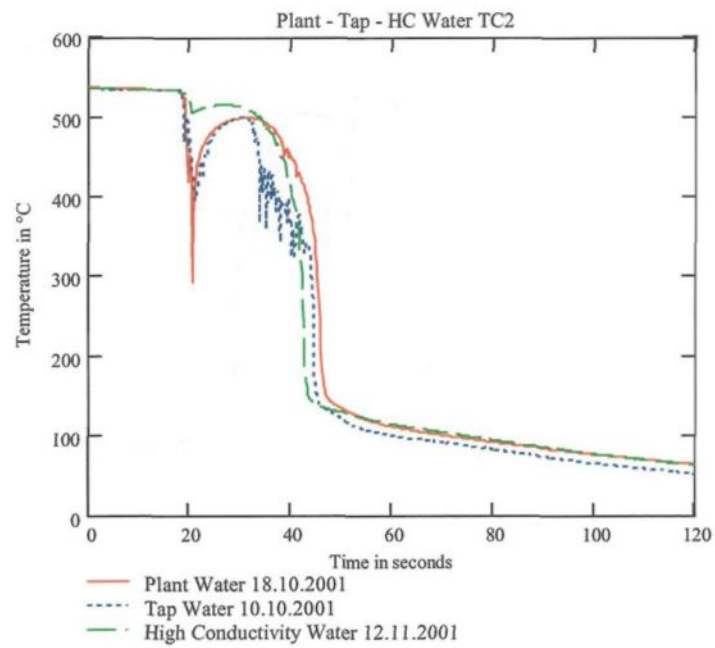


Figure 6.7: Temperature curves on a machined ingot at position TC2 (a)

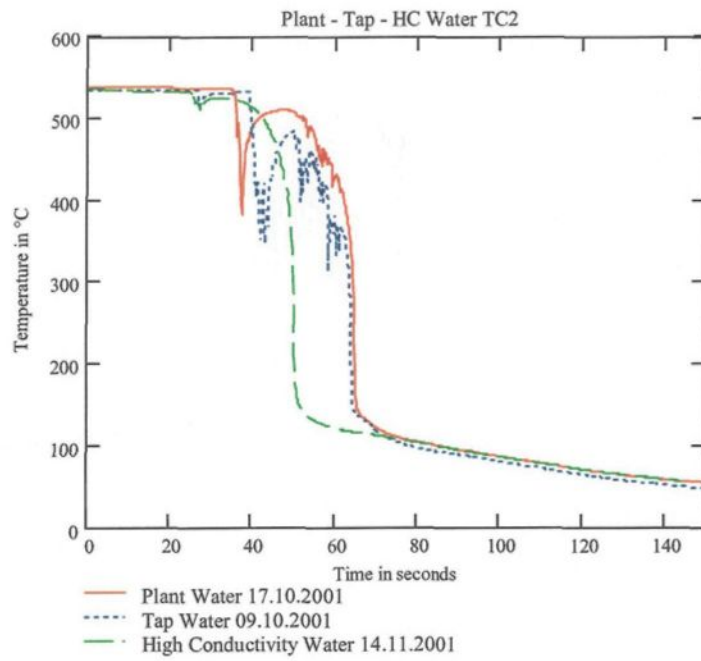


Figure 6.8: Temperature curves on machined ingot at position TC2 (b)

smooth and has almost no fluctuations. The temperature vs time for plant water plant water first displays the distinct first temperature drop, then the curve stabilizes in seconds before the major cooling fall occurs. We also can see some fluctuations before the temperature falls to  $110\text{ }^{\circ}\text{C}$ . The cooling curve for tap water shows the same behavior similar to that of the plant water. However it has more fluctuations. This behavior is reflected in the heat flux to temperature graphs too (see Figure 6.9). From these figures we can conclude that higher the water conductivity is, less the fluctuations are in the cooling curve. A further

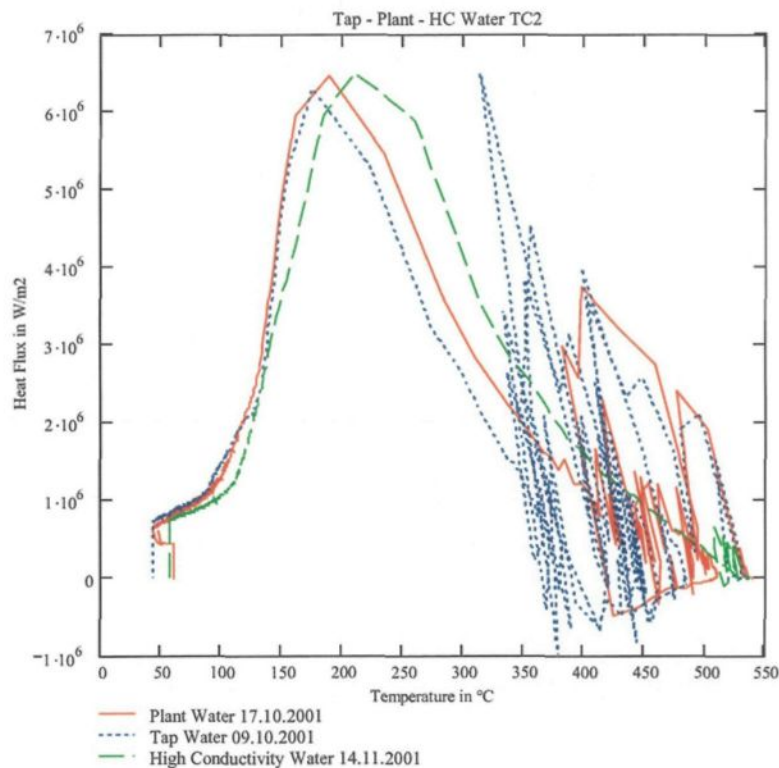


Figure 6.9: Comparison of different water types on a machined ingot in a heat flux to temperature graph (TC2)

proof of this statement is seen if the temperature vs time data (see Figure Figure 6.10) of a rough ingot is studied. The effect of plant and high conductivity water on temperature is less

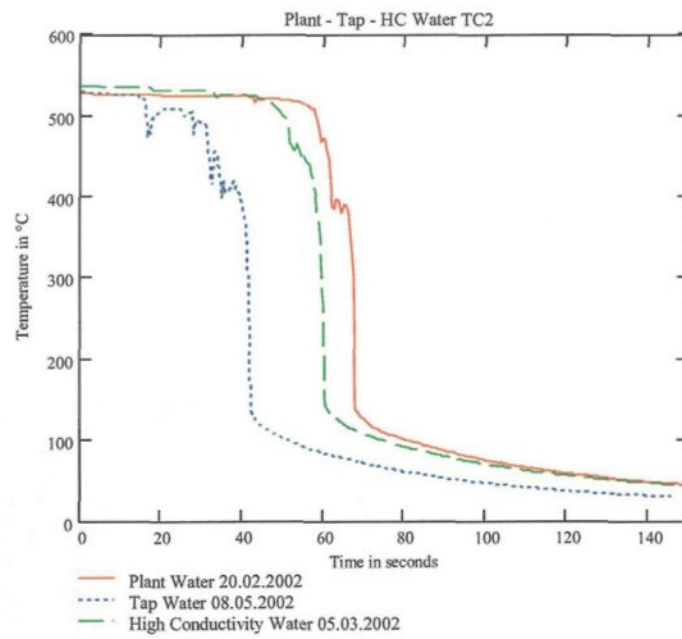


Figure 6.10: Comparison of different water types on a rough ingot at position TC2

significant, but the tap water shows again more fluctuations. To continue the investigation in this direction we will discuss the results at the other measurement points. Figure 6.11 and Figure 6.12 show the temperature vs time measurements at position TC3 and TC4 on the same dates. We observe again the smoothness of the data using high conductivity

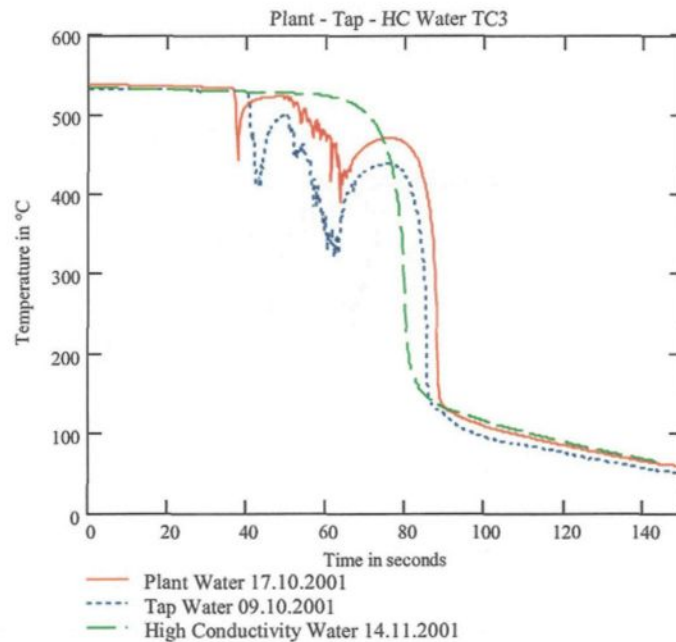


Figure 6.11: Measurement results on machined ingot at position TC3

water. But if we compare the data obtained using plant and the tap water we see that there is almost no difference between them. The same behavior is noticeable on the rough surface ingot as denoted in Figure 6.13 for the measurement point TC3. Thus the statement "higher the electrical conductivity is, smaller the fluctuations are in the cooling curve" is not valid for all measurement points. On the contrary, there is almost no difference when plant and tap water are used neither on a machined nor on a rough ingot about 180 mm below

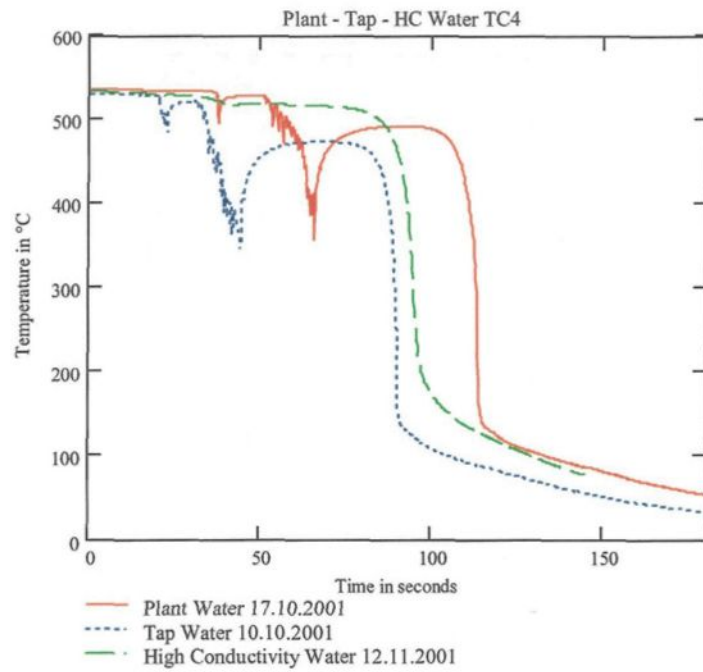


Figure 6.12: Temperature curves on machined ingot at position TC4

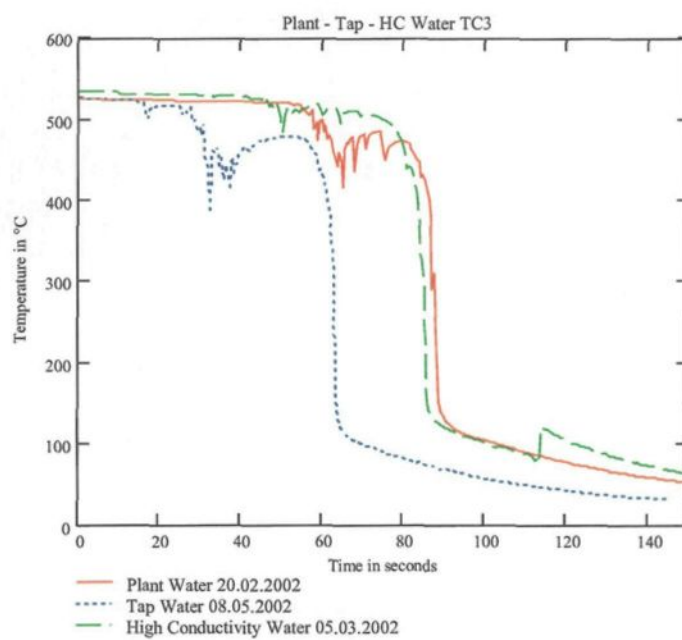


Figure 6.13: Temperature history on a rough ingot at position TC3

the impingement point. However, as we have seen in previously presented graphs using high conductivity water causes less fluctuations during the cooling and the data is smooth. This is also reflected in the heat flux to temperature curves (see Figure 6.14). In Figure

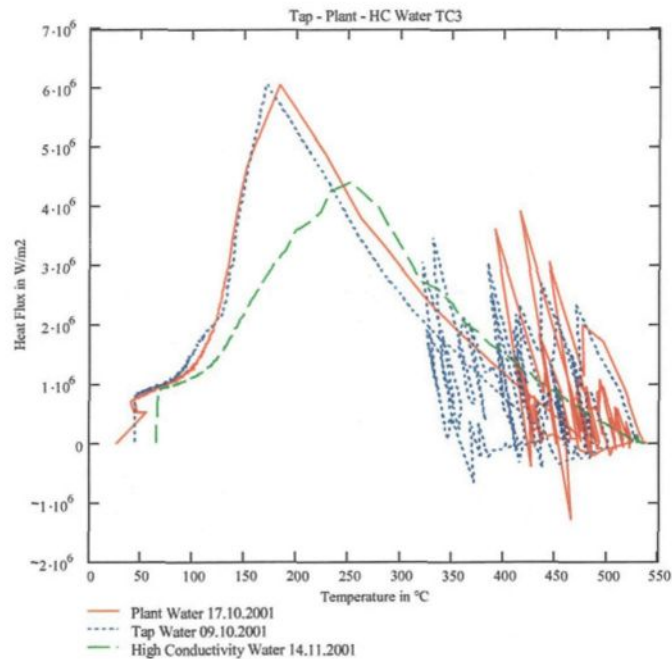


Figure 6.14: Heat flux to temperature graph on machined ingot at position TC3

6.14 it can be seen that the peak observed in heat flux using the high conductivity water is smaller than the other types of water. This is due to an accumulation of a scale layer at the surface, as the high conductivity tests on the machined ingot were conducted last. After we have recognized the influence of the scale layer we tried to suppress the accumulating scale layer by applying a weak phosphoric acid to the surface after each test (see Subsection 6.7.2). Then we repeated the tests using the high conductivity water with the cleaned ingot surface. Taking a look on the heat flux vs temperature graph for the rough ingot we can

not confirm a decrease in the maximal heat flux using high conductivity water (see Figure 6.15). The test using high conductivity water was carried out directly after the test using

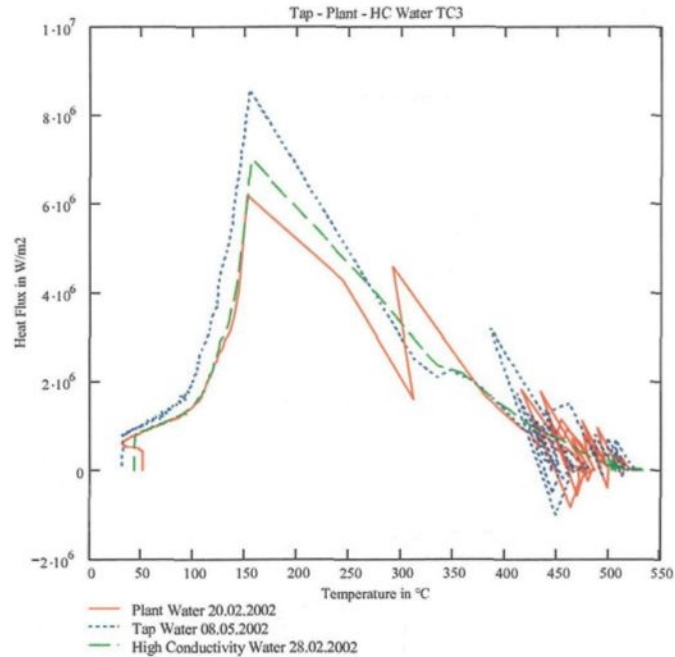


Figure 6.15: Heat flux to temperature result on rough ingot at TC3

plant water, therefore, the surface should not have changed much.

### 6.3 Water with Additives

The investigation of the effects of water additives added into the cooling water was not finished when this thesis was written. In addition, a broken heater element delayed the experiments using water additives and water with oil. Nevertheless, the effect of three water additives and a water-oil mixture on the cooling rate were investigated.

### 6.3.1 Biodispersant

The biodispersant water additive was delivered by the company BetzDearborn. This product is a water-based deposit control agent. The mixture ratio suggested by the company was  $10 \frac{\text{mg}}{\text{l}}$  and  $100 \frac{\text{mg}}{\text{l}}$ . Unfortunately the quantity we received was not enough to perform the test with both concentrations. Therefore the results presented below were obtained with a solution of  $10 \frac{\text{mg}}{\text{l}}$ . Between the tests the surface of the ingot was cleaned with a one percent phosphoric acid ( $H_3PO_4$ ). In Figure 6.16 and Figure 6.17 two representative measurement results are shown. These figures show the differences observed in

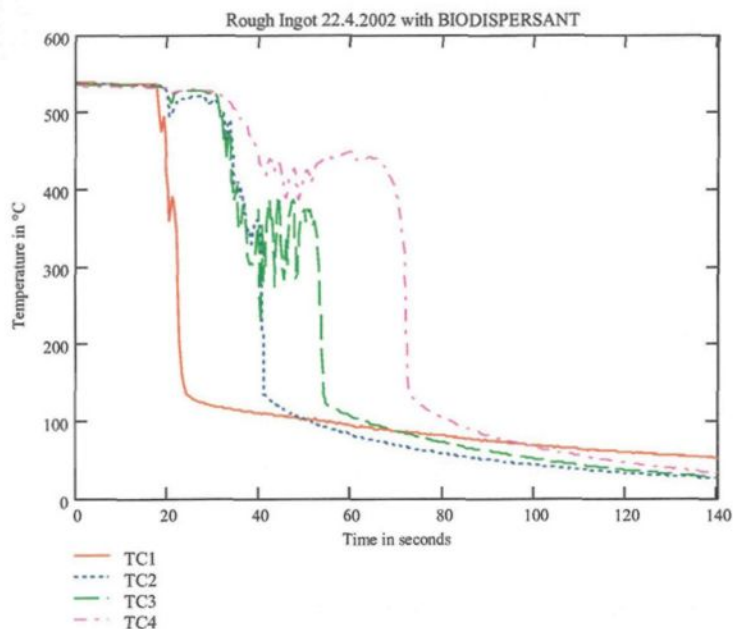


Figure 6.16: Surface temperature results from 22.04.2002 made with BIODISPERSANT

the measurements with and without biodispersant using tap water at measurement point TC3 after the first temperature decrease. Once the main temperature fall occurs at mea-

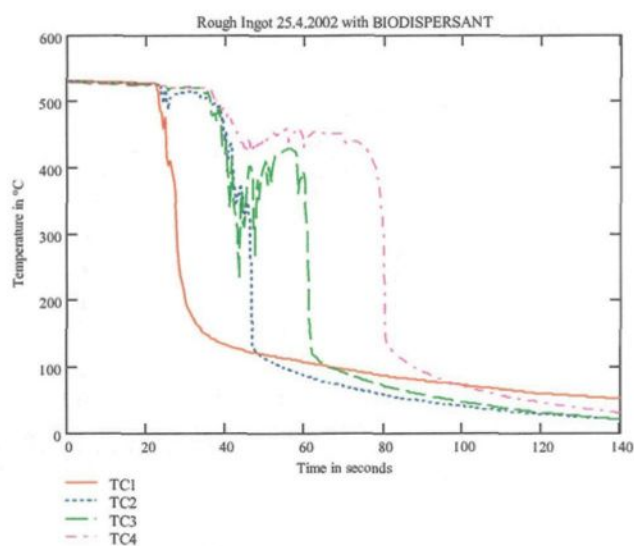


Figure 6.17: Surface temperature measurements from 25.04.2002 made with BIODISPERSANT on a rough ingot

surement point TC2 the temperature at TC3 fluctuates around  $350\text{ }^{\circ}\text{C}$ . This behavior was already observed in the experiment with tap water without biodispersant (see Figure 6.18) but the fluctuations were around  $460\text{ }^{\circ}\text{C}$ . Of course there are also some differences at the other measurement points. However, a difference between the tap water and the water with the biodispersant agent can only be shown at measurement point TC3. It can be seen in the heat flux to temperature graphs how far the fluctuations are similar at all measurement points. In Figures 6.19, 6.20, 6.21 and 6.22, the results of the tap water experiments are compared with those of two biodispersant water tests at the measurement points TC1, TC2, TC3 and TC4, respectively. If these figures are compared we can only find a distinct difference between the two water types at measurement position TC3. The rest of the heat flux results are quite similar. To explain why there is a difference only at the position TC3 we must understand the cooling mechanism at the surface. We will explain the actual hy-

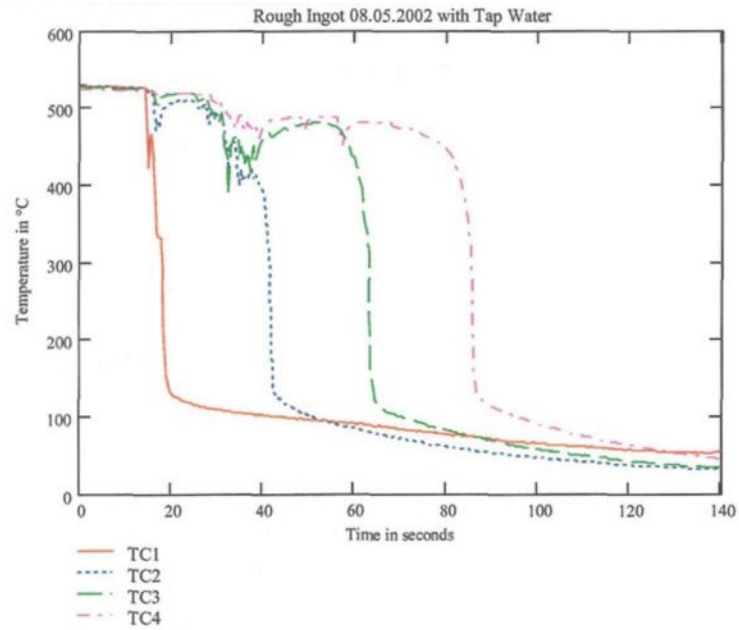


Figure 6.18: Experiment with tap water on the same rough ingot as for the biodispersant tests

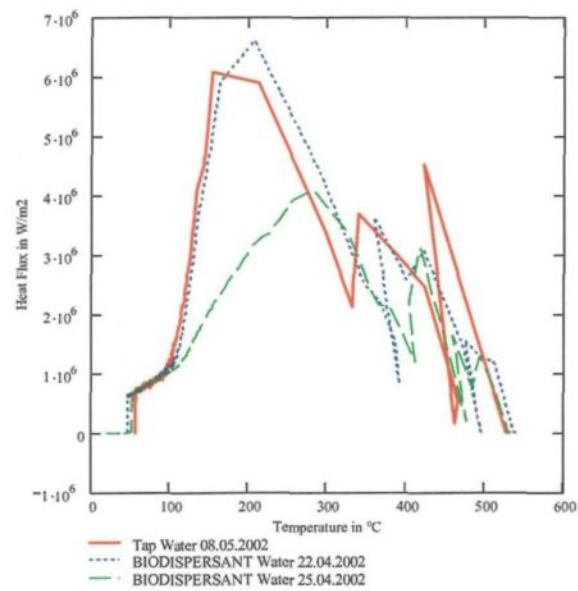


Figure 6.19: Comparison of heat flux measured using tap and biodispersant water at position TC3

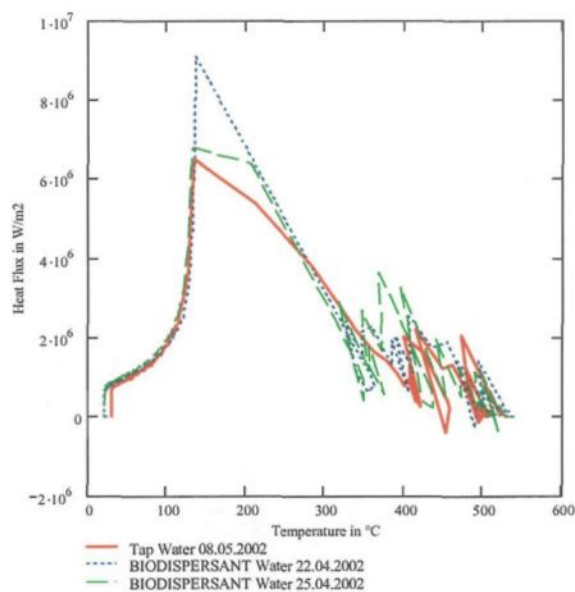


Figure 6.20: Comparison of heat flux measured using tap and biodispersant water at position TC2

pothesis in the next chapter. Here only the observations will be stated. It was also observed that the biodispersant agent caused a light foam development in the cooling water.

### 6.3.2 Surfactant

The surfactant is a liquid cleaner additive from BetzDearborn. The suggested mixture ratio was  $50 \frac{\text{mg}}{\text{l}}$  and  $250 \frac{\text{mg}}{\text{l}}$ . After two tests with the surfactant additive on the rough ingot (PL 2) we had to change the ingot because of its strong deformation. Before continuing the experiments with the additive a reference test with tap water was conducted using new rough surface ingot (PL 3). After this reference measurement we made one test using  $50 \frac{\text{mg}}{\text{l}}$  surfactant liquid and another test using  $250 \frac{\text{mg}}{\text{l}}$  of the additive. We have seen that the result depends on the ingot surface. Therefore we will compare only the test

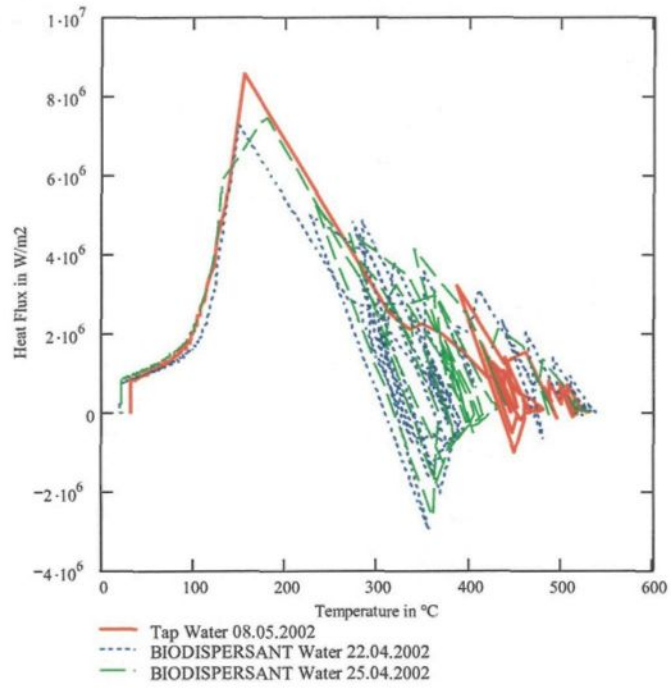


Figure 6.21: Comparison of heat flux measured using tap and biodispersant water at position TC3

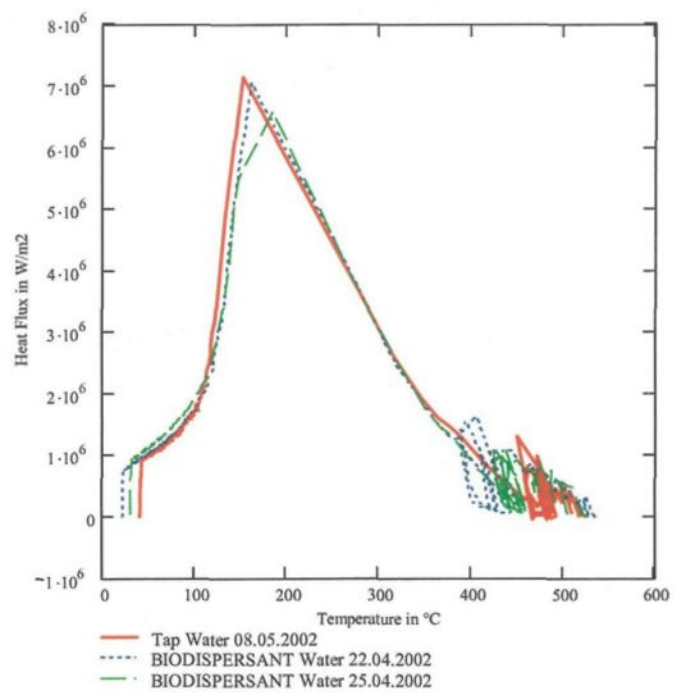


Figure 6.22: Comparison of heat flux measured using tap and biodispersant water at position TC4

conducted on the same ingot. The reference measurement with tap water on the rough surface ingot PL 2 is already shown in Figure 6.18. We will compare this result with the temperature cooling curves shown in Figures 6.23 and 6.24. The two tests were carried out at a concentration of  $50 \frac{\text{mg}}{\text{l}}$  surfactant in the cooling water. Comparing the tap water

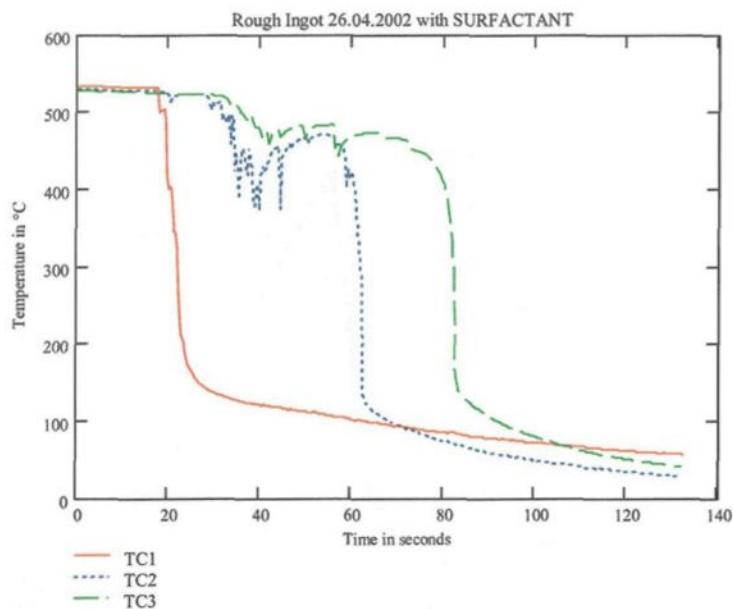


Figure 6.23: Cooling curves on the 26.04.2002 with 50 mg/l surfactant

results with the surfactant temperature curves we do not see a significant difference. The fact that there seems to be no difference between the tap water and the surfactant tests can be further supported by the heat flux vs temperature graphs. In Figures 6.25, 6.26 and 6.27 the results of tap water experiments are compared with that of two surfactant water tests at the measurement points TC1, TC3 and TC4, respectively. We will now present the results obtained from the other rough surface ingot (PL 3). The reference test on the plate PL 3 with tap water is shown in Figure 6.28. The temperatures measured using  $50 \frac{\text{mg}}{\text{l}}$

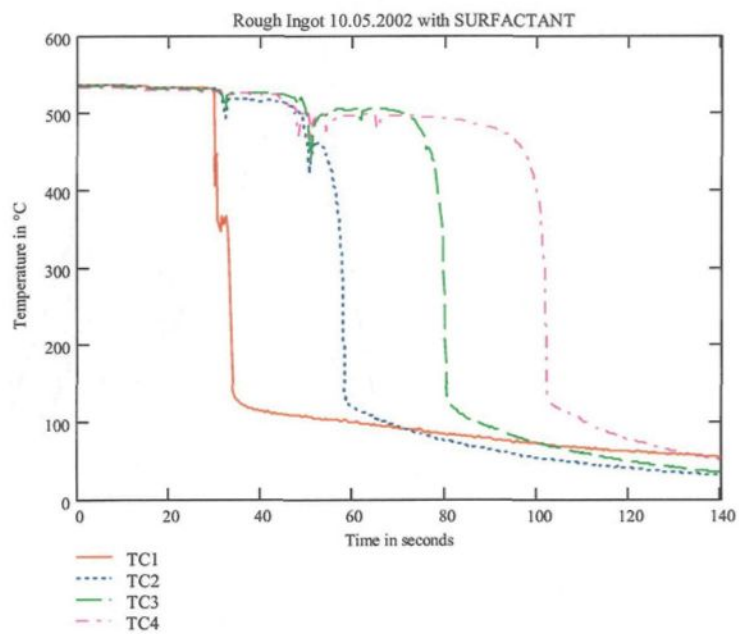


Figure 6.24: Cooling curves on the 10.05.2002 with 50 mg/l surfactant

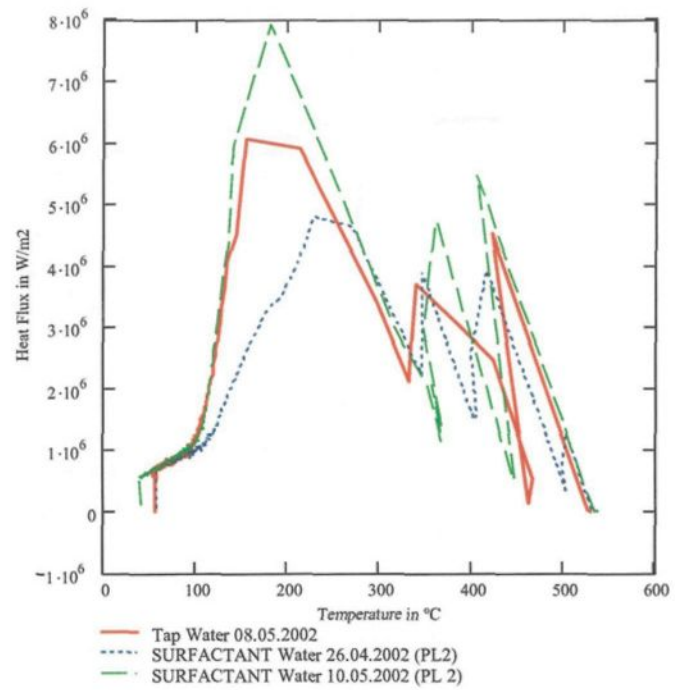


Figure 6.25: Heat flux comparison between tap and surfactant water at position TC1

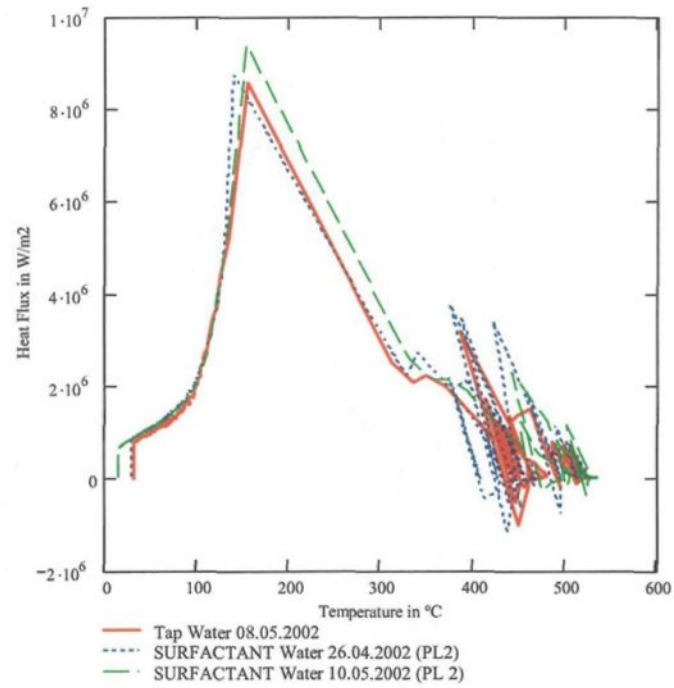


Figure 6.26: Heat flux comparison between tap and surfactant water at position TC3

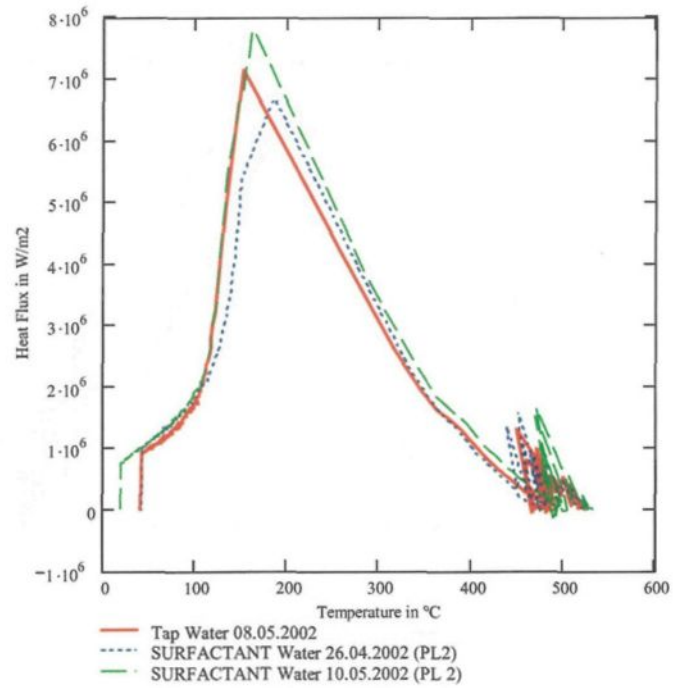


Figure 6.27: Heat flux comparison between tap and surfactant water at position TC4

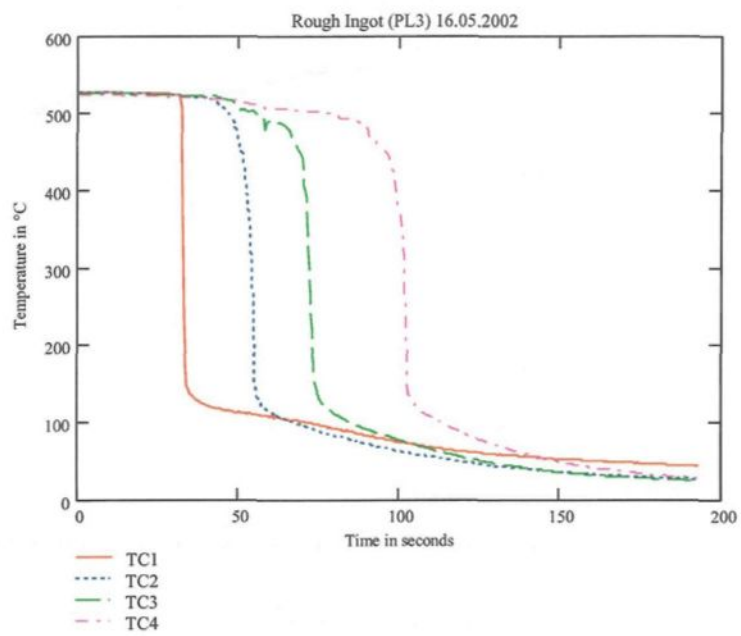


Figure 6.28: Reference test with tap water on the rough surface ingot PL 3

surfactant on the plate PL 3 are shown in Figure 6.29. As we have already seen from the

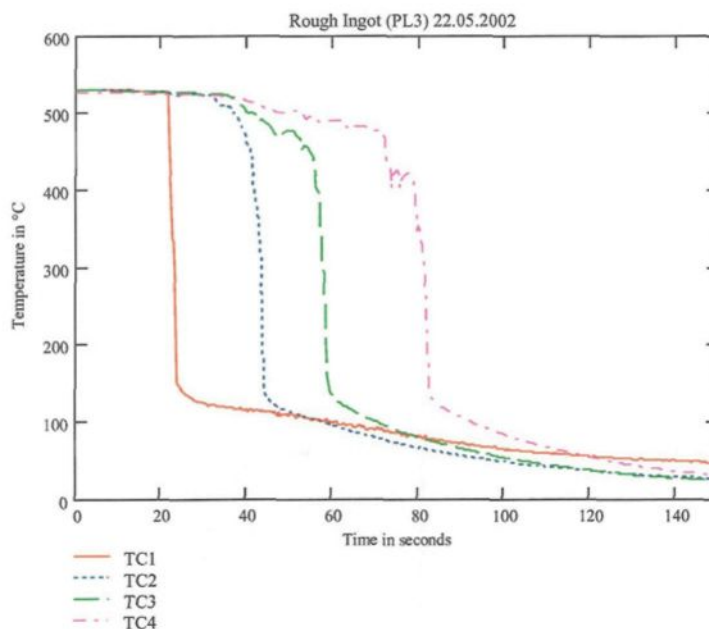


Figure 6.29: Test on the 22.05.2002 made on plate PL 3 with 50 mg/l Solve CA

comparison of the results using the plate PL 2, there is no obvious difference between the results using tap water and the water with surfactant. Thus we can conclude that there is no difference in cooling when tap water or the water with  $50 \frac{\text{mg}}{\text{l}}$  surfactant are used. In the experiment on the 23.05.2002 we used a surfactant concentration of  $250 \frac{\text{mg}}{\text{l}}$ . The temperature curves of this experiment are shown in Figure 6.30. We can see in this figure that only the temperature measurement at the position TC1 has a sharp distinct drop. The other cooling curves show a slower cooling. This tendency was not observed in the tap water experiments. Furthermore we have several strong fluctuations during the fast dropping part of the cooling. All these characteristics are new. The cooling rate is lower, that is the change in temperature per time is less pronounced when tap water is used compared to those when

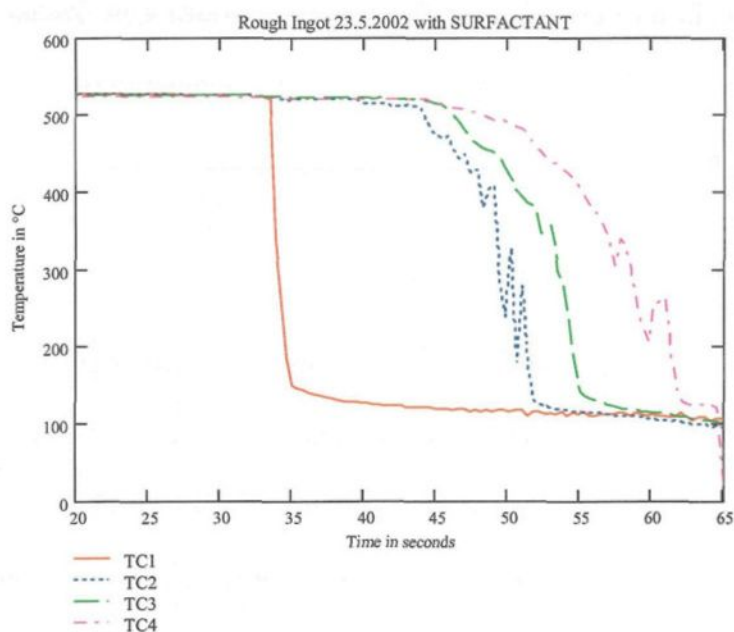


Figure 6.30: Test made on the 23.05.2002 with 250 mg/l surfactant on rough surface ingot PL 3

surfactant is used. On the other hand the total cooling time is shorter with surfactant compared to the experiments where only tap water is used. Generally, cooling takes about 65 seconds ( $\pm 5$  s) when tap water is used. As it is shown in Figure 6.30, the duration from the first drop at TC 1 to the last temperature drop under 150 °C is about 30 seconds when surfactant is used. Thus the total cooling time is less than the half of the cooling time using only tap water. Unfortunately the surfactant sample we received from BetzDearborn was finished after the first test using 250  $\frac{\text{mg}}{\text{l}}$ . It would be necessary to repeat the test with the higher concentration of surfactant to see if this result is reliable. This effect might be due to the change of the surface tension of the cooling water. The surface tension influences the formation of the stable and unstable vapor film. It also has an effect on the separating water jets and droplets which may be in turn responsible for the slope in the temperature

curves. Due to the fact that the surfactant additive works like a detergent, the formation of a foam might cause slower decrease in the temperature curves. Further explanations are given in the next chapter.

### 6.3.3 Water-Oil Mixture

The water-oil mixture was delivered by the company Alcoa in Baie-Comeau. The mixture was ready to use. The water-oil mixture was mixed by the pump before each test to obtain a uniform dispersion of the oil droplets in the water. Due to the delay caused by the broken heater elements the experiments started later than planned. Three experiments were successfully completed. It was observed that the color of the water-oil mixture changed after each test. Especially after the first test the water color changed from deep dark black into light brown. The water samples taken must be analysed. Although we do not know precisely the composition of the water-oil sample, non-negligible quantity of solid particle were visually observed. After about a week of storage, the solid content sedimented on the bottom of the container and the bulk of the water became transparent. In Figure 6.31, the reference measurement with tap water on the rough surface ingot (PL3) is shown. The temperature cooling curves obtained with the water oil mixtures are shown in Figures 6.32, 6.33 and 6.34.

If we compare the measurements using oil-water with the reference measurement in Figure 6.31 there is almost no difference. The water-oil mixture result has more fluctuations before the main temperature drop occurs at the measurement position TC3. We observed the bigger change in color of the water-oil mixture between the first and second test, although there is no difference in the temperature measurements between the first test

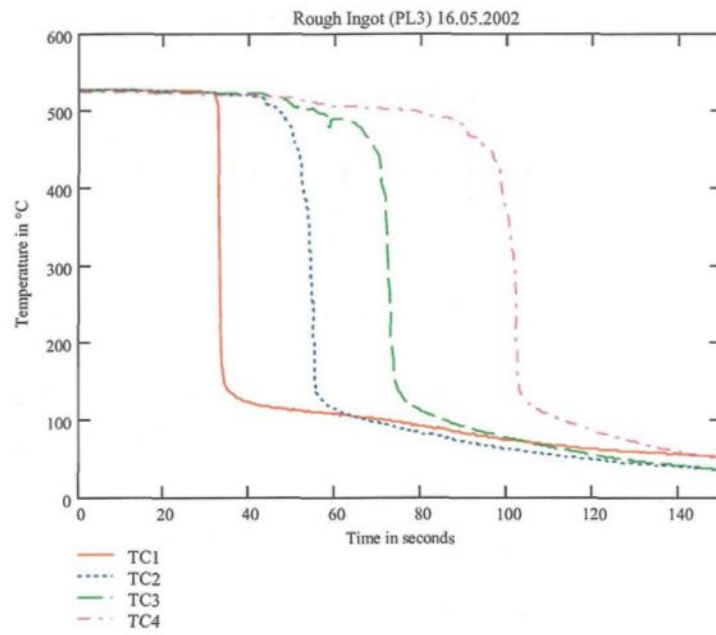


Figure 6.31: Reference measurement on a rough surface ingot (PL3) with tap water

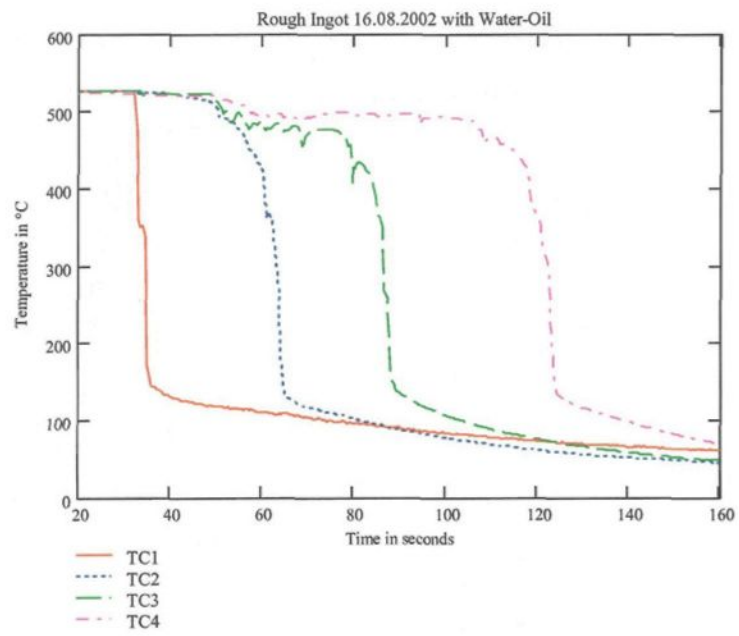


Figure 6.32: Water-oil mixture on a rough surface ingot (PL3) on the 16.08.2002

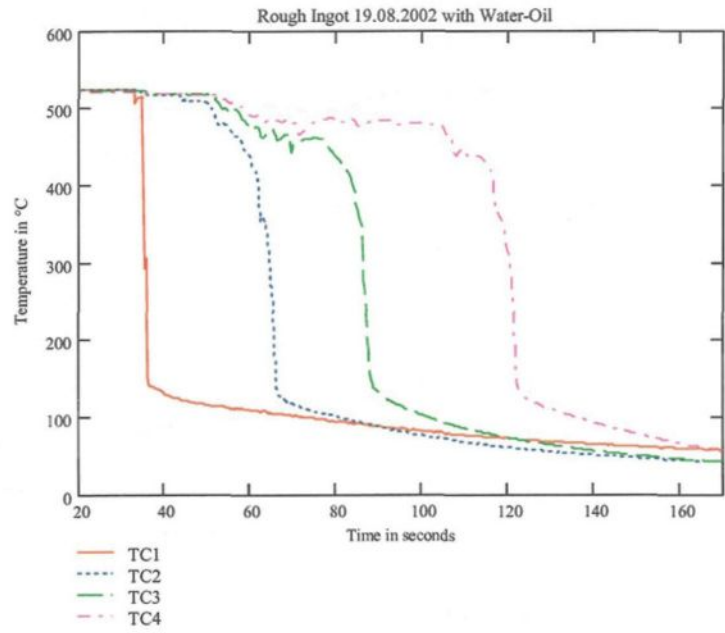


Figure 6.33: Water-oil mixture on a rough surface ingot (PL3) on the 19.08.2002

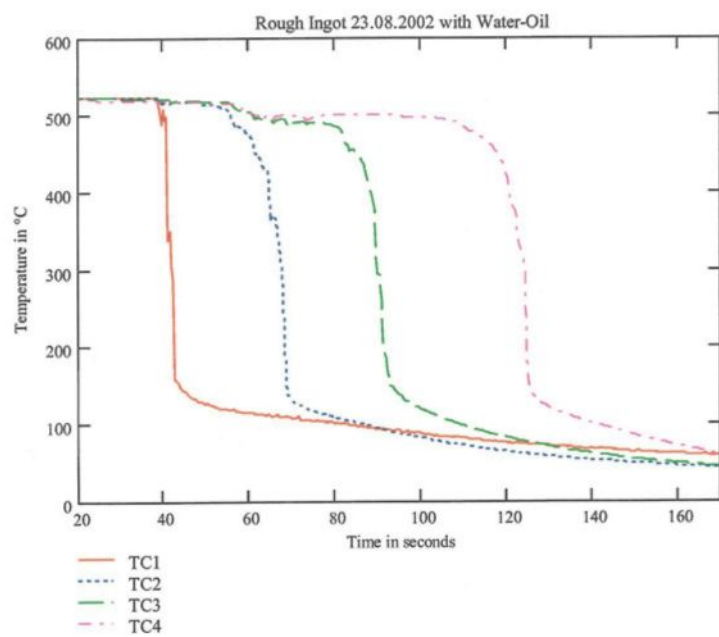


Figure 6.34: Water-oil mixture on a rough surface ingot (PL3) on the 23.08.2002

(see Figure 6.32) and the second test (see Figure 6.33). This indicates a good repeatability of the water-oil experiments. The only difference between the tap water experiment and water-oil mixture test is a short temperature relapse which occurs during the main temperature drop. This relapse can be best seen in the heat flux graphs. If we compare the graph in Figure 6.35 with the one in Figure 6.36 we will recognize that there is a peak in front of the main peak in the water-oil heat flux results. This peak corresponds to the temperature

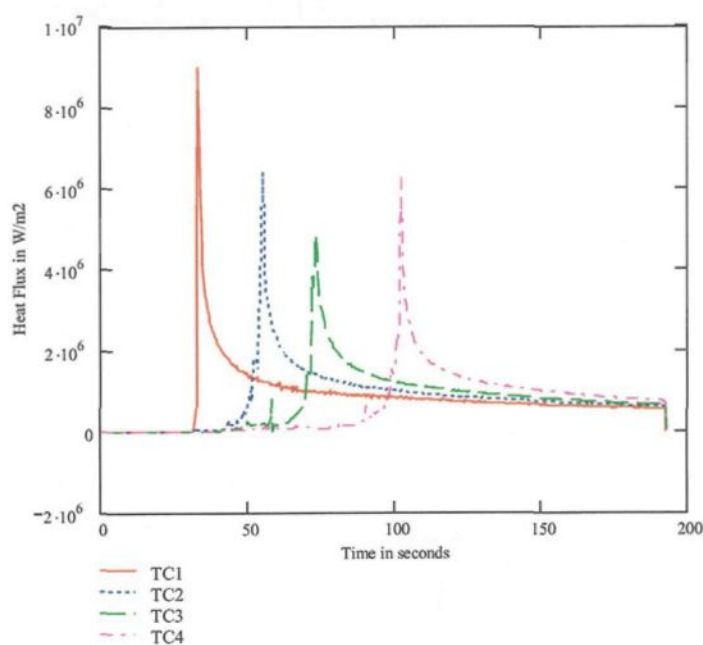


Figure 6.35: Heat flux vs time data using tap water on rough surface ingot (PL3) on the 16.05.2002

relapse in the cooling curve. This temperature relapse is magnified for the measurement positions TC1 and TC2 shown in Figure 6.37. These temperature relapses are not specific to the cooling curves conducted with a water-oil mixture. They were already observed in tests with tap, plant and high conductivity waters too. The comparison of the heat flux vs temperature data of tap water experiment with that of the water-oil mixture experiment

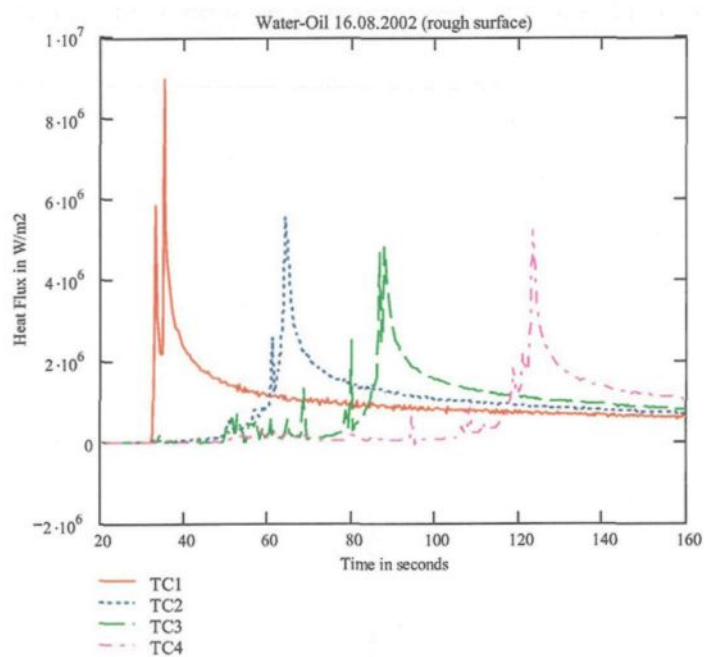


Figure 6.36: Heat flux vs time data using a water-oil mixture on a rough surface ingot (PL3) on the 16.08.2002

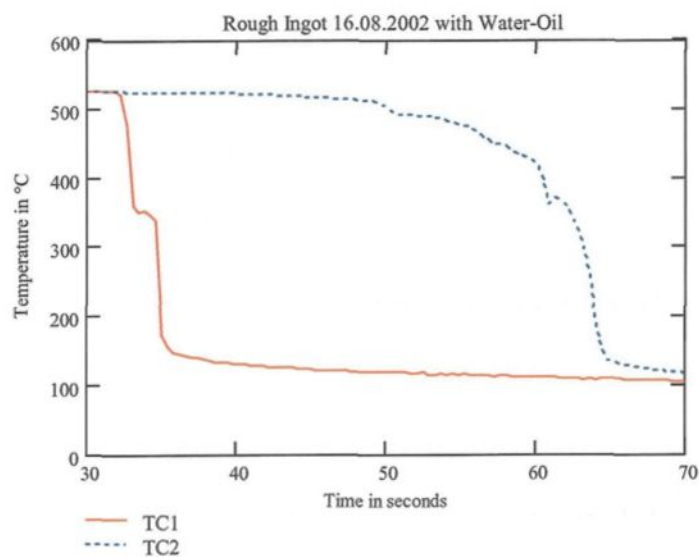


Figure 6.37: Temperature relapse during the water-oil mixture cooling

is shown in Figure 6.38. Since there is no significant difference between the results using

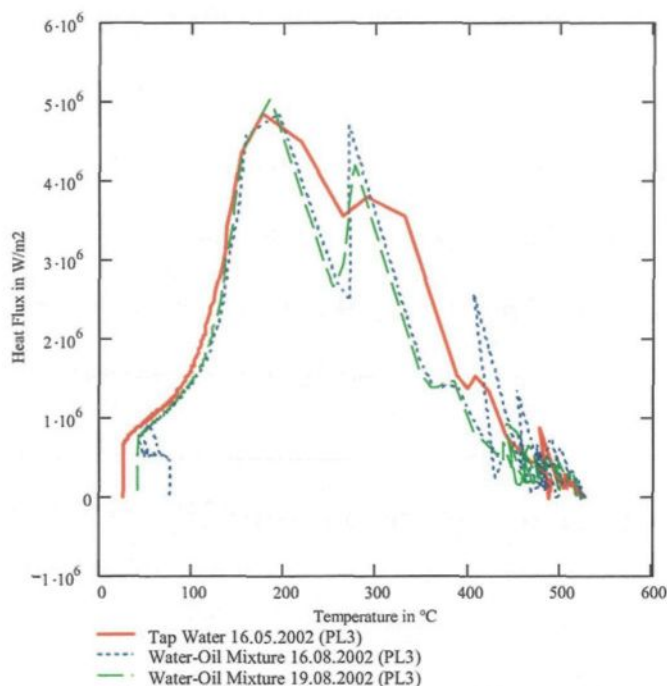


Figure 6.38: Difference between tap water and water-oil mixture

tap water or oil-water mixture as shown in this figure, we can conclude that there is no significant difference between the cooling curves obtained by a water-oil mixture and tap water. We must emphasize that the conclusion about the negligible influence of the oil holds only for oil-water mixture investigated which came from the Baie Coumeau plant.

## 6.4 Mechanism of Cooling

The surface cooling mechanism is one of the most important phenomena that has to be understood. It is the basis of the different characteristics observed in the cooling

curves. The cooling mechanism was investigated using experimental temperature vs time data and the visualization of experiments. Their synchronization allowed us to analyze the boiling phenomena at the surface. However, it is very difficult to visualise boiling processes at the ingot surface. Due to the long preparation time of each experiment, we could not try a large number of parameter variations as necessary. The explications given in the following are based on our observations and measurement data. As they are, we have to treat them as hypothesis, which need further investigation and validation.

## 6.5 Structure of the Falling Water Film

The formation of the water film during the cooling is dominated by the free fall of the water, the adhesion of the water to the surface and the different boiling regimes on the ingot surface. There are several stages of the formation of the water film. As soon as the pump is started, water droplets and non continuous water jets are ejected from the mould nozzles. In the first instant when the first water droplets hit the hot aluminium surface a phenomenon similar to the Leidenfrost effect is observed. The water touches the surface and evaporates instantly. The developed vapor film repels the water droplets (see Figure 6.39). This phenomenon is not exactly identical to the classical Leidenfrost effect because the water droplet is not floating on the vapor film. We estimate that once the water touches the surface the evaporation pushes away the water droplet so that the droplet falls down along the surface. The Figure 6.40 represents this phenomenon at earlier times in the regions close to the impingement zone. A few milliseconds later, a stable water jet forms and leaves the mould nozzle. Then the similar phenomenon takes place for the entire water film

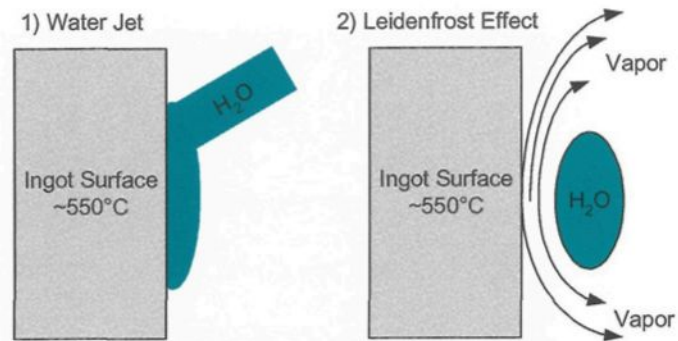


Figure 6.39: Vertical Leidenfrost effect

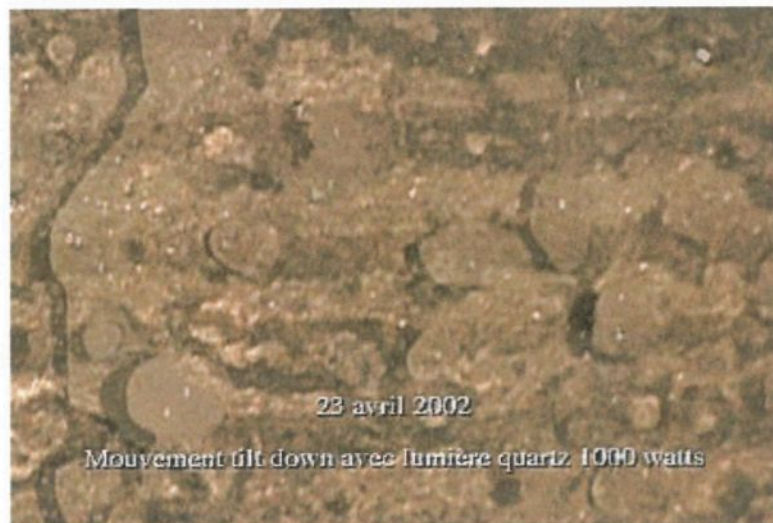


Figure 6.40: Droplet separation from the surface

instead of a droplet. The film is separated from the plate surface due to the evaporation for a very short time (less than 0.5 seconds). This is shown in Figure 6.41. Starting from the

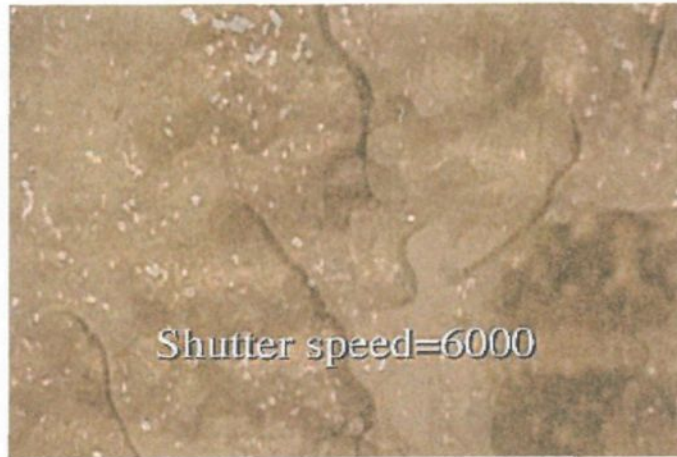


Figure 6.41: Separated water film

point where the water touches the surface (the impingement zone) four zones are observed along the ingot (see Figure 6.42).

### 6.5.1 Three Dimensional Surface Water Flow

It has to be clear at this point that the cooling water film cannot be treated as a two-dimensional structure, transitionally symmetric in the horizontal direction. It has a complex flow in three dimensions along the surface of the ingot. The profile denoted in Figure 6.42 imparts only an idea of the phenomena that takes place. In addition, the zone partition changes during the cooling as it will be explained later. First we want to give a general description of the structure of the flow. The three dimensional character of the flow influences also the temperature measurements. In Figure 6.43 we see the formation of

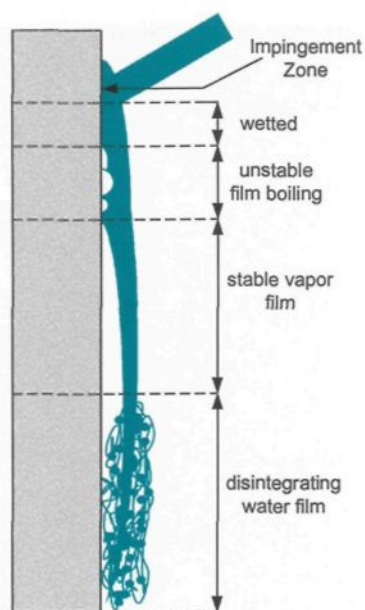


Figure 6.42: Four zones along the ingot

"individual" water jets from the water film. We can see that there are regions where there are water jets and others where there is no water. The jets will continuously change place until they disappear. There is a droplet separation from these jets. The individual jets as well as the droplets can touch the surface. This leads to a fluctuation in the surface cooling which is different for each experiment. But even when a closed, continuous water film has established, this film randomly touches the surface and causes surface heat flux fluctuations. In Figure 6.44 we see a wavy water film indicated by the different colors of the water. At several places this film may touch the ingot surface although the re-wetting zone is much higher (see Figure 6.45). Due to the fact that this is a random process the experimental results are never entirely identical the different zones observed on the surface of the hot ingot when there is a water jet hitting its surface will be explained in the following sections.



Figure 6.43: Separating water jets



Figure 6.44: Wavy water film at the surface

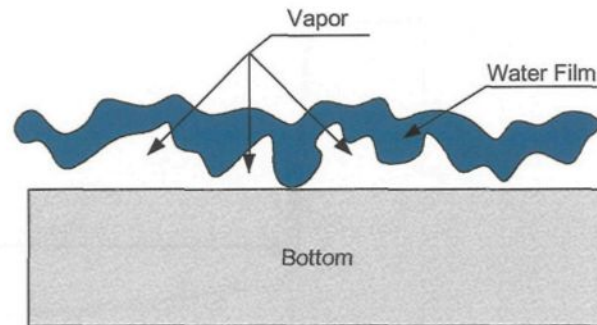


Figure 6.45: Wavy surface water film (horizontal section)

### 6.5.2 Wetted Zone

The wetted zone is the region where the water attached to the surface due to adhesive forces. The temperature in this zone is not high enough to develop a surface boiling. The length of this zone increases with the descending re-wetting zone or unstable film boiling zone. At this stage, we cannot define exactly at which instant of the cooling curve the wetted zone starts. We assume the start of the wetted zone is around  $100\text{ }^{\circ}\text{C}$  then the cooling taking place cause a linear decrease in the temperature until the end of the process. This zone is shown in Figure 6.46.

### 6.5.3 Unstable Film Boiling

Directly below the wetted zone the unstable film boiling zone is observed. This zone is also known as re-wetting zone. The unstable film boiling means that the water touches the hot surface at where it evaporates. The vapor pushes away the water for some

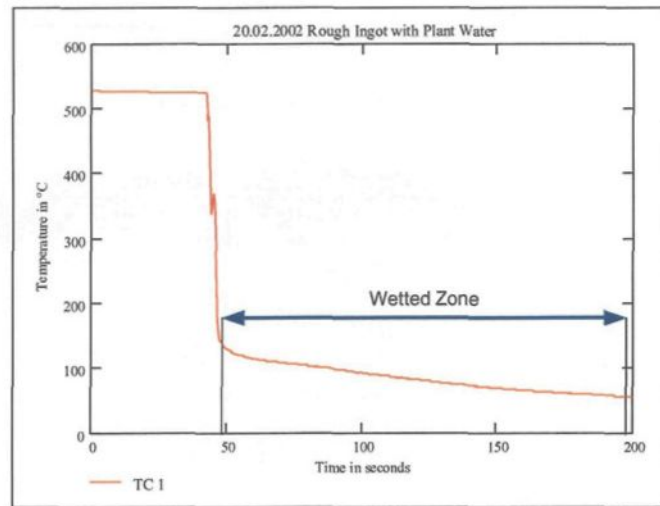


Figure 6.46: Estimated wetted zone borders

milliseconds and then the water film contacts the surface again. Causing fluctuations, this zone is quite small. As observed during the visualization the unstable film boiling zone is about 2 mm long. Sometimes the fluctuations of this zone are less and the temperature measurements do not show any fluctuations.

#### 6.5.4 Stable Vapor Film

The stable vapor film zone is the region where there is enough vapor which can separate the water film from the surface. We assume that one part of the vapor comes from the unstable film boiling zone. Then, this vapor is pushed downwards by the water film and forms an insulating vapor cushion. The main part of the vapor in the insulating cushion was evaporated from the liquid film covering the vapor layer. The heat radiation emitted from the hot surface passes through the vapor layer and provokes evaporation in the vicinity of the continuous water film (see Figure 6.47).

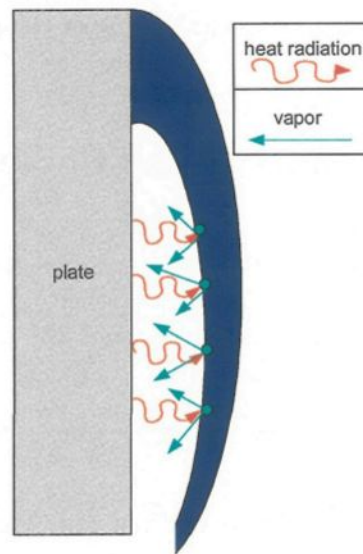


Figure 6.47: Heat radiation causes evaporation of the covering water film

### 6.5.5 Disintegrating Water Jet

The water film separated from the vapor cushion falls down along the ingot. If the re-wetting zone is high enough which means that the length of fall is long enough the water film starts to separate in form of smaller jets and droplets. The water film separation is caused by three phenomena. The first one is the downwards acceleration of water. The acceleration thins the water film. The second phenomenon causing a separation is related to the viscous effects at the liquid-gas interface. The friction between the liquid and the gas generate waves. Finally, we have the tendency to minimize the surface. Minimisation of free energy the water film minimizes the surface, thus jets and droplets are formed.

The separating water jet zone is very turbulent and unstable, with random fluctuations. Thus each experiment is slightly different. Once the unstable film boiling zone

moved down approximately to the middle of the plate it disappears.

## 6.6 Characteristics of the Cooling Curves

In the previous Section we have seen the development of the cooling film during the experiment. Now we want to explain the characteristics of the temperature cooling curve which helps to identify the different zones observed on the ingot surface.

### 6.6.1 Temperature Drop before the Re-wetting Zone passed

A temperature drop is observed before the re-wetting zone passes especially for the machined ingot. However, this phenomenon is observed on the rough surface ingot as well. In Figure 6.48 a typical temperature measurement is shown. As soon as the water jet hits

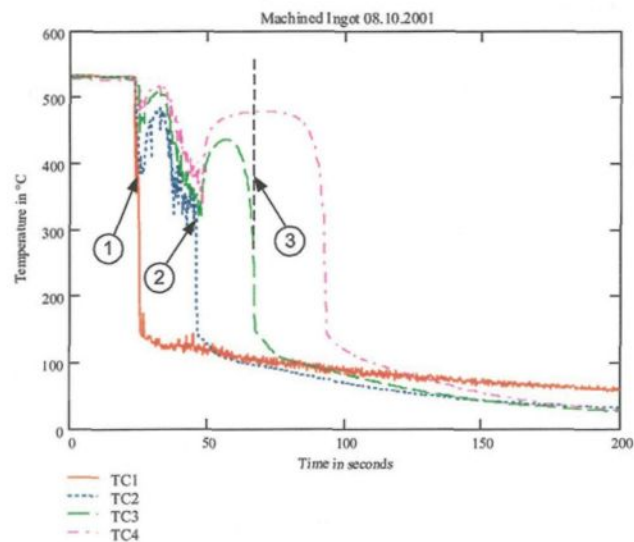


Figure 6.48: Temperature measurement on a machined ingot

the surface for the first time there is a temperature fall at measurement position TC1 but even at the measurement positions situated at lower positions a slightly less temperature decline occurs (see Point 1 in Figure 6.48). After this point the temperature increases again for a certain time before the second temperature decline takes place as shown by point 2. At point 3 (see Figure.6.48), there is no temperature decrease measured by thermocouple TC4. As observed during the visualisation of cooling, we know that when the re-wetting zone passes, the temperature drops below 200 °C. The re-wetting zone could not pass the measurement point TC4 at the same instant as it passed the measurement point TC2, as it would be the case in point 2 according to Figure 6.48. So the question is, what causes these temperature drops occurring at the same time. The answer is given by the wavy surface flow and the water jets and droplets from the cooling film. At the beginning of the cooling the re-wetting zone is at the upper part of the ingot. As the continuous water film separated by the vapor layer it starts splitting up into several water jets and droplets (see Figure 6.43). These jets and droplets fall down on the ingot and touch randomly the surface. The heat extraction capacities of the water droplets and water jets touching the surface for a very short time are not high enough to decrease the temperature below 200 °C. The point where the water cooled partially the surface is heated up again by conduction from the backside and the sides of the ingot. Therefore the temperature increases again. We assume that not only the separating jets and droplets are responsible for the fluctuations before the re-wetting zone passes. Another mechanism that may cause the fluctuations is the wavy behavior of the water film. As already indicated in Figure 6.45 the continuous water film can touch the surface although there is a vapor film between surface and cooling water film.

In Figure 6.49 a photo of the water film is shown. Inside the red bordered parts the color of the water film is very different from the outside area shown in red. The difference in color indicate the wavy character of the water film. In this wavy zone, the water film can

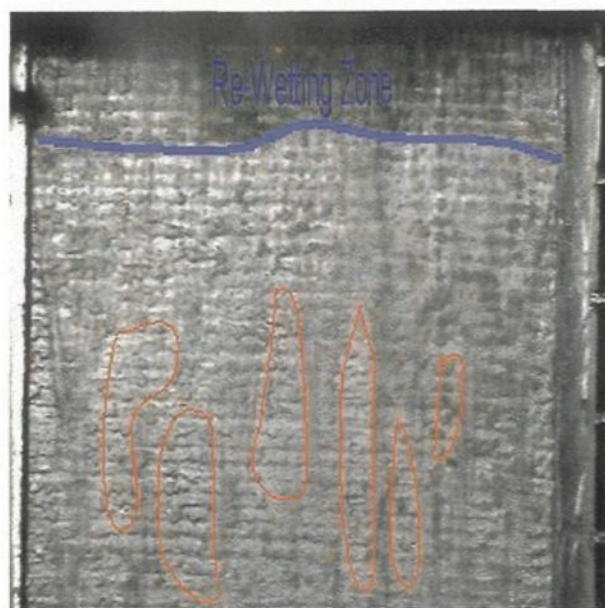


Figure 6.49: Water film touches the surface due to its wavy setup

touch the surface randomly. A second fact becomes visible having a closer look on the photo presented before (see Figure 6.49). We can see that there are no red bordered areas close to the re-wetting zone. Thus we have a quite stable vapor film close to the re-wetting zone. This stable film is also the reason why there is no temperature drop at point 3 in Figure 6.48. Once the re-wetting zone passed approximately the middle of the plate the film does not separate into jets and droplets anymore. The wavy behavior also disappears if the cooling water film is short enough. In that case, the measurement points are situated under a stable liquid film which is insulated by a vapor cushion from the surface (see Figure 6.50).

Before the re-wetting zone reaches the measurement points the temperature increases due

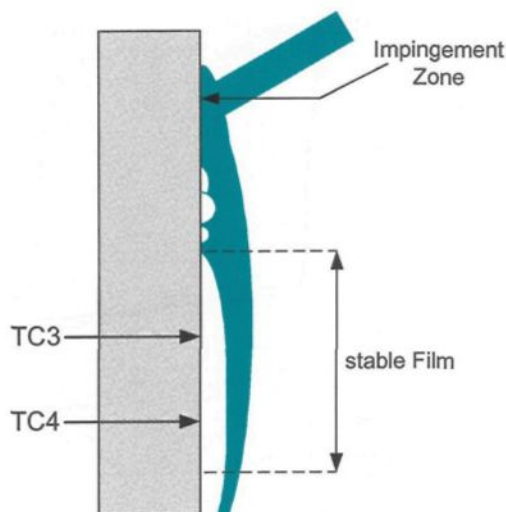


Figure 6.50: Stable cooling film

to the conduction by the sides and the backside.

The cooling curve shown in Figure 6.48 was obtained using a machined ingot. The same effect, only less distinct can be observed on a rough surface ingot as well. In Figure 6.51 we see the measurement results using a rough surface plate and tap water. Here we can even recognize several drops in the signal of TC4 before the re-wetting zone passed the measurement position TC3. On the other hand there are also experiments with the same setup which are not affected by the water cooling film separation in jets and droplets. Sometimes there is only one measurement point touched by the separated turbulent water jets. Due to the turbulent nature of this water jets and their unpredictable formation, the experimental results can vary significantly even if they are carried out under the same experimental conditions.

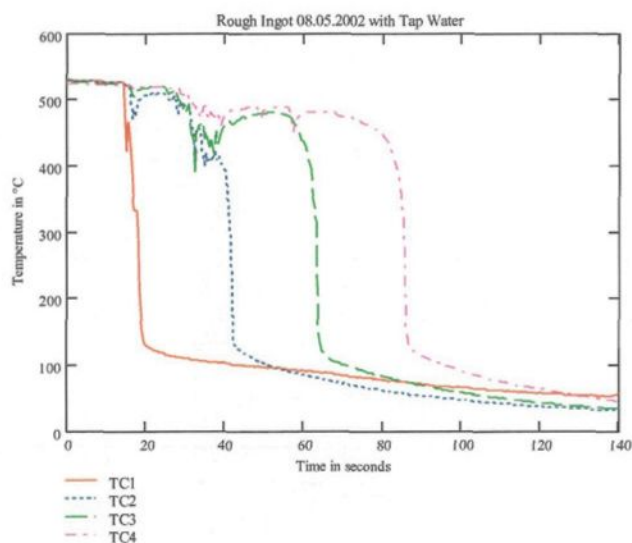


Figure 6.51: Less distinct behavior on a rough ingot

### 6.6.2 The Positioning of the Measurement Points Along a Rough Surface

In the cooling curves of the rough ingot experiments we observed a temperature relapse at certain measurement points. Figure 6.52 show a temperature measurement result on a rough ingot with plant water for TC1. At the points 1 and 2 -which are marked with a circle- we can see a temperature relapse, seen as an increase of the temperature for a short time before it continues to fall. The relapse is especially observed for the first measurement position TC1. Sometimes the temperature relapse occurs also at the position TC2. We assume the temperature relapse is caused by a vapor bubble or a vapor layer that was formed under the water film and collapsed immediately. Thus we assume that the characteristics of the surface around these measurement positions are responsible for such a behavior. To investigate the relapse more in detail we took pictures of the surface structure at the measurement positions for two different plates on which this effect is present. The

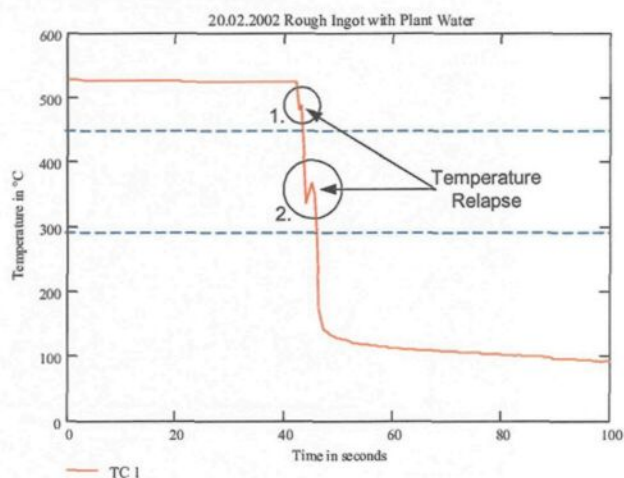


Figure 6.52: Temperature relapse during the main cooling fall

pictures are shown in Figures 6.53 and 6.54. It can be seen that one measurement point is below a dent (plate B, see Figure 6.54) and the other is not (plate A, see Figure 6.53). Thus, the dent just above the measurement position is not responsible for the temperature relapse. Although we do not have a lot of experimental results for the machined ingot at position TC1, the temperature relapse was observed on a machined ingot too. According to these observations the temperature relapse is a phenomenon which occurs independently of the surface structure and roughness. If the measurement data is studied closely it can be seen that the temperature does not fall back quickly after relapse. In Figure 6.55 a temperature measurement with a relapse was magnified. The measurement points are marked with a cross. We can see that the cooling from approximately from 520°C to 150°C takes about 4 seconds (from 42 to 46 seconds in Figure 6.55). Studying the measurement points we can say that there might be a loss of contact with the cooling water film for a fraction of a



Figure 6.53: Surface structure around the measurement point TC1 on plate A

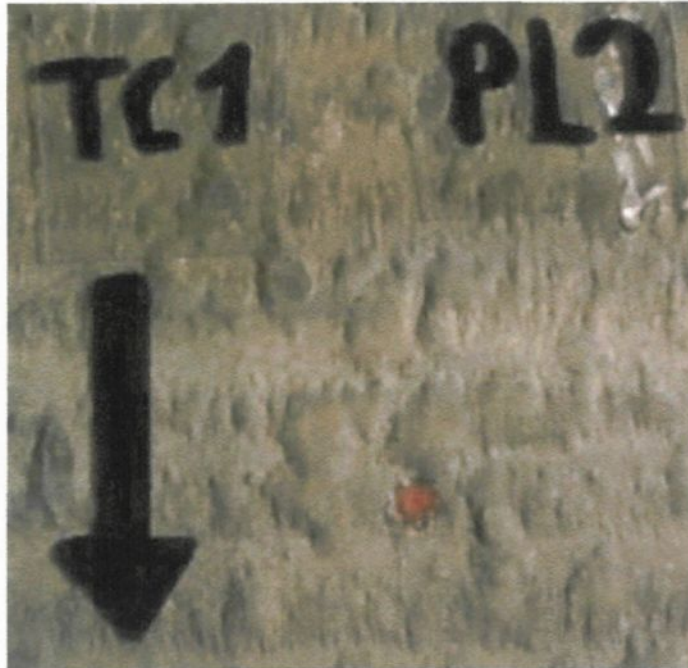


Figure 6.54: Surface structure around measurement point TC1 on plate B

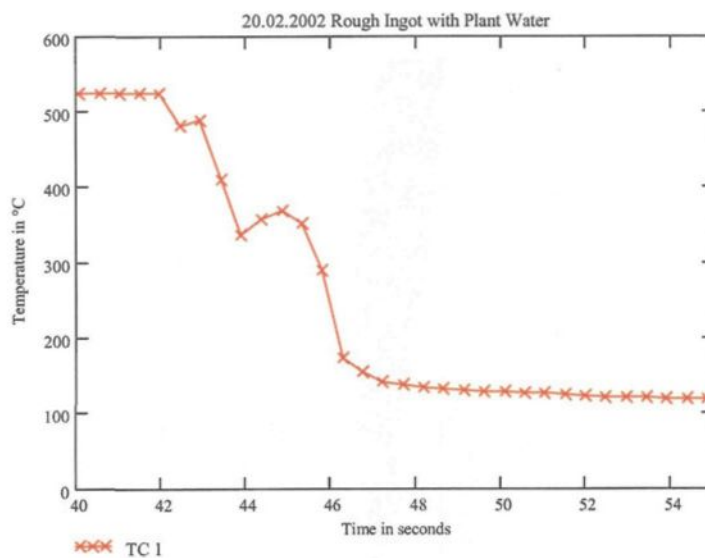


Figure 6.55: Magnified temperature relapse

second. This effect may indicate a kind of unstable film boiling. The wetted zone is pushed back by a vapor layer that is very unstable and disappearing directly as soon as it forms. In the sketch shown in Figure 6.56 this effect is demonstrated. As can be seen in Figure 6.56 A the vapor layer insulates the surface from the water film. After a fraction of a second this layer collapses (see Figure 6.56, part B.) and the cooling process continues. Comparing the temperature history from another measurement position points out the unstable character of this effect. In Figure 6.57 the temperature history from the same measurement presented in Figure 6.55 is shown at the position TC2. In this case, the temperature decrease takes longer time. The water film was touched and pushed back several times by a newly forming vapor layer. This measurement indicates a fluctuation of the insulating vapor layer.

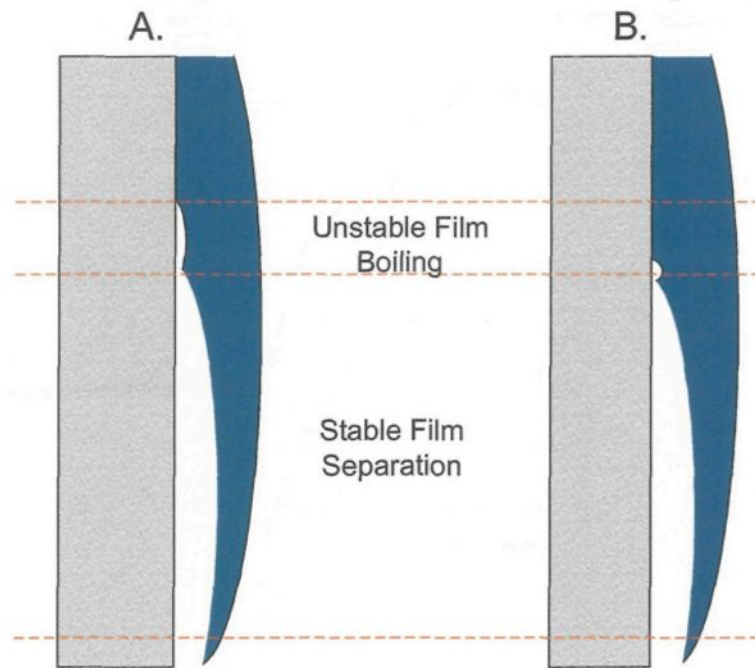


Figure 6.56: Unstable vapor layer which collapses

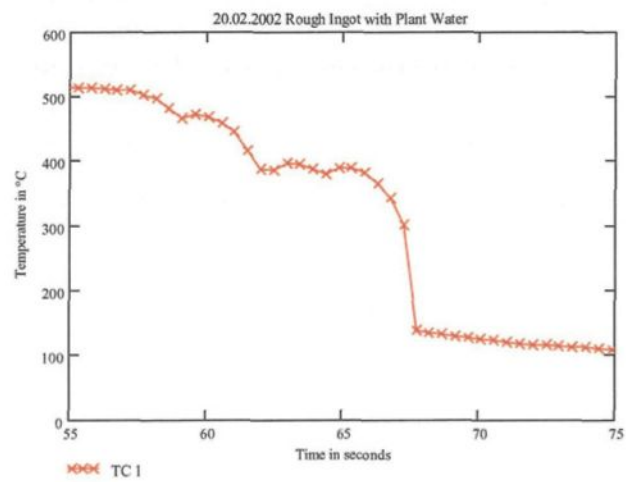


Figure 6.57: Temperature relapse at measurement position TC2

### 6.6.3 Re-wetting

We have already seen that the structure of the cooling film changes during the cooling. It was observed the shape of the re-wetting zone also changes. In Figure 6.58 we see a photo from one of the first tests with a newly installed rough surface plates. The re-wetting zone (red highlighted) is almost straight and horizontal. If we compare this photo

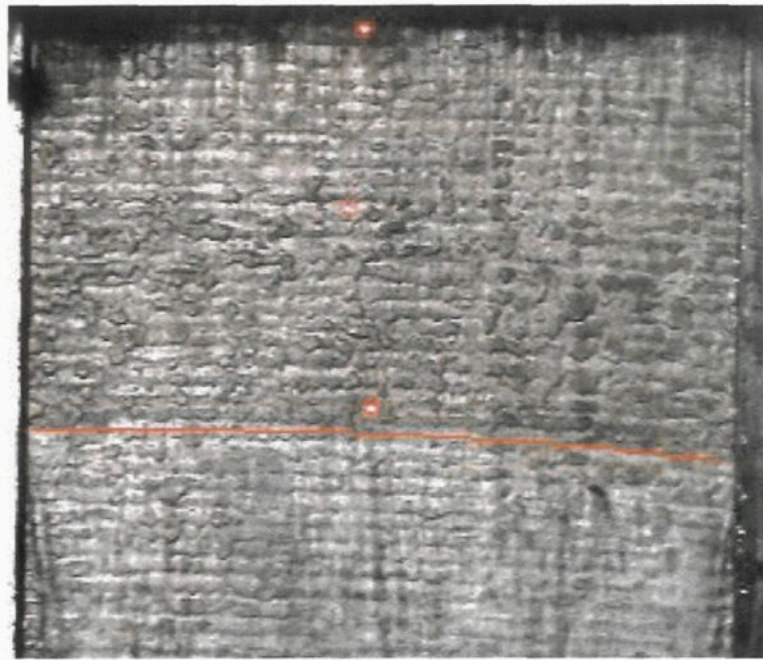


Figure 6.58: Straight re-wetting zone of test 20.02.2002 on a rough surface ingot

with another shown in Figure 6.59 we see that the shape of the re-wetting zone changed. Although in both tests tap water was used and the photos were taken at the same position<sup>1</sup> the shape is different in two cases. Unfortunately we can not say when this effect occurred the first time, because each experiment was not filmed. The re-wetting zone changed its shape after four experiments. Since then this effect is observed during each test as shown in

<sup>1</sup>Just below measurement point TC3, indicated by the red laser points in the photo.



Figure 6.59: Curved re-wetting zone of experiment 22.04.2002

Figures 6.60 and 6.59. It can be seen from these figures that the re-wetting zone is straight



Figure 6.60: Curved re-wetting zone of experiment 23.04.2002

directly after the start of the cooling. Approximately after 20 seconds the line starts to deform. In Figure 6.61 a series of photos taken during the cooling are shown. The first picture was captured 20 seconds after the pump was turned on, then at every 2nd second another one was taken. We assume that the curve in the re-wetting zone is caused by the deformation of the plate. We see a strong deformation of the plate in the part below the impingement zone. The thermal stress caused by the high temperature differences during the cooling is responsible for this deformation. In the non-cooled part there is almost no deformation. The shape of the bottom of the plate deformed and became round during



Figure 6.61: Series of pictures during the cooling from experiment 22.04.2002

the experiments (see Figure 6.62). The distance between the curved center and the sides



Figure 6.62: Photo of the plate deformation

is 8.25 mm on a total depth of 301 mm of the plate (see Figure 6.63). The deformation is decreasing in the direction of the impingement zone. The first remarkable deformation could be found directly at the impingement zone at a height of 127 mm (measured from the top of the plate). Here the deformation is still small within a range of 2.5 mm. At a height of 200 mm (measured from the top of the plate) the distance between the sides and the center is already 6 mm. This is exactly where the re-wetting zone started to deform and became curved as it is shown in Figure 6.61 scene 2. Thus we might conclude that the deformation of the plate causes the curved character of the re-wetting zone during the cooling. It explains also why the re-wetting zone is straight and horizontal during the experiment when we first used a new plate. After the first heat up the plate is already deformed and the re-wetting zone descends non-uniformly.

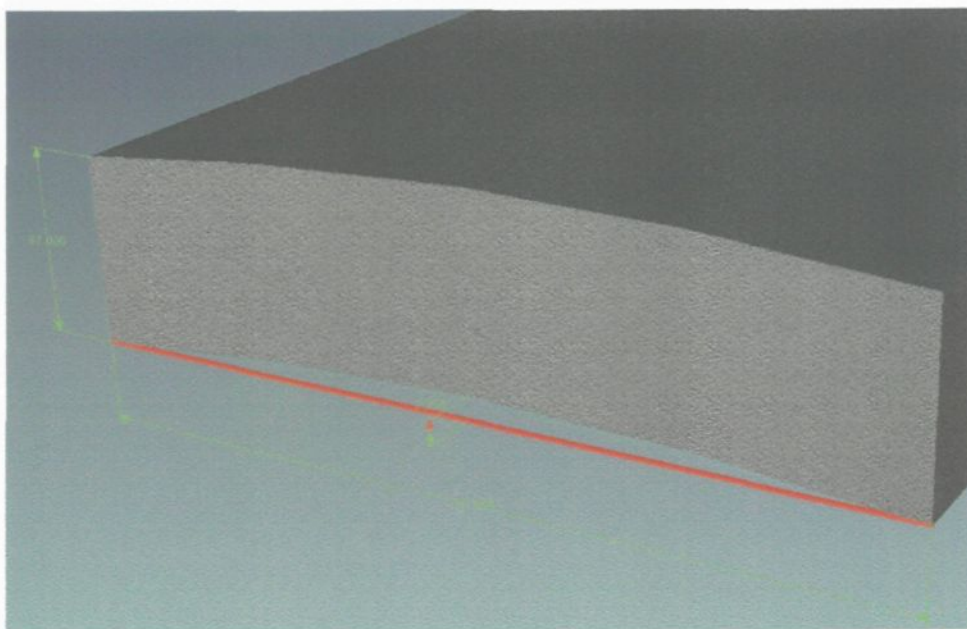


Figure 6.63: Deformation of the plate (bottom view)

## 6.7 Repeatability of the Boiling Phenomena

A very important point in performing the cooling experiment is its repeatability of the boiling phenomena. Due to the presence of turbulent flow along the surface and due to the effects of instable film boiling the results vary randomly among the experiments. Nevertheless there is a certain stable tendency in the results. To reduce the effects of randomly varying factors that do not reflect the general tendency of the phenomena, we repeated each experiment with the same boundary conditions three times. In this manner it was observed the results may vary but show the same trend as the other measurements. However, to give an idea of the variation among the experiments using the same setup some comparisons will be presented now. The change of temperature or heat flux results with respect to time are not suitable for a comparison because the cooling did not start at the same instant at each

experiment. Thus the results would be hard to compare without shifting the data. Comparing heat flux vs temperature data overcomes this difficulty. In Figure 6.64, the heat flux results from the experiments using tap water sprayed on a machined ingot at measurement point TC3 are shown. As we can see the heat flux is quite similar between the different

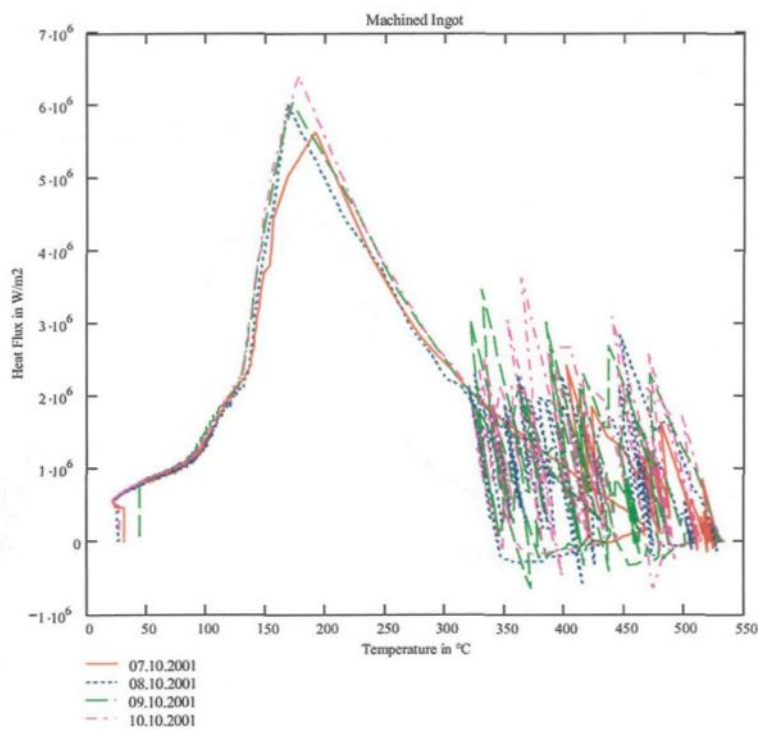


Figure 6.64: Measurement results made with a machined ingot and tap water

measurements in the zone up to 320 degree Celsius. In the fluctuating zone above 320 °C the results are hard to compare. To prove that the repeatability is also valid for an ingot with a rough surface we present the results for this ingot in Figure 6.65. The experiments shown in this figure were carried out also with tap water and the measurement point is TC3. Similarly as shown in Figure 6.64 for the machined ingot, here we can also see a certain

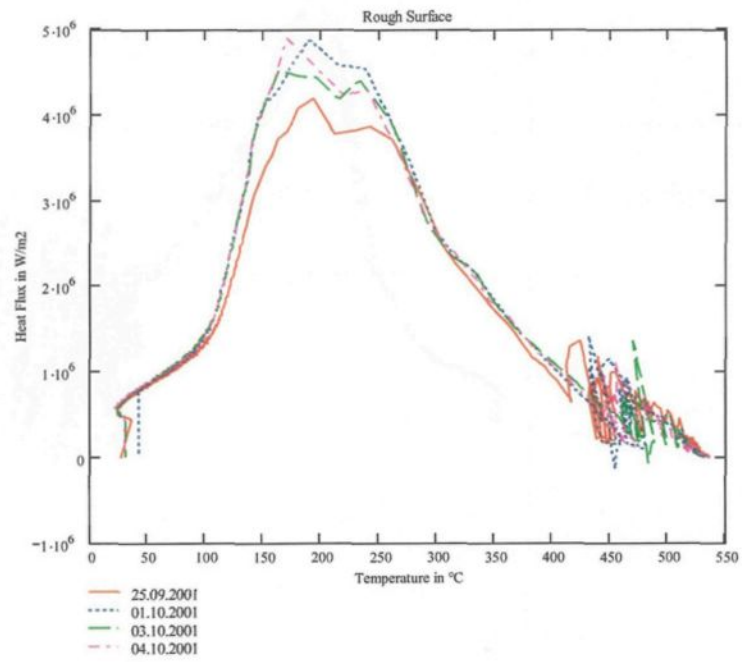


Figure 6.65: Heat flux results on a rough surface ingot with tap water at TC3

similarity in the shape of the heat flux curve. Although the maximal heat fluxes are not equal we might say that within a certain tolerance the results are comparable.

### 6.7.1 Repeatability depending on the Measurement Position

We have seen in figures shown previously that we can achieve a quite good repeatability. But the comparison in the former section was carried out only at measurement position TC3. Thus we will have a closer look to the heat flux vs temperature curves for the other measurement positions now. In Figure 6.66 and Figure 6.67 we see the results for a rough and a machined ingot for the measurement position TC2. Especially for the

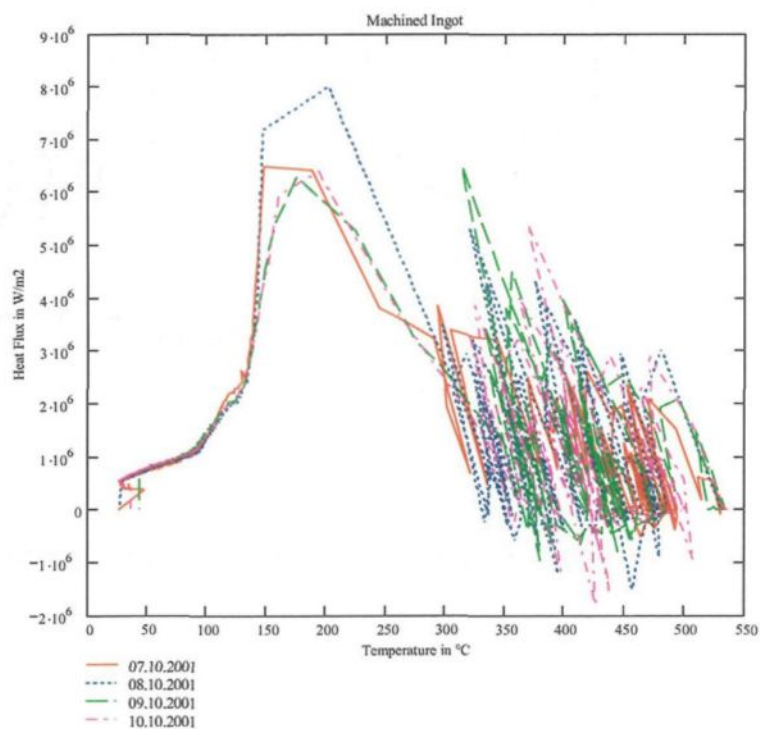


Figure 6.66: Heat flux vs temperature data at the measurement point TC2 on machined ingot

rough surface we observe less similarities between the measurements. Of course there are

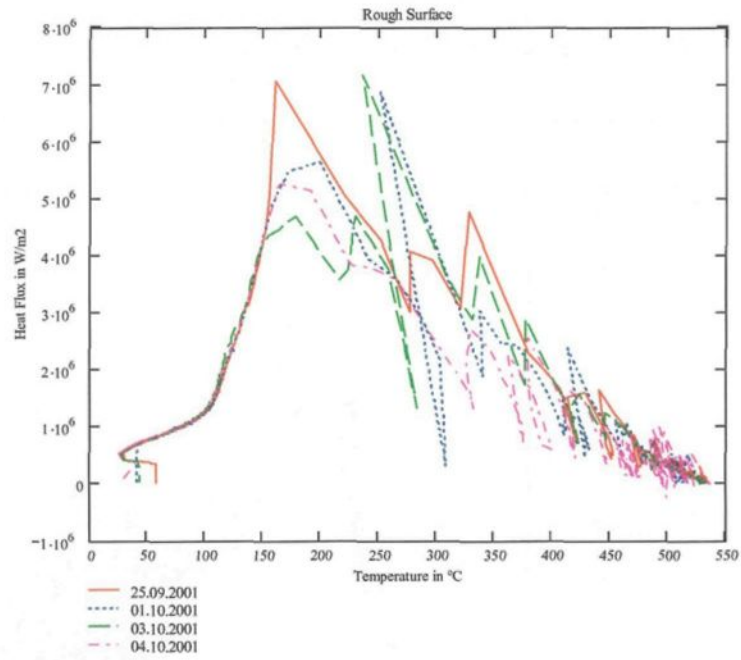


Figure 6.67: Heat flux vs temperature at the measurement point TC2

some tendencies in certain curves which can be retrieved in the others but the results are more diverse than those for measurement point TC3. To take a closer look at the results at measurement point TC4 the graphs for the rough and machined ingot are shown in Figure 6.68 and Figure 6.69, respectively. Here we can find a repeatability that is approximately

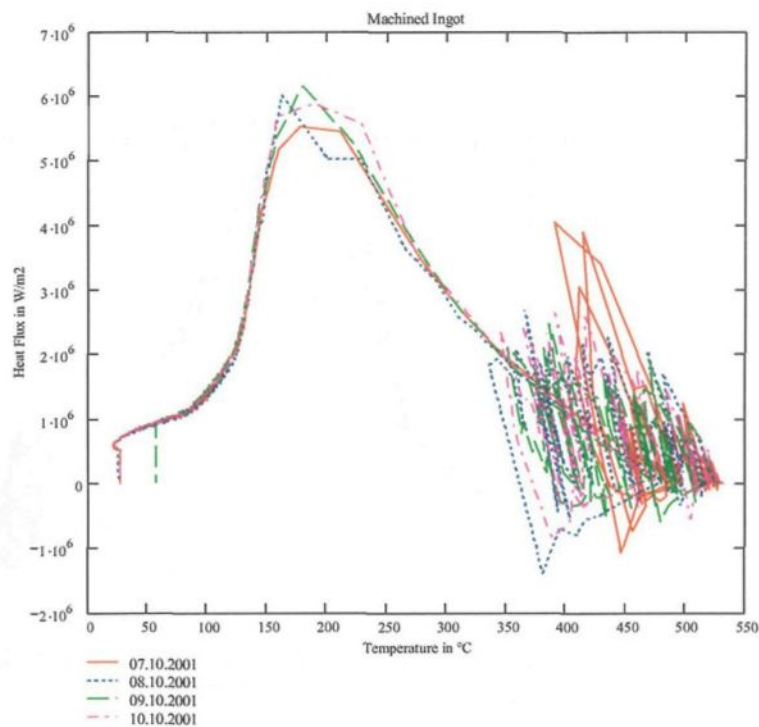


Figure 6.68: Results at measurement point TC4

equal to that of measurement point TC3. To conclude we can say that heat transfer measurements taken at the points TC3 and TC4 are more repetitive than those at TC2, where the initial random fluctuations are stronger. TC1 is directly in the impingement zone, where the heat flux is fluctuating the most randomly. It was also the point, where we lost the thermocouple contact the most frequently.

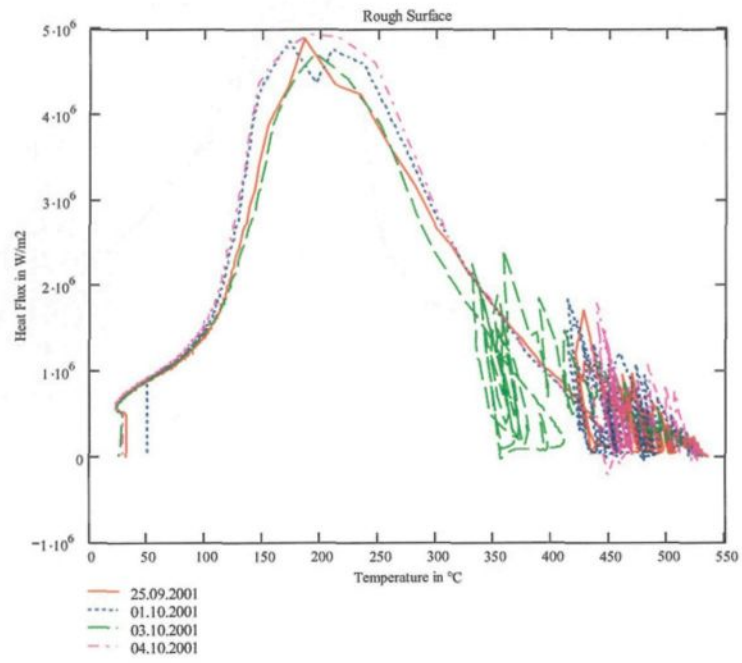


Figure 6.69: Results at measurement point TC4 on a rough ingot

### 6.7.2 Scale Deposition

After the last tests with the machined ingot we have seen a white to beige colored layer on the surface. The layer became more dense after each consecutive test. It was possible to remove the layer with a weak acid. Thus we assumed that this layer was scale which accumulated on the ingot surface. We observed an influence of the scale layer on the measured heat flux . The maximal heat flux measured during the last test was lower than those measured during the former tests when the scale layer was less dense. From that point of time we always treated the ingot surface with a weak phosphoric acid (1% of  $H_3PO_4$ ) before each test. After we treated the surface with the acid there was no sign of any scale deposition.

## Chapter 7

# Conclusions

The secondary cooling process of an aluminium ingot in DC casting has a complex character involving subcooled nucleate boiling, film boiling, re-wetting, forced convection heat transfer etc. Besides obtaining practically usable information about the heat flux, the study aimed also toward the exploration of the underlying mechanisms.

In the frame of my master thesis work my responsibility was to participate in the development, construction and testing of the experimental technique as well as to develop a simulation software. Thus, I constructed an operational experimental setup that can simulate the cooling process of an aluminium ingot, while also creating and investigating a measurement method to determine the heat flux without disturbing the ingot surface. During this investigation we developed a new measurement method using an open tipped thermocouple to measure the heat flux in a small size, null-point calorimetric cavity. With this method three consecutive experiments can be carried out, then the thermocouples have to be replaced and the cavities should be checked. This method of surface temperature

measurement is now working very well and leaves little room for further improvement. The method used for the visualization of the surface flow still needs more investigations to be able to characterize the surface boiling regimes in more detail. The problem of the illumination has to be solved to obtain better quality films of the cooling. In addition the laser sheet and laser illumination of the re-wetting zone must be tested with a stronger laser source. Another task should be the development of a precise synchronization of the D.A.Q system with the digital video camera.

I developed a simulation program which is used to determine if the Cook-Felderman equation is applicable to our needs. The results have shown that the Cook-Felderman equation is not precise for each measurement point. Also, the model has shown that the heat transfer through the ingot has to be treated at least in two dimensions to obtain reliable results.

These are the major findings of the work done during this project. The project provided already a lot of answers to the initial questions as demonstrated in proper sections, but there are still a lot of room for further experiments and investigations to understand the experimental observations and to obtain further answers to the still uncertain aspects of the project.

## **7.1 Experimental Results**

All the tests presented in the subsection 4.6 were compared to analyze the surface heat flux. Figure 7.1 shows the test series and conclusions drawn. The listed groups refer to the groups described in Table 4.23.

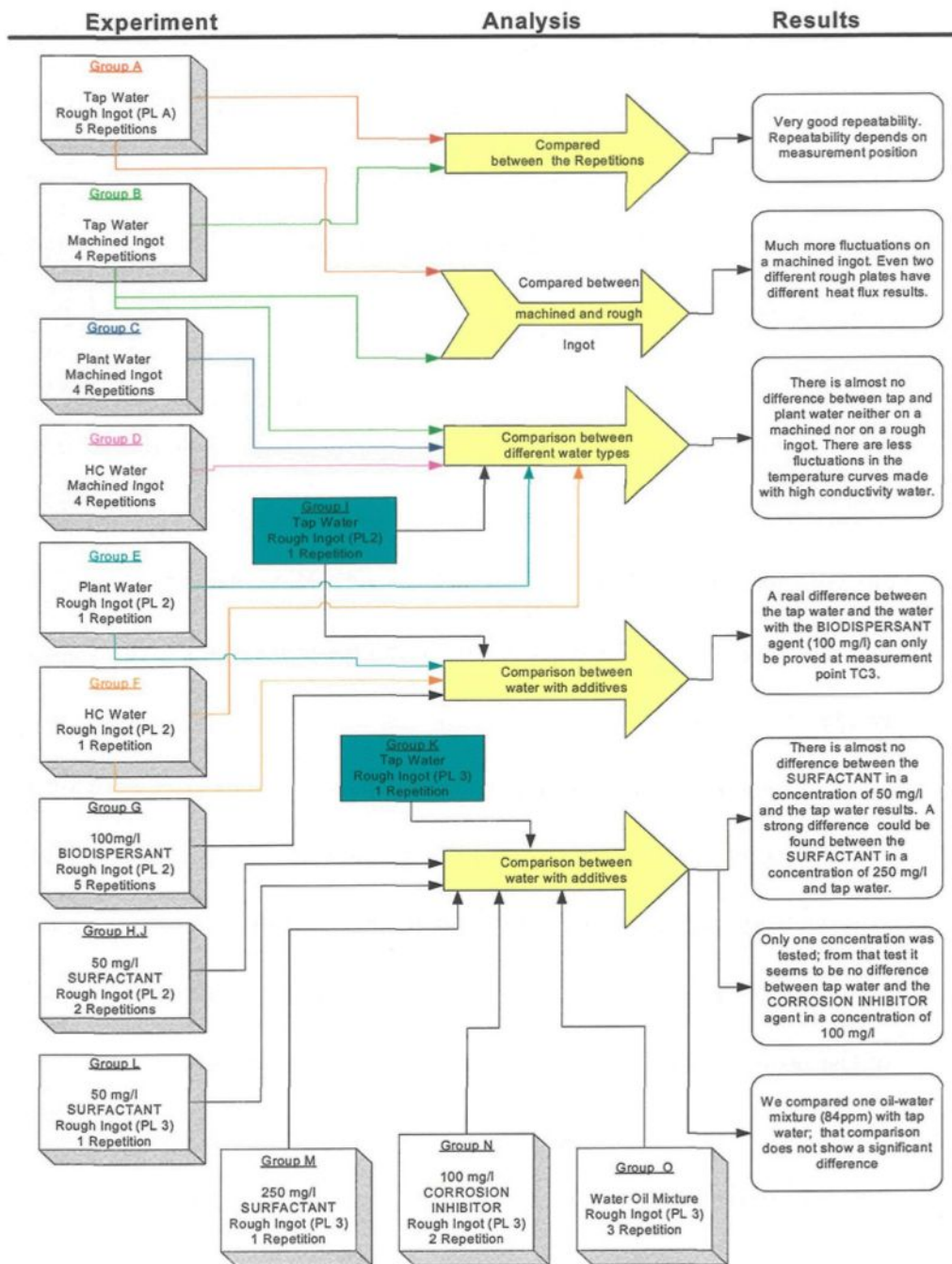


Figure 7.1: Comparison of the tests and their results

### **7.1.1 Repeatability**

We must distinguish between the repeatability of the heat transfer phenomena and that of the measurement technique. It could be found that in overall, the experiments have a very good repeatability. The repeatability is the best for the same plate and depends on the measurement position. This dependence can be explained with the vapor film formation and its fluctuations on the ingot surface, because at the beginning certain parts of the water film are less stable (see Section 6.5). Thus the thermocouples at measurement positions close to the impingement zone are more affected by the unstable water film fluctuations.

### **7.1.2 Comparison of a Machined and a Rough Ingot**

It was shown that the machined ingot has stronger fluctuations in the zone above 300 °C. The temperature curves of the rough ingot have less random fluctuations, however, different rough surface ingots do not produce the same surface heat flux results. There are several differences in the factors that influence surface boiling in the case of rough and machined plates. The reason why there are more fluctuations on a machined ingot than on a rough one can only be explained by the surface structure and microstructure. The difference in surface microstructure influences the number of nucleation sites. The varying orientation of the surface elements results in different retention forces for the liquid film, which ultimately influences the stability of the vapor bubbles on the surface.

### **7.1.3 Different Water Types and Additives**

The experiments have shown that there are less fluctuations in the cooling curves when high conductivity water is used than in those carried out with tap or plant water. A

difference between tap and plant water could not be detected. The biodispersant water agent in a concentration of  $10\frac{\text{mg}}{\text{l}}$  as well as the surfactant water additive a concentration of  $50\frac{\text{mg}}{\text{l}}$  showed almost the same cooling characteristics as tap water. Only in a concentration of  $250\frac{\text{mg}}{\text{l}}$  of the surfactant water additive resulted in a shorter cooling time and a slighter drop in the temperature decrease. In addition there are more fluctuations during the temperature decrease when surfactant water additive is used compared to the results obtained using the tap water. This difference might be explained with the foam development in the water and vapor film during the cooling. During the tests with the water corrosion inhibitor only one concentration was used. All experiments conducted with a concentration of  $100\frac{\text{mg}}{\text{l}}$  did not show a difference compared the results with tap water. Tests were also performed with a water-oil mixture of 84 ppm on a rough surface ingot. So far we could not find a significant difference, when the results with oil-water mixture were compared to tap water results.

#### **7.1.4 Characteristics of the cooling curves**

There are certain characteristics of the cooling curves which can be explained by the dynamics and morphology of the cooling water film. It was discovered that once the water film is separated from the ingot there are at least two different zones. The zone directly under the re-wetting line is quite stable. This means there is almost no water touching the surface. In the zone below that we find a disintegrating water film, forming jets and droplets. These jets and droplets touch randomly the surface and cause a temperature drop before the re-wetting line arrives. In addition, the three dimensional and wavy character of the separated water film can produce randomly contacts with the surface too (see Section 6.5). When the temperature decreases sometimes there is a temperature relapse in the

zone between 450 °C and 300 °C. We could observe this effect especially at the impingement zone (measurement position TC 1). We assume the unstable film boiling zone causes the temperature relapse (see Subsection 6.6.2).

It was observed that the re-wetting line changes its shape while descending. The deformation of the plate causes the curvature of the re-wetting zone during the cooling.

### 7.1.5 Summary

We have seen that we developed a reliable experimental procedure that reflects well the details of the cooling experiment. The surface boiling phenomenon has a randomly fluctuating character that varies along the height of the plate. Both the unstable film boiling and the waves and jets in the falling liquid film are responsible for these fluctuations. Based on the collected results we conclude that even different rough surface ingots do not produce the same surface heat flux results. This means that although there exist a similarity, it is difficult to compare the obtained results of two different ingots. In addition about 10 - 12 tests can be carried out with the same ingot due to the mechanical deformations.

It was observed that there are less fluctuations in the cooling curves if water with high conductivity is used. Although some results indicate a difference for certain measurement points the results using tap and plant water can be treated as practically identical. Similarly, it can be concluded that the effect of different additives on heat transfer does not seem very significant. We observe a difference in results with additives compared to the tap water results at the measurement position TC3 (about 180 mm below the impingement zone) and at higher concentrations that cause foaming. It was also discovered that the surface flow has a complicated spatial structure (morphology) with fluctuations. The effects

of these fluctuations on the temperature measurements were explained. It was also found that during repeated experiments, the deformation of the plate causes the re-wetting line to become curved. The influences of the water quality on the heat flux can be summarized as follows. The experiments have shown that there is only a noticeable influence on heat flux through the ingot when the water conductivity is high (about  $3200\mu S$ ). Using plant water with a conductivity of  $1900\mu S$  or tap water which has a conductivity of  $90\mu S$  did not show any differences. The Water-oil mixture, as received from the plant, did not show any affects on the heat flux at the ingot surface.

## 7.2 Numerical Results

The heat transfer through the ingot has to be treated at least in two dimensions to obtain reliable results. The maximal value (peak) of the vertical heat flux caused by the temperature gradient around the re-wetting zone has about the same magnitude as the horizontal surface heat flux. The results have shown that calculations carried out using the Cook-Felderman Equation are not precise for measurement points where the boundary conditions are not constant along the surface. The heat flux result calculated by the Cook-Felderman equation does not follow the random fluctuations in the temperature recordings fast enough. Thus it can be said that the Cook-Felderman Equation smoothes out the surface heat flux fluctuations. Our plate is not thick enough to represent a semi infinite solid as it is required by the Cook-Felderman equation.

### 7.3 Short Conclusions from the Comparison of the Numerical and Analytical Results

- The Cook-Felderman equation assumes one-dimensional heat conduction in a semi-infinite solid. Under the experimental conditions used during this project there are important deviations from the one-dimensional distribution and the ingot used is not thick enough to assume a semi-infinite solid.
- The difference between the results obtained using the Cook-Felderman equation and the numerical solution can reach more than 100% at the impingement zone (measurement position TC1); the error is smaller at lower positions.
- The Cook-Felderman solution smoothes out the heat flux curves.
- The Cook-Felderman equation cannot be applied to a measurement point near an insulated portion of the heat transfer surface.

### 7.4 Short Experimental Conclusions

- The experimental repeatability is very good, however, it is dependent on the measurement position.
- There are more fluctuations on a machined ingot. Even two different rough plates have different heat flux results.
- There is almost no difference between tap and plant water results neither on a machined nor on a rough ingot. There are less fluctuations in the temperature curves

obtained using high conductivity water.

- A real difference between the tap water and the water with biodispersant (100 mg/l) can only be observed about 0.2m below the impingement point (at measurement point TC3).
- There is almost no difference between the results obtained using a surfactant agent with a concentration of 50 mg/l and the tap water results. A significant difference was found between the results using surfactant agent with a concentration of 250 mg/l and those of tap water.
- Only one concentration was tested using a corrosion inhibitor; from that test it seems that there is no significant difference between tap water results and the results obtained using corrosion inhibitor agent with a concentration of 100 mg/l.
- We compared the experimental results using one oil-water mixture (84 ppm oil content) with those of tap water; that comparison does not show a significant difference

# Bibliography

- [1] [Http://srdata.nist.gov/its90/download/download.html](http://srdata.nist.gov/its90/download/download.html).
- [2] V. S. Arpaci. *Conduction Heat Transfer*. Addison-Wesley, University of Michigan, 1966.
- [3] R. Comolet. *Mécanique Expérimentale Des Fluides*. MASSON ET, 1969.
- [4] C.T.Kidd. *High Heat Flux Measurements and Experimental Calibrations*. NASA Conference Publication 3161, Langley Research Center, Hampton, Virginia (USA), 1992.
- [5] M. S. B. Frank Kreith. *Principles of Heat Transfer*. Harper and Row, fourth edition, 1986.
- [6] D. P. D. Frank P. Incropera. *Fundamentals of Heat and Mass Transfer*. John Wiley and Sons, fourth edition, 1996.
- [7] J. J. H.S. Carslaw. *Conduction of Heat in Solids*. Oxford at the Clarendon Press, second edition, 1959.
- [8] [Http://Loca.Neep.Wisc.Edu/~sam/2phase/ALL/Main/Node28.Html](http://Loca.Neep.Wisc.Edu/~sam/2phase/ALL/Main/Node28.Html).

- [9] C. C. James V. Beck, Ben Blackwell. *Inverse Heat Conduction , Ill-Posed Problems*. Wiley-Interscience Publication, 1985.
- [10] J.P.Holman. *Experimental Methods for Engineers*, volume 6. 1994.
- [11] A. N. K. Kurpisz. *Applying BEM and Sensitivity Coefficient Concept to Inverse Heat Conduction*. Springer Verlag, Hamburg, 1990.
- [12] A. N. K. Kurpisz. *Inverse Thermal Problems*. Computational Mechanics Publications, 1995.
- [13] R. B. L. Kiss, A. Charette. Determination of the heat transfer coefficients along the surface of a water film cooled ingot. 1996.
- [14] H. K. V. . W. Malalasekera. *An Introduction to Computational Fluid Dynamics, The Finite Volume Method*. Person Education, 1995.
- [15] T. Meenken. Determination of heat transfer coefficients on a water cooled ingot, 2000.
- [16] G. E. Myers. *Analytical Methods in Conduction Heat Transfer*, volume Second Edition. AMCHT Publications, 1998.
- [17] I. OMEGA Engineering. *OMEGA Complete Temperature Measurement Handbook and Encyclopedia*, volume 28. OMEGA Engineering, Inc., 1992.
- [18] C. Scott. *Transient Experimental Techniques for Surface Heat Flux Rates*. University of Minnesota, Minneapolis.
- [19] R. Vidal. Transient surface temperature measurements. In *Measurement in Unsteady Flow*, New York, May 1962. ASME Hydraulic Div. Conf.

- [20] Y. C. W. Rohsenow, J. Hartnett. *Handbook of Heat Transfer*. MCGraw-Hill, 3 edition, 1998.
- [21] F. M. White. *Fluid Mechanics*. McGRaw-HILL,INC., third edition, 1994.

## Appendix A

# Voltage to Temperature

## Conversion Mathcad Worksheet

### Transformation from Voltage in degree Celsius

$$b := \begin{pmatrix} 0 \\ 3.8689610^1 \\ -1.08267 \\ 4.7020510^{-2} \\ -2.1216910^{-6} \\ -1.1727210^{-4} \\ 5.3928010^{-6} \\ -7.9815610^{-8} \end{pmatrix} \quad a := \begin{pmatrix} 0 \\ 2.50835510^1 \\ 7.86010610^{-2} \\ -2.50313110^{-1} \\ 8.31527010^{-2} \\ -1.22803410^{-2} \\ 9.80403610^{-4} \\ -4.41303010^{-5} \\ 1.05773410^{-6} \\ -1.05275510^{-8} \end{pmatrix}$$

$$\text{ConversionK}(T) := \sum_{i=1}^{10} a_i (T \cdot 10^3)^{i-1} \quad \text{ConversionN}(T) := \sum_{i=1}^8 b_i (T \cdot 10^3)^{i-1}$$

$$\text{Convert\_VtoT\_K}(x) := \begin{array}{l} P \leftarrow \text{rows}(x) \\ \text{for } i \in 2..P \\ \quad \text{new}_{i-1} \leftarrow \text{ConversionK}(x_i) + \text{ReferenzTemp} \\ \text{new} \end{array}$$

$$\text{Convert\_VtoT\_N}(x) := \begin{array}{l} P \leftarrow \text{rows}(x) \\ \text{for } i \in 2..P \\ \quad \text{new}_{i-1} \leftarrow \text{ConversionN}(x_i) + \text{ReferenzTemp} \\ \text{new} \end{array}$$

$$\text{TC1} := \text{Convert\_VtoT\_N}(\text{TC1}) \quad \text{TC1}_1 = 527.505$$

$$\text{TC2} := \text{Convert\_VtoT\_N}(\text{TC2}) \quad \text{TC2}_1 = 527.521$$

$$\text{TC3} := \text{Convert\_VtoT\_N}(\text{TC3}) \quad \text{TC3}_1 = 526.227$$

$$\text{TC4} := \text{Convert\_VtoT\_N}(\text{TC4}) \quad \text{TC4}_1 = 524.728$$

Transformation of voltage to temperature

## Appendix B

# Main Calculation Loop

```
// initialization of the nodes
Node **nod;
nod=init_node(nodex,nodey,0);
// time loop
for (int t=0;t<timesteps;t++){
cout<<"Time loop: time step "<<t<<" is calculated now"<<endl;
// after the first time step the nodes are recalculated instead of reinitialized
    if (t>0) fill_node(nod,t);
//showcoeff();
//iteration cylce
    for (int it=0;it<ititeration;it++){
// loop for the space coordinates
        for (int x=0;x<=nodex;x++) {
```

```

for(int y=0;y<=nodey;y++) {
    if(x==0)
        help[y]=(nod[0][y].Su+nod[0][y].aP0* (Told[0][y])+(temperature[1][y])*
(nod[0][y].aE));
    if(x>0 && x<nodex)
        help[y]=(nod[x][y].Su+nod[x][y].aP0* (Told[x][y])+(nod[x][y].aW)*
(temperature[x-1][y])+(temperature[x+1][y])* (nod[x][y].aE));

    if(x==nodex)
        help[y]=(nod[nodex][y].Su+nod[nodex][y].aP0* (Told[nodex][y])+
(nod[nodex][y].aW)* (temperature[nodex-1][y]));

}

// arrays are prepared for the TDMA
for(int j=0;j<=nodey;j++){
    Ltdma[j]=nod[x][j].aN;
    Dtdma[j]=nod[x][j].aP;
    Utdma[j]=nod[x][j].aS;
    Ctdma[j]=help[j];
}

//TDMA is called with the prepared variables

```

```

        tdma(Ltdma,Dtdma,Utdma,Ctdma,x);
    }
}

//saves the results
    if (!fmod(t,each)) {    showtemp();

                            savezones(t);

                            savetemp(t);

                            save_q(file_info.heat_flux_x,qx,t);
                            save_q_zones(file_info.heat_flux_x_zone,qx,t);

                            save_q(file_info.heat_flux_y,qy,t);
                            save_q_zones(file_info.heat_flux_y_zone,qy,t);

                            //getch();

    }

// the temperature result is written in the matrix of the old temperature values
for (int x=0;x<=nodex;x++)
    for(int y=0;y<=nodey;y++)
        Told[x][y]=temperature[x][y];

de_alloc_node(nod);
}

```

## Appendix C

# Heat Flux Determination with Mathlab Worksheet

```
%calculates vertical heat flux with interpolation for each row
T=load('Flux_p39_nod60.txt','-ascii');
points=5; %how many points are taken for the fitting
degree=3; %order of the polynom
dy=0.0081666; %difference between two points(in x)
nodey=40; %row number of one submatrix (for one timestep)
%initialisation of variables
f=0;
t=0;
fit=0;
derfit=0;
count=0;
q=0;
%point where the fulx is calculated
x=3*dy;
for i=1:points
t(1,i)=i*dy;
end
```

```
for i=1:size(T,1)-4
f(1,1:points)=T(i,1:points);
temp(i,1:points)=f(1,1:points);
q(i)=(f(1,4)-f(1,3))/dy/2*237;
fit=polyfit(t,f,degree);
derfit=polyder(fit);
g(i)=0;
for j=1:degree
g(i)=g(i)+derfit(1,degree+1-j)*x^(j-1);
end
end
out=237*g'
out1=q';
save 'result_qy_surface_fit_60p2.txt' out -ascii
save 'result_qy_surface_diff.txt' out1 -ascii
```

## **Appendix D**

# **Mathcad Worksheet**

### **D.1 Comparison Analytical and Numerical Solution**

## D.2 Measurement Data Work Sheet

## Comprison analytic and numerical solution

### Definitions

ORIGIN := 1 needed variable for mathcad to define the nullpoint at 1  
Mathcad definition, to set the point zero to one

Lx := 0.1 length in x-direction

Ly := 0.25 length in y-direction

thermal conductivity , density , specific heat

k := 237  $\rho$  := 2703 cp := 903

M := 20 number of mesh in x direction

N := 20 number of mesh in y direction

$\Delta x := \frac{Lx}{M}$  \*  $\Delta x = 5 \times 10^{-3}$   $\Delta y := \frac{Ly}{N}$  \*  $\Delta y = 0.013$

$\alpha := \frac{k}{\rho \cdot cp}$  \* thermal diffusivity  $\alpha = 9.71 \times 10^{-5}$

$\Delta t := 1$  time difference, given by the measurment

i := 1 .. M j := 1 .. N helping variables

Kelvin := 274.15

P := 10 maximal number pf time steps

$Fo := \frac{\alpha \cdot \Delta t \cdot P}{Lx^2}$  \* Fourier Number at the last time step in x-direction

Fo = 0.097

$Fo(t) := \frac{\alpha \cdot t}{Lx^2}$  \* Function to calculate the Fourier Number at the any time step (in sec,) in x-direction

### Analytical Solution

$T_{init} := 100$  Initial temperature

$p := 40$  time step indication variable

This time step ( $p$ ) represents a real time (in sec.) of  $t := \Delta t \cdot p$  \*  $t = 40$

eigennumbers := 20 Total number, how many eigenvalues are be calculated

Eigenvalues for y-direction

Eigenvalues for x-direction

$$\delta n(n) := \frac{(2 \cdot n - 1)}{2 \cdot L_y} \cdot \pi$$
 \*

$$\delta m(n) := \frac{(2 \cdot n - 1)}{2 \cdot L_x} \cdot \pi$$
 \*

Definitions of the dimensionless length for the analytical solution

$$u_x(x) := \frac{x}{M}$$
 \*

$$u_y(y) := \frac{y}{N}$$
 \*

Analytical solution of the temperature distribution for a one-dimensional heat conduction problem by Ozisik (1985).

For the following boundary conditions:

$$\frac{d}{dy} T = 0 \text{ at } y = 0, t > 0 \text{ and } T = 0 \text{ at } y = L_y, t > 0$$

$$T_{y\_serie}(t, y) := \frac{4}{\pi} \cdot \sum_{n=1}^{\text{eigennumbers}} \frac{(-1)^{n+1}}{2 \cdot n - 1} \cdot e^{-\alpha \cdot t \cdot \delta n(n)^2} \cdot \cos(\delta n(n) \cdot y)$$
 \*

$$T_{x\_serie}(t, x) := \left[ \frac{4}{\pi} \cdot \sum_{n=1}^{\text{eigennumbers}} \frac{(-1)^{n+1}}{2 \cdot n - 1} \cdot e^{-\alpha \cdot t \cdot \delta m(n)^2} \cdot \cos(\delta m(n) \cdot x) \right]$$
 \*

Two dimensional temperature function

$$T_{2dim\_serie2}(x, y, t) := T_{y\_serie}(t, y) \cdot T_{x\_serie}(t, x)$$

Creation of the temperature matrix at the same nodal points as the numerical solution

$$T_{\text{matrix\_function}}(i) := \begin{cases} \text{for } x \in 0 \dots M - 1 \\ \text{for } y \in 0 \dots N - 1 \\ T_{\text{matrix}}_{y+1, x+1} \leftarrow T_{2\text{dim\_serie}2}\left(x \cdot \Delta x + \frac{\Delta x}{2}, y \cdot \Delta y + \frac{\Delta y}{2}, \Delta t \cdot i\right) \cdot T_{\text{init}} \\ T_{\text{matrix}} \end{cases}$$

$$M := M - 1 \quad * \quad N := N - 1 \quad *$$

$$T_x(i) := \begin{cases} \text{for } x \in 1 \dots M \\ T_{m_x} \leftarrow T_{x\_serie}(i \cdot \Delta t, \Delta x \cdot x) \\ T_m \end{cases} \quad T_y(i) := \begin{cases} \text{for } y \in 1 \dots N \\ T_{m_y} \leftarrow T_{y\_serie}(i \cdot \Delta t, \Delta y \cdot y) \\ T_m \end{cases}$$

Vector field is created calculating each matrix for every instant of time in the following function

$$T_{\text{analytic}} := \begin{cases} \text{for } p \in 0 \dots P \\ T_{\text{analytic}}_{p+1} \leftarrow T_{\text{matrix\_function}}(p) \\ T_{\text{analytic}} \end{cases}$$

Reading the results of the COSMOS software in the variable save

save :=

 C:\.\Cosmos\_5sec.txt

converting the variable save into the here used matrix form

```
cosmos :=
  u ← 1
  m ← 2
  n ← 1
  for i ∈ 1 .. (N·M)
    helpi ← saven,m
    m ← m + 2 if m < 6
    m ← 2 otherwise
    n ← n + 1 if m = 2
  for m ∈ 1 .. M
    for n ∈ 1 .. N
      cosmosn,m ← helpu
      u ← u + 1
  cosmos
```

N := N + 1 \*      M := M + 1 \*

### Numerical Solution

T :=

  
C:\..6\_sec\_1degree\_new\_2.txt

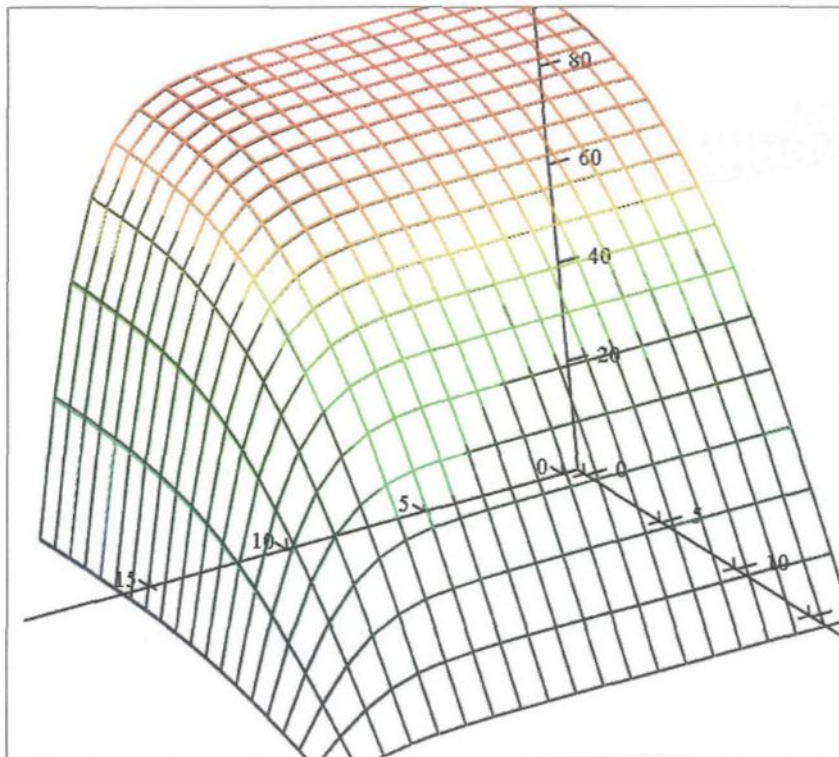
The numerical solution was saved in a file

The numerical solution was calculated with a time difference  $dt = 0.1$  seconds

$p := 6$  For this time step the following graphs will be plotted

The real time is:  $t := \Delta t \cdot p$   $t = 6$  seconds

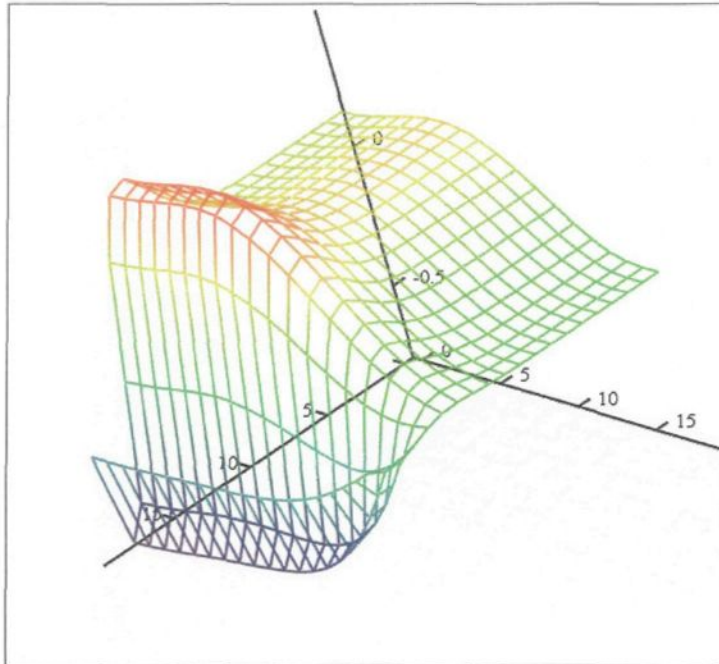
### Comparison in a 3D Plot



Tmatrix\_function(p), T

The plot shows the analytical solution plotted in colored grid and the numerical solution in black.

The difference in percent is plotted in the following graph



$$\frac{T_{\text{matrix\_function}}(p) - T}{T_{\text{init}}} \cdot 100$$

The maximal difference between the numerical and analytical solution in percent is:

$$\max\left(\frac{T_{\text{matrix\_function}}(p) - T}{T_{\text{init}}} \cdot 100\right) = 0.455 \%$$

$$\min\left(\frac{T_{\text{matrix\_function}}(p) - T}{T_{\text{init}}} \cdot 100\right) = -0.724 \%$$

$$\text{mean}\left(\frac{T_{\text{matrix\_function}}(p) - T}{T_{\text{init}}} \cdot 100\right) = 0.024 \%$$

**Experiment on 05.03.2002**

ORIGIN := 1

Data :=

  
 C:\..05.03.2002.txt

RefData :=

  
 C:\..\refblock.txt

P := zeilen(Data)      P = 482

Data := submatrix(Data, 2, P, 1, 24)

k := 237      ρ := 2702      cp := 903

K Type ThermocoupleWaterTempMould\_time := Data<sup><1></sup>WaterTempMould := Data<sup><2></sup>N Type Thermocouples measurment in DC VoltageTC1\_time := Data<sup><3></sup>      TC1\_time := submatrix(TC1\_time, 1, P - 2, 1, 1)TC1 := Data<sup><4></sup>      TC1<sub>1</sub> = 0.017TC2\_time := Data<sup><5></sup>      TC2\_time := submatrix(TC2\_time, 1, P - 2, 1, 1)TC2 := Data<sup><6></sup>TC3\_time := Data<sup><7></sup>      TC3\_time := submatrix(TC3\_time, 1, P - 2, 1, 1)TC3 := Data<sup><8></sup>TC4\_time := Data<sup><9></sup>      TC4\_time := submatrix(TC4\_time, 1, P - 2, 1, 1)TC4 := Data<sup><10></sup>N Type Thermocouple already in degree CelsiusBacksideTemp\_timeTC1 := Data<sup><11></sup>BacksideTempTC1 := Data<sup><12></sup>BacksideTemp\_timeTC2 := Data<sup><13></sup>BacksideTempTC2 := Data<sup><14></sup>

BacksideTemp\_timeTC3 := Data<sup>(15)</sup>

BacksideTempTC3 := Data<sup>(16)</sup>

BacksideTemp\_timeTC4 := Data<sup>(17)</sup>

BacksideTempTC4 := Data<sup>(18)</sup>

WaterTemp\_timeTC1 := Data<sup>(19)</sup>

WaterTempTC1 := Data<sup>(20)</sup>

WaterTemp\_timeTC2 := Data<sup>(21)</sup>

WaterTempTC2 := Data<sup>(22)</sup>

WaterTemp\_timeTC3 := Data<sup>(23)</sup>

WaterTempTC3 := Data<sup>(24)</sup>

RefBlockTemp := RefData<sup>(2)</sup>      already in degree Celsius

P := P - 1

dt := TC1\_time<sub>4</sub> - TC1\_time<sub>3</sub>      dt = 0.475

N := zeilen(RefData)      N = 86

### **Average Reference Block Temperature**

N := zeilen(RefBlockTemp)

$$\text{ReferenzTemp} := \frac{\sum_{i=2} \text{RefBlockTemp}_i}{N - 1}$$

ReferenzTemp = 25.234

## Transformation from Voltage in degree Celsius

$$b := \begin{pmatrix} 0 \\ 3.86896 \cdot 10^1 \\ -1.08267 \\ 4.70205 \cdot 10^{-2} \\ -2.12169 \cdot 10^{-6} \\ -1.17272 \cdot 10^{-4} \\ 5.39280 \cdot 10^{-6} \\ -7.98156 \cdot 10^{-8} \end{pmatrix}$$

$$a := \begin{pmatrix} 0 \\ 2.508355 \cdot 10^1 \\ 7.860106 \cdot 10^{-2} \\ -2.503131 \cdot 10^{-1} \\ 8.315270 \cdot 10^{-2} \\ -1.228034 \cdot 10^{-2} \\ 9.804036 \cdot 10^{-4} \\ -4.413030 \cdot 10^{-5} \\ 1.057734 \cdot 10^{-6} \\ -1.052755 \cdot 10^{-8} \end{pmatrix}$$

$$\text{ConversionK}(T) := \sum_{i=1}^{10} a_i \cdot (T \cdot 10^3)^{i-1}$$

$$\text{ConversionN}(T) := \sum_{i=1}^8 b_i \cdot (T \cdot 10^3)^{i-1}$$

$$\text{ConversionK}(10.23) = -1.279 \times 10^{28}$$

$$\text{Convert\_VtoT\_K}(x) := \begin{cases} P \leftarrow \text{zeilen}(x) \\ \text{for } i \in 2..P \\ \text{new}_{i-1} \leftarrow \text{ConversionK}(x_i) + \text{ReferenzTemp} \\ \text{new} \end{cases}$$

$$\text{Convert\_VtoT\_N}(x) := \begin{cases} P \leftarrow \text{zeilen}(x) \\ \text{for } i \in 2..P \\ \text{new}_{i-1} \leftarrow \text{ConversionN}(x_i) + \text{ReferenzTemp} \\ \text{new} \end{cases}$$

$$TC1_3 = 0.0172$$

$$\text{ConversionK}(TC1_3) = 418.988$$

$$TC1 := \text{Convert\_VtoT\_N}(TC1)$$

$$TC1_1 = 537.022$$

$$TC2 := \text{Convert\_VtoT\_N}(TC2)$$

$$TC2_1 = 537.022$$

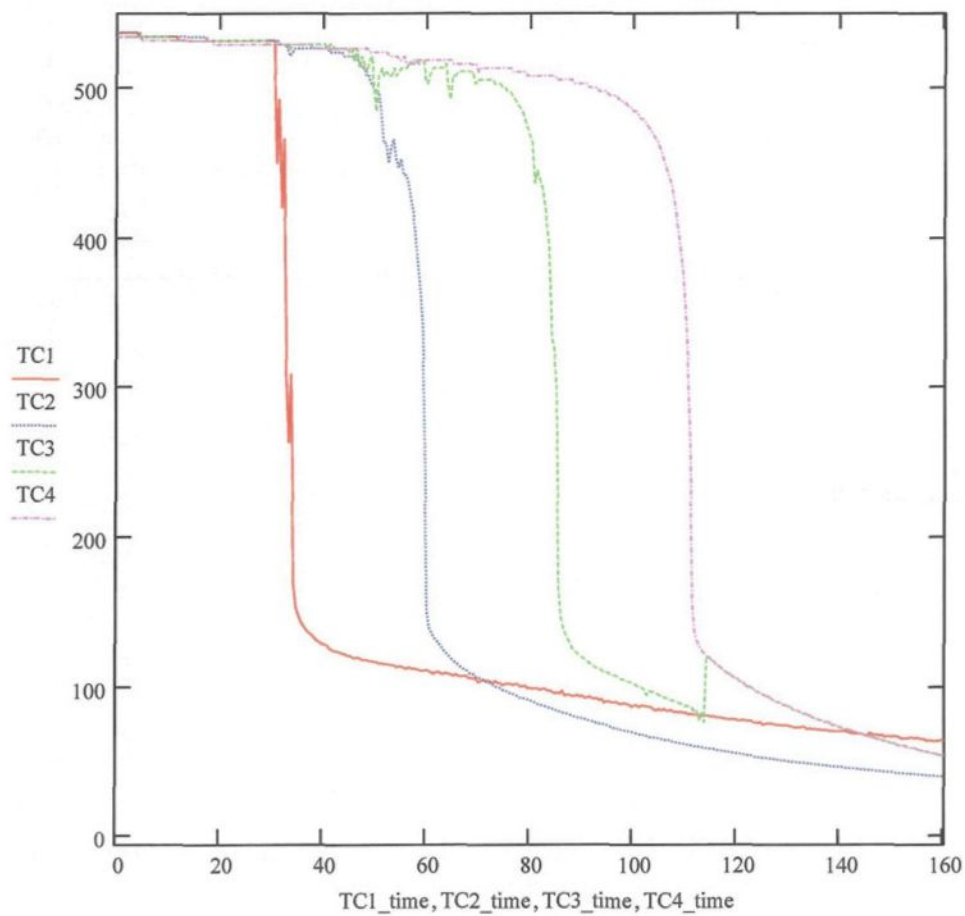
$$TC3 := \text{Convert\_VtoT\_N}(TC3)$$

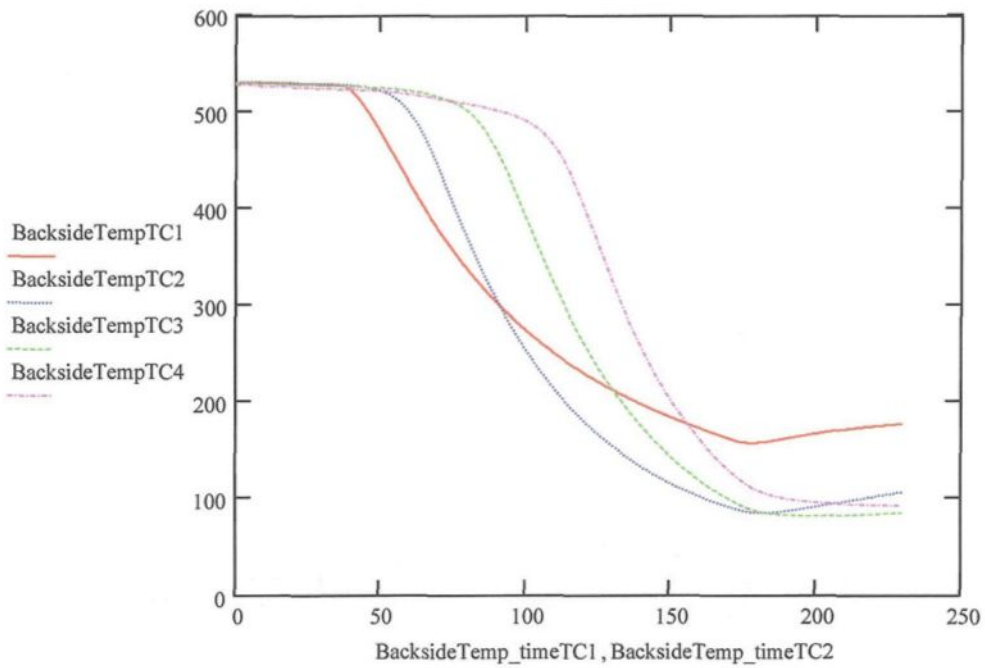
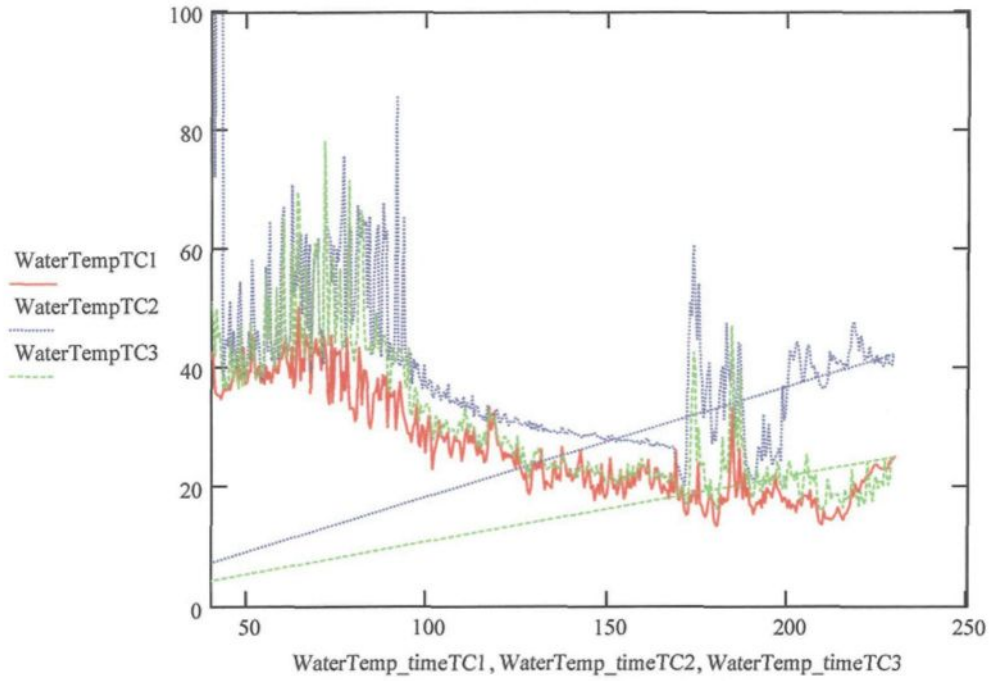
$$TC3_1 = 534.416$$

$$TC4 := \text{Convert\_VtoT\_N}(TC4)$$

$$TC4_1 = 534.416$$

$$\text{step} := 1 .. P$$





**Calculation of the heat flux using the Cook- Felderman Equation**

$$dt := TC1\_time_4 - TC1\_time_3 \quad dt = 0.475 \quad TC1\_time_1 = 0.052$$

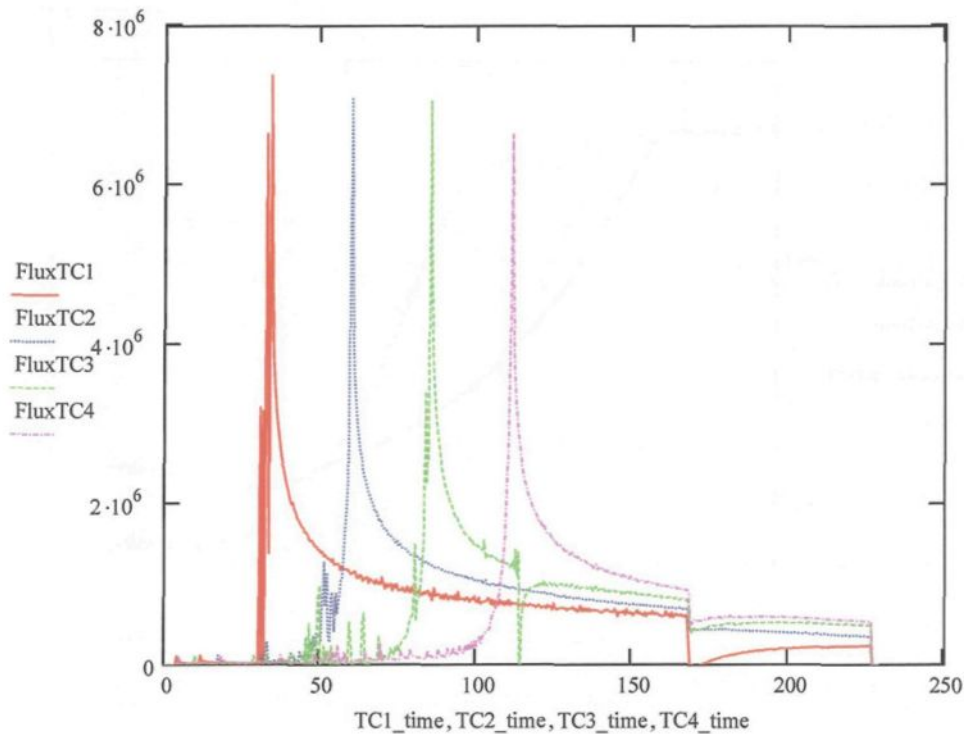
$$\text{flux}(\text{Temp}, \text{Zeit}) := \begin{cases} \text{for } p \in 2..P-6 \\ qf_p \leftarrow -2 \sqrt{\frac{k \cdot \rho \cdot cp}{\pi}} \cdot \sum_{i=2}^p \frac{(\text{Temp}_i - \text{Temp}_{i-1})}{(\sqrt{\text{Zeit}_p - \text{Zeit}_i} + \sqrt{\text{Zeit}_p - \text{Zeit}_{i-1}})} \\ qf_p \leftarrow 0 \\ qf \end{cases}$$

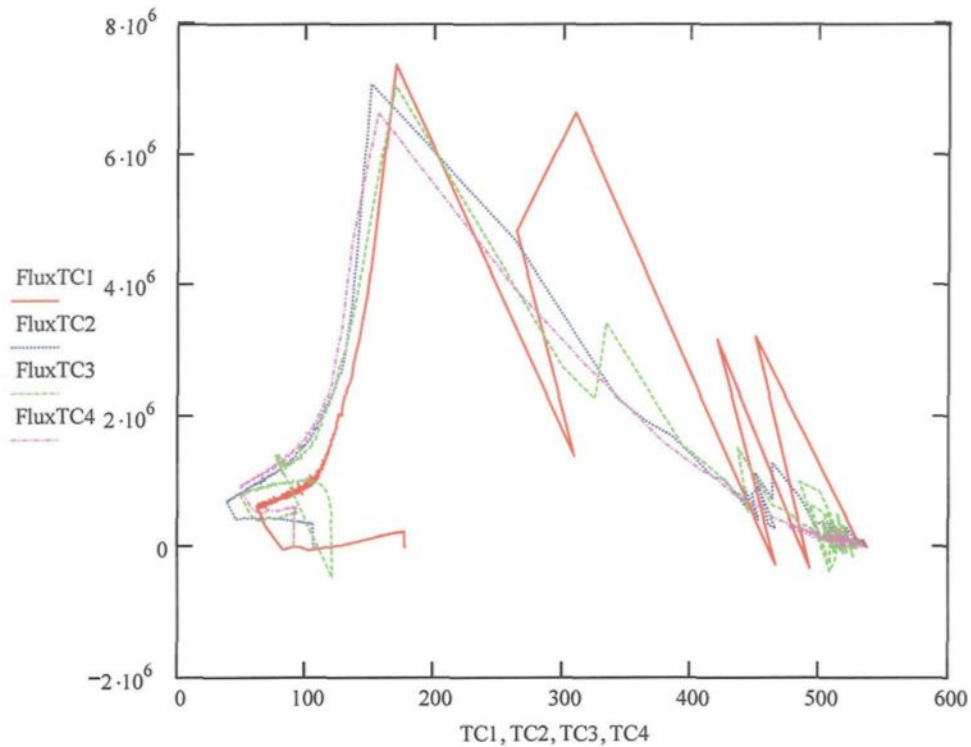
$$\text{FluxTC1} := \text{flux}(\text{TC1}, \text{TC1\_time})$$

$$\text{FluxTC2} := \text{flux}(\text{TC2}, \text{TC2\_time})$$

$$\text{FluxTC3} := \text{flux}(\text{TC3}, \text{TC3\_time})$$

$$\text{FluxTC4} := \text{flux}(\text{TC4}, \text{TC4\_time})$$





### Alarm Limits

$dt := TC1\_time_4 - TC1\_time_3$        $dt = 0.475$

16:13:52.119	Low Limit	103	Scan = 99 , Value = 0.00421097 =TC1
16:14:13.621	Low Limit	104	Scan = 144 , Value = 0.00312406=TC2
16:14:34.229	Low Limit	105	Scan = 187 , Value = 0.00351753=TC3
16:14:59.616	Low Limit	106	Scan = 240 , Value = 0.00351968=TC4

Start time: 16:13:05.405

Alarm 1:  $99 \cdot dt = 47.025$  s

Alarm 2:  $144 \cdot dt = 68.4$  s

Alarm 3:  $187 \cdot dt = 88.825$  s

Alarm 4:  $240 \cdot dt = 114$  s

```
FluxTC1 := submatrix(FluxTC1, 1, P - 1, 1, 1)
FluxTC2 := submatrix(FluxTC2, 1, P - 1, 1, 1)
FluxTC3 := submatrix(FluxTC3, 1, P - 1, 1, 1)
FluxTC4 := submatrix(FluxTC4, 1, P - 1, 1, 1)

zeilen(TC1) = 480  zeilen(TC1_time) = 480  zeilen(FluxTC1) = 480
```

```
Ausgabe := | Out ← TC1_time
            | Out ← erweitern(Out, TC1)
            | Out ← erweitern(Out, FluxTC1)
            | Out ← erweitern(Out, TC2_time)
            | Out ← erweitern(Out, TC2)
            | Out ← erweitern(Out, FluxTC2)
            | Out ← erweitern(Out, TC3_time)
            | Out ← erweitern(Out, TC3)
            | Out ← erweitern(Out, FluxTC3)
            | Out ← erweitern(Out, TC4_time)
            | Out ← erweitern(Out, TC4)
            | Out ← erweitern(Out, FluxTC4)
            | Out
```

 C:\..\Out.txt

Ausgabe

## Appendix E

# Finite Volume Program Code

### E.1 Finite Volume Source Code in C++

```
// Solver.cpp: implementation of the Solver class.  
  
//  
  
////////////////////////////////////  
  
#include "stdafx.h"  
  
#include "Solver.h"  
  
#include "Node.h"  
  
#include "Properties.h"  
  
#include "calculation_properties.h"  
  
#include "File.h"// schauen ob noetig  
  
#include "Matrix.h"  
  
#include "b_element.h"  
  
#include <iostream.h>
```

```
#include <iomanip.h>

#include <fstream.h>

#include <stdlib.h>

#include <string.h>

#include <math.h>

#define stringmax 250

////////////////////////////////////

// Construction/Destruction

////////////////////////////////////

Solver::Solver()

{

// physical properties are insterted by the properties object

//Properties Platte;

file_info.read_file("work_folder.txt");

    Platte.readfile(file_info.property);

    Tinit=Platte.Tinit;

    nodey=Platte.nodey;

    nodex=Platte.nodex;

    dx=Platte.dx;

    dy=Platte.dy;

    k=Platte.conductivity;

// calculation values are taken from the cal. object
```

```

//calculation_properties info;

calc_info.read_properties(file_info.calculation);

each=calc_info.each;

timesteps=calc_info.timesteps;

ititeration=calc_info.ititeration;

dt=calc_info.dt;

}

Solver::~Solver()

{

Platte::~Properties();

file_info::~File();

calc_info::~calculation_properties();

b::b_element();

}

//-----

void Solver::solve(){

double **qx;

double **qy;

// initialization of the matrices

Matrix point(nodex+1,nodey+1);

temperature=point.init(Tinit);

Told=point.init(Tinit);

```

```

qx=point.init(0);

qy=point.init(0);

point.~Matrix();

// arrays for the TDMA

double *Ltdma=new double[nodey+1];

double *Dtdma=new double[nodey+1];

double *Ctdma=new double[nodey+1];

double *Utdma=new double[nodey+1];

double *help=new double[nodey+1];

// initialization of the nodes

Node **nod;

nod=init_node(nodex,nodey,0);

// time loop

for (int t=0;t<timesteps;t++){

cout<<"Time loop: time step "<<t<<" is calculated now"<<endl;

// after the first time step the nodes are recalculated instead of reinitialized

    if (t>0) fill_node(nod,t);

//showcoeff();

//iteration cylce

    for (int it=0;it<ititeration;it++){

// loop for the space coordinates

        for (int x=0;x<=nodex;x++) {

```

```

for(int y=0;y<=nodey;y++) {

if(x==0)

    help[y]=(nod[0][y].Su+nod[0][y].aP0*(Told[0][y])+(temperature[1][y])*(nod[0][y].aE));

if(x>0 && x<nodex)

    help[y]=(nod[x][y].Su+nod[x][y].aP0*(Told[x][y])+(nod[x][y].aW)*(temperature[x-1][y])+(tempera

if(x==nodex)

    help[y]=(nod[nodex][y].Su+nod[nodex][y].aP0*(Told[nodex][y])+(nod[nodex][y].aW)*(temperature

1[y]));

}

// arrays are prepared for the TDMA

for(int j=0;j<=nodey;j++){

    Ltdma[j]=nod[x][j].aN;

    Dtdma[j]=nod[x][j].aP;

    Utdma[j]=nod[x][j].aS;

    Ctdma[j]=help[j];

}

//TDMA is called with the prepared variables

tdma(Ltdma,Dtdma,Utdma,Ctdma,x);

}

```

```

    }

make_qx(qx);

make_qy(qy);

//saves the results

    if (!fmod(t,each)) {    showtemp();

                            savezones(t);

                            savetemp(t);

                            save_q(file_info.heat_flux_x,qx,t);

                            save_q_zones(file_info.heat_flux_x_zone,qx,t);

                            save_q(file_info.heat_flux_y,qy,t);

                            save_q_zones(file_info.heat_flux_y_zone,qy,t);

                            //getch();

    }

/*

extract(nodex,6,t,"Textract_1.txt",temperature);

extract(nodex,10,t,"Textract_2.txt",temperature);

extract(nodex,14,t,"Textract_3.txt",temperature);

extract(nodex,17,t,"Textract_4.txt",temperature);

extract(0,6,t,"qx_extract_1.txt",qx);

extract(0,9,t,"qx_extract_2.txt",qx);

```

```

extract(0,13,t,"qx_extract_3.txt",qx);

extract(0,16,t,"qx_extract_4.txt",qx);

extract(0,6,t,"qy_extract_1.txt",qy);

extract(0,9,t,"qy_extract_2.txt",qy);

extract(0,13,t,"qy_extract_3.txt",qy);

extract(0,16,t,"qy_extract_4.txt",qy);

*/

// the temperature result is written in the matrix of the old temperature values

for (int x=0;x<=nodex;x++)

    for(int y=0;y<=nodey;y++)

        Told[x][y]=temperature[x][y];

//showtold();

//showtemperature();

de_alloc_node(nod);

}

delete [] help;

delete [] Ltdma;

delete [] Dtdma;

delete [] Utdma;

delete [] Ctdma;

}

//-----

```

```

void Solver::tdma(double *Ltdma,double *Dtdma,double *Utdma,double *Ctdma,int xposition){

int nodenumber;

nodenumber=nodey+1;

double temp;

double *P=new double[nodenumber+1];

double *Q=new double[nodenumber+1];

double *X=new double[nodenumber+1];

//showrow(Dtdma,nodenumber);

for (int i=0;i<=nodenumber;i++){

P[i]=Q[i]=0;

}

for ( i=0;i<=nodenumber;i++){

if (i!=0){ temp=Dtdma[i]+Ltdma[i]*P[i-1] ;

Q[i]=(Ctdma[i]-Ltdma[i]*Q[i-1])/temp;

P[i]=-Utdma[i]/temp;

}

else { temp=Dtdma[i];

Q[i]=(Ctdma[i]-Ltdma[i])/temp;

P[i]=-Utdma[i]/temp;

}

}

}

```

```

//solution[nodenumbr]=P[nodenumbr]+Q[nodenumbr];

X[nodenumbr]=Ctdma[nodenumbr]/Dtdma[nodenumbr];

for ( i=(nodenumbr-1);i>=0;i-){

    X[i]=P[i]*(X[i+1])+Q[i];

    //    cout<<X[i]<<endl;

}

for (i=0;i<=nodenumbr;i++){

    temperature[xposition][i]=X[i];

//cout<<temperature[xposition][i]<<endl;

}

    delete [] X;

delete [] P;

delete [] Q;

//

// return 0;

//    return X;

}

//-----

Node **Solver::init_node(int max_x,int max_y,int time){

```

```

cout<<" The nodes are initialized here for the time step: "<<time<<endl;

max_x++;

max_y++;

//max_x=max_y=2;

Node **table;

table= new Node *[max_x];

for (int i=0;i<=max_x;i++){

    table[i]= new Node [max_y];

}

/*for (int y=0;y<max_y;y++)

    delete [] table[y];

delete [] table;

*/

for (int x=0;x<=max_x-1;x++){

    for (int y=0;y<=max_y-1;y++){

        table[x][y].make_coeff(x,y,time,file_info,Platte,calc_info,b);

        table[x][y].write_coeff();

    }

}

```

```
return table;

}

//-----

void Solver::fill_node(Node ** table,int time){

cout<<" The nodes are re-calculated here for the time step: "<<time<<endl;

for (int x=0;x<=nodex;x++){

for (int y=0;y<=nodey;y++){

table[x][y].make_coeff(x,y,time,file_info,Platte,calc_info,b);

//table[x][y].write_coeff();

}

}

}

//-----

void Solver::de_alloc_node(Node **nods){

for (int x=0;x<=nodex;x++){

for (int y=0;y<=nodey;y++){

nods[x][y].~Node();

}
```

```

    }

}

/*

for (int y=0;y<nodey+2;y++)

    delete [] nods[y];

delete [] nods;

*/

}

//-----

// calculates the heat flux distribution along the horizontal lines

void Solver::make_qx(double **qx){

for (int y=0;y<=nodey;y++)

    for (int x=0;x<nodex;x++)

        qx[x][y]=-k/dx*(temperature[x][y]-temperature[x+1][y]);

}

//-----

//-----

// calculates the heat flux distribution along the vertical lines

void Solver::make_qy(double **qy){

for (int x=0;x<=nodex;x++)

```

```
    for (int y=0;y<nodey;y++)

        qy[x][y]=-k/dy*(temperature[x][y]-temperature[x][y+1]);

    }

    //-----

    //-----

    // saves the temperature result in a matrix form in a txt file

    void Solver::extract(int x, int y,int count,char filename[stringmax],double **matrix){

    char quo="";

    char Title[20];

    char name[stringmax];

    strcpy(Title,"Conduction");

    ofstream outdaten;

    File output;

    strcpy(name,output.path);

    output.~File();

    strcat(name,filename);

    if(count==0)

        outdaten.open(name,ios::trunc);

    else

        outdaten.open(name,ios::app);
```

```

    if (!outdaten.good()){ cout<<" Error: Could NOT open the file: "<<name<<endl;

        cout<<" Error occurred in Class: Solver::extract()"<<endl;

        exit(-1);

    }

        outdaten<<dt*count<<"    ";

        outdaten<<setiosflags(ios::scientific)<<setprecision(10)<<matrix[x][y];

        outdaten<<"\n";

        outdaten.close();

    }

    //-----

    // saves the temperature result in a matrix form in a txt file

    void Solver::save_q(char name[stringmax],double **q,int count){

        char quo="";

        char Title[20];

        strcpy(Title,"Heat Flux");

        ofstream outdaten;

        /*

        File output;

        strcpy(name,output.temp_matrix);

```

```

output.~File();

*/

if(count==0)

    outdaten.open(name,ios::trunc);

else

    outdaten.open(name,ios::app);

if (!outdaten.good()){ cout<<" Error: Could NOT open the file: "<<name<<endl;

                        cout<<" Error occurred in Class: Solver::save_q()"<<endl;

                        exit(-1);

                    }

    if (count==0){

outdaten<<"Title="<<quo<<Title<<quo<<"\n";

outdaten<<"Variables: "<<"dx = "<<dx <<" dy= "<<dy<<" dt= "<<dt <<"\n";

        outdaten<<"values in x: "<<nodex<<"\n";

        outdaten<<"values in y: "<<nodey<<"\n";

        outdaten<<"\ntimestep= "<< count<<"\n";

    }

else

outdaten<<"\ntimestep= "<< count <<"\n";

```

```

    for (int y=0;y<=nodey;y++){

        for (int x=0;x<=nodex;x++){

            outdaten<<setiosflags(ios::scientific)<<setprecision(10)<<q[x][y]<<"    ";

        }

        outdaten<<"\n";

    }

    outdaten.close();

}

//-----

// saves the temperature result in a matrix form in a txt file

void Solver::savetemp(int count){

    char quo="";

    char Title[20];

    char name[stringmax];

    strcpy(Title,"Conduction");

    ofstream outdaten;

    strcpy(name,file_info.temp_matrix);

    /*

    File output;

    strcpy(name,output.temp_matrix);

    output.~File();

```

```

*/

if(count==0)

    outdaten.open(name,ios::trunc);

else

    outdaten.open(name,ios::app);

if (!outdaten.good()){ cout<<" Error: Could NOT open the file: "<<name<<endl;

                        cout<<" Error occurred in Class: Solver::savetemp()"<<endl;

    exit(-1);

}

if (count==0){

outdaten<<"Title="<<quo<<'Title<<quo<<"\n";

outdaten<<"Variables: "<<"dx = "<<dx <<" dy= "<<dy<<" dt= "<<dt <<"\n";

    outdaten<<"values in x: "<<nodex<<"\n";

    outdaten<<"values in y: "<<nodey<<"\n";

    outdaten<<"\ntimestep= "<< count<<"\n";

}

else

outdaten<<"\ntimestep= "<< count <<"\n";

for (int y=0;y<=nodey;y++){

```

```

        for (int x=0;x<=nodex;x++){

outdaten<<setiosflags(ios::scientific)<<setprecision(10)<<temperature[x][y]<<"    ";

        }

outdaten<<"\n";

        }

outdaten.close();

}

//-----

//-----

// saves the heat flux result in a TECPlot format.

void Solver::save_q_zones(char name[stringmax],double **q,int count){

char quo="";

int imax=nodex+1;

int jmax=nodey+1;

char Title[20];

//char name[stringmax];

strcpy(Title,"Heat flux");

//File output;

//strcpy(name,output.temp_zones);

//output.~File();

ofstream outdaten;

```

```

if(count==0)

    outdaten.open(name,ios::trunc);

else

    outdaten.open(name,ios::app);

if (!outdaten.good()){ cout<<" Error: Could NOT open the file: "<<name<<endl;

                        cout<<" Error occurred in Class: Solver::savezones()"<<endl;

    exit(-1);

}

if (count==0){

outdaten<<"Title="<<quo<<Title<<quo<<"\n";

outdaten<<"Variables= "<<quo<<"X"<<quo<<" "<<quo<<"Y"<<quo<<" "<<quo<<"Z"<<quo<<"\n";

}

outdaten<<"Zone"<<" "<<"T="<<quo<<count<<quo<<" I="<<imax<<" "<<"J="<<jmax<<"

"<<"F=Point"<<"\n";

for (int x=0;x<=nodex;x++){

    for (int y=0;y<=nodey;y++){

        outdaten<< (x+1)*dx << " ";    //the values are seperated by a tab

        outdaten<< (y+1)*dy << " ";

        outdaten<<setiosflags(ios::scientific)<<setprecision(10)<< q[x][nodey-y];

        outdaten<<"\n";// a endlime is written after the three values

```

```
    }

}

    outdaten.close();    // stream is closed

}

//-----
//-----

// saves the temperatuer result in a TECPlot format.

void Solver::savezones(int count){

char quo="";

int imax=nodex+1;

int jmax=nodey+1;

char Title[20];

char name[stringmax];

strcpy(Title,"Conduction");

File output;

strcpy(name,output.temp_zones);

output.~File();

ofstream outdaten;
```

```

if(count==0)

    outdaten.open(name,ios::trunc);

else

    outdaten.open(name,ios::app);

if (!outdaten.good()){ cout<<" Error: Could NOT open the file: "<<name<<endl;

                        cout<<" Error occurred in Class: Solver::savezones()"<<endl;

    exit(-1);

}

if (count==0){

outdaten<<"Title="<<quo<<Title<<quo<<"\n";

outdaten<<"Variables="<<quo<<"X"<<quo<<" "<<quo<<"Y"<<quo<<" "<<quo<<"Z"<<quo<<"\n";

}

outdaten<<"Zone"<<" "<<"T="<<quo<<count<<quo<<" I="<<imax<<" "<<"J="<<jmax<<"

"<<"F=Point"<<"\n";

for (int x=0;x<=nodex;x++){

    for (int y=0;y<=nodey;y++){

        outdaten<< (x+1)*dx << " ";    //the values are seperated by a tab

        outdaten<< (y+1)*dy << " ";

        outdaten<<setiosflags(ios::scientific)<<setprecision(10)<< temperature[x][nodey-y];

        outdaten<<"\n";// a endlene is written after the three values

```

```
    }  
  
    }  
  
    outdaten.close();    // stream is closed  
  
    }  
  
    //-----  
    //-----  
  
    void Solver::showtemp(){  
  
    cout << "\n This is the contents of the temperature matrix " << endl;  
  
    for (int y=0;y<=nodey;y++){  
  
    for (int x=0;x<=nodex;x++){  
  
    cout<< temperature[x][y] << " ";  
  
    }  
  
    cout<<endl;  
  
    }  
  
    //getch();  
  
    }  
  
    //-----
```

```
//-----  
  
void Solver::showtold(){  
  
cout << "\n This is the contents of the told matrix " << endl;  
  
for (int y=0;y<=nodey;y++){  
  
for (int x=0;x<=nodex;x++){  
  
cout << Told[x][y] << " ";  
  
}  
  
cout << endl;  
  
}  
  
//getch();  
  
}  
  
//-----  
  
void Solver::showrow(double *row,int number){  
  
cout << "\n This is the contents of the row ";  
  
for (int y=0;y<=number;y++){  
  
cout << "\n " << row[y] ;  
  
}  
  
}  
  
//-----
```

```
void Solver::set_itteration(int zahl){  
  
    itteration=zahl;  
  
}  
  
//-----  
  
//-----  
  
void Solver::set_timeinterval(double zahl){  
  
    dt=zahl;  
  
}  
  
//-----  
  
void Solver::set_timesteps(int zahl){  
  
    timesteps=zahl;  
  
}  
  
//-----  
  
void Solver::set_each(int zahl){  
  
    each=zahl;  
  
}  
  
//-----
```